Planetary-Scale Impacts and their Geophysical Consequences

Inauguraldissertation

der Philosophisch-naturwissenschaftlichen Fakultät

der Universität Bern

vorgelegt von

Harry Ballantyne

von United Kingdom

Leiter der Arbeit:

PD Dr. Martin Jutzi

Space Research & Planetary Sciences (WP)

This work is licensed under the Creative Commons Attribution-NonCommercial 4.0 International License. To view a copy of this license, visit http://creativecommons.org/licenses/by-nc/4.0/ or send a letter to Creative Commons, PO Box 1866, Mountain View, CA 94042, USA.

source: https://doi.org/10.48549/3879 | downloaded: 25.4.2024

Planetary-Scale Impacts and their Geophysical Consequences

Inauguraldissertation

der Philosophisch-naturwissenschaftlichen Fakultät

der Universität Bern

vorgelegt von

Harry Ballantyne

von United Kingdom

Leiter der Arbeit:

PD Dr. Martin Jutzi

Space Research & Planetary Sciences (WP)

Von der Philosophisch-naturwissenschaftlichen Fakultät

angenommen.

Bern, 09.09.2022

Der Dekan:

Prof. Dr. Marco Herwegh

Contents

1 Introduction **5**

2 Modelling Impact Events using SPHLATCH **20**

2.1 Lagrangian Fluid Dynamics 21

2.2 Smoothed Particle Hydrodynamics (SPH) 23

2.2.1 Kernel Interpolation 24

2.2.2 Discretisation into Particles 26

2.3 Particle-Based Fluid Dynamics 28

2.3.1 Treatment of Shocks 31

2.3.2 Solid Mechanics 32

2.3.3 Conserving Angular Momentum with Strength 38

2.3.4 Variable Smoothing Length 41

2.3.5 Time Integration 46

2.4 Equation of State 48

2.5 Gravity and Particle Neighbours 57

2.5.1 Gravity 57

2.6 Barnes-Hut Tree 59

2.6.1 Multipole Approximation 59

2.6.2 Tree 60

2.6.3 Particle Neighbour Search 62

2.7 Composition and Strength 65

3 Coupling Impact Models with Geophysics **75**

3.1 Spherical Grid 76

3.2 Crust Production Scheme 80

3.2.1 Magma 82
3.2.2 Crust Crystallisation 83
3.2.3 Primordial Crust 84
3.2.4 Mantle Depletion 86
3.2.5 Intact Crust 88
3.2.6 Particle Distribution 88
3.3 Coupling with Long-Term Interior Evolution 94
3.3.1 StagYY 96
3.3.2 Coupling with SPH simulations 97
3.3.3 Preliminary Results 101

4 Investigating an Impact-Induced Martian Dichotomy 110

5 Sputnik Planitia as an Impactor Remnant 170

6 Acknowledgements 195

Chapter 1

Introduction

The formation of celestial bodies is dictated by collisions at all length-scales. At the largest scales, collisions between galaxies can drive accelerated bouts of star formation (e.g. Struck, 1999). At the smallest scales, (sub)micron-sized dust grains orbiting such stars collide and coagulate (e.g. Birnstiel et al., 2016). In the intermediate of these two extremes, planetary-sized ($\sim$1000 km radius) objects experience large-scale impacts that can have profound consequences not only for their immediate post-impact characteristics, but also for their subsequent evolution over geological time.

Understanding the relevance of these planetary-scale impacts in the general context of planetary systems requires knowledge of the events that lead to their occurrence, and thus an understanding of how the dust grains in the initial protoplanetary disc around the star grew to become massive rocky bodies with intersecting orbital paths. For very small grains, growth is driven by van der Waals forces which cause dust particles to coagulate. As these grains grow, however, the relative importance of such forces decreases, increasing the likelihood of grains bouncing off of one and other or fragmenting rather than sticking together to form larger aggregates. With greater grain-size also comes greater relative velocities (Weidenschilling, 1977), and laboratory experiments have shown that such high relative velocities make fragmentary collisions the most-likely outcome, thereby leading to a limit in aggregate growth (Beitz et al., 2011). Additionally, at similar sizes to this *fragmentation barrier*, the drag force on the dust grains caused by the slower-moving, surrounding gas reaches a maximum, causing systematic radial drift towards (and eventual accretion

onto) the central star, thus causing another growth limit known as the *radial-drift barrier* (e.g. Gonzalez et al., 2017). These effects are most prominent at centimetre to metre length-scales, leading to their collective name as the *metre-size barrier*. This barrier is a persistent problem for planet formation theory, and, although there are various proposed scenarios to circumvent this barrier such as dust traps at gas pressure maxima (Johansen et al., 2007; Gonzalez et al., 2017), it remains an open question in astrophysical research.

Regardless of how these barriers are overcome, observations of rocky objects with sizes far greater than a few metres prove that growth cannot be entirely halted in reality. Once bodies reach sizes of at least a kilometre, they are large enough to withstand the head-wind drag force of the gas and thus avoid significant radial drift towards the star. Such bodies are known as *planetesimals*. Accretion then continues through low-velocity, merging collisions. Bodies are now large enough for gravity to become important: the more massive the body, the more its gravity bends the trajectory of nearby objects, and thus the more likely these bodies are to experience collisions. This preferential growth in more massive bodies leads to *runaway growth*, which causes initially small differences in mass to be exponentially magnified (Greenberg et al., 1978; Wetherill and Stewart, 1989). These massive bodies then take on a new moniker as so-called *planetary embryos*. Once the mass ratio between embryos and planetesimals becomes too large ($\sim$100), however, the strong gravity fields of the embryos act to excite the orbits of the planetesimals, increasing their velocity dispersion. This dramatically affects the efficiency of accretion, effectively curbing this initial phase of rapid growth. Instead, a new phase of accretion occurs, known as *oligarchic growth*, whereby the accretion-rate of planetary embryos decreases with increasing mass-ratio (Kokubo and Ida, 1998, 2000). This causes accretion rates to become gradually slower as the embryo mass ratios approach unity, and thus leads to a few tens to hundreds of remaining embryos in the inner disc of similar mass, around that of Mars (see Figure 1.1). Further out, temperatures are cold enough for ices to readily form on the dust grains (i.e. beyond the *snow line*), and this extra solid material allows some embryos to reach a large enough mass to accrete significant gas and potentially become gas giants.

During oligarchic growth, the embryos in the inner disc are orderly spaced, and

the surrounding planetesimals keep their orbits stable and circular through dynamical friction. Eventually, the planetesimal population becomes too depleted to maintain this stability, leading to a chaotic stage of embryo interactions and collisions. This is the final stage of planet formation known as the *giant impact epoch*, and, while its precise timing may be affected by the potential migration of gas giants (Walsh et al., 2011), the planetary-scale collisions it induces shape the final—and most striking—characteristics of planets in a planetary system.

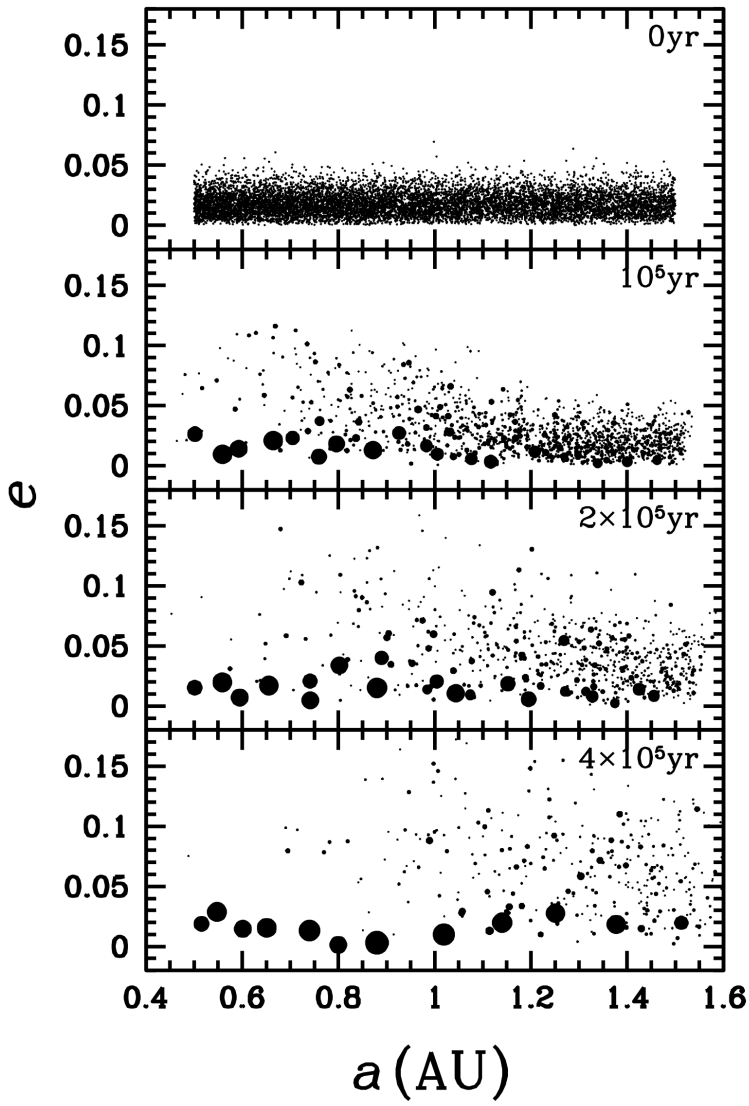

Figure 1.1: An example N-body simulation displaying oligarchic growth of planetary embryos, from Kokubo and Ida (2002); Raymond et al. (2014). Each plot shows a snapshot in time of a planetesimal system in eccentricity, e, and semi-major axis, a, in astronomical units. The circles represent individual bodies and have radii proportional to the true value.

In the Solar System, these impacts are thought to be responsible for many of the most distinguishing features of its planetary inhabitants. Possibly the most well-known of these features is that the existence of our Moon, which is widely accepted to be the result of a giant impact between a Mars-sized object (often named *Theia*) and the proto-Earth. The initial motivation for this impact came from the analogously large mass-ratio between the Earth and the Moon, which leads to an unusually high total angular momentum of the system (Cameron and Ward, 1976). This scenario is difficult to explain in what were the main competing hypotheses of the time, co-accretion and capture, but is a natural outcome of an oblique giant impact which propels significant mantle rock into Earth-orbit which quickly accumulates to form a massive satellite. Further support for the giant impact hypothesis comes from Apollo measurements of both seismic activity and chemical composition (through returned rock samples). Seismic analysis indicates that the Moon has a dense iron core, but it is only 4% of the Moon's total mass, which is extremely small compared to Earth's core fraction of $\sim$30%, or Mars' of $\sim$25% (Khan et al., 2022), which are comparable to the free iron mass fraction in unmelted *chondrites* (the primitive building blocks of planets). Lunar samples prove to be overwhelmingly igneous with very little water and volatiles. These properties are well-aligned with the giant impact scenario, as the Moon would have formed predominantly from rocky mantle material as the iron present in Theia would have almost entirely merged with the dense proto-Earth core, and this rocky material would have been initially liquid (and even partially vaporised) due to the both decompression and shock heating (Asphaug, 2014).

In terms of core mass fraction, Mercury is at the other end of the spectrum with an iron core that is $\sim$60–70% of its total mass. This may also be the result of a giant impact in one of two possible scenarios. In the first, the more massive proto-Mercury experienced a high velocity ($\sim$ 30 km/s), near head-on impact from a smaller body that caused the loss of a large fraction of its mantle material as it was stripped away and ejected from Mercury's gravitational grasp (Benz et al., 2007). In the second, and more recently proposed scenario, the proto-Mercury instead took on the role of the smaller body in a collision, where it collided with a larger body at an oblique angle while retaining enough momentum to remain unbound to the

system in a so-called *hit-and-run* collision (Asphaug and Reufer, 2014). As the proto-Mercury grazes the larger body, it loses a fraction of its mantle, while the larger body survives almost entirely intact (see Figure 1.2). The high core mass fraction of Mercury can be achieved in a single, catastrophic event at high impact velocities, or a combination of several less dramatic hit-and-run collisions.

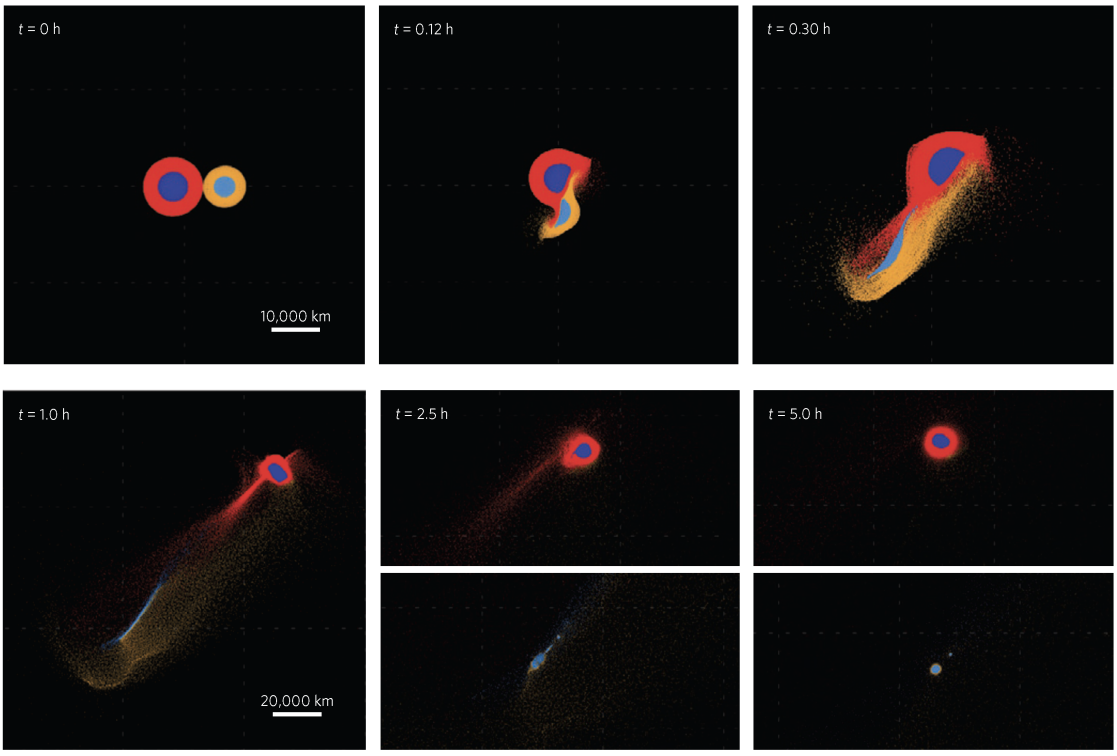

Figure 1.2: A Mercury-forming hit-and-run impact, from Asphaug and Reufer (2014). These plots come from an SPH simulation, and display the two bodies as a slice through the impact plane, revealing their interior. The colours indicate composition, with purple/blue denoting iron core material and red/orange denoting rocky mantle. Here, we see that the larger body remains largely intact during the impact, while the smaller body experiences the ejection of almost its entire rocky mantle, leaving an iron-rich, Mercury-like body.

While Mars' core mass is in reasonable proportion to its total mass, other prominent characteristics of the Red Planet are thought to be the result of a giant impact. The most notable of these is the so-called *Martian Dichotomy*: a stark contrast in both elevation and crustal thickness between the two Martian hemispheres (e.g. Andrews-Hanna et al., 2008). Due to the near-elliptical shape of the so-called *northern lowlands*, this feature has been attributed to a large-scale impact that excavated

the uppermost material of Mars and left a huge impact crater in its place that has remained to the present (Marinova et al., 2008; Andrews-Hanna et al., 2008; Nimmo et al., 2008). Such an impact may have also led to the birth of Mars' two moons, Phobos and Deimos. The tiny pair of satellites bear some resemblance to asteroids; however, their near-circular, equatorial orbits make asteroid-capture difficult to reconcile. Formation from an impact-induced debris-disc such as that produced by the aforementioned collision, on the other hand, would naturally produce such orbital properties, while also matching the high porosities predicted of the moons (Rosenblatt et al., 2020, and references therein).

Although the dynamical circumstances that could lead to planetary-scale impacts beyond the inner Solar System are not well understood, there are still several properties of the outer-system inhabitants that may be a consequence of such events. Uranus, for instance, has an extremely tilted spin-axis relative to the plane of the ecliptic, which may be the result of an oblique impact from a projectile of at least Earth mass (Safronov, 1969; Slattery et al., 1992; Reinhardt et al., 2020). Neptune may have also experienced a similar, but head-on impact, which would deposit significant mass and energy into its deep interior, potentially explaining its higher heat flux and mass than Uranus (Reinhardt et al., 2020).

At much smaller scales, the Pluto system also exhibits unusual properties that motivate a potential giant impact origin. Relative to its size, Pluto harbours the largest moon in the Solar System, known as Charon (Stern et al., 2018, and references therein). By analogy to our own Moon (e.g. Canup, 2004), this gives the system an unusually high angular momentum, and is widely regarded to be the result of a giant impact (McKinnon, 1989; Canup, 2005, 2011). Unlike the lunar scenario, however, Charon is thought to have formed intact, with its progenitor impacting Pluto at an oblique angle that propelled the impacting body directly into Pluto's orbit (Canup, 2005, 2011). The other moons of Pluto are much smaller, displaying near-coplanar orbits with Charon that are close to circular, thus suggesting that all of Pluto's moons are of the same impact origin, where Charon's tiny siblings serve as the surviving remnants of the initial impact-induced debris-disc (Canup, 2011).

Scientific investigations into these collisions are almost always performed via shock-physics simulations based on fluid dynamics theory. While small-scale impacts

are well-suited to grid based codes such as iSALE (Amsden et al., 1980; Collins et al., 2004; Wünnemann et al., 2006), the highly deformed surfaces and abundance of ejecta in planetary-scale impacts make mesh-free methods such as *smoothed-particle hydrodynamics* (*SPH*) an ideal choice. Such methods accurately model the immediate effects of an impact, but can only simulate these events for short timescales on the order of days (post-impact). In reality, however, the dramatic consequences of a planetary-scale impact can have great influence on the evolution of a body's properties over geological timescales of millions, or even billions of years.

Pluto is useful example in this regard, as its most recognisable feature (other than its largest moon Charon) is a huge, elongated basin known as Sputnik Planitia (Stern et al., 2015), that makes up the majority of the dwarf planet's much-loved "heart" (i.e. the Lombaugh Regio). Recent observations from NASA's New Horizons space probe show this feature to be one of the deepest regions of Pluto (Stern et al., 2015; Schenk et al., 2018), which, along with its quasi-elliptical shape, has led to suggestions of an impact-origin. However, various geophysical changes are thought to have occurred since its emplacement. First, a thick layer of nitrogen ice accumulated in the basin over a roughly 10,000 year time period, thus concealing its original depth (Bertrand and Forget, 2016). Then, a geophysical phenomenon known as *true polar wander* occurred, which caused the feature to move (relative to Pluto's spin-axis) towards the equator, eventually settling in its current, near-equator position. The precise nature of this true polar wander stage is under debate, as an additional mass excess beneath the basin is required for the intended equatorward motion (Keane et al., 2016); however, it is clear that the long-term geophysical effects must be considered if this feature is to be scientifically explained.

The origin of the Martian Dichotomy is also deeply embedded in the field of geophysics. Outside of the impact hypothesis, separate investigations utilising sophisticated mantle convection models have sought to explain Mars' crustal disparity via preferential mantle upwelling beneath the southern hemisphere that leads to increased crust production relative to the north (Zhong and Zuber, 2001; Zhong et al., 2008; Keller and Tackley, 2009). While this requirement can be successfully fulfilled in these models, they have thus far been incapable of adhering to the strict time constraints of the Dichotomy's formation, which is known to have occurred within

the first ∼900 Myr (Frey, 2006). These issues motivated a proposed hybrid-scenario, whereby the Dichotomy-forming impact instead occurred in Mars' southern hemisphere, and the significant impact-induced melt crystallised to form a crust that is thicker than the primordial crust in the north (Reese and Solomatov, 2006, 2010; Reese et al., 2010; Golabek et al., 2011). This may in fact be a more consistent scenario, as the energies involved in an impact large enough to excavate crust from almost the entire northern hemisphere of Mars would undoubtedly introduce melting and thus potential post-impact crust production (Ballantyne et al., 2022). The great temperature anomaly introduced to Mars by such an impact will almost certainly influence the long-term evolution of its interior, however, and so studying this scenario comprehensively requires an accurate model of the impact coupled with a sophisticated mantle convection model that can predict long-term crust production. A proof-of-concept study by Golabek et al. (2018) gave a glimpse into the possibilities of such a coupled model (see Figure 1.3), but only modelled mantle convection for ∼500,000 years after impact.

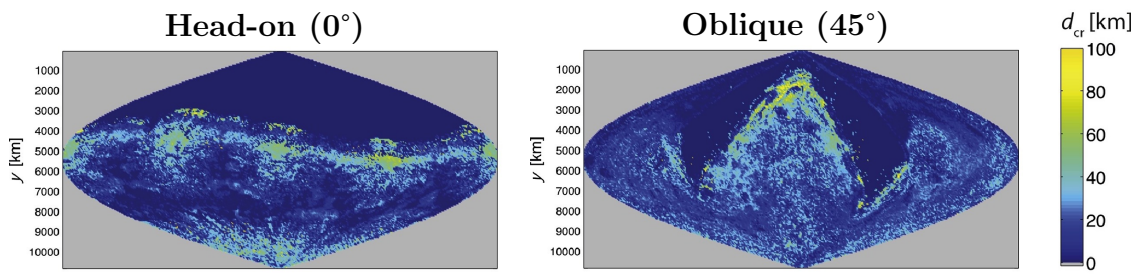

Figure 1.3: Crust distribution for a Mars-like body from combined SPH simulations with long-term interior evolution models. Adapted from Golabek et al. (2018). Colour displays crustal thickness ∼0.5 Myr after impact from a 1000 km radius impactor at an angle 0° (left) and 45° (right) from the surface normal.

Clearly, planetary-scale impacts are a topic that sits comfortably at the crossroads of the traditional disciplines of astrophysics and geophysics, and must be approached accordingly. In this thesis, such an approach is adopted throughout, as SPH simulations are coupled with geophysical models to study both the immediate and long-term effects of planetary-scale impacts. In Chapter 2, the SPH code used for this purpose, SPHLATCH, is described in detail, including derivations of the background continuum mechanics theory along with descriptions of any practical

developments applied to the code. In Chapter 3, the application of these SPH impact simulations to geophysical investigations is described. A particular focus of this chapter is the crust distribution inferred by an impact simulation; a novel scheme that estimates post-impact crust across a body directly from SPH simulations is described, as well as a more sophisticated approach involving a long-term mantle convection code. In the remaining chapters, these methods are applied in two scientific studies: Chapter 4 investigates the feasibility of an impact-induced Martian Dichotomy through a large suite of SPH simulations coupled with the crust-production scheme of Chapter 3, and finally, Chapter 5 presents a previously undiscovered impact regime that may explain the Sputnik Planitia region of Pluto.

Bibliography

A. A. Amsden, H. M. Ruppel, and C. W. Hirt. SALE: A Simplified ALE computer program for fluid flow at all speeds. Technical Report June, Los Alamos Scientific Lab, NM (USA), 1980.

J. C. Andrews-Hanna, M. T. Zuber, and W. B. Banerdt. The Borealis basin and the origin of the martian crustal dichotomy. *Nature*, 453(7199):1212–1215, 2008. ISSN 14764687. doi: 10.1038/nature07011.

E. Asphaug. Impact origin of the moon? *Annual Review of Earth and Planetary Sciences*, 42:551–578, 2014. ISSN 00846597. doi: 10.1146/annurev-earth-050212-124057.

E. Asphaug and A. Reufer. Mercury and other iron-rich planetary bodies as relics of inefficient accretion. *Nature Geoscience*, 7(8):564–568, 2014. ISSN 17520908. doi: 10.1038/ngeo2189.

H. A. Ballantyne, M. Jutzi, G. J. Golabek, L. Mishra, K. W. Cheng, A. B. Rozel, and P. Tackley. Investigating the Feasibility of an Impact-Induced Martian Dichotomy. *Icarus (in review)*, 2022.

E. Beitz, C. Güttler, J. Blum, T. Meisner, J. Teiser, and G. Wurm. Low-velocity collisions of centimeter-sized dust aggregates. *Astrophysical Journal*, 736(1), 2011. ISSN 15384357. doi: 10.1088/0004-637X/736/1/34.

W. Benz, A. Anic, J. Horner, and J. A. Whitby. The origin of Mercury. *Space Science Reviews*, 132(2-4):189–202, 2007. ISSN 00386308. doi: 10.1007/s11214-007-9284-1.

T. Bertrand and F. Forget. Observed glacier and volatile distribution on Pluto from atmosphere-topography processes. *Nature*, 540(7631):86–89, 2016. ISSN 14764687. doi: 10.1038/nature19337.

T. Birnstiel, M. Fang, and A. Johansen. Dust Evolution and the Formation of Planetesimals. *Space Science Reviews*, 205(1-4):41–75, 2016. ISSN 15729672. doi: 10.1007/s11214-016-0256-1.

A. G. Cameron and W. R. Ward. The origin of the moon. *Lunar and Planetary Science Conference*, 7, 1976. ISSN 00368075. doi: 10.1126/science.29.754.936.

R. M. Canup. Simulations of a late lunar-forming impact. *Icarus*, 168(2):433–456, 2004. ISSN 00191035. doi: 10.1016/j.icarus.2003.09.028.

R. M. Canup. A giant impact origin of Pluto-Charon. *Science*, 307(5709):546–550, jan 2005. ISSN 00368075. doi: 10.1126/science.1106818.

R. M. Canup. On a giant impact origin of charon, Nix, and Hydra. *Astronomical Journal*, 141(2):35, dec 2011. ISSN 00046256. doi: 10.1088/0004-6256/141/2/35.

G. S. Collins, H. J. Melosh, and B. A. Ivanov. Modeling damage and deformation in impact simulations. *Meteoritics and Planetary Science*, 39(2):217–231, feb 2004. ISSN 10869379. doi: 10.1111/j.1945-5100.2004.tb00337.x.

H. V. Frey. Impact constraints on, and a chronology for, major events in early Mars history. *Journal of Geophysical Research*, 111(E8):E08S91, aug 2006. ISSN 0148-0227. doi: 10.1029/2005JE002449.

G. J. Golabek, T. Keller, T. V. Gerya, G. Zhu, P. J. Tackley, and J. A. Connolly. Origin of the martian dichotomy and Tharsis from a giant impact causing massive magmatism. *Icarus*, 215(1):346–357, sep 2011. ISSN 0019-1035. doi: 10.1016/J.ICARUS.2011.06.012.

G. J. Golabek, A. Emsenhuber, M. Jutzi, E. I. Asphaug, and T. V. Gerya. Coupling SPH and thermochemical models of planets: Methodology and example of a Mars-sized body. *Icarus*, 301:235–246, 2018. ISSN 10902643. doi: 10.1016/j.icarus.2017.10.003.

J. F. Gonzalez, G. Laibe, and S. T. Maddison. Self-induced dust traps: Overcoming planet formation barriers. *Monthly Notices of the Royal Astronomical Society*, 467 (2):1984–1996, 2017. ISSN 13652966. doi: 10.1093/mnras/stx016.

R. Greenberg, J. F. Wacker, W. K. Hartmann, and C. R. Chapman. Planetesimals to planets: Numerical simulation of collisional evolution. *Icarus*, 35(1):1–26, jul 1978. ISSN 10902643. doi: 10.1016/0019-1035(78)90057-X.

A. Johansen, J. S. Oishi, M. M. M. Low, H. Klahr, T. Henning, and A. Youdin. Rapid planetesimal formation in turbulent circumstellar disks. *Nature*, 448(7157): 1022–1025, aug 2007. ISSN 14764687. doi: 10.1038/nature06086.

J. T. Keane, I. Matsuyama, S. Kamata, and J. K. Steckloff. Reorientation and faulting of Pluto due to volatile loading within Sputnik Planitia. *Nature 2016 540:7631*, 540(7631):90–93, nov 2016. ISSN 1476-4687. doi: 10.1038/nature20120.

T. Keller and P. J. Tackley. Towards self-consistent modeling of the martian dichotomy: The influence of one-ridge convection on crustal thickness distribution. *Icarus*, 202(2):429–443, 2009. ISSN 00191035. doi: 10.1016/j.icarus.2009.03.029.

A. Khan, P. A. Sossi, C. Liebske, A. Rivoldini, and D. Giardini. Geophysical and cosmochemical evidence for a volatile-rich Mars. *Earth and Planetary Science Letters*, 578:117330, jan 2022. ISSN 0012821X. doi: 10.1016/j.epsl.2021.117330.

E. Kokubo and S. Ida. Oligarchic growth of protoplanets. *Icarus*, 131(1):171–178, jan 1998. ISSN 10902643. doi: 10.1006/icar.1997.5840.

E. Kokubo and S. Ida. Formation of Protoplanets from Planetesimals in the Solar Nebula. *Icarus*, 143(1):15–27, jan 2000. ISSN 00191035. doi: 10.1006/icar.1999.6237.

E. Kokubo and S. Ida. Formation of Protoplanet Systems and Diversity of Planetary Systems. *The Astrophysical Journal*, 581(1):666–680, dec 2002. ISSN 0004-637X. doi: 10.1086/344105.

M. M. Marinova, O. Aharonson, and E. Asphaug. Mega-impact formation of the Mars hemispheric dichotomy. *Nature*, 453(7199):1216–1219, 2008. ISSN 14764687. doi: 10.1038/nature07070.

W. B. McKinnon. On the origin of the Pluto-Charon binary. *The Astrophysical Journal*, 344:L41, sep 1989. ISSN 0004-637X. doi: 10.1086/185526.

F. Nimmo, S. D. Hart, D. G. Korycansky, and C. B. Agnor. Implications of an impact origin for the martian hemispheric dichotomy. *Nature*, 453(7199):1220–1223, 2008. ISSN 14764687. doi: 10.1038/nature07025.

S. N. Raymond, E. Kokubo, A. Morbidelli, R. Morishima, and K. J. Walsh. Terrestrial Planet Formation at Home and Abroad. *Protostars and Planets VI*, 2014. doi: 10.2458/azu_uapress_9780816531240-ch026.

C. C. Reese and V. S. Solomatov. Fluid dynamics of local martian magma oceans. *Icarus*, 184(1):102–120, 2006. ISSN 00191035. doi: 10.1016/j.icarus.2006.04.008.

C. C. Reese and V. S. Solomatov. Early martian dynamo generation due to giant impacts. *Icarus*, 207(1):82–97, 2010. ISSN 00191035. doi: 10.1016/j.icarus.2009.10.016.

C. C. Reese, C. P. Orth, and V. S. Solomatov. Impact origin for the Martian crustal dichotomy: Half emptied or half filled? *J. Geophys. Res*, 115, 2010. ISSN 00191035. doi: 10.1016/j.icarus.2011.03.028.

C. Reinhardt, A. Chau, J. Stadel, and R. Helled. Bifurcation in the history of uranus and neptune: The role of giant impacts. *Monthly Notices of the Royal Astronomical Society*, 492(4):5336–5353, jul 2020. ISSN 13652966. doi: 10.1093/MNRAS/STZ3271.

P. Rosenblatt, R. Hyodo, F. Pignatale, A. Trinh, S. Charnoz, K. Dunseath, M. Dunseath-Terao, and H. Genda. The Formation of the Martian Moons. In *Oxford Research Encyclopedia of Planetary Science*. Oxford University Press, sep 2020. doi: 10.1093/acrefore/9780190647926.013.24.

V. Safronov. Evolution of the protoplanetary cloud and formation of the earth and the planets: copy translated from russian. 1969.

P. M. Schenk, R. A. Beyer, W. B. McKinnon, J. M. Moore, J. R. Spencer, O. L. White, K. Singer, F. Nimmo, C. Thomason, T. R. Lauer, S. Robbins, O. M.

Umurhan, W. M. Grundy, S. A. Stern, H. A. Weaver, L. A. Young, K. E. Smith, and C. Olkin. Basins, fractures and volcanoes: Global cartography and topography of Pluto from New Horizons. *Icarus*, 314:400–433, nov 2018. ISSN 0019-1035. doi: 10.1016/J.ICARUS.2018.06.008.

W. L. Slattery, W. Benz, and A. G. Cameron. Giant impacts on a primitive Uranus. *Icarus*, 99(1):167–174, sep 1992. ISSN 10902643. doi: 10.1016/0019-1035(92)90180-F.

S. A. Stern, F. Bagenal, K. Ennico, G. R. Gladstone, W. M. Grundy, W. B. McKinnon, J. M. Moore, C. B. Olkin, J. R. Spencer, H. A. Weaver, L. A. Young, T. Andert, J. Andrews, M. Banks, B. Bauer, J. Bauman, O. S. Barnouin, P. Bedini, K. Beisser, R. A. Beyer, S. Bhaskaran, R. P. Binzel, E. Birath, M. Bird, D. J. Bogan, A. Bowman, V. J. Bray, M. Brozovic, C. Bryan, M. R. Buckley, M. W. Buie, B. J. Buratti, S. S. Bushman, A. Calloway, B. Carcich, A. F. Cheng, S. Conard, C. A. Conrad, J. C. Cook, D. P. Cruikshank, O. S. Custodio, C. M. Dalle Ore, C. Deboy, Z. J. Dischner, P. Dumont, A. M. Earle, H. A. Elliott, J. Ercol, C. M. Ernst, T. Finley, S. H. Flanigan, G. Fountain, M. J. Freeze, T. Greathouse, J. L. Green, Y. Guo, M. Hahn, D. P. Hamilton, S. A. Hamilton, J. Hanley, A. Harch, H. M. Hart, C. B. Hersman, A. Hill, M. E. Hill, D. P. Hinson, M. E. Holdridge, M. Horanyi, A. D. Howard, C. J. Howett, C. Jackman, R. A. Jacobson, D. E. Jennings, J. A. Kammer, H. K. Kang, D. E. Kaufmann, P. Kollmann, S. M. Krimigis, D. Kusnierkiewicz, T. R. Lauer, J. E. Lee, K. L. Lindstrom, I. R. Linscott, C. M. Lisse, A. W. Lunsford, V. A. Mallder, N. Martin, D. J. McComas, R. L. McNutt, D. Mehoke, T. Mehoke, E. D. Melin, M. Mutchler, D. Nelson, F. Nimmo, J. I. Nunez, A. Ocampo, W. M. Owen, M. Paetzold, B. Page, A. H. Parker, J. W. Parker, F. Pelletier, J. Peterson, N. Pinkine, M. Piquette, S. B. Porter, S. Protopapa, J. Redfern, H. J. Reitsema, D. C. Reuter, J. H. Roberts, S. J. Robbins, G. Rogers, D. Rose, K. Runyon, K. D. Retherford, M. G. Ryschkewitsch, P. Schenk, E. Schindhelm, B. Sepan, M. R. Showalter, K. N. Singer, M. Soluri, D. Stanbridge, A. J. Steffl, D. F. Strobel, T. Stryk, M. E. Summers, J. R. Szalay, M. Tapley, A. Taylor, H. Taylor, H. B. Throop, C. C. Tsang, G. L. Tyler, O. M. Umurhan, A. J. Verbiscer, M. H. Versteeg, M. Vincent, R. Webbert, S. Weidner, G. E. Weigle, O. L. White, K. Whittenburg, B. G. Williams, K. Williams,

S. Williams, W. W. Woods, A. M. Zangari, and E. Zirnstein. The pluto system: Initial results from its exploration by New Horizons. *Science*, 350(6258), 2015. ISSN 10959203. doi: 10.1126/science.aad1815.

S. A. Stern, W. M. Grundy, W. B. Mckinnon, H. A. Weaver, and L. A. Young. The Pluto System After New Horizons. *Annual Review of Astronomy and Astrophysics*, 56:357–392, 2018.

C. Struck. Galaxy collisions. *Physics Report*, 321(1-3):1–137, nov 1999. ISSN 03701573. doi: 10.1016/S0370-1573(99)00030-7.

K. J. Walsh, A. Morbidelli, S. N. Raymond, D. P. O'Brien, and A. M. Mandell. A low mass for Mars from Jupiter's early gas-driven migration. *Nature*, 475(7355): 206–209, 2011. ISSN 00280836. doi: 10.1038/nature10201.

S. J. Weidenschilling. Aerodynamics of solid bodies in the solar nebula. *Monthly Notices of the Royal Astronomical Society*, 180(2):57–70, sep 1977. ISSN 0035-8711. doi: 10.1093/mnras/180.2.57.

G. W. Wetherill and G. R. Stewart. Accumulation of a swarm of small planetesimals. *Icarus*, 77(2):330–357, 1989. ISSN 10902643. doi: 10.1016/0019-1035(89)90093-6.

K. Wünnemann, G. S. Collins, and H. J. Melosh. A strain-based porosity model for use in hydrocode simulations of impacts and implications for transient crater growth in porous targets. *Icarus*, 180(2):514–527, feb 2006. ISSN 00191035. doi: 10.1016/j.icarus.2005.10.013.

S. Zhong and M. T. Zuber. Degree-1 mantle convection and the crustal dichotomy on Mars. *Earth and Planetary Science Letters*, 189(1-2):75–84, 2001. ISSN 0012821X. doi: 10.1016/S0012-821X(01)00345-4.

S. Zhong, A. McNamara, E. Tan, L. Moresi, and M. Gurnis. A benchmark study on mantle convection in a 3-D spherical shell using CitcomS. *Geochemistry, Geophysics, Geosystems*, 9(10):1–32, 2008. ISSN 15252027. doi: 10.1029/2008GC002048.

Chapter 2

Modelling Impact Events using SPHLATCH

This chapter describes the theoretical method used to model the impacts studied in this thesis, which is applied practically in the SPHLATCH code. First, the classical description of fluid dynamics is described (Section 2.1). Next, the application of the *Smoothed Particle Hydrodynamics* (or *SPH*) method to such a fluid description is explained, including specific aspects of the SPHLATCH code and the method used to model solid-state material (Section 2.2 and Section 2.3). The implementation of gravity forces in a computationally efficient manner is then described (Section 2.5). Finally, a short review of the yield strength models used in this thesis is given (Section 2.7).

As for personal contributions I made to the SPHLATCH code, several developments that I implemented are described throughout the chapter. To summarise, they include: the discovery and correction of an incorrect rotation rate tensor notation widespread in the research field that causes significant non-conservation of angular momentum if overlooked at planetary-scales (Section 2.3.3); the integration of a Mars-specific solidus into the equation of state and material strength model (Section 2.4); a new neighbour search method that ensures symmetry between SPH sums (Section 2.6.3); and the introduction of a realistic ice strength model for pressure and temperature conditions relevant to icy dwarfs (Section 2.7).

2.1 Lagrangian Fluid Dynamics

Fluid dynamics is a classical branch of physics that describes the flow of a fluid (i.e. a gas or a liquid), and involves the calculation of various physical properties such as density, velocity, temperature and pressure. The formulation of fluid dynamics theory relies upon the continuum assumption, whereby the medium can be sub-divided down to infinitesimally points in space while still retaining these bulk physical properties. This assumption therefore states that a fluid fills the space it occupies entirely, and is therefore continuous; while we know that this is not the case in reality—at the microscopic level they are composed of molecules in truth—this assumption is highly accurate for macroscopic length scales much larger than inter-atomic distances.

With the continuum assumption at hand, we can begin considering how fluid flow influences (or equivalently, is *itself* influenced by) physical properties at a fixed point in space. Conservation of mass gives a simple formula known as the ***continuity equation***:

$$\frac{\partial \rho}{\partial t} + \vec{\nabla} \cdot (\rho \boldsymbol{v}) = 0, \tag{2.1}$$

where ρ is density, t is time and $\boldsymbol{v}$ is velocity. Conservation of momentum, on the other hand, is not quite as simple; the most general expression (when neglecting non-Newtonian and relativistic effects) that results from this principle is the ***Navier-Stokes equation***:

$$\rho \left(\frac{\partial}{\partial t} + \boldsymbol{v} \cdot \vec{\nabla} \right) \boldsymbol{v} = -\vec{\nabla} p + \eta \vec{\nabla}^2 \boldsymbol{v} + \left(\zeta + \frac{1}{3}\eta \right) \vec{\nabla} \left(\vec{\nabla} \cdot \boldsymbol{v} \right) + \rho \boldsymbol{g}, \tag{2.2}$$

where $\boldsymbol{v}$ is velocity, P is pressure and $\boldsymbol{g}$ represents any external body accelerations (e.g. due to gravity or an electric field) and η and ζ are the shear and bulk viscosities, respectively. This equation is discussed further in Chapter 3. If we neglect viscosity, we arrive at the ***Euler momentum equation***:

$$\left(\frac{\partial}{\partial t} + \boldsymbol{v} \cdot \vec{\nabla} \right) \boldsymbol{v} = -\frac{\vec{\nabla} P}{\rho} + \rho \boldsymbol{g}. \tag{2.3}$$

This equation can be simplified further if, rather than considering a fixed point in space, our reference frame follows that of a very small fluid parcel whose mass is constant[1]. This is known as the Langrangian reference frame, and is related to the

[1] In general, the volume of this fluid parcel can vary and is therefore considered *compressible*. The volume is often kept constant, however, which leads to fluid being considered *incompressible*.

fixed (Eulerian) reference frame via the Lagrangian derivative:

$$\frac{\mathrm{d}}{\mathrm{d}t} \equiv \frac{\partial}{\partial t} + \boldsymbol{v} \cdot \vec{\nabla}. \tag{2.4}$$

If we substitute this into Eq. 2.3 and neglect any external body forces, we are left with

$$\boxed{\frac{\mathrm{d}\boldsymbol{v}}{\mathrm{d}t} = -\frac{\vec{\nabla} P}{\rho}} \tag{2.5}$$

The continuity equation (Eq. 2.1) can also be converted to the Lagrangian reference frame via Eq. 2.4:

$$\boxed{\frac{\mathrm{d}\rho}{\mathrm{d}t} = -\rho \vec{\nabla} \cdot \boldsymbol{v}} \tag{2.6}$$

Conservation of energy is enforced through an expression that directly follows from the (adiabatic) first law of thermodynamics,

$$\mathrm{d}U = -P \ \mathrm{d}V \tag{2.7}$$

where U is internal energy and V is volume. If we consider that volume is given by

$$V = m/\rho \tag{2.8}$$

where m is mass, we find the following equation for specific internal energy, u:

$$\mathrm{d}u = -P \ \mathrm{d}\left(\frac{1}{\rho}\right) = -\frac{P}{\rho^2} \ \mathrm{d}\rho \tag{2.9}$$

which, when differentiated with respect to time, leads to

$$\frac{\mathrm{d}u}{\mathrm{d}t} = -\frac{P}{\rho^2} \frac{\mathrm{d}\rho}{\mathrm{d}t}. \tag{2.10}$$

Combining Eq. 2.10 with Eq. 2.1 then gives the ***Euler energy equation***:

$$\boxed{\frac{\mathrm{d}u}{\mathrm{d}t} = -\frac{P}{\rho} \vec{\nabla} \cdot \boldsymbol{v}} \tag{2.11}$$

.

Eq. 2.5, Eq. 2.6 and Eq. 2.11 are collectively known as the *convective Euler equations*. These make up the basis for the more advanced fluid dynamics theory

that will be presented in the rest of this chapter; however, to be used practically they must be a closed set, which is not the case as pressure, P, is currently an unknown variable. This problem is resolved through an expression that relates P to our known variables (i.e. ρ and u), known as an *equation of state*. This expression varies depending on the application. The equations of state applicable to the work of this thesis, and that are applied in the SPHLATCH code, are discussed in Section 2.4.

2.2 Smoothed Particle Hydrodynamics (SPH)

The Euler equations provide the necessary theoretical framework to calculate the flow of an inviscid, Newtonian fluid. In many physical scenarios of interest, however, calculating this flow analytically is not possible due to the complexity of the system. Numerical methods are therefore necessary. Many of these methods use a grid for this purpose, utilising the Euler equations in the Eulerian reference frame to calculate the fluid properties at each grid cell coordinates. However, such grid-based methods struggle to handle deformed boundaries. This motivated the formulation of the the Smoothed Particles Hydrodynamics (SPH) method which instead utilises the Lagrangian reference frame, following interpolation points of fixed mass known as *SPH particles* to calculate the fluid properties "on-the-fly". These particles have no arbitrary requirement for any specific distribution, and therefore have no issue in resolving highly deformed fluid flow in three-dimensions. Clearly, SPH succeeded in it's primary goal, but this was not the only advantage discovered over its grid-based predecessors. For example, advection in SPH is naturally calculated exactly (it is simply the movement of particles), allowing for material tracking within the fluid without any numerical diffusion encountered in grid-based methods. Moreover, numerical calculations scale with the number of particles in a given region, meaning that computational cost is focused upon the (densest) regions of most interest, avoiding excessive calculations of near-empty grid-cells. These advantages make SPH a natural choice to study the effects of planetary-scale impacts, which involve extreme deformation to each of the impacting bodies and often require tracking of both composition and parent body to infer meaningful results that can be compared with observations.

2.2.1 Kernel Interpolation

Deriving the SPH method begins with the following (trivial) mathematical identity:

$$B(\boldsymbol{r}) \approx \int_{\Omega} B(\boldsymbol{r'})\delta(\boldsymbol{r}-\boldsymbol{r'})\ d\boldsymbol{r'}, \tag{2.12}$$

where B is a function of the position vector r, $\delta(\boldsymbol{r}-\boldsymbol{r'})$ is the Dirac delta distribution and Ω is the volume of the integral that encompasses B. This integral is exact on the condition that $B(r)$ is fully-defined and continuous within Ω.

In SPH, Eq. 2.12 is approximated by replacing $\delta(\boldsymbol{r}-\boldsymbol{r'})$ with a smoothing kernel $W(\boldsymbol{r}-\boldsymbol{r'},h)$, giving

$$\boxed{B(\boldsymbol{r}) \approx \int_{\Omega} B(\boldsymbol{r'})W(\boldsymbol{r}-\boldsymbol{r'},h)\ d\boldsymbol{r'}} \tag{2.13}$$

where h is the characteristic smoothing length of the smoothing kernel. For this approximation to hold, the kernel function must obey the *normalisation condition*,

$$\int_{\Omega} W(\boldsymbol{r}-\boldsymbol{r'},h)\ d\boldsymbol{r'} = 1, \tag{2.14}$$

and the *Dirac delta distribution property*,

$$\lim_{h\to 0} W(\boldsymbol{r}-\boldsymbol{r'},h) = \delta(\boldsymbol{r}-\boldsymbol{r'}), \tag{2.15}$$

thus uniting Eq. 2.12 and Eq. 2.13 in the exact case.

Initially, the smoothing kernel was chosen to be the Gaussian function,

$$W(\boldsymbol{r}-\boldsymbol{r'},h) = \frac{1}{\pi h^2}\exp\left(-\frac{(\boldsymbol{r}-\boldsymbol{r'})^2}{h^2}\right), \tag{2.16}$$

as this is the usual example of a function that converges to the the Dirac delta distribution in the limit $h \to 0$. However, in modern SPH-based research it has become standard practice to use a smoothing kernel with *compact support*, where

$$W(\boldsymbol{r}-\boldsymbol{r'},h) = 0 \qquad \text{when} \qquad |\boldsymbol{r}-\boldsymbol{r'}| \geq \kappa h, \tag{2.17}$$

with κ being a constant. A major advantage of this condition is that the domain of Eq. 2.13, Ω, can be confined to a sphere of radius κh, rather than the infinite bounds of Eq. 2.16, making it better applicable to numerical calculation.

The divergence of $B(\boldsymbol{r})$ is approximated by simply inserting the del operator, $\vec{\nabla}$, into Eq. 2.13, giving

$$\vec{\nabla} \cdot B(\boldsymbol{r}) \approx \int_{\Omega} [\vec{\nabla} \cdot B(\boldsymbol{r'})] W(\boldsymbol{r} - \boldsymbol{r'}, h) \, d\boldsymbol{r'}. \tag{2.18}$$

If we consider the identity,

$$\begin{aligned} &[\vec{\nabla} \cdot B(\boldsymbol{r'})] W(\boldsymbol{r} - \boldsymbol{r'}, h) \\ &\quad = \vec{\nabla} \cdot [B(\boldsymbol{r'}) W(\boldsymbol{r} - \boldsymbol{r'}, h)] - B(\boldsymbol{r'}) \cdot \vec{\nabla}[W(\boldsymbol{r} - \boldsymbol{r'}, h)], \end{aligned} \tag{2.19}$$

then Eq. 2.18 becomes

$$\begin{aligned} \vec{\nabla} \cdot B(\boldsymbol{r}) \approx \int_{\Omega} \vec{\nabla} \cdot [B(\boldsymbol{r'}) W(\boldsymbol{r} - \boldsymbol{r'}, h)] \, d\boldsymbol{r'} \\ - \int_{\Omega} B(\boldsymbol{r'}) \cdot \vec{\nabla}[W(\boldsymbol{r} - \boldsymbol{r'}, h)] \, d\boldsymbol{r'}. \end{aligned} \tag{2.20}$$

Using Gauss' theorem, the first term of 2.20 can be converted to surface integral, giving

$$\begin{aligned} \vec{\nabla} \cdot B(\boldsymbol{r}) \approx \int_{S} B(\boldsymbol{r'}) W(\boldsymbol{r} - \boldsymbol{r'}, h) \cdot \hat{\boldsymbol{n}} \, dS \\ - \int_{\Omega} B(\boldsymbol{r'}) \cdot \vec{\nabla}[W(\boldsymbol{r} - \boldsymbol{r'}, h)] \, d\boldsymbol{r'}, \end{aligned} \tag{2.21}$$

where S is the surface of the volume Ω, and $\hat{n}$ is the corresponding unit normal vector.

Eq. 2.21 brings us to the next major benefit of using a kernel with compact support; $|\boldsymbol{r} - \boldsymbol{r'}| = \kappa h$ at the surface of the volume Ω, and therefore $W(\boldsymbol{r} - \boldsymbol{r'}, h) = 0$, making the surface integral term of Eq. 2.21 also equal to zero. For such a smoothing kernel, therefore, Eq. 2.21 can be written as

$$\boxed{\vec{\nabla} \cdot B(\boldsymbol{r}) \approx - \int_{\Omega} B(\boldsymbol{r'}) \cdot \vec{\nabla}[W(\boldsymbol{r} - \boldsymbol{r'}, h)] \, d\boldsymbol{r'}} \tag{2.22}$$

The cubic B-spline function is commonly used as a smoothing kernel for SPH, as is the case in SPHLATCH, and is given by

$$W(\boldsymbol{r} - \boldsymbol{r'}, h) = W(|\boldsymbol{r} - \boldsymbol{r'}|, h) = \alpha \begin{cases} 1 - \frac{3}{2}q^2 + \frac{3}{4}q^3 & 0 \leq q \leq 1 \\ \frac{1}{4}(2 - q)^3 & 1 < q < 2 \\ 0 & q \geq 2 \end{cases}, \tag{2.23}$$

where $q = |\boldsymbol{r} - \boldsymbol{r'}|/h$ and α is $\frac{2}{3h}$, $\frac{10}{7\pi h^2}$ or $\frac{1}{\pi h^3}$ in the 1, 2 and 3 dimensional cases, respectively. A plot of this kernel in the one-dimensional case is shown in Figure 2.1.

The spatial derivative of $W(\boldsymbol{r} - \boldsymbol{r'}, h)$ is therefore given by

$$\vec{\nabla} W(\boldsymbol{r} - \boldsymbol{r'}, h) = \frac{\boldsymbol{r} - \boldsymbol{r'}}{|\boldsymbol{r} - \boldsymbol{r'}|} \alpha \begin{cases} 1 - 3q + \frac{9}{4}q^2 & 0 \leq q \leq 1 \\ \frac{3}{4}(2-q)^2 & 1 < q < 2 \\ 0 & q \geq 2 \end{cases} \tag{2.24}$$

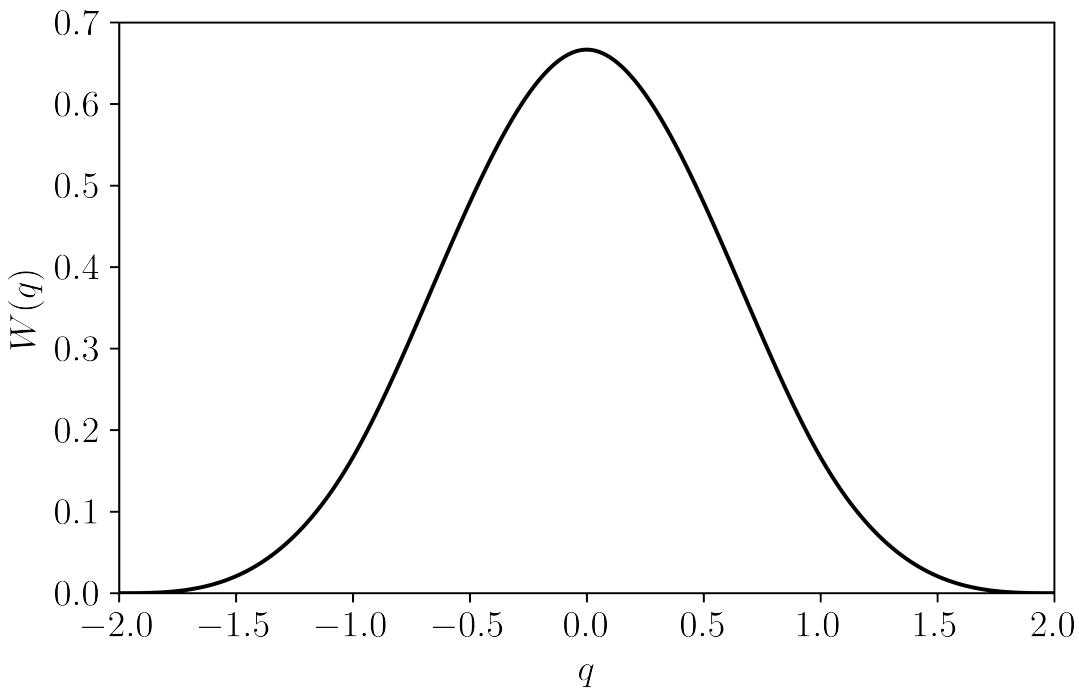

Figure 2.1: The one-dimensional cubic B-spline kernel of Eq. 2.23.

2.2.2 Discretisation into Particles

The previous section describes the *smoothed* aspect of SPH, but thus far has left us with an integral approximation that is highly non-trivial to evaluate analytically for complex fluid systems. This is where the *particle* aspect comes in: the integral in Eq. 2.13 is approximated by a sum over a finite number, N, of data points, or *particles*, as follows:

$$\boxed{B(\boldsymbol{r}) \approx \sum_{\jmath}^{N} V_\jmath B_\jmath W(\boldsymbol{r} - \boldsymbol{r}_\jmath, h)} \tag{2.25}$$

where the subscript j represent each neighbouring particle that contributes to the sum; B_j is the value of the quantity of interest, B, and V_j is the volume, for each of these neighbours.

Eq. 2.25 now allows any quantity $B(\boldsymbol{r})$ to be calculated by simply summing up the contributions of each neighbouring particle, which proves to be a highly effective method in numerically solving the equations of Section 2.1. The position vector can be chosen, allowing us to probe the fluid continuum for $B(\boldsymbol{r})$ at any position within the computational domain. While this position usually corresponds to a particle, i, whose properties we wish to calculate, it can also be useful to instead calculate the fluid properties on a uniform grid of coordinates, as will be described further in Chapter 3.

When calculating the properties of each particle by summing over all of its neighbours, one must be careful when choosing the smoothing length to be used in the kernel. At first glance, it seems an obvious choice to use the smoothing length of each contributing neighbour, h_j; however, this leads to an issue of asymmetry between particle contributions if the smoothing length of central particle, h_i, is not equal to that of the neighbour, as the distance between the two particles, $|(\boldsymbol{r}-\boldsymbol{r}_j|$, is equal, but the smoothing kernel (i.e. $W(\boldsymbol{r}_i-\boldsymbol{r}_j,h_i)\neq W(\boldsymbol{r}_i-\boldsymbol{r}_j,h_j)$ when $h_i\neq h_j$). In SPHLATCH, this problem is resolved by averaging the smoothing length of the two particles in all SPH sum calculations, which motivates the following notation:

$$h_{ij}=\frac{h_i+h_j}{2} \qquad \boldsymbol{r}_{ij}=\boldsymbol{r}_i-\boldsymbol{r}_j \qquad W_{ij}=W(\boldsymbol{r}_{ij},h_{ij}) \qquad \vec{\nabla}W_{ij}=\frac{\partial W_{ij}}{\partial \boldsymbol{r}_i} \tag{2.26}$$

Eq. 2.25 now becomes

$$\boxed{B_i=\sum_j^N V_j B_j W_{ij}} \tag{2.27}$$

Eq. 2.22 in its discretised, particle-based form becomes

$$\boxed{\vec{\nabla}\cdot B_i=\sum_j^N V_j B_j\cdot\vec{\nabla}W_{ij}} \tag{2.28}$$

Computing the divergence is only valid when B is a vector, and so it is useful to also define the gradient of B applicable to scalar quantities. This can be found by simply replacing $W_{\imath\jmath}$ with $\vec{\nabla}W_{\imath\jmath}$, i.e.

$$\boxed{\vec{\nabla}B_\imath = \sum_{\jmath}^{N} V_\jmath B_\jmath \vec{\nabla}W_{\imath\jmath}} \tag{2.29}$$

As a final note on notation, the magnitude of $\boldsymbol{r}_{\imath\jmath}$ will be refered to as $r_{\imath\jmath}$ throughout this thesis, i.e.

$$r_{\imath\jmath} = |\boldsymbol{r}_{\imath\jmath}| \tag{2.30}$$

2.3 Particle-Based Fluid Dynamics

In this section, we will apply the particle-based approach to the fluid dynamics theory of Section 2.1.

Density

When setting up an SPH simulation, each particle is assigned a mass and initial position. The mass, m, is constant for each particle, by analogy to the constant-mass fluid parcels at the heart of the fluid dynamics theory. With mass and position at hand, it is therefore logical to first derive an equation for density, ρ, which is achieved by simply substituting the variable into Eq. 2.27, giving

$$\rho_\imath = \sum_{\jmath}^{N} V_\jmath \rho_\jmath W_{\imath\jmath}. \tag{2.31}$$

However, we known that

$$V_\jmath = \frac{m_\jmath}{\rho_\jmath}, \tag{2.32}$$

where $m_\jmath$ and $\rho_\jmath$ are the mass and density of the particle. This expression can therefore be substituted into Eq. 2.31, leading to a simplified form that is independent of $\rho_\jmath$, and that can be evaluated using only the aforementioned input parameters of particle mass and position:

$$\boxed{\rho_\imath = \sum_{\jmath}^{N} m_\jmath W_{\imath\jmath}} \tag{2.33}$$

Alternatively, the density can be calculated via the continuity equation (Eq. 2.6), which gives the time derivative of the density,

$$\frac{\mathrm{d}\rho_i}{\mathrm{d}t} = -\rho_i(\vec{\nabla} \cdot \boldsymbol{v})_i. \tag{2.34}$$

From Eq. 2.29, $\vec{\nabla} \cdot \boldsymbol{v}_i$ can in principle be calculated using the particle sum

$$(\vec{\nabla} \cdot \boldsymbol{v})_i = \sum_j^N \frac{m_j}{\rho_j} \boldsymbol{v}_j \cdot \vec{\nabla} W_{ij}, \tag{2.35}$$

but this form has the undesirable property of between asymmetric between particles. We therefore adopt the approach of Monaghan (1992) and instead use the expression

$$\vec{\nabla} \cdot \boldsymbol{v} = \frac{1}{\rho}\left(\vec{\nabla} \cdot (\rho \boldsymbol{v}) - \boldsymbol{v} \cdot \vec{\nabla}\rho\right) \tag{2.36}$$

which, using Eq. 2.28 and Eq. 2.29, can be written as

$$(\vec{\nabla} \cdot \boldsymbol{v})_i = \frac{1}{\rho_i} \sum_j^N \frac{m_j}{\rho_j} \rho_j \boldsymbol{v}_j \cdot \vec{\nabla} W_{ij} - \frac{1}{\rho_i} \boldsymbol{v}_i \cdot \sum_j^N \frac{m_j}{\rho_j} \rho_j \vec{\nabla} W_{ij} \tag{2.37}$$

which can be simplified by introducing the notation $\boldsymbol{v}_{ij} = \boldsymbol{v}_i - \boldsymbol{v}_j$, giving

$$\boxed{(\vec{\nabla} \cdot \boldsymbol{v})_i = -\frac{1}{\rho_i} \sum_j^N m_j \boldsymbol{v}_{ij} \cdot \vec{\nabla} W_{ij}}. \tag{2.38}$$

By substituting this into Eq. 2.34, we arrive at the simple expression

$$\boxed{\frac{\mathrm{d}\rho_i}{\mathrm{d}t} = \sum_j^N m_j \boldsymbol{v}_{ij} \cdot \vec{\nabla} W_{ij}} \tag{2.39}$$

which can then be (numerically) integrated to find the density for each particle.

Both Eq. 2.33 and Eq. 2.39 are mathematically valid, and thus the choice of which to use in the SPH model purely of numerical reasoning. Both are commonly used in SPH codes, and SPHLATCH is capable of following either scheme. Due to minor advantages of the integrated density scheme (Eq. 2.39) to define a planetary surface, as shown in Emsenhuber et al. (2018), this scheme was used for all SPH calculations carried out for this thesis.

Momentum

Applying the particle approach to the momentum equation (Eq. 2.5) yields

$$\frac{\mathrm{d}\boldsymbol{v}_\imath}{\mathrm{d}t} = -\frac{1}{\rho_\imath}\sum_{\jmath}^{N}\frac{m_\jmath}{\rho_\jmath}P_\jmath\vec{\nabla}W_{\imath\jmath}. \tag{2.40}$$

This equation again suffers from an asymmetry between a particle and its neighbour in the SPH sum, however, and again motivates a more sophisticated approach to retain conservation. If we consider the identity

$$\frac{\vec{\nabla}P}{\rho} = \vec{\nabla}\left(\frac{P}{\rho}\right) + \frac{P}{\rho^2}\vec{\nabla}\rho, \tag{2.41}$$

and apply the particle gradient of Eq. 2.29, giving

$$\frac{\vec{\nabla}P_\imath}{\rho_\imath} = \sum_{\jmath}^{N}\frac{m_\jmath}{\rho_\jmath}\left(\frac{P_\jmath}{\rho_\jmath}\right)\vec{\nabla}W_{\imath\jmath} + \frac{P_\imath}{\rho_\imath^2}\sum_{\jmath}^{N}\frac{m_\jmath}{\rho_\jmath}\vec{\nabla}W_{\imath\jmath}, \tag{2.42}$$

which can be substituted back into the momentum equation of Eq. 2.5 to give the following expression:

$$\boxed{\frac{\mathrm{d}\boldsymbol{v}_\imath}{\mathrm{d}t} = \sum_{\jmath\neq\imath}^{N} m_\jmath\left(\frac{P_\imath}{\rho_\imath^2} + \frac{P_\jmath}{\rho_\jmath^2}\right)\vec{\nabla}W_{\imath\jmath}} \tag{2.43}$$

which yields symmetric sum contributions as required.

Internal Energy

The Euler energy equation (Eq. 2.11) can be easily discretised into a particle sum by substituting in the symmetric velocity divergence expression of Eq. 2.38, leading to

$$\frac{\mathrm{d}u_\imath}{\mathrm{d}t} = \frac{P_\imath}{\rho_\imath^2}\sum_{\jmath}^{N} m_\jmath\boldsymbol{v}_{\imath\jmath}\cdot\vec{\nabla}W_{\imath\jmath}. \tag{2.44}$$

Although this expression is symmetric between particles, it is not consistent with the symmetric momentum equation (Eq. 2.43), and thus requires some manipulation. For this purpose, we again utilise the divergence identity trick of Monaghan (1992), allowing us to rewrite Eq. 2.11 as

$$\frac{\mathrm{d}u}{\mathrm{d}t} = -\vec{\nabla}\cdot\left(\frac{P\boldsymbol{v}}{\rho}\right) + \boldsymbol{v}\cdot\vec{\nabla}\left(\frac{P}{\rho}\right) \tag{2.45}$$

which, using the SPH divergence of Eq. 2.28 becomes

$$\frac{\mathrm{d}u_\imath}{\mathrm{d}t} = -\sum_{\jmath}^{N} m_\jmath \frac{p_\jmath \boldsymbol{v}_\jmath}{\rho_\jmath^2} \cdot \vec{\nabla} W_{\imath\jmath} + \boldsymbol{v}_\imath \sum_{\jmath}^{N} m_\jmath \frac{p_\jmath}{\rho_\jmath^2} \cdot \vec{\nabla} W_{\imath\jmath} = \sum_{\jmath}^{N} m_\jmath \boldsymbol{v}_{\imath\jmath} \frac{p_\jmath}{\rho_\jmath^2} \cdot \vec{\nabla} W_{\imath\jmath}. \tag{2.46}$$

Eq. 2.44 and Eq. 2.46 are then averaged to give the expression

$$\boxed{\frac{\mathrm{d}u_\imath}{\mathrm{d}t} = \frac{1}{2} \sum_{\jmath}^{N} m_\jmath \left(\frac{P_\imath}{\rho_\imath^2} + \frac{P_\jmath}{\rho_\jmath^2} \right) \boldsymbol{v}_{\imath\jmath} \cdot \vec{\nabla}_\imath W_{\imath\jmath}} \tag{2.47}$$

whose symmetric terms match with those of the momentum equation (Eq. 2.43).

2.3.1 Treatment of Shocks

Thus far, the described hydrodynamic model has been entirely isentropic and therefore dissipationless. In many fields of research, however, and particularly in planetary-impact studies, this assumption is not valid due the occurrence of shock waves. Shock waves are a dissipative, irreversible process whereby kinetic energy is converted into heat, and leads to discontinuities on the shock front in the fluid approximation of various quantities such as density and pressure. In numerical schemes these discontinuities lead to significant, spurious oscillations behind the shock front. In SPH, there are two main approaches to mitigate these issues. The first method is to utilise a Riemann solver to solve the Riemann problem for each particle against its neighbours. This is known as the *Godunov method* (Monaghan, 1997). The second method, and the approach that is implemented in SPHLATCH, is to introduce an artificial viscosity term that acts to broaden the shock across a few smoothing lengths, removing the discontinuities and thus avoiding the unphysical effects. Specifically, we follow the formulation of Monaghan (1992):

$$\Pi_{\imath\jmath} = \begin{cases} \frac{-\alpha c_{\imath\jmath} \mu_{\imath\jmath} + \beta \mu_{\imath\jmath}^2}{\rho_{\imath\jmath}} & \text{if } \boldsymbol{r}_{\imath\jmath} \cdot \boldsymbol{v}_{\imath\jmath} < 0 \\ 0 & \text{otherwise} \end{cases} \quad \text{where} \quad \mu_{\imath\jmath} = \frac{h_{\imath\jmath} \boldsymbol{r}_{\imath\jmath} \cdot \boldsymbol{v}_{\imath\jmath}}{|\boldsymbol{r}_{\imath\jmath}|^2 + \epsilon h_{\imath\jmath}^2} \tag{2.48}$$

where $\rho_{\imath\jmath}$ and $c_{\imath\jmath}$ are average density and sound speed averaged for the two particles $\imath$ and $\jmath$. α, β and ϵ are constants, usually chosen to take values of $\alpha = 1$, $\beta = 2$ and ϵ. The α-term represents the bulk and shear viscosities of a generalised fluid. The β-term is known as the *von Neumann* term (Von Neumann and Richtmyer,

1950) that is necessary to model strong shocks where $\boldsymbol{v}_{ij}$ becomes large. Finally, the ϵ-term is included to avoid the possibility of a singularity.

This term is then implemented in the momentum equation (Eq. 2.43) as follows:

$$\boxed{\frac{\mathrm{d}\boldsymbol{v}_i}{\mathrm{d}t} = \sum_{j\neq i}^{N} m_j \left(\frac{P_i}{\rho_i^2} + \frac{P_j}{\rho_j^2} + \Pi_{ij} \right) \vec{\nabla} W_{ij}} \tag{2.49}$$

In order to conserve energy, the artificial viscosity term must also be included in the energy equation (Eq. 2.47):

$$\boxed{\frac{\mathrm{d}u_i}{\mathrm{d}t} = \frac{1}{2} \sum_{j}^{N} m_j \left(\frac{P_i}{\rho_i^2} + \frac{P_j}{\rho_j^2} + \Pi_{ij} \right) \boldsymbol{v}_{ij} \cdot \vec{\nabla}_i W_{ij}} \tag{2.50}$$

2.3.2 Solid Mechanics

Although the SPH method is derived from fluid dynamics, it can be adapted to also model the mechanics of solids. In the context of astrophysical impacts between bodies composed predominantly of solid material, the complexity and importance of these adaptations depend on the mass-scale of the two bodies. For very massive bodies, the force of gravity dominates over any solid properties (or solid *strength*) of material composition, meaning the pure fluid description described thus far is sufficient. As mass is decreased, solid effects become increasingly more important. The most obvious visible difference that indicates the importance of these effects is the geometry of the bodies. Very massive bodies, such as Earth, are ellipsoid in shape, which is the natural result of fluid body in hydrostatic equilibrium. Conversely, small bodies such as asteroids display a wide variety of irregular shapes, as the rigidity of their solid composition is able to withstand the forces of gravity. The precise transition mass between these two regimes is unclear, however. Traditionally, rocky bodies with radii greater than $\sim$1 km were deemed large enough for solid properties to be neglected, based on investigations into the catastrophic disruption of asteroids (e.g. Benz and Asphaug, 1999); however, later studies on such catastrophic collisions showed that solid strength is still important at much larger scales than previous estimates, suggesting a transition at scales of 100-1000 km (Jutzi,

2015). More recently, this value has been pushed to even larger scales, with studies modelling large-scale (1000 km-radius) impactors colliding with a Mars-like body finding significant differences between the fluid and solid cases for the SPH method (Emsenhuber et al., 2018; Golabek et al., 2018). The work presented in the later chapters (Chapter 4 and Chapter 5) of this thesis further support this conclusion, confirming the importance of strength at Mars-scale, and revealing a previously overlooked impact regime for Pluto-scale icy bodies that relies upon the inclusion of such solid properties.

The first step in adapting the SPH method to handle material strength is to generalise the pressure terms of our hydrodynamic model into a stress tensor $\sigma^{\alpha\beta}$. The momentum equation (Eq. 2.5) thus becomes

$$\boxed{\frac{\partial v^{\alpha}}{\partial t} = \frac{1}{\rho}\frac{\partial \sigma^{\alpha\beta}}{\partial x^{\beta}}} \tag{2.51}$$

where x is spatial position and each index can be an integer of 1, 2 or 3, corresponding with three-dimensional Euclidean space. The Einstein summation convention has been used (i.e. repeated indices are summed), as is commonly the case for tensor notation.

It is convenient to decompose the stress tensor into a hydrostatic pressure component and deviatoric stress component

$$\sigma^{\alpha\beta} = -P\delta^{\alpha\beta} + S^{\alpha\beta} \tag{2.52}$$

where $\delta^{\alpha\beta}$ is the Kronecker delta and $S^{\alpha\beta}$ is the deviatoric stress tensor. The deviatoric stresses can only be supported by a solid material, and we see that in the limiting case where $S^{\alpha\beta} = 0$ the stress tensor is reduced to simply the pressure component along the diagonal, agreeing with the momentum equation for fluids. It should also be noted that $S^{\alpha\beta}$ is traceless, and so has no net effect on the total hydrostatic pressure.

Elasticity

To model the elasticity of solids, we assume Hooke's law, which states that strain (deformation) is proportional to stress. For an isotropic, continuous medium, this

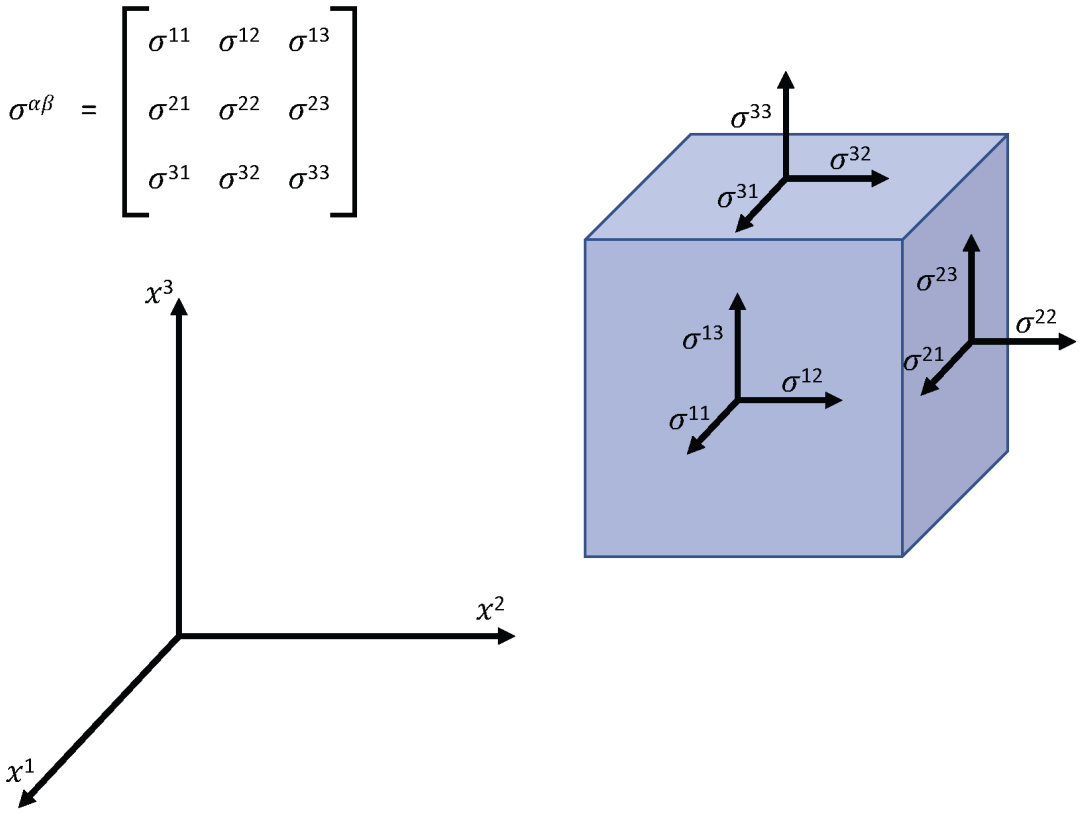

Figure 2.2: Schematic diagram illustrating the geometry of the stress tensor, $\sigma^{\alpha\beta}$.

allows us to write $S^{\alpha\beta}$ as

$$S^{\alpha\beta} = 2\Gamma\left(\varepsilon^{\alpha\beta} - \frac{1}{3}\varepsilon^{\gamma\gamma}\delta^{\alpha\beta}\right) \tag{2.53}$$

where Γ is a constant of proportionality known as the *shear modulus* and $\varepsilon^{\alpha\beta}$ is a second-order tensor that describes the strain within the medium[2]. Note that the superscript γ is a dummy index for the Einstein summation rule, and that the second term ensures that $S^{\alpha\beta}$ is traceless.

To model time evolution, $S^{\alpha\beta}$ is differentiated to give

$$\dot{S}^{\alpha\beta} = 2\Gamma\left(\dot{\varepsilon}^{\alpha\beta} - \frac{1}{3}\dot{\varepsilon}^{\gamma\gamma}\delta^{\alpha\beta}\right) \tag{2.54}$$

this formulation, however, is dependent on reference frame, which is unsuitable for the constitutive equations. To transform this expression into an equivalent, frame-invariant version we utilise the Jaumann rate to obtain the form

$$\boxed{\dot{S}^{\alpha\beta} = 2\Gamma\left(\dot{\varepsilon}^{\alpha\beta} - \frac{1}{3}\dot{\varepsilon}^{\gamma\gamma}\delta^{\alpha\beta}\right) + S^{\alpha\gamma}R^{\gamma\beta} + S^{\beta\gamma}R^{\gamma\alpha}} \tag{2.55}$$

where $R^{\alpha\beta}$ and $\dot{\varepsilon}^{\alpha\beta}$ are the rotation rate tensor and strain rate tensor, respectively, defined by

$$R^{\alpha\beta} = \frac{1}{2}\left(\frac{\partial v^{\alpha}}{\partial x^{\beta}} - \frac{\partial v^{\beta}}{\partial x^{\alpha}}\right) \tag{2.56}$$

$$\dot{\varepsilon}^{\alpha\beta} = \frac{1}{2}\left(\frac{\partial v^{\alpha}}{\partial x^{\beta}} + \frac{\partial v^{\beta}}{\partial x^{\alpha}}\right) \tag{2.57}$$

To conserve energy, Eq. 2.11 must also be generalised into tensor form

$$\frac{\mathrm{d}u}{\mathrm{d}t} = \frac{1}{\rho}\sigma^{\alpha\beta}\dot{\varepsilon}^{\alpha\beta} \tag{2.58}$$

which can also be decomposed into a hydrostatic and deviatoric component

$$\boxed{\frac{\mathrm{d}u}{\mathrm{d}t} = -\frac{P}{\rho}(\vec{\nabla}\cdot\boldsymbol{v}) + \frac{1}{\rho}S^{\alpha\beta}\dot{\varepsilon}^{\alpha\beta}} \tag{2.59}$$

[2]The equivalent constant for the diagonal components of stress tensor is known as the *bulk modulus*, and is included in our equation of state for calculating the isotropic pressure, P.

The application of these equations in the SPH method simply requires the generalisation of each pressure and position term to their tensor equivalents, thus meaning that Eq. 2.43 and Eq. 2.47 become

$$\boxed{\frac{\mathrm{d}v_i^\alpha}{\mathrm{d}t} = \sum_{j\neq i}^{N} m_j \left(\frac{\sigma_i^{\alpha\beta}}{\rho_i^2} + \frac{\sigma_j^{\alpha\beta}}{\rho_j^2} \right) \frac{\partial W_{ij}}{\partial x_i^\beta}} \tag{2.60}$$

$$\boxed{\frac{\mathrm{d}u_i}{\mathrm{d}t} = -\frac{1}{2} \sum_{j\neq i}^{N} m_j \left(\frac{\sigma_i^{\alpha\beta}}{\rho_i^2} + \frac{\sigma_j^{\alpha\beta}}{\rho_j^2} \right) v_{ij}^\alpha \frac{\partial W_{ij}}{\partial x_i^\beta}} \tag{2.61}$$

where the subscripts denote the particle i and its neighbour j, as in previous sections. Note that the negative sign at the beginning of Eq. 2.61 is not present in the fluid description of the SPH energy equation (Eq. 2.47) because it cancels with the negative sign on the pressure term; in the generalised form using the stress tensor, this negative sign is still included, but only applies to the hydrostatic pressure terms along the diagonal and not the off-diagonal shear terms, which therefore necessitates the minus sign outside of the sum.

To calculate the time derivative of the stress tensor in the discretised, particle approach, we only need a way to determine the spatial derivative of velocity in each dimension, $\frac{\partial v^\alpha}{\partial x^\beta}$, which is simply derived from Eq. 2.29 to give

$$\frac{\partial v_i^\alpha}{\partial x_i^\beta} = -\sum_{j\neq i} \frac{m_j}{\rho_j} v_{ij}^\alpha \frac{\partial W_{ij}}{\partial x_i^\beta} \tag{2.62}$$

Plasticity

The solid model described thus far is valid for a purely elastic body, which would re-establish its original shape if all stresses (and thus strains) were released. Above a threshold stress, however, solids exhibit plastic behaviour whereby deformations become permanent. In many SPH models, including SPHLATCH, this effect is implemented via the *von Mises* model that was originally developed for ductile metals (e.g. Benz and Asphaug, 1994, 1995; Collins et al., 2004; Jutzi et al., 2015, and references therein). In this model, stresses greater than the threshold stress, Y,

known as the *yield strength*, cause the deviatoric stress tensor to be reduced as

$$S^{\alpha\beta} \to f S^{\alpha\beta}, \tag{2.63}$$

where we follow the Collins et al. (2004) formulation for f given by

$$f = \min\left(\frac{Y}{\sqrt{J_2}}, 1\right), \tag{2.64}$$

with J_2 being the second invariant of the stress tensor,

$$J_2 = \frac{1}{2} S^{\alpha\beta} S^{\alpha\beta} \tag{2.65}$$

In reality, geological materials such as rock and ice exhibit more complex behaviour than that of ductile metals. At high enough strains, these materials experience brittle failure and begin to fracture. This causes a change in the material's ability to support stress that is reflected in the yield strength, usually as a reduction. In addition, the large pressures present in planetary interiors have a significant effect on the yield strength, with higher pressures leading to substantially stronger material.

Both of these effects are included in our model through the formulation of Collins et al. (2004). For intact material, yield strength, Y_i, follows a smooth fit from experimental data:

$$Y_\mathrm{i} = Y_0 + \frac{\mu_\mathrm{i} P}{1 + \frac{\mu_\mathrm{i} P}{Y_\mathrm{M} - Y_0}} \tag{2.66}$$

where μ_i is the coefficient of interal friction for intact material, Y_0 is the yield strength at zero pressure (often called the *cohesion*) and Y_M is the yield strength at infinite pressure, known as the *von Mises plastic limit*.

For fully fractured (granular) material, a Coulomb dry-friction law is used:

$$Y_\mathrm{d} = \mu_\mathrm{d} P \tag{2.67}$$

where μ_d is the coefficient of internal friction for fully fractured material.

The degree of fracturing within the medium is referred to as the *damage*, D, where $D = 0$ for entirely intact material and increases up to a maximum of $D = 1$ for fully damaged, granular material. This allows us to calculate the yield strength for material in the intermediate of the two end-member cases via

$$Y = Y_\mathrm{i}(1 - D) + Y_\mathrm{d} D. \tag{2.68}$$

Damage is calculated through fracture models that usually incorporate a threshold (or *activation*) strain beyond which cracks form and accumulate. At the planetary-scales of the work of this thesis, however, all material is considered fully-damaged due to the large overburden pressures greater than such a threshold, and thus no fracture model is implemented. For further reading on commonly used fracture models in impact studies, see Collins et al. (2004) or Jutzi et al. (2008).

Pressure is not the only quantity that effects the yield strength of solid materials. As a material approaches its melting temperature, its shear strength decreases, eventually reaching zero as it becomes a fluid. An expression approximating this behaviour is again taken from Collins et al. (2004) (after Ohnaka (1995)):

$$Y \to Y \tanh\left(\xi\left(\frac{T_{\text{melt}}}{T} - 1\right)\right) \tag{2.69}$$

where T is temperature, T_{melt} is the melting temperature and ξ is a constant known as the *thermal softening parameter* that is dependent on the material composition. Further details on the choice of strength parameters for specific materials are described in Section 2.7.

2.3.3 Conserving Angular Momentum with Strength

Generalising the the fluid model into the more complex continuum model that can handle both fluid and solid materials requires careful consideration of conservation laws. In particular, there have been multiple discoveries of angular momentum non-conservation in the planetary-scale impact regime, which I will highlight in this section.

Rigid-Body Rotation

When applying the strength model described, it was discovered that the scheme does not conserve angular momentum when attempting to simulate rigid body rotation. This is due to the discretisation error caused by particle disorder. To correct this in SPHLATCH, we follow the approach of Schäfer et al. (2007), who applied a correction tensor, $C^{\gamma\beta}$, to the spatial derivatives of velocity according to

$$\frac{\partial v_i^\alpha}{\partial x_i^\beta} = -\sum_j^N \frac{m_j}{\rho_j} v_{ij}^\alpha \sum_\gamma^N \frac{\partial W^{ij}}{\partial x_i^\gamma} C^{\gamma\beta} \tag{2.70}$$

where the inverse of $C^{\gamma\beta}$ is given by

$$\left(C^{\gamma\beta}\right)^{-1} = -\sum_{\jmath}^{N} \frac{m_\jmath}{\rho_\jmath} x_{\imath\jmath}^{\alpha} \frac{\partial W^{\imath\jmath}}{\partial x_\imath^\gamma} \tag{2.71}$$

such that

$$-\sum_{\jmath} \frac{m_\jmath}{\rho_\jmath} x_{\imath\jmath}^{\alpha} \sum_{\gamma} \frac{\partial W^{\imath\jmath}}{\partial x_\imath^\gamma} C^{\gamma\beta} = \delta^{\alpha\beta} \tag{2.72}$$

This correction tensor forces first-order consistency in angular momentum. A series of test cases illustrating the effectiveness of this method for planetary-scale collisions on a Mars-like target can be seen in Figure 2.3

Rotation Rate Tensor

Using the Jaumann stress rate to achieve frame-invariance in the deviatoric stress tensor computation is standard practice for SPH simulation involving solid bodies. The precise form of this expression is not consistent in the literature, however, and can lead to severe errors that particularly affect angular momentum conservation.

Initially, SPHLATCH followed the formulation of Benz and Asphaug (1994), given by

$$\dot{S}^{\alpha\beta} = 2\Gamma\left(\dot{\varepsilon}^{\alpha\beta} - \frac{1}{3}\dot{\varepsilon}^{\gamma\gamma}\delta^{\alpha\beta}\right) + S^{\alpha\gamma}R^{\beta\gamma} + S^{\beta\gamma}R^{\alpha\gamma}. \tag{2.73}$$

This formulation has been used in a large number of subsequent studies (e.g. Benz and Asphaug, 1995, 1999; Jutzi and Asphaug, 2011; Emsenhuber et al., 2018); however, if we compare this formulation to that of Eq. 2.55, we see a discrepancy in the indices of the rotation rate terms, which read in the opposite order. If such index swapping occurred in the deviatoric stress tensor, there would be no change in the expression as it is symmetric. The rotation rate tensor, on the other hand, is anti-symmetric, meaning that its transpose is equal to its negative[3], i.e.

$$R^{\alpha\beta} = -R^{\alpha\beta} \tag{2.74}$$

The expression presented in Eq. 2.55 instead follows Schäfer et al. (2007) (and related subsequent work such as Schäfer et al. (2016)). This discrepancy was discovered due to SPH simulations of planetary-scale impacts on Mars that were performed

[3]Note that anti-symmetry is only possible for *hollow* matrices, whereby all components along the main diagonal are equal to zero.

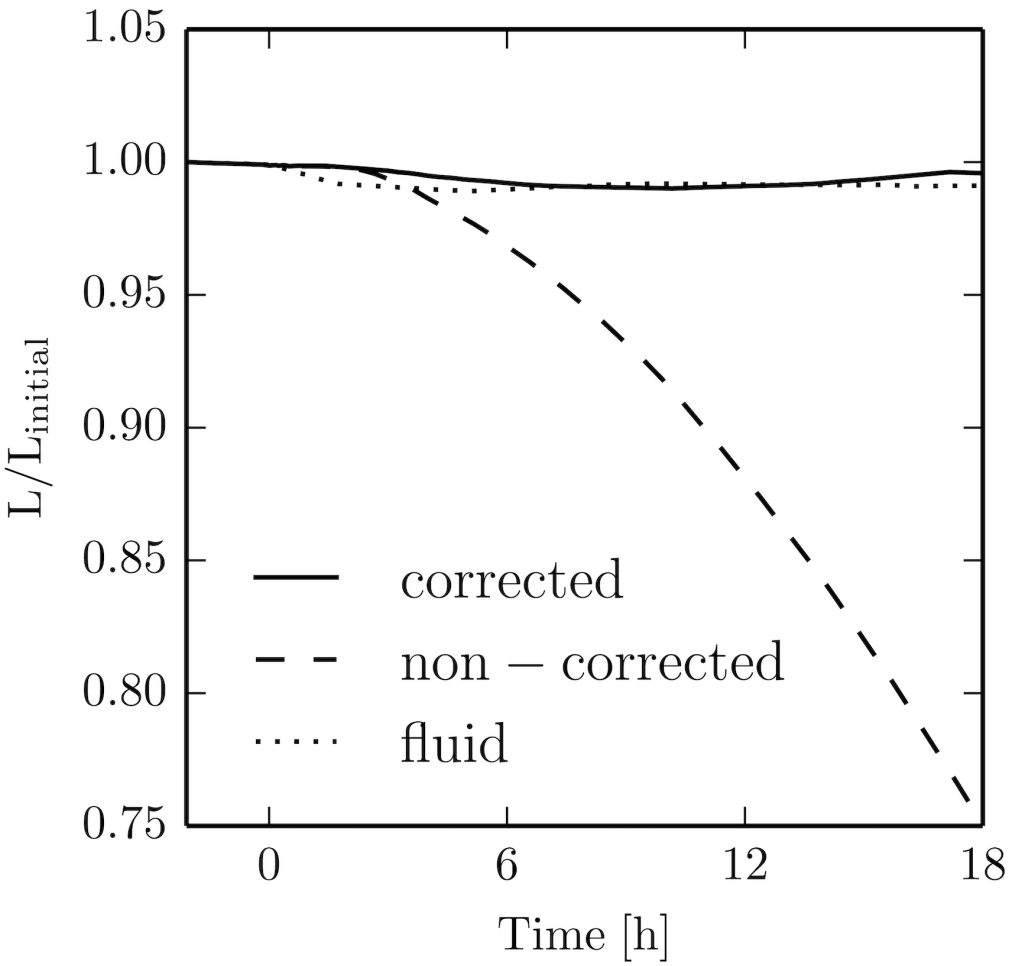

Figure 2.3: Angular momentum as a function of time (after impact) for SPHLATCH simulations of an oblique, planetary-scale impact on a Mars-like body in the case of no solid strength (fluid), strength without the Schäfer et al. (2007) correction tensor (non-corrected) and strength with the correction (corrected), taken from Emsenhuber (2017). Angular momentum, L, is normalised to its initial value, L_{initial}, and should therefore have a constant value of 1 if angular momentum is fully conserved. Here we see that, after rigid-rotation of the target is initiated by the oblique impact, angular momentum is gradually lost from the system, leading to a decrease in total angular momentum of ∼25% after 18 hours post-impact. After applying the correction tensor, angular momentum is conserved to the same degree as the fluid case.

for the study presented in Chapter 4. When using the form of Eq. 2.73, total angular momentum was seen to increase significantly after impact.

To investigate this issue further, vary tests were made for a simple simulation of a rotating Mars-like body without any impact. Some of these test cases are shown in Figure 2.4. These tests confirmed that the Schäfer et al. (2007) form for the rotation rate tensor indices is correct, which yields angular conservation comparable to the fluid case without strength. Interestingly, following the incorrect form of Benz and Asphaug (1994) with the inclusion of the correction tensor leads to a continuous increase of angular momentum as the rotating body "spins up" over time, in contrast to the case without the correction tensor, which dampens the body's rotation causing it to "spin down" over time, eventually reaching a stationary state of zero angular momentum.

Clearly, using the correct form of Eq. 2.55 is of great importance for angular momentum conservation in the size-regime of Mars. At smaller scales, however, the errors introduced by the Eq. 2.73 form do not have as significant an effect. Tests were also performed for a giant impacts on a Pluto-like body using a different SPH code (Benz and Asphaug, 1995; Jutzi et al., 2008; Jutzi, 2015), which found only minor differences in the total angular momentum for each rotation rate tensor form. The insignificance of this error at smaller scales also explains why this discrepancy has remained unnoticed until now, as the great majority of previous works including the solid description in their SPH model have been conducted for investigations into small bodies such as asteroids. As shown in Chapter 4 and Chapter 5, however, solid strength is important even at Pluto and Mars scales, meaning that there will likely be many future studies including strength in these regimes where the error induced by the incorrect rotation rate tensor formulation is significant.

2.3.4 Variable Smoothing Length

By construct of the SPH method, particle positions can change over time according to the momentum equation (Eq. 2.43). This means the number density of particles can change over time. For optimum resolution, however, the number of neighbours, N_{N}, that contribute to the SPH sum for a given particle should be roughly constant. This number depends on the choice of SPH kernel; for the B-spline kernel used

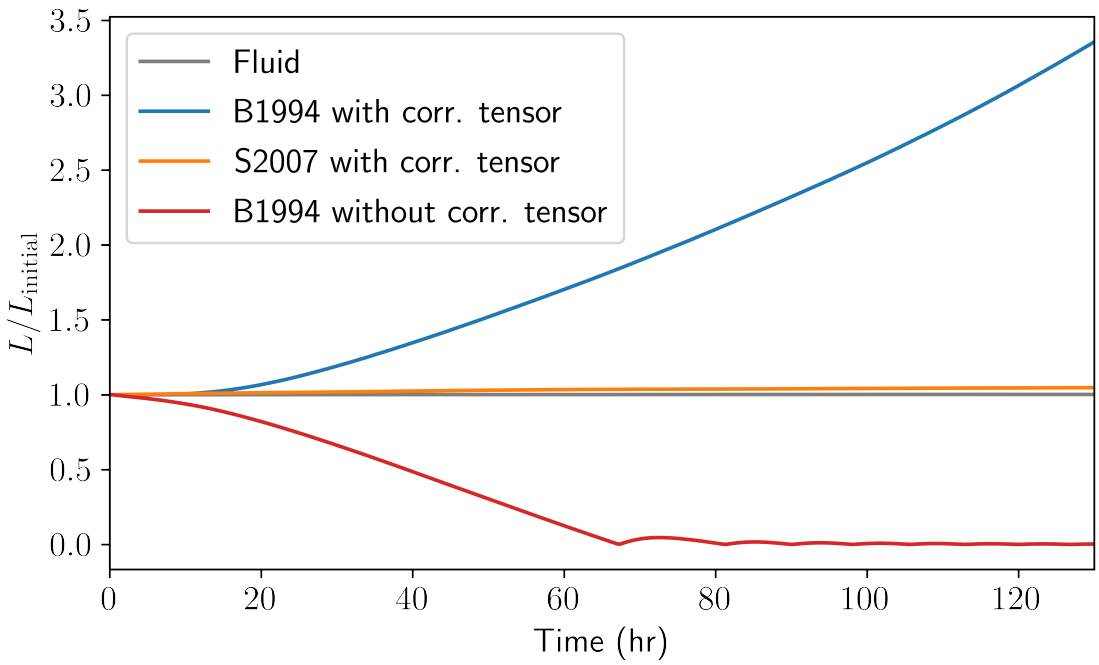

Figure 2.4: Angular momentum as a function of time for various SPH test cases of Mars-like body with an initial rotation period of 10 hours. B1994 refers to the Benz and Asphaug (1994) rotation rate tensor formulation, while S2007 denotes the Schäfer et al. (2007) form now used in SPHLATCH.

in SPHLATCH, a number of $N_{\mathrm{N,opt}} = 50$ is preferred. The smoothing length of each particle must therefore be varied such that $N_{\mathrm{N}} \approx N_{\mathrm{N,opt}}$, within its sphere of influence (radius $2h$ for the B-spline kernel).

As the mass of each particle is constant, a decrease in the number density of particles also corresponds to a decrease in mass density. To keep $N_{\mathrm{N}} \approx N_{\mathrm{N,opt}}$ in this scenario, the sphere defined the smoothing length of a particle must increase. The cubed smoothing length should therefore be inversely proportional to the density, i.e.

$$h_\imath^3 \propto \frac{1}{\rho_\imath} \tag{2.75}$$

For time variation of the smoothing length, we can therefore differentiate Eq. 2.75 with respect to time. To do this, we first re-write the equation as an equality via the inclusion of a constant of proportionality, κ,

$$h_\imath = \kappa \rho_\imath^{-\frac{1}{3}} \tag{2.76}$$

which, when differentiated with respect to time, becomes

$$\frac{\mathrm{d}h_\imath}{\mathrm{d}t} = -\frac{\kappa}{3}\rho_\imath^{-\frac{4}{3}}\frac{\mathrm{d}\rho_\imath}{\mathrm{d}t}. \tag{2.77}$$

By substituting Eq. 2.76 back into Eq. 2.77, κ cancels, and we are left with

$$\frac{\mathrm{d}h_\imath}{\mathrm{d}t} = -\frac{h_\imath}{3\rho_\imath}\frac{\mathrm{d}\rho_\imath}{\mathrm{d}t}, \tag{2.78}$$

which, according to Eq. 2.6, can also be written as

$$\boxed{\frac{\mathrm{d}h_\imath}{\mathrm{d}t} = \frac{h_\imath}{3}\left(\nabla \cdot \boldsymbol{v}\right)_\imath} \tag{2.79}$$

Eq. 2.79 can be calculated via particle sum using Eq. 2.38, and keeps the number of neighbours exactly constant if density evolves isotropically. In most cases, and particularly in impact models, this is not the case, and the number of neighbours can therefore greatly deviate from the optimum. To account for this in SPHLATCH, additional terms are introduced that act to progressively increase or decrease the smoothing length time derivative as the number of neighbours falls further below or above the optimum, respectively. These terms are based on the global maximum velocity divergence across all particles, $(\nabla \cdot \boldsymbol{v})_{\mathrm{max}}$, at a given time, and are

implemented as follows:

$$\boxed{\frac{\mathrm{d}h_\imath}{dt} = h_\imath \left(k_1 \left(\nabla \cdot \boldsymbol{v}\right)_{\max} + k_2 \frac{1}{3} \left(\nabla \cdot \boldsymbol{v}\right)_\imath - k_3 \left(\nabla \cdot \boldsymbol{v}\right)_{\max} \right)} \tag{2.80}$$

where

$$\begin{aligned} k_1 &= \frac{1}{2}\left[1 + \tanh\left(-\frac{N_\mathrm{N} - N_\mathrm{N,min}}{5}\right)\right] \\ k_2 &= 1 - k_1 - k_3 \\ k_3 &= \frac{1}{2}\left[1 + \tanh\left(\frac{N_\mathrm{N} - N_\mathrm{N,max}}{5}\right)\right] \end{aligned} \tag{2.81}$$

with

$$N_\mathrm{N,min} = \frac{2}{3} N_\mathrm{N,opt} \quad \text{and} \quad N_\mathrm{N,max} = \frac{5}{3} N_\mathrm{N,opt} \tag{2.82}$$

A plot illustrating how these correction factors change with respect to the number of neighbours is given in Figure 2.5. When $N_\mathrm{N,min} < N_\mathrm{N} < N_\mathrm{N,max}$, the k_2-term dominates, and thus gives similar results to Eq. 2.79. When $N_\mathrm{N} < N_\mathrm{N,min}$ or $N_\mathrm{N} > N_\mathrm{N,max}$, the k_1 or k_3 term dominates, respectively, leading to a sharper rate of change in smoothing length towards the desired number $N_\mathrm{N,opt}$.

Eq. 2.80 keeps the number of neighbours within a suitable range for most cases. However, in scenarios involving highly non-uniform particle distributions with very steep gradients in density and velocity, the range of smoothing lengths where the k_2-term dominates can become very small relative to the $h\left(\nabla \cdot \boldsymbol{v}\right)$ terms. This causes the correction terms to consistently over-correct in each direction, never landing within the k_2 range. The smoothing length time derivatives therefore fluctuate between large positive and negative values, thus leading to very short time-steps in the numerical model (see Section 2.3.5 for further details on time-step calculation).

In impact simulations, this regime corresponds with events that produce significant but sparse ejecta material. As the ejecta particles move away from the target, they move from the dense planet to a near-vacuum. If their environment does not contain enough nearby ejecta particles to fulfill the $N_\mathrm{N} \approx N_\mathrm{N,opt}$ requirement, then a portion of their neighbours in the SPH sum will need to come from those of the target planet, even though the ejecta particles now have dramatically larger smoothing lengths than those of the planet. A small fractional change in smoothing length for the ejecta therefore causes a very large change in the number of neighbours, thus leading to the fluctuating smoothing length time derivative as described.

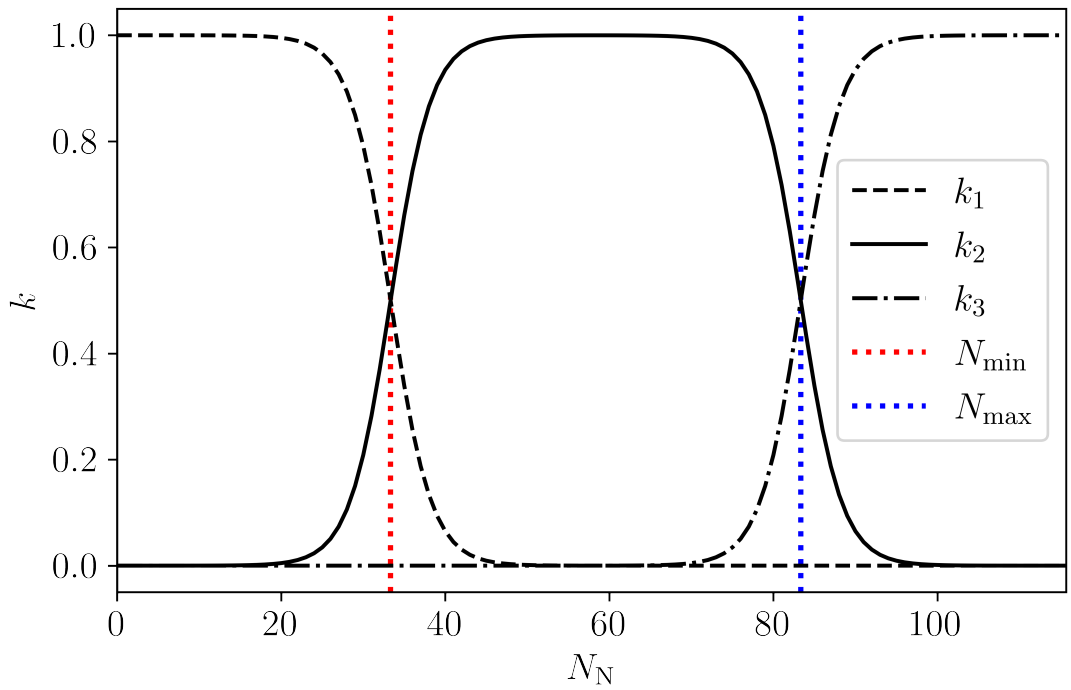

Figure 2.5: Each correction factor used in the smoothing length time derivative calculation (Eq. 2.80) as a function of a particle's number of neighbours. The optimum number of neighbours is set to $N_{\mathrm{N,opt}} = 50$, as is the case for the B-spline kernel used in SPHLATCH. The vertical coloured lines depict N_{min} and N_{max}, and correspond with the intersection of the correction factors.

2.3.5 Time Integration

Predictor-Corrector Scheme

The SPH scheme described thus far, together with the pressure and gravity calculations described in Section 2.4 and Section 2.5, provides a rigorous numerical method to calculate a closed set of time derivatives of various quantities such as internal energy and velocity, which can be integrated over time to simulate the dynamics of a continuum medium. In SPHLATCH, the numerical scheme used to perform this integration is the *predictor-corrector method* (e.g. Hairer et al., 2008). This method only requires two derivatives per time-step, which makes it particularly suitable for the SPH method where derivative calculations require computationally expensive SPH sums. For first order integration of any variable, B, the prediction step is given by

$$B^{(1/2)} = B^{(0)} + \frac{1}{2}\left(3\dot{B}^{(0)} - \dot{B}^{(-1)}\right)\Delta t \tag{2.83}$$

and the following correction step is given by

$$B^{(1)} = B^{(0)} + \frac{1}{2}\left(\dot{B}^{(0)} + \dot{B}^{(1/2)}\right)\Delta t \tag{2.84}$$

where $\dot{B}$ is the time derivative of B and Δt is the time-step. The bracketed superscripts denote time-step, with (0) being the current time-step before integration, (-1) the previous time-step, (1) the next time-step (i.e. after integration) and (-1/2) the intermediate value after the prediction but before the correction. The two derivative calculations are made to find $\dot{B}^{(0)}$ and $\dot{B}^{(1/2)}$ from $B^{(0)}$ and $B^{(1/2)}$, respectively, requiring the SPH sums described in the previous sections for each. $\dot{B}^{(-1)}$ is simply the retained value from the previous time-step. As there is no previous time-step at initialisation, $\dot{B}^{(-1)}$ is initially set to equal $\dot{B}^{(0)}$.

The above scheme allows us to integrate most variables directly, but not position as the momentum equation (Eq. 2.43) is the time derivative of velocity. To find the evolution of position over time this integral must therefore be differentiated twice. This is achieved by simply performing the numerical integration twice, first to find velocity and then to find position.

Time-step

The time-step, Δt, in the integration scheme cannot simply be chosen freely, rather it must fulfil various criteria. The most fundamental of these criteria is the *Courant-Friedrichs-Lewy* or *CFL* condition, which ensures that information cannot travel further than the distance between "mesh elements" of the hydrodynamic scheme. If this condition is not met, the scheme becomes unstable. As the "mesh" in the SPH scheme is represented by particles, the inter-particle distances define this maximum, which is well represented by the smoothing length. As information (i.e a wave) travels at the sound speed, c_s, the condition for a given particle $\imath$ is given by

$$\Delta t_\imath^{\mathrm{CFL}} = C_{\mathrm{CFL}} \frac{h_\imath}{c_{s,\imath}} \tag{2.85}$$

where CFL is a constant, given in SPHLATCH as CFL = 0.4.

The next criterion is dictated by the acceleration; for the scheme to remain stable, particle velocities (and therefore positions) should not change by several smoothing length magnitudes within one step. This leads to the expression

$$\Delta t_\imath^{\mathrm{A}} = C_{\mathrm{A}} \sqrt{\frac{h_\imath}{|\boldsymbol{a}_\imath|}} \tag{2.86}$$

where C_{A} is another constant, taken as $C_{\mathrm{A}} = 0.25$.

For all other variables, the change during a time-step cannot be too large relative to the pre-integrated value, i.e.

$$\Delta t_\imath^{\mathrm{B}} = C_{\mathrm{B}} \frac{B_\imath}{|\dot{B}_\imath|} \tag{2.87}$$

where the constant C_{B} depends on the variable; in SPHLATCH we use values in the range of 0.1–0.3. The only integrated variable this criterion is not applied to is the shear stress tensor components, as it was found to remain stable without such a time-step limit.

For most variables, a minimum value is enforced. This is most important for the smoothing length or density (if the density is found by integrating the continuity equation), as negative values would cause the entire SPH method to fail.

One caveat to the predictor-corrector scheme is that it requires an equal time-step across all particles. This means that any particles in extreme environments—such as those described in Section 2.3.4 for ejecta material—can dramatically reduce

the time-step across all particles, even if the errors caused by the particles in such extreme regions would have little to no effect on the majority. This therefore exacerbates the fluctuating smoothing length issue even further. At high resolutions, the chance of at least one particle being in such an environment at any given time increases. Clearly, a fix must be made to this issue in the future if SPHLATCH is to be used in high resolution studies of impacts involving significant ejecta.

2.4 Equation of State

As already mentioned, pressure is calculated in impact codes using an equation of state (EOS), which links the natural variables of the hydrodynamic model to thermodynamic quantities. The most simple EOS only calculates pressure (e.g. the *Murnaghan EOS)*, however more sophisticated models can provide other quantities such as temperature, entropy and sound speed that are often important in the scientific analysis of the results.

In SPH, the EOS is ideally a function of density and internal energy, as these are both natural output quantities of the model. For problems involving the evolution of simple gas, the ideal gas law can serve as a suitable equation of state. In impact studies, however, an equation of state able to model geological materials in solid and fluid phases.

One of the most prevalent models used for this purpose is the *Tillotson* EOS (Tillotson, 1962), which is a closed system of analytical equations that were originally derived for hypervelocity impacts of metals via explosive shock-wave experiments and statistical atomic structure models (*Mie-Grüneisen*, *Thomas-Fermi* and *Thomas-Fermi-Dirac*) These were later adapted to also represent geological materials (e.g. Melosh, 1989). The Tillotson EOS is convenient in SPH as it requires the intended input parameters of internal energy and density and is computationally fast. Its output only provides pressure and sound speed, however, thus excluding useful quantities such as temperature and entropy. Furthermore, the EOS only provides a highly simplified model of phase state, neglecting precise phase transitions and their respective latent heats.

A more thermodynamically rigorous EOS is ANEOS (Thompson and Lauson,

1972a; Thompson, 1990), which derives analytic expressions for various thermodynamic quantities including pressure, temperature and entropy via the minimisation of the Helmholtz free energy, F. The native variables of F are density and temperature (i.e. $F(\rho, T)$), and thus requires a root-finder to instead use internal energy as provided by SPH. Phase transitions are supported in this approach, along with mixed phases.

To fully distinguish these phases, a value for the latent heat of fusion must be provided. Without such a value, ANEOS only distinguishes between a *one-phase* state and a *two-phase* state; the latter corresponds to the region of parameter-space where there is a gas-solid or gas-liquid mixture, and the former therefore corresponds with all other states. Note that the "one-phase" moniker is misleading, as regions of the parameter space that would lead to a solid-liquid mixture are also included here. Including this value allows for the additional computation of the solid-liquid transition. The phase states described in ANEOS are distinguished by a *phase number*. given as follows (from Thompson and Lauson (1972b)):

1. A one-phase state for ANEOS without latent heat.
2. A liquid-gas or solid-gas.
3. Invalid (Indicates that a negative pressure has been set to zero).
4. A solid state for ANEOS with latent heat.
5. A liquid-solid state for ANEOS with latent heat.
6. A fluid state for ANEOS with latent heat. This also includes pure vapor states.

Here we see that the solids and fluids are distinguished along with their intermediate, mixed states. The final phase number (i.e. 6) describes a general fluid, encompassing liquid, gas and supercritical phases. Fortunately, ANEOS also provides a critical point as output for our material, which allows distinguish between these fluid phases. If the pressure and temperature are both above their respective critical values, the material is determined to be supercritical. If this is not the case, then the critical density is used to distinguish liquid from gas, with densities above this value indicating liquid, and densities below indicating gas.

In the work of this thesis, three material compositions were used for ANEOS: iron, water and dunite. For iron, the parameters are native to ANEOS, and are provided in Thompson (1990). The water parameters are those used in various previous impact studies (Reufer et al., 2010; Reufer, 2011; Reufer et al., 2012; Asphaug and Reufer, 2013). Both of these include a value for latent heat, and therefore the phases can be distinguished. Phase diagrams for these parameters are given in Figure 2.6 and Figure 2.7 for iron and water respectively.

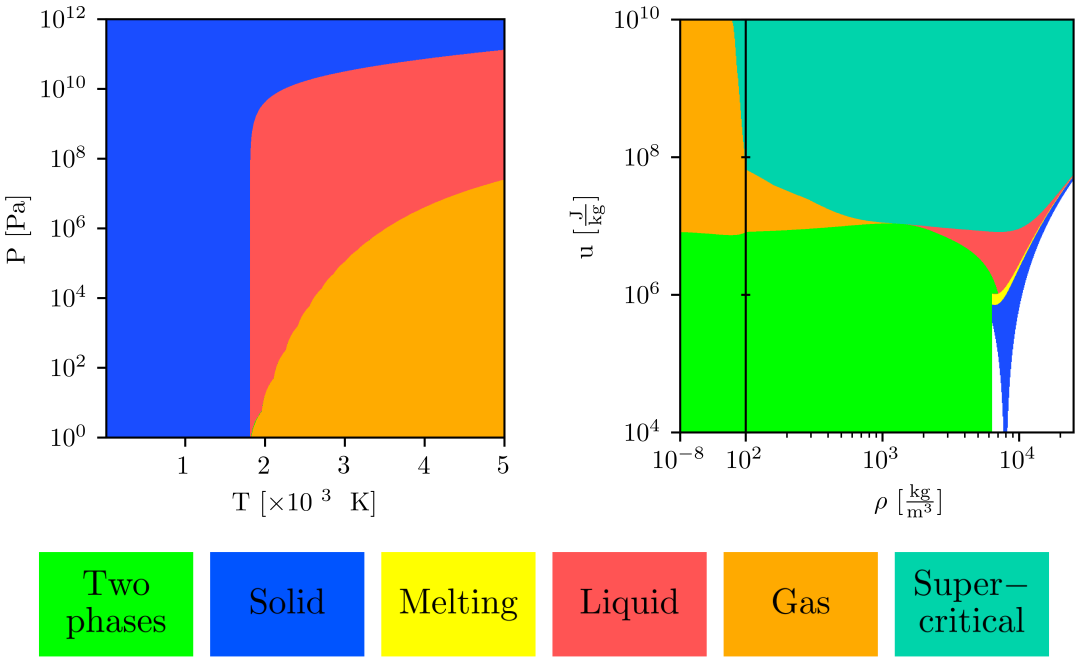

Figure 2.6: ANEOS phase diagrams for iron. (Left): a pressure-temperature diagram across a suitable range for the material. (Right): internal energy against density across the entire table used during the simulations. Colours indicate the phase of the material across the parameter-space. The vertical line indicates the transition from the low density table to the high density table. Note that the parameter-space of the pressure-temperature diagram is not the equivalent of energy-density plot.

The dunite parameters are taken from Benz et al. (1989), but do not include a value for latent heat. An additional melting curve is therefore used to distinguish the phases. Several options are included in SPHLATCH for this purpose, each providing the melting temperature as a function of pressure. The first is a simple formula given

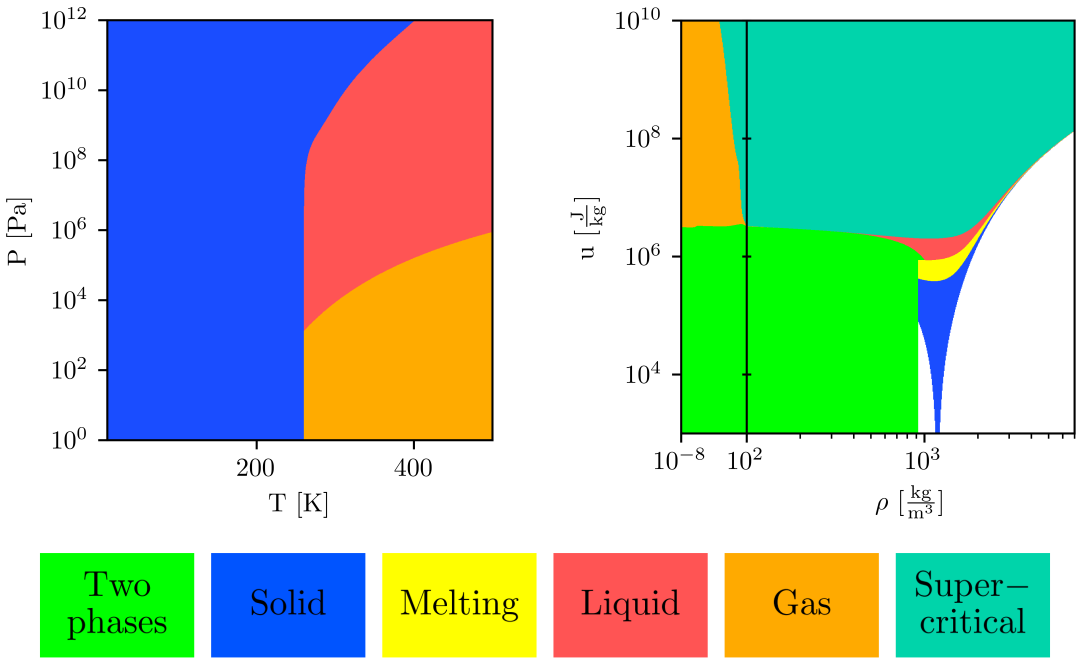

Figure 2.7: ANEOS phase diagrams for water. (Left): a pressure-temperature diagram across a suitable range for the material. (Right): internal energy against density across the entire table used during the simulations. Colours indicate the phase of the material across the parameter-space. The vertical line indicates the transition from the low density table to the high density table. Note that the parameter-space of the pressure-temperature diagram is not the equivalent of energy-density plot.

in Senft and Stewart (2009):

$$T_{\text{melt,dunite}}(\text{K}) = \begin{cases} 2000 & P < 0.7 \text{ GPa} \\ 2000 + (P - 0.7) * 85.7 & \text{otherwise} \end{cases} \tag{2.88}$$

which leads to the phase diagrams given in Figure 2.8.

At very high densities and internal energies ($\rho \gtrsim 4 \times 10^3$ kg/m^3 and $u \gtrsim 10^9$ J/kg), the Senft and Stewart (2009) melting curve suggests a solid-phase region in the parameter-space that is increasing in size for greater internal energies, but this has no physical reasoning (compare to the phase diagrams for iron and water where this region is all supercritical fluid). To avoid this, an alternative option is provided in SPHLATCH taken from González-Cataldo et al. (2016), who used *First Principles Molecular Dynamics* simulations (i.e. quantum-mechanical simulations of atomic-scale interactions) to predict the melting curve for SiO_2 up to multimegabar pressures, given by

$$T_{\text{melt,SiO}_2}(\text{K}) = 1968.5 + 478.7P^{0.426} \tag{2.89}$$

with P in units of GPa and the respective phase diagrams given in Figure 2.9.

The final melting curve for rock available in SPHLATCH is that of Duncan et al. (2018), who used multianvil experiments to predict the solidus of Mars' mantle via a simplified compositional analogue. This was implemented into SPHLATCH for the Martian Dichotomy studies of Chapter 3 and Chapter 4, and is given by

$$T_{\text{sol,Mars}}(\text{K}) = \begin{cases} -4.877P^2 + 120.2P + 1361 & P \leq 10 \text{ GPa} \\ -1.323(P - 10)^2 + 38.18(P - 10) + 2075 & 10 \text{ GPa} < P \leq 23 \text{ GPa} \\ 77.75(P - 23) + 2348 & P > 23 \text{ GPa} \end{cases} \tag{2.90}$$

leading to the phase diagrams of Figure 2.10. Here we again see a potentially spurious high-energy high-density region of solid material, but this region is not encountered in the work of this thesis and therefore is not considered to have a large effect on the results.

The most important reason to include the solid-liquid phase change in the SPH model is to determine whether the strength model needs to be calculated, as it only applies to solid material. Moreover, for particles within a solid the melting

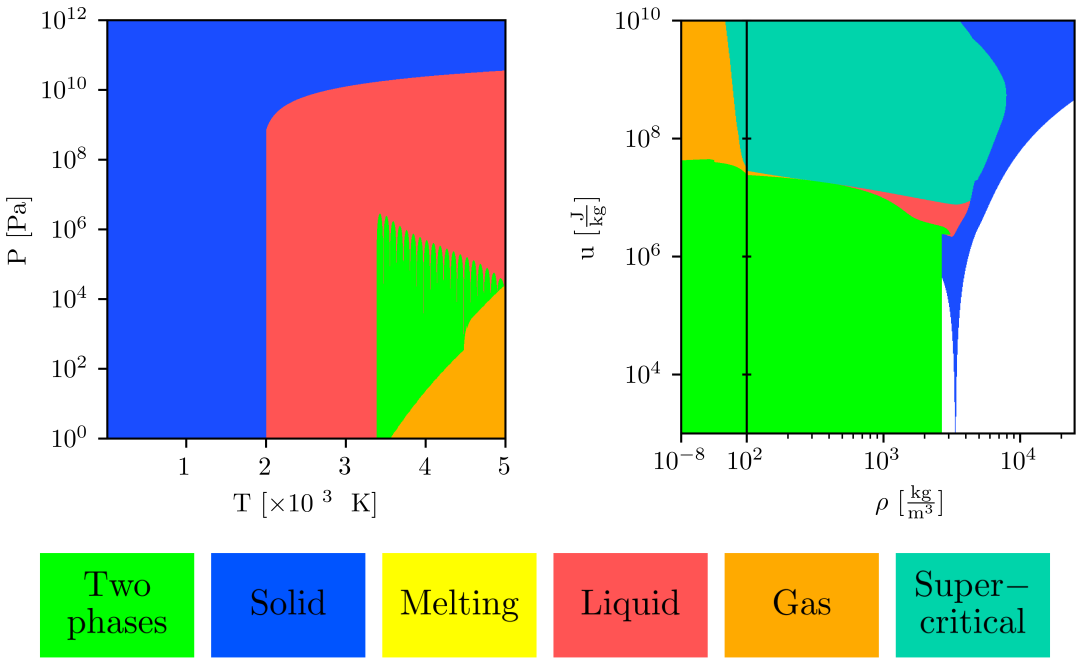

Figure 2.8: ANEOS phase diagrams for dunite using the Senft and Stewart (2009) melting curve. (Left): a pressure-temperature diagram across a suitable range for the material. (Right): internal energy against density across the entire table used during the simulations. Colours indicate the phase of the material across the parameter-space. The vertical line indicates the transition from the low density table to the high density table. Note that the parameter-space of the pressure-temperature diagram is not the equivalent of energy-density plot.

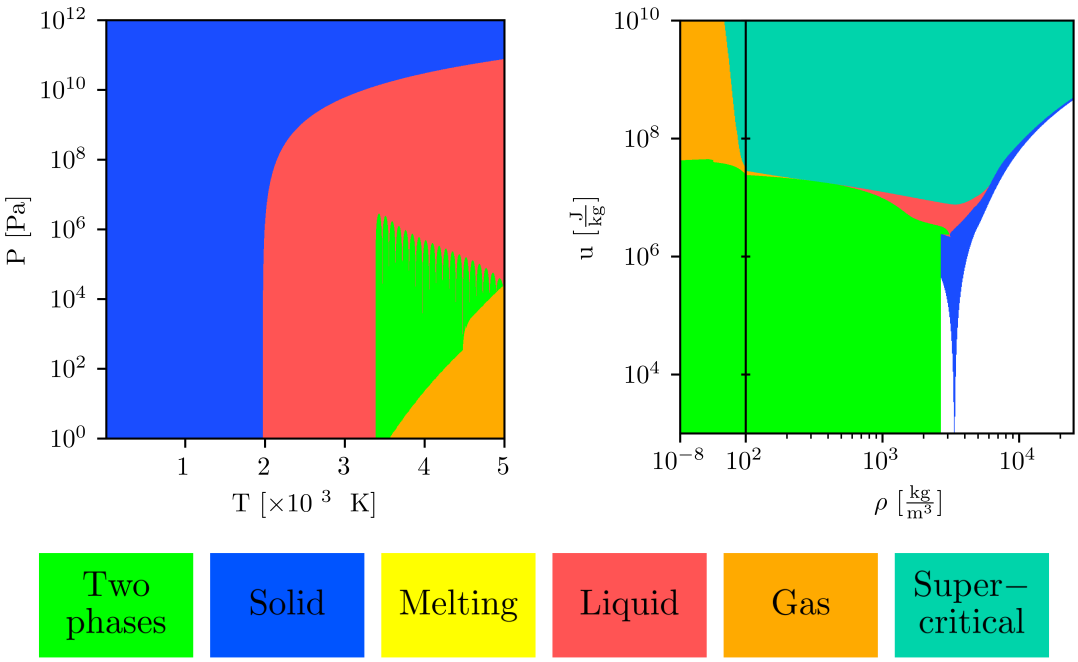

Figure 2.9: ANEOS phase diagrams for dunite using the González-Cataldo et al. (2016) melting curve. (Left): a pressure-temperature diagram across a suitable range for the material. (Right): internal energy against density across the entire table used during the simulations. Colours indicate the phase of the material across the parameter-space. The vertical line indicates the transition from the low density table to the high density table. Note that the parameter-space of the pressure-temperature diagram is not the equivalent of energy-density plot.

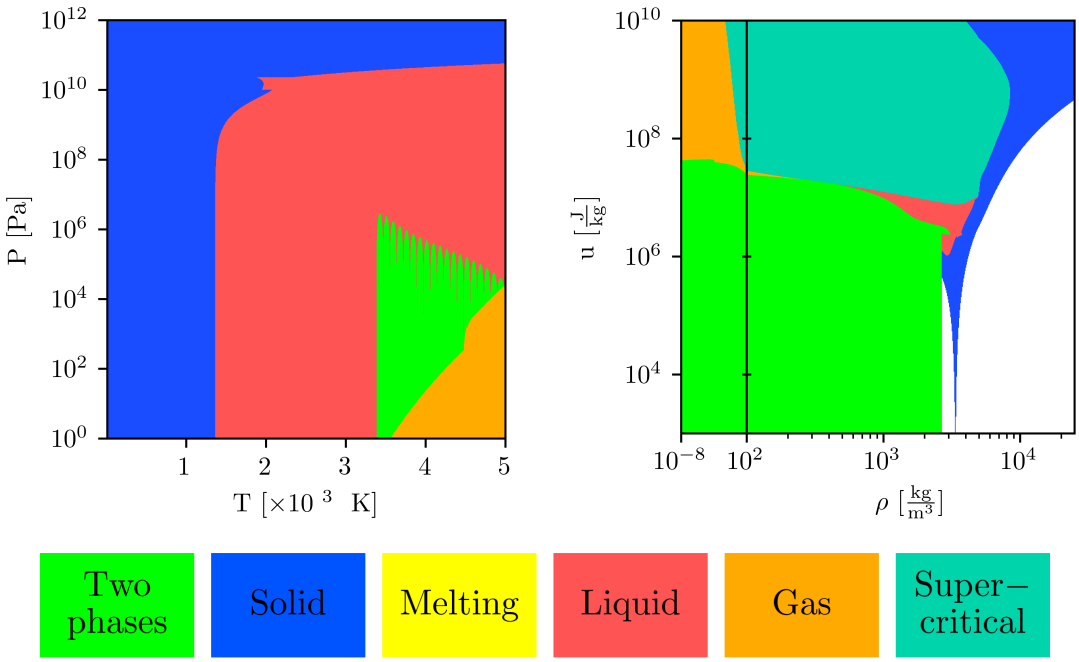

Figure 2.10: ANEOS phase diagrams for dunite using the Duncan et al. (2018) melting curve. (Left): a pressure-temperature diagram across a suitable range for the material. (Right): internal energy against density across the entire table used during the simulations. Colours indicate the phase of the material across the parameter-space. The vertical line indicates the transition from the low density table to the high density table. Note that the parameter-space of the pressure-temperature diagram is not the equivalent of energy-density plot.

temperature corresponding with particle's pressure must be known in order to calculate the extent of thermal softening (from Eq. 2.69). For rock, this simply means substituting the particle's current pressure into the chosen melting curve; for water and iron, however, the melting temperature must be derived from the knowledge of phase numbers. This is achieved by identifying the small temperature interval (for a given particle's pressure) in which the phase number changes to liquid using a root-finder. The temperature at which the phase first changes to liquid is the melting temperature we use.

The root-finder used for this purpose, and to enable the use of internal energy rather than temperature as input to ANEOS, is *Brent's method*, which is a hybrid algorithm combining the *bisection method*, the *secant method* and *inverse quadratic interpolation*. This root-finding step is computationally expensive, however. SPHLATCH therefore performs the root-finding steps on a large grid of points within the parameter-space prior to the simulation run, and saves these in a table. This table is then interpolated during the simulation to find the quantities of interest. This method proves to be significantly faster than repeatedly root-finding throughout the simulation, and is the usual method when dealing with a complex equation of state such as ANEOS.

Specifically, two logarithmic tables are used to enable efficient storage across a wide range of densities: a low density table across 100 equally spaced points (in log-space) from 10^{-8} kg/m^3 to 10^2 kg/m^3, and a high density table across 500 equally spaced points from 10^2 kg/m^3 to a maximum of 7×10^3 kg/m^3 for water and 25×10^3 kg/m^3 for rock and iron. The higher resolution for the high density table is necessary as density-dependent phase changes occur within this range. For each density, 1500 points in internal energy and entropy are stored, thus leading to a total of four tables for each material.

Note that the root-finding method takes latent heating into account, as this is including in the phase number calculation of ANEOS. The melting curve method for rock, however, does not include any latent heat. This means that the solid strength for rock is slightly underestimated, as there are regions considered liquid in the parameter-space where the rock would in fact still be solid. In addition, for Mars, the melting curve used is in fact the solidus, which therefore also causes weak-

ened strength compared to the results that would come from a higher temperature liquidus.

Finally, it is also possible to skip these calculations entirely and simply supply a constant melting temperature to be used for the solid strength model. For many materials, the melting temperature only changes at high pressures ($\gtrsim$1 GPa), and so a constant value can be a reasonable approximation. This method is useful in that the melting temperature can be applied precisely as obtained from experiments, rather than relying on the calculations of EOS. This method was used for water in the Pluto study of Chapter 5, as ANEOS underestimates the melting temperature by $\sim$15 K (see Figure 2.7), and the pressures within the dwarf planet mantle do not get high enough to have a strong influence on the melting temperature.

2.5 Gravity and Particle Neighbours

2.5.1 Gravity

In Eq. 2.3 it was noted that external forces can influence the momentum of a fluid parcel. At the scales investigated in astrophysical studies, each SPH particle represents a large mass of material and therefore necessitates the inclusion of the force of gravity. In a similar manner to the SPH method described thus far, this force is smoothed (or *softened*) over the smoothing kernel to enable a continuum distribution to be modelled using discrete particle.

To achieve this smoothing, the local gravitational potential for a given particle is approximated as

$$\Phi_\imath = G \sum_{\jmath}^{N} m_\jmath \phi \left(r_{\imath\jmath}, \lambda_\imath \right) \tag{2.91}$$

where G is the gravitational constant and $\phi \left(\boldsymbol{r}_{\imath\jmath}, \lambda_\imath \right)$ is known as the gravitational softening kernel, with $\lambda_\imath$ being its associated softening length for particle $\imath$. In SPH, this softening length is usually set to be equivalent to the smoothing length, i.e. $\lambda = h$.

The force per unit mass for particle $\imath$, and thus the contribution in the particle's

associated momentum equation SPH sum, therefore follows as

$$\boxed{\boldsymbol{a}_{\mathrm{g},\imath} = -\nabla\Phi = -G\sum_{\jmath}^{N} m_\jmath \frac{\partial\phi(r_{\imath\jmath}, h_\imath)}{\partial r}\left(r_{\imath\jmath}, h_\imath\right)\frac{\boldsymbol{r}_{\imath\jmath}}{r_{\imath\jmath}}} \tag{2.92}$$

An expression for the softening kernel follows from *Poisson's equation* given by

$$\nabla^2\Phi(\mathbf{r}) = 4\pi G\rho(\boldsymbol{r}) \tag{2.93}$$

which, through substitution of Eq 2.33 and Eq. 2.91 and the use of spherical polar co-ordinates (and with the implicit assumption that particles are spherically symmetric), leads to the following expression for the smoothing kernel:

$$W(r,h) = \frac{1}{4\pi r^2}\frac{\partial}{\partial r}\left(r^2\frac{\partial\phi(r,h)}{\partial r}\right) \tag{2.94}$$

which can be rearranged to give

$$\frac{\partial\phi}{\partial r} = \frac{4\pi}{r^2}\int_0^r r'^2 W\left(r'\right)\mathrm{d}r' \tag{2.95}$$

which, for the B-spline kernel (Eq 2.23), gives

$$\frac{\partial\phi}{\partial r} = \frac{1}{h^2}\begin{cases} \frac{4}{3}q - \frac{6}{5}q^3 + \frac{1}{2}q^4 & 0 \le q < 1 \\ \frac{8}{3}q - 3q^2 + \frac{6}{5}q^3 - \frac{1}{6}q^4 - \frac{1}{15q^2} & 1 \le q < 2 \\ q^2 & q \ge 2 \end{cases} \tag{2.96}$$

which can be integrated to give

$$\phi(r,h) = \frac{1}{h}\begin{cases} \frac{2}{3}q^2 - \frac{3}{10}q^4 + \frac{1}{10}q^5 - \frac{7}{5} & 0 \le q < 1 \\ \frac{4}{3}q^2 - q^3 + \frac{3}{10}q^4 - \frac{1}{30}q^5 - \frac{8}{5} + \frac{1}{15q} & 1 \le q < 2 \\ -q & q \ge 2 \end{cases} \tag{2.97}$$

These equations allow the force of gravity to be correctly handled in the SPH model. It is also straightforward to keep track of the total gravitational potential energy, which is simply mass times gravitational potential summed across all particles, i.e.

$$\begin{aligned} \Psi &= G\sum_{\imath}^{N} m_\imath \sum_{\jmath\le\imath}^{N} m_\jmath \phi_{\imath\jmath}\left(h_\imath\right) \\ &= \frac{G}{2}\sum_{\imath}^{N}\sum_{\jmath}^{N} m_\imath m_\jmath \phi_{\imath\jmath}\left(h_\imath\right) \end{aligned} \tag{2.98}$$

where the factor half is due to double sum over all the particles (i.e. including terms where $\imath = \jmath$). By substituting in Eq. 2.91 we are left with

$$\Psi = \frac{1}{2}\sum_{\imath}^{N} m_\imath \Phi_\imath \tag{2.99}$$

The total energy of the system can now be calculated as the sum of kinetic energy ($\frac{1}{2}mv^2$), internal energy (u), and gravitational potential (Φ) for all particles

$$E = \sum_{\imath} m_\imath \left(\frac{1}{2}\mathbf{v}_\imath \cdot \mathbf{v}_\imath + u_\imath + \frac{1}{2}\Phi_\imath\right) \tag{2.100}$$

which gives an important check of energy conservation during the SPH simulations.

2.6 Barnes-Hut Tree

2.6.1 Multipole Approximation

As can be seen from the softening kernel expressions Eq. 2.96 and Eq. 2.97, the contributions to the SPH sum extend to neighbours beyond the compact support of the smoothing kernel; indeed, *all* particles should contribute to each SPH sum. This leads to a complexity of $\mathcal{O}(N^2)$, which is not computationally feasible for SPH simulations with $N \approx 10^6$ particles. To combat this, SPHLATCH utilises the *multipole approximation*, whereby distant particles are approximated as a single body (or *cluster*) through a sum of gravity contributions known as their *multipole moments*. To recover an exact solution with this approximation one would require an infinite number of multipole moments; however, their significance rapidly decreases with increasing order, thus making an approximation with relatively few moments accurate enough for practical use. In SPHLATCH, the first two non-zero multipole moments are used for this approximation, known as the *monopole* and *quadrupole* moments.

The expression for gravitational potential of a cluster of mass M_C at a distance $\boldsymbol{r}$ from its center of mass in this approximation is given by

$$\phi(\boldsymbol{r}) = G\left(\underbrace{-\frac{M_\mathrm{C}}{|\boldsymbol{r}|}}_{\text{monopole}} \underbrace{-\frac{Q^{\alpha\beta}r^\alpha r^\beta}{2|\boldsymbol{r}|^5}}_{\text{quadrupole}}\right) \tag{2.101}$$

and the associated force per unit mass

$$a_g^\tau = -\nabla^\tau \phi(\boldsymbol{r}) = -G \left(\underbrace{\frac{M_\mathrm{C}}{|\boldsymbol{r}|^2} \frac{r^\tau}{|\boldsymbol{r}|}}_{\text{monopole}} + \underbrace{\frac{Q^{\alpha\beta}}{|\boldsymbol{r}|^4} \left(\frac{\delta^{\alpha\tau} r^\beta}{|\boldsymbol{r}|} + \frac{5 r^\alpha r^\beta r^\tau}{2|\boldsymbol{r}|^3} \right)}_{\text{quadrupole}} \right) \tag{2.102}$$

where the Einstein summation rule is again used for the tensor indices α, β and τ, which each can take values of 1, 2 or 3, corresponding with three-dimensional Euclidean space.

From these equations, we see that the monopole contribution is simply the gravity calculation as if the cluster is a point mass. The quadrupole contribution is more complex, with the $Q^{\alpha\beta}$ term given by

$$Q^{\alpha\beta} = \sum_c m_c \left(3 r_c^\alpha r_c^\beta - |\boldsymbol{r}_c|^2 \delta^{\alpha\beta} \right) \tag{2.103}$$

where m_c is the mass of each particle c in the cluster, and $\boldsymbol{r}_c$ is the position vector from the cluster center of mass to each particle.

This approximation can also be applied to a cluster of clusters by simply included their respective quadrupole moments $Q_c^{\alpha\beta}$ in the sum , i.e.

$$Q^{\alpha\beta} = \sum_c \left[M_c \left(3 r_c^\alpha r_c^\beta - |\boldsymbol{r}_c|^2 \delta^{\alpha\beta} \right) + Q_c^{\alpha\beta} \right] \tag{2.104}$$

where M_c signifies that this is a sum over clusters rather than individual particles.

2.6.2 Tree

To reap the computational benefits of the the multipole approximation, a Barnes and Hut (1986) tree algorithm is used which efficiently groups the particles into clusters. The algorithm begins by creating a base (or *root*) cubic cell with a volume that encompasses all particles in the simulation. The cell is then subdivided into 8 equal-volume *daughter* cells, each with a length that is half that of the *parent*. This process is then repeated on each subsequent daughter cell until there is exactly one particle in every cell. The tree has now been constructed. An illustration of such a tree in two dimensions is given in Figure 2.11.

Each cell then has its associated multipole approximation calculated. To find the gravity contributions on a given particle, the tree is walked down from the the root

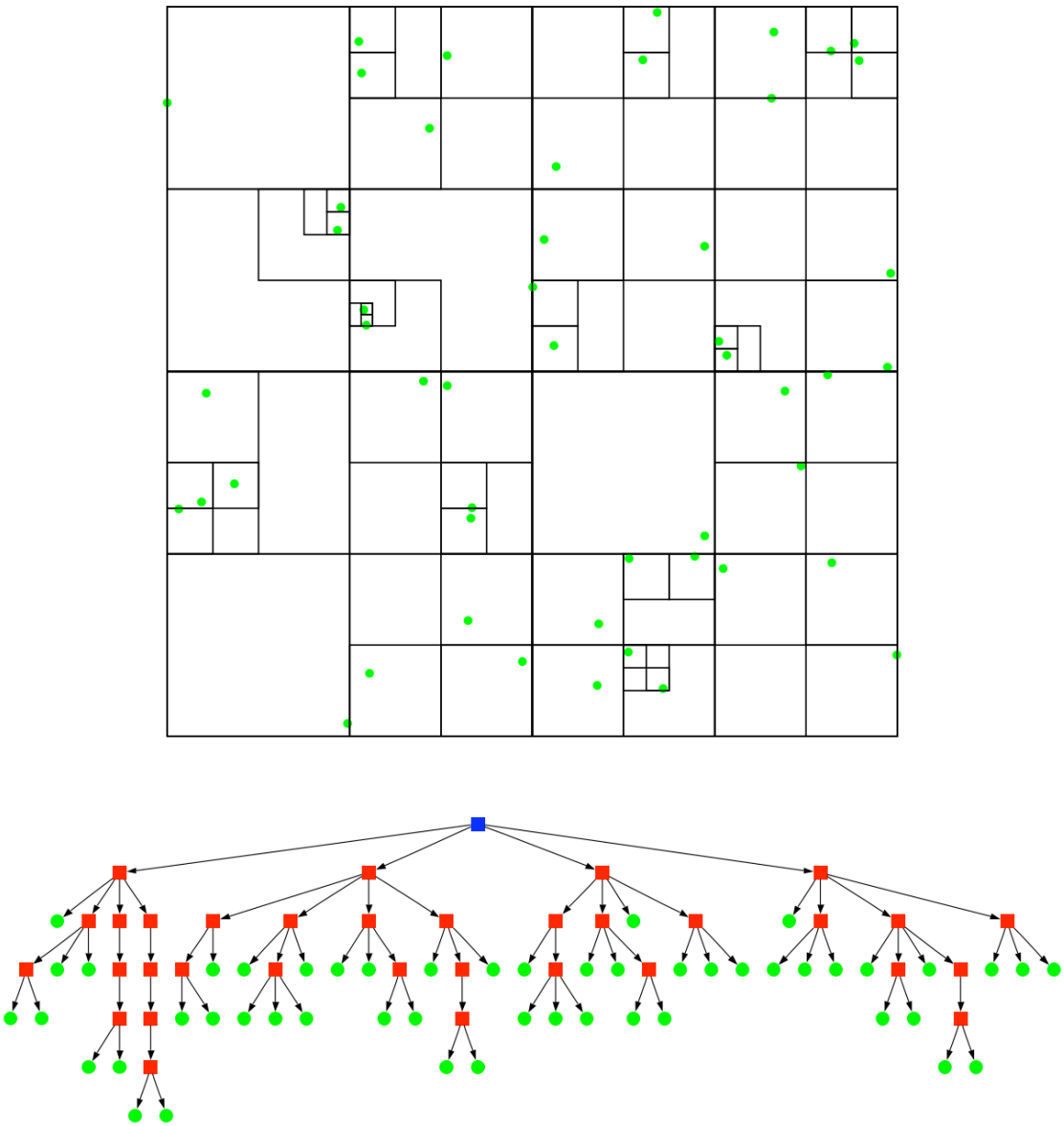

Figure 2.11: Example tree calculation for 50 randomly distributed particles in two dimensional space, taken from Reufer (2011). (Top): the cell distribution of the tree, with each particle indicated as a green point. (Bottom): a visualisation of the tree construction, where each green point represents a cell with only one particle inside, the red squares represent the parent cells and the blue square represents the root cell. Note that each division is by 4 rather than 8, due to this calculation being made in two dimensions rather than three.

cell. For each encountered daughter cell, a criterion is evaluated that determines whether the multipole approximation is valid, given by

$$\frac{l_{\mathrm{C}}}{|\boldsymbol{r}_i - \boldsymbol{r}_C|} < \theta \tag{2.105}$$

where l_{C} is the length of the cell, $\boldsymbol{r}_C$ is the position vector of the cell's center of mass, $\boldsymbol{r}_i$ is the position vector of the particles whose gravitational acceleration is being calculated, and θ is constant known as the *opening angle* taken as $\theta = 0.7$ in SPHLATCH. If this criterion is fulfilled, the gravitational contribution is calculated through the multipole approximation and thus the daughter cells are skipped. If not fulfilled, the tree walk continues. If the walk reaches a cell containing only one particle (a *leaf* cell) which therefore has no daughter cells, the gravity calculation is carried out explicitly. Calculating the gravity contributions in this way reduces the complexity of the computation down to $\mathcal{O}(N \log N)$.

2.6.3 Particle Neighbour Search

The tree algorithm also provides an efficient method of finding the neighbours that will contribute to the SPH sums for each particle. Due to the compact support aspect of the kernel, only neighbours within $2h$ need to be considered. To find the neighbours for a given particle the tree is first walked upwards, starting from the particle's leaf cell through its parents, until a cell is reached that encompasses the entire sphere of radius $2h$. This subtree is then is then iteratively searched for neighbours in a optimised manner, skipping cells whenever possible.

Originally, the SPH contributions were calculated for each neighbour when encountered during the tree walk. For a simulation including hydrodynamics, solid strength and the necessary correction tensor for rigid-body rotation, this would mean performing the neighbour search three times for one integration step. A much more efficient method, now implemented in SPHLATCH, is to instead perform the neighbour search only once, assigning each particle with a (pointer) list of its neighbours. Each sum can then be performed over this list, without the need for any further neighbour searches for a given time-step, thus increasing computational efficiency significantly.

Creating lists in this way also allows for the resolution of an additional issue

with the old implementation of SPHLATCH. The efficiency of the neighbour search largely stems from the ability confine the search to a volume close to a sphere of radius $2h$. This must be predefined prior to the tree walk, and so naturally takes the smoothing length to be that of the central particle, $\imath$, whose neighbours are being searched for. However, to maintain symmetry, the SPH sum contributions are actually calculated using the arithmetic mean of the central particle smoothing length, $h_\imath$, and the contributing neighbour smoothing length, $h_\jmath$, i.e. $h_{\imath\jmath} = \frac{h_\imath + h_\jmath}{2}$. Of course, symmetry between particle contributions only occurs if particle j is included in particle i's sum *and* vice versa. Unfortunately, this is not the case if neighbours are only searched within $2h_\imath$ rather than $2h_{\imath\jmath}$. If the distance between two particles is $r_{\imath\jmath}$, the asymmetry occurs when $r_{\imath\jmath} > 2h_\jmath$ but $r_{\imath\jmath} < 2h_\imath$ and $r_{\imath\jmath} < 2h_{\imath\jmath}$. Here, particle $\jmath$ will contribute to particle $\imath$'s SPH sum, but not the other way round, as is illustrated in Figure 2.12.

This issue was resolved by adding the central particle to its neighbour's neighbour list if the above conditions for asymmetry are met. When performing the SPH sums, the neighbour contributions are then guaranteed to be symmetric (see Figure 2.13 for improvement in angular momentum conservation). In practice, this does reduce some computational efficiency as SPHLATCH is a parallelised code (i.e. many computations can be carried out simultaneously across many CPU *cores* to reduce simulation run-time), which require certain conditions to remain optimally efficient. In the case of each neighbour search being able to access and write to each particle's neighbour list at any given time, a so-called *data race* can occur, where one CPU core attempts to write to a neighbour list (i.e. to add a neighbour) while one or more other cores are already accessing the same list (either reading or writing). This causes the program to experience a segmentation fault and thus crash. To avoid this issue, computational *locks* are used that exclude the simultaneous access of the neighbour lists. Individual cores may therefore need to wait for other cores to complete their neighbour list related tasks before completing their own, thus reducing computational efficiency. Fortunately, the neighbour asymmetry issue does not occur frequently enough for these locks to cause significant slowing of the simulation calculations in the parameter-space studied in this thesis, and thus the increase in physical consistency from better adherence to momentum conservation laws is

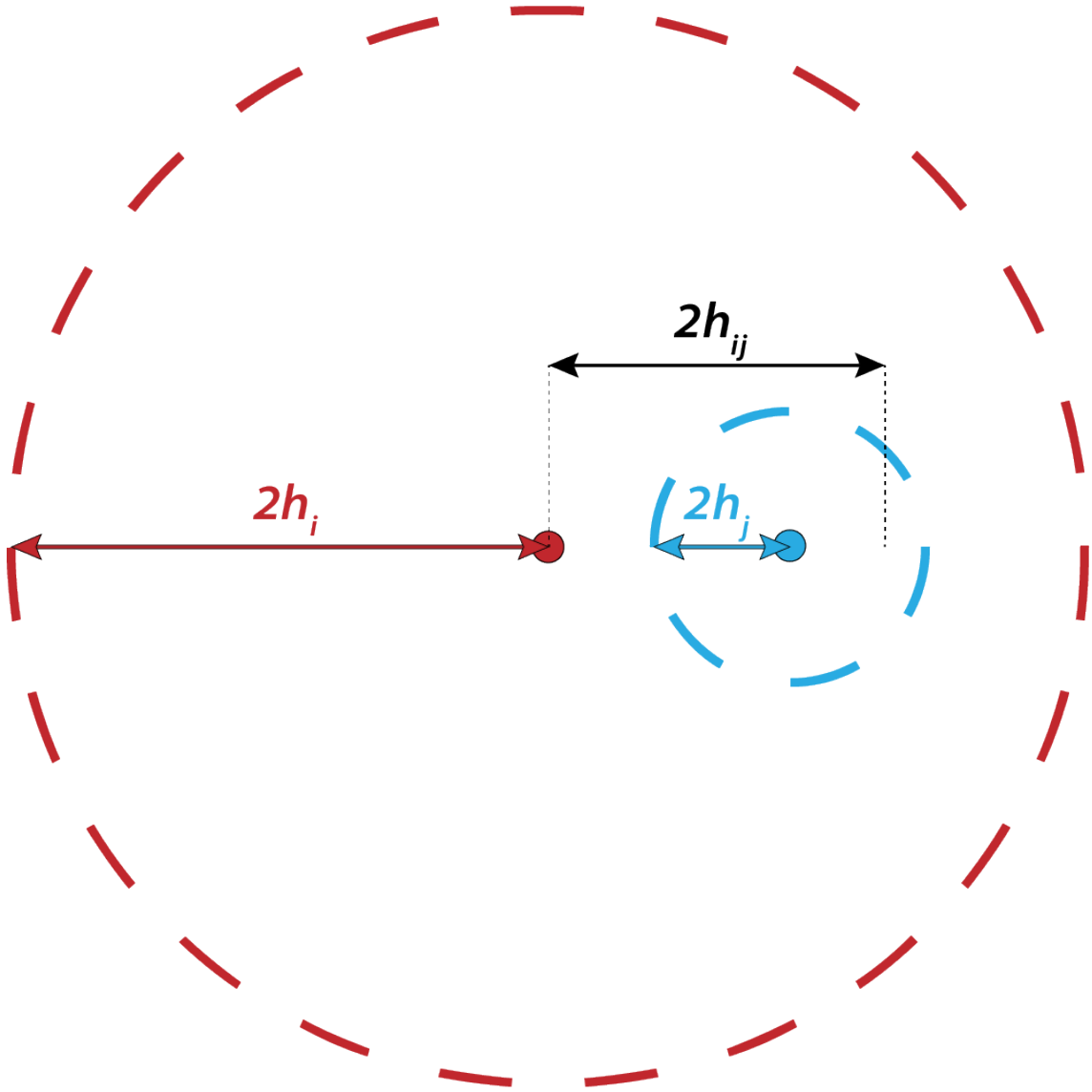

Figure 2.12: A schematic diagram illustrating the asymmetry in the SPH sum calculations if only neighbours within $2h_i$ are considered. Here, the distance between the two particles is less than $2h_{ij}$, meaning they will contribute to each other's SPH sums; however, particle i will not be found in particle j's neighbour search within $2h_j$.

considered worth the small increase in computation time.

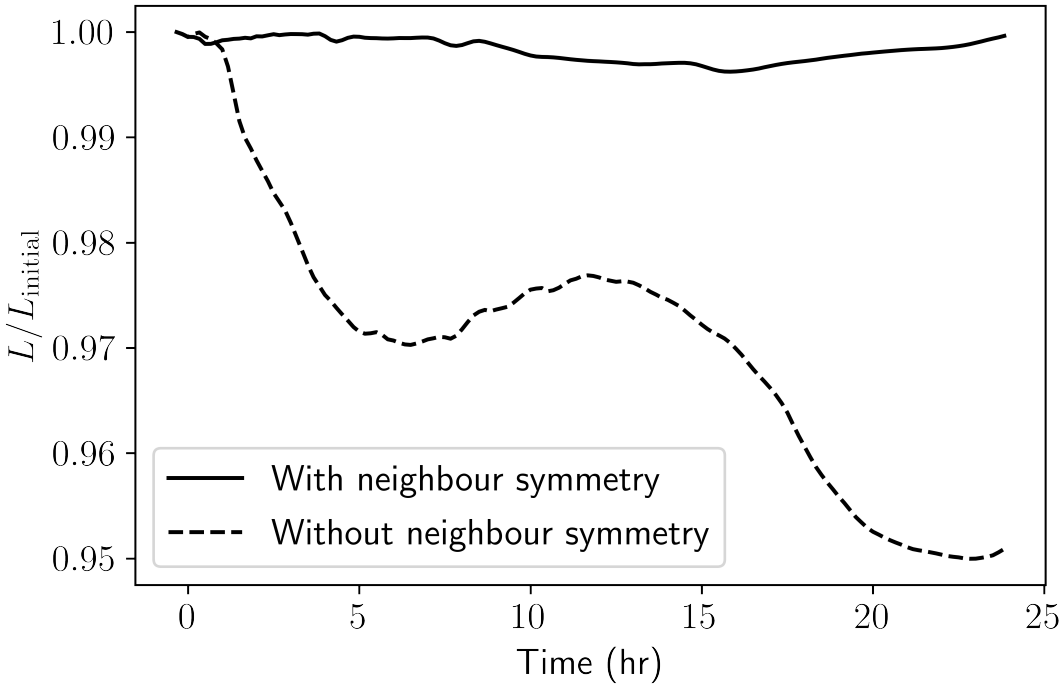

Figure 2.13: Angular momentum as a function of time (after impact) for SPHLATCH simulations of an oblique, planetary-scale impact on a Mars-like body with and without the neighbour symmetry correction Solid strength was not included in these simulations. Angular momentum, L, is normalised to its initial value, L_{initial}, and should therefore have a constant value of 1 if angular momentum is fully conserved.

2.7 Composition and Strength

The specific input parameters used in the strength model depend on the material composition, which is coupled with the equation of state (see Section 2.4). For the work of this thesis, specific strength models were used for iron, dunite and water, summarised in Table 2.1.

For iron, we use the same parameters as Emsenhuber et al. (2018). Iron is always used to represent planetary cores of differentiated bodies for this thesis, particularly Mars; at such high pressures, and at depths beyond much of the most important aspects of the simulations, the results of these simulations are likely not particularly

Table 2.1: Parameters used in the material strength model. The parameters for ice come from Senft and Stewart (2011) and Beeman et al. (1988). The parameters for dunite are from Benz et al. (1989) and Emsenhuber et al. (2018). The parameters for iron are from Emsenhuber et al. (2018).

Parameter	Description	Value for ice	Value for dunite	Value for Iron
Y_m	Shear strength at $P = \infty$	115 MPa	3.5 GPa	680 MPa
Y_0	Cohesion	0	0	0
$Y_{0,h}$	Y-intercept of high pressure model	8.3 MPa	0	0
μ_i	Coefficient of friction for intact material	2	2	2
$\mu_{d,l}$	Coefficient of friction for damaged material at low pressure	0.55	0.8	0.8
$\mu_{d,h}$	Coefficient of friction for damaged material at high pressure	0.2	0.8	0.8
ξ	Thermal softening parameter	1.84	1.2	1.2
G	Shear modulus	3.52 GPa	72 GPa	76 GPa

sensitive to the precise strength model used. It should be noted, however, that the frictional coefficients and thermal softening parameter are identical to those of the rock compositions (basalt or dunite). This is likely not the case in reality, as there is no reason to assume that iron should behave similarly to rock in this regard. Better care should therefore be taken to ensure realistic choices for these parameters in future studies that are more dependent on the iron strength model.

For dunite, we use the the parameters of Benz et al. (1989) and Emsenhuber et al. (2018). The strength model is illustrated in Figure 2.14 for the pressure regimes relevent in this thesis. For the high pressures encountered in the Mars studies, the most important parameter is the plastic limit, Y_{m}, as the strength model has converged towards this limit. The high temperatures also make the thermal softening parameter of great significance, as this determines how weakened the material's strength is as it approaches the melting temperature. For dunite in the Pluto studies, the most important parameter is instead the friction coefficient for damaged material, μ_{d}. This is because the pressure of the Pluto core lie in a region where the damaged yield strength, Y_{d}, has not crossed the intact yield strength Y_{i}, and in our fully-damaged model we always use the damaged yield strength if it is smaller than that of intact material. This would not be the case if the plastic limit was reduced, as the intersection of these two models would intersect at significantly lower pressure.

Water (or ice) was modelled using slightly modified strength parameters of Senft

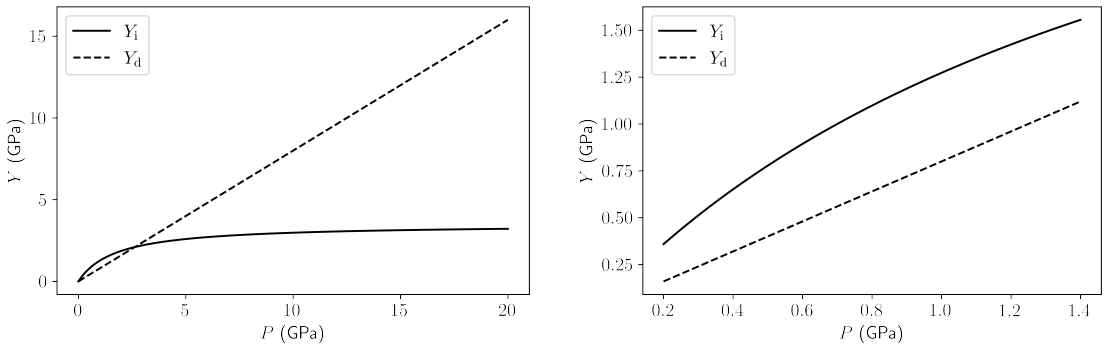

Figure 2.14: Yield strength, Y, against pressure, P, for the dunite strength model at pressures relevant to Mars' mantle (left) and Pluto's core (right). In each case, the bodies were modelled as fully-damaged, meaning that the yield strength used in the SPH simulations used the minimum of the damaged yield strength, Y_d, and the intact yield strength, Y_i.

and Stewart (2011); these parameters are based on Senft and Stewart (2008), who derived values by fitting to experimental data on the quasi-static shear strength, friction and dynamic tensile strength. Senft and Stewart (2011) adapted these parameters to represent the cold temperatures of large icy satellites such as Ganymede and Europa, which better fit the conditions of Pluto. It should be noted, however, that other, more recent studies have used different strength parameters for ice that would result in significantly higher yield strength(Bray et al., 2014; Silber et al., 2017; Denton et al., 2021). These studies do not give in-depth justification of these parameters, and state some values that appear to be erroneous (e.g. a damaged coefficient of friction, μ_d, of 0.8, which should be 0.2 according to their reference of Beeman et al. (1988)). As such, we opted for the more rigorously justified parameters of Senft and Stewart (2011), with our only modification being the calculation of yield strength for damaged (fractured) ice, where we use the following equation given in Beeman et al. (1988):

$$Y_d = \min(Y_{d,l}, Y_{d,h}) \tag{2.106}$$

with

$$Y_{d,l} = \mu_{d,l} P \tag{2.107}$$

and

$$Y_{d,h} = \mu_{d,h} P + Y_{0,h} \tag{2.108}$$

where P is pressure, $\mu_{d,l}$ and $\mu_{d,h}$ are the coefficients of friction for damaged ice at low and high pressures, respectively, and $Y_{0,h}$ is the y-intercept of empirical fit to the high pressure experiment data. Finally, it should be noted that the original strength parameters of ice implemented in SPHLATCH were those of Benz and Asphaug (1999). They suggested a plastic limit of 1 GPa; this is extremely high in comparison to the other studies, and should therefore be avoided. All of these ice strength models are illustrated in Figure 2.15.

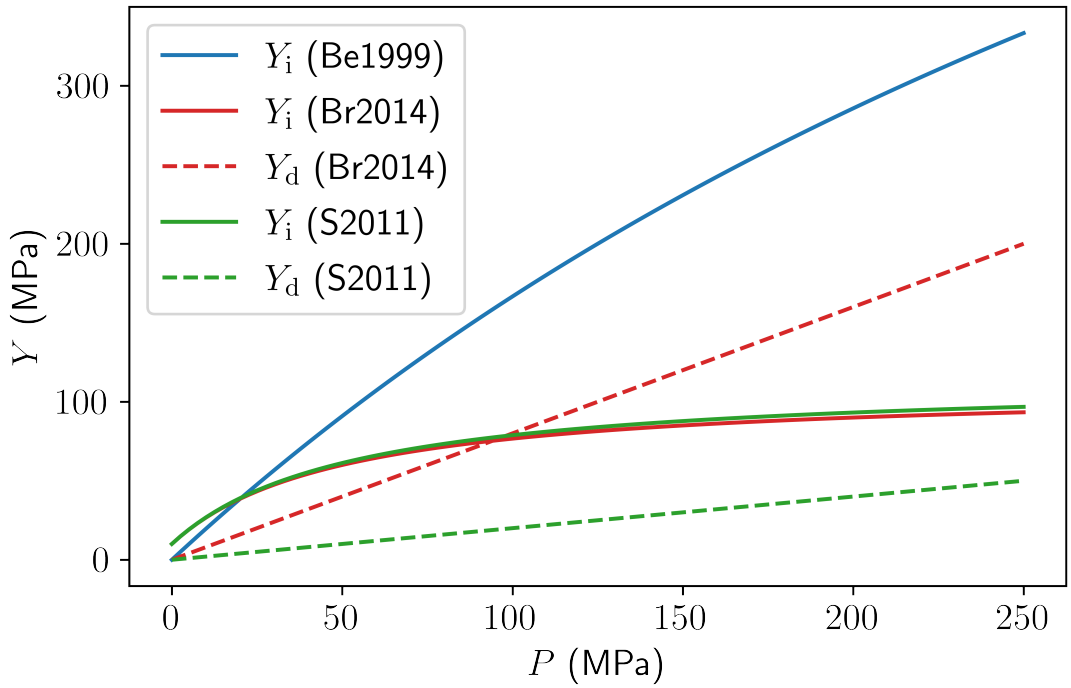

Figure 2.15: Yield strength, Y, against pressure, P, for the various literature ice strength models at pressures relevant to Pluto's mantle. In each case, the bodies were modelled as fully-damaged, meaning that the yield strength used in the SPH simulations used the minimum of the damaged yield strength, Y_d, and the intact yield strength, Y_i. Be1999 refers to Benz and Asphaug (1999), Br2014 to Bray et al. (2014) and S2011 to Senft and Stewart (2011). Note that the work of Benz and Asphaug (1999) used a simpler strength model whereby the yield strength was set to the plastic limit, Y_m, for all pressures. We plot here the modern, pressure-dependent strength model using the Benz and Asphaug (1999) value for Y_m (with $\mu_\mathrm{i} = 2$) as to compare with the other models, and because this is the model that was in place in SPHLATCH before the developments made during the work of this thesis were implemented.

Bibliography

E. Asphaug and A. Reufer. Late origin of the Saturn system. *Icarus*, 223(1):544–565, mar 2013. ISSN 00191035. doi: 10.1016/j.icarus.2012.12.009.

J. Barnes and P. Hut. A hierarchical O(N log N) force-calculation algorithm. *Nature 1986 324:6096*, 324(6096):446–449, 1986. ISSN 1476-4687. doi: 10.1038/324446a0.

M. Beeman, W. B. Durham, and S. H. Kirby. Friction of ice. *Journal of Geophysical Research*, 93(B7):7625–7633, jul 1988. ISSN 01480227. doi: 10.1029/JB093iB07p07625.

W. Benz and E. Asphaug. Impact Simulations with Fracture. I. Method and Tests. *Icarus*, 107(1):98–116, 1994. ISSN 10902643. doi: 10.1006/icar.1994.1009.

W. Benz and E. Asphaug. Simulations of brittle solids using smooth particle hydrodynamics. *Computer Physics Communications*, 87(1-2):253–265, 1995. ISSN 00104655. doi: 10.1016/0010-4655(94)00176-3.

W. Benz and E. Asphaug. Catastrophic Disruptions Revisited. *Icarus*, 142(1):5–20, nov 1999. ISSN 0019-1035. doi: 10.1006/ICAR.1999.6204.

W. Benz, A. G. Cameron, and H. J. Melosh. The origin of the Moon and the single-impact hypothesis III. *Icarus*, 81(1):113–131, sep 1989. ISSN 10902643. doi: 10.1016/0019-1035(89)90129-2.

V. J. Bray, G. S. Collins, J. V. Morgan, H. J. Melosh, and P. M. Schenk. Hydrocode simulation of Ganymede and Europa cratering trends – How thick is Europa's crust? *Icarus*, 231:394–406, mar 2014. ISSN 0019-1035. doi: 10.1016/J.ICARUS.2013.12.009.

G. S. Collins, H. J. Melosh, and B. A. Ivanov. Modeling damage and deformation in impact simulations. *Meteoritics and Planetary Science*, 39(2):217–231, feb 2004. ISSN 10869379. doi: 10.1111/j.1945-5100.2004.tb00337.x.

C. A. Denton, B. C. Johnson, S. Wakita, A. M. Freed, H. J. Melosh, and S. A. Stern. Pluto's Antipodal Terrains Imply a Thick Subsurface Ocean and Hydrated Core. *Geophysical Research Letters*, 48(2):e2020GL091596, jan 2021. ISSN 1944-8007. doi: 10.1029/2020GL091596.

M. S. Duncan, N. C. Schmerr, C. M. Bertka, and Y. Fei. Extending the Solidus for a Model Iron-Rich Martian Mantle Composition to 25 GPa. *Geophysical Research Letters*, pages 211–220, 2018. ISSN 19448007. doi: 10.1029/2018GL078182.

A. Emsenhuber. *Collisions during planetary systems formation.* PhD thesis, University of Bern, 2017.

A. Emsenhuber, M. Jutzi, and W. Benz. SPH calculations of Mars-scale collisions: The role of the equation of state, material rheologies, and numerical effects. *Icarus*, 301:247–257, oct 2018. ISSN 10902643. doi: 10.1016/j.icarus.2017.09.017.

G. J. Golabek, A. Emsenhuber, M. Jutzi, E. I. Asphaug, and T. V. Gerya. Coupling SPH and thermochemical models of planets: Methodology and example of a Mars-sized body. *Icarus*, 301:235–246, 2018. ISSN 10902643. doi: 10.1016/j.icarus.2017.10.003.

F. González-Cataldo, S. Davis, and G. Gutiérrez. Melting curve of SiO2 at multimegabar pressures: Implications for gas giants and super-Earths. *Scientific Reports*, 6(April):1–7, 2016. ISSN 20452322. doi: 10.1038/srep26537.

E. Hairer, G. Wanner, and S. P. Nørsett. *Solving Ordinary Differential Equations I: Nonstiff Problems.* Springer Berlin Heidelberg, 3 edition, 2008.

M. Jutzi. SPH calculations of asteroid disruptions: The role of pressure dependent failure models. *Planetary and Space Science*, 107(1):3–9, 2015. ISSN 00320633. doi: 10.1016/j.pss.2014.09.012.

M. Jutzi and E. Asphaug. Forming the lunar farside highlands by accretion of a companion moon. *Nature*, 476(7358):69–72, 2011. ISSN 00280836. doi: 10.1038/nature10289.

M. Jutzi, W. Benz, and P. Michel. Numerical simulations of impacts involving porous bodies. I. Implementing sub-resolution porosity in a 3D SPH hydrocode. *Icarus*, 198(1):242–255, nov 2008. ISSN 00191035. doi: 10.1016/j.icarus.2008.06.013.

M. Jutzi, K. Holsapple, K. Wünneman, and P. Michel. Modeling asteroid collisions and impact processes. In *Asteroids IV*, pages 679–699. University of Arizona Press, Tucson, 2015. ISBN 9780816532186. doi: 10.48550/arXiv.1502.01844.

H. Melosh. *Impact Cratering: A Geologic Process*. Oxford University Press, 1989. ISBN 9780195042849.

J. Monaghan. Smoothed Particle Hydrodynamics. *Annual Review of Astronomy and Astrophysics*, 30:543–574, 1992. ISSN 0066-4146.

J. J. Monaghan. SPH and Riemann Solvers. *Journal of Computational Physics*, 136 (2):298–307, 1997. ISSN 00219991. doi: 10.1006/jcph.1997.5732.

M. Ohnaka. A shear failure strength law of rock in the brittle-plastic transition regime. *Geophysical Research Letters*, 22(1):25–28, jan 1995. ISSN 19448007. doi: 10.1029/94GL02791.

A. Reufer. *Collisions in Planetary Systems*. PhD thesis, Universität Bern, 2011.

A. Reufer, N. Thomas, W. Benz, S. Byrne, V. Bray, C. Dundas, and M. Searls. Models of high velocity impacts into dust-covered ice: Application to Martian northern lowlands. *Planetary and Space Science*, 58(10):1160–1168, aug 2010. ISSN 00320633. doi: 10.1016/j.pss.2010.04.008.

A. Reufer, M. M. Meier, W. Benz, and R. Wieler. A hit-and-run giant impact scenario. *Icarus*, 221(1):296–299, sep 2012. ISSN 00191035. doi: 10.1016/j.icarus.2012.07.021.

C. Schäfer, R. Speith, and W. Kley. Collisions between equal-sized ice grain agglomerates. *Astronomy and Astrophysics*, 470(2):733–739, 2007. ISSN 00046361. doi: 10.1051/0004-6361:20077354.

C. Schäfer, S. Riecker, T. I. Maindl, R. Speith, S. Scherrer, and W. Kley. A smooth particle hydrodynamics code to model collisions between solid, self-gravitating objects. *Astronomy and Astrophysics*, 590:A19, jun 2016. ISSN 14320746. doi: 10.1051/0004-6361/201528060.

L. E. Senft and S. T. Stewart. Impact crater formation in icy layered terrains on Mars. *Meteoritics & Planetary Science*, 43(12):1993–2013, dec 2008. ISSN 1945-5100. doi: 10.1111/J.1945-5100.2008.TB00657.X.

L. E. Senft and S. T. Stewart. Dynamic fault weakening and the formation of large impact craters. *Earth and Planetary Science Letters*, 287(3-4):471–482, oct 2009. ISSN 0012-821X. doi: 10.1016/J.EPSL.2009.08.033.

L. E. Senft and S. T. Stewart. Modeling the morphological diversity of impact craters on icy satellites. *Icarus*, 214(1):67–81, jul 2011. ISSN 0019-1035. doi: 10.1016/J.ICARUS.2011.04.015.

E. A. Silber, G. R. Osinski, B. C. Johnson, and R. A. Grieve. Effect of impact velocity and acoustic fluidization on the simple-to-complex transition of lunar craters. *Journal of Geophysical Research: Planets*, 122(5):800–821, 2017. ISSN 21699100. doi: 10.1002/2016JE005236.

S. Thompson. ANEOS Analytic Equations of State for shock physics codes input manual. *SANDIA Report*, 3, 1990.

S. Thompson and H. Lauson. Improvements in the CHART-D Radiation-hydrodynamic Code III: Revised Analytic Equations of State. Technical report, Sandia National Laboratories, 1972a.

S. L. Thompson and H. S. Lauson. Improvements in the CHART D radiation-hydrodynamic code III: revised analytic equations of state. Technical report, Sandia National Laboratories, Albuquerque, N. Mex., USA, 1972b.

J. H. Tillotson. Metallic equations of state for hypervelocity impact. Technical report, General Dynamics San Diego CA General Atomic DIV, 1962.

J. Von Neumann and R. D. Richtmyer. A method for the numerical calculation of hydrodynamic shocks. *Journal of Applied Physics*, 21(3):232–237, apr 1950. ISSN 00218979. doi: 10.1063/1.1699639.

Chapter 3

Coupling Impact Models with Geophysics

This chapter describes the methods behind coupling SPHLATCH with geophysical models, with a particular focus on post-impact crust production and re-distribution. In Section 3.1, a method of mapping SPH results onto a spherical grid is described, with an example application to SPHLATCH simulation results. Section 3.2 describes a newly developed scheme that applies geophysical arguments of melt fraction and crust-production to spherically gridded SPH impact results to predict the post-impact crust distribution caused by displaced primordial crust and crystallising impact-induced melt. Finally, Section 3.3 describes a more sophisticated geophysical model that uses SPH impact results as initial conditions for long-term (Gyr) interior evolution simulations that model mantle convection and its associated crust production. This method is applied to study the impact-origin of the sharp contrast in crustal thickness between the two hemispheres of Mars (the so-called *Martian Dichotomy*), and some preliminary results are shown.

In terms of personal contribution, I designed and implemented both the spherical grid scheme of Section 3.1 and the geophysical model of Section 3.2. I also performed the SPH simulations of Section 3.3, developed the preparation step required to transfer the SPH simulations to the geodynamic model and participated in countless discussions on the applied Martian Dichotomy study.

3.1 Spherical Grid

Typically, geophysical analysis of a planetary body is performed in spherical polar coordinates. This presents a challenge for SPH simulation results, as the mesh-free nature of the Lagrangian method means that the coordinates of each data point (i.e. each particle) are distributed in an arbitrary, non-uniform structure. It is important to remember, however, that particles can be thought of as interpolation points within a continuum medium, which can be probed at any point using Eq. 2.27. This therefore allows us to smooth the SPH results onto a spherical grid with a resolution of our choosing; a higher resolution than the number of particles is useful to ensure that the results are not under-sampled during this transfer onto a grid, but this need not be too refined as this leads to a much larger data file without much (if any) gain in accuracy. For simplicity, we use equally-spaced grid points in each coordinate. In addition, the centre of mass coordinates for the target mantle are subtracted from the Cartesian particle coordinates prior to spherical grid construction to ensure that the polar axis will be central to the body. Simply smoothing all of our thermodynamic quantities in this manner would be inconsistent with our equation of state, however, as it is only internal energy and density that are calculated solely with SPH. We therefore mirror the simulation method; only smoothing these two values directly onto the grid, then using these as input to the ANEOS equation of state to calculate all other thermodynamic values such as pressure and temperature.

One caveat of this method is ANEOS' inability to determine the physical properties of a mixture of two (or more) materials, only using one integer material number for each calculation. As a practical solution, we assign each SPH particle with the mass fraction for each material (either a 1 or 0 as each particle is made up of only 1 material) and then use Eq. 2.27 again to calculate a continuous mass fraction at every point on our grid for each material. The material number corresponding to the largest mass fraction is then passed to ANEOS. For the majority of material in the spherical grid, the composition is close to 100% in one of the materials, meaning that the equation of state returns accurate results. However, at transition regions between materials, composition fractions can be close to 50%, causing the equation of state to instead yield spurious results. This is due to the density and internal energy sums including significant contributions from both materials, yet ANEOS

performs its thermodynamic calculations as if the material was composed solely of the majority material.

Figure 3.1 and Figure 3.2 illustrate the density and internal energy, respectively, for an SPH-simulated Mars-like body after being smoothed onto a spherical grid. Figure 3.3 and Figure 3.4 show the temperature and density, respectively, returned by ANEOS using the density and internal energy values of the same spherically gridded data. Here, we see that the crossover region between the high-density iron core and the lower-density silicate mantle (i.e. the *core-mantle boundary*) leads to sudden, unphysical contrasts in the ANEOS calculated quantities due to the compositional issues.

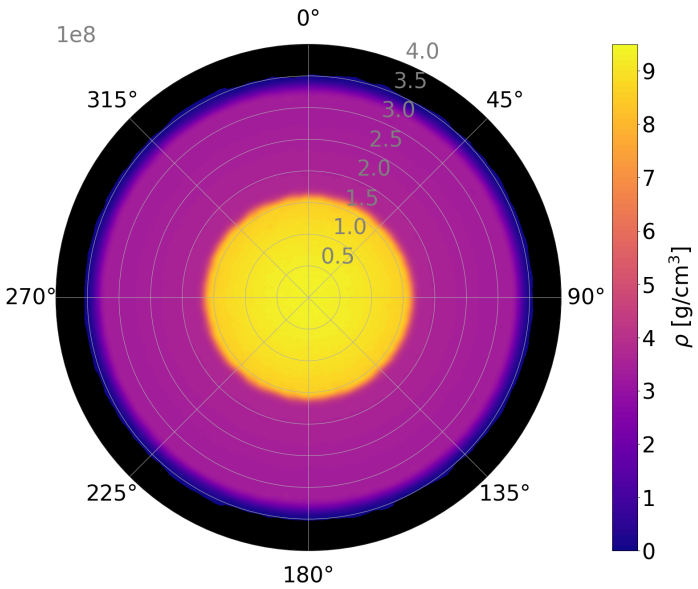

Figure 3.1: The density distribution of an SPH-simulated Mars-like body after the data has been smoothed onto a spherical grid using Eq. 2.27. A slice has been made in the impact plane to display the interior. The resolution of the grid is $13.\dot{3}$ km in radius and $\frac{\pi}{100}$ in latitude and longitude. A density cut-off has been made at $\rho = 0.01$ g/cm^3, meaning that any grid-points corresponding with a lower density have been plotted as black. The axes are angle (in degrees) and radius (in cm).

The internal energy distribution in Figure 3.2 also displays a region with inconsistent values at the core-mantle boundary. This illustrates that the issue of mixed SPH sums between different materials is not limited to the grids calculation, but indeed affects calculations made between particles during the SPH simulations. Al-

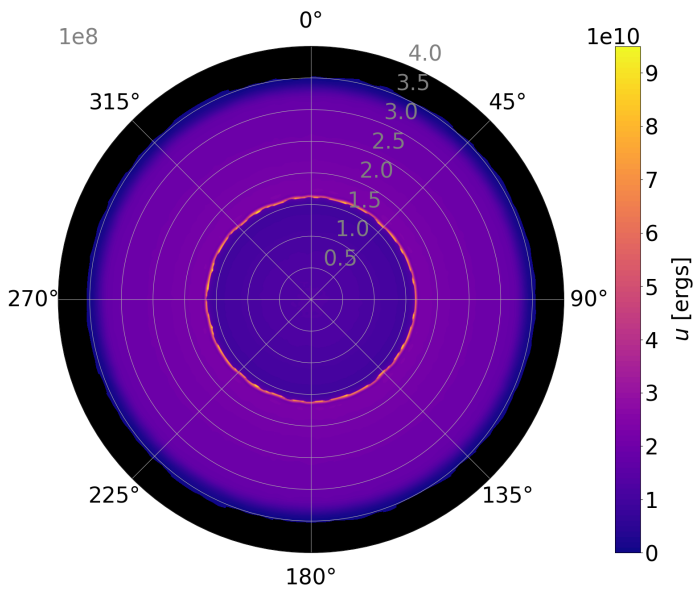

Figure 3.2: The internal energy distribution of an SPH-simulated Mars-like body after the data has been smoothed onto a spherical grid using Eq. 2.27, with the same grid and plot parameters as Figure 3.1.

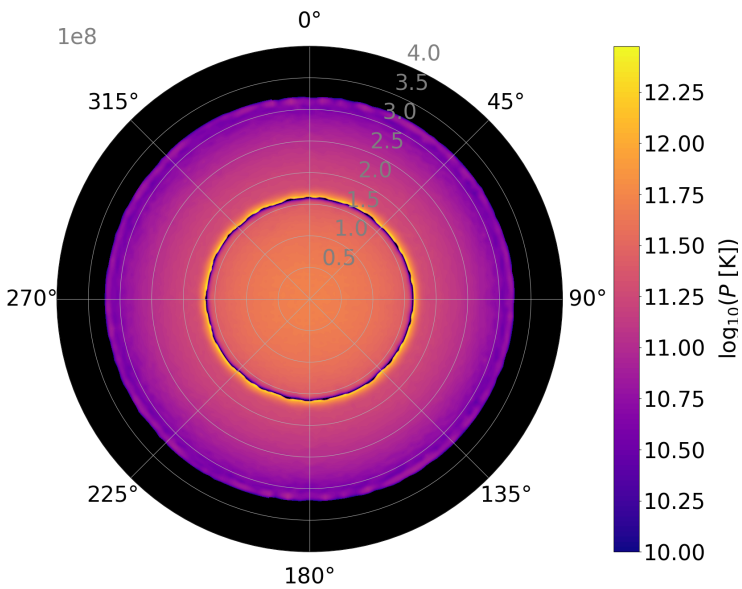

Figure 3.3: The (log-)pressure distribution of an SPH-simulated Mars-like body calculated through ANEOS using the density and internal energy values illustrated in Figure 3.1 and Figure 3.2, respectively. The same grid and plot parameters as Figure 3.1 are used, but with an additional cut-off for pressures below 10^{10} ergs.

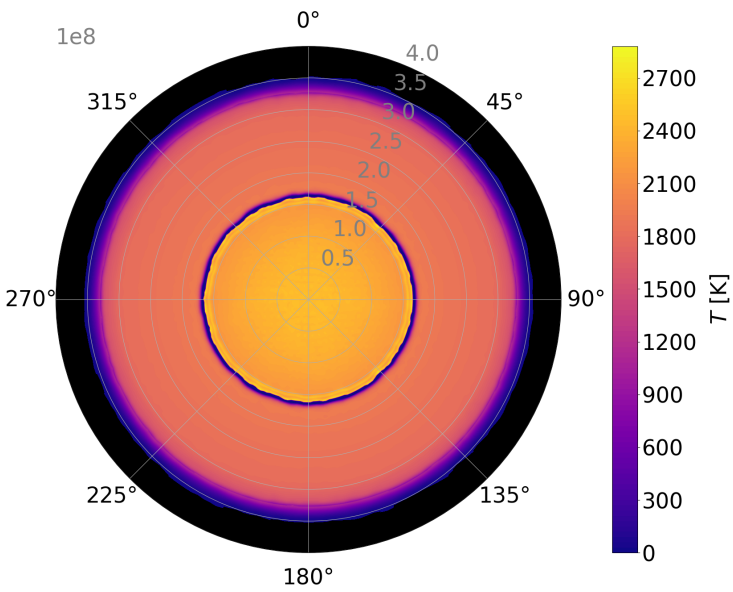

Figure 3.4: The temperature distribution of an SPH-simulated Mars-like body calculated through ANEOS using the density and internal energy values illustrated in Figure 3.1 and Figure 3.2, respectively. The grid and plot parameters are the same as Figure 3.1.

though each particle has a defined composition, the densities will still be calculated as an intermediate between iron and rock near the core-mantle boundary. This leads to the density of the iron particles to be underestimated, and the density of rock particles to be overestimated. This then affects both the internal energy calculation from the energy equation (Eq. 2.47) and the pressure calculation in ANEOS; in fact, a negative feedback loop is formed as the internal energy is calculated using the pressure, which is calculated in ANEOS using the internal energy. Fortunately, the region that yields spurious results is only a small portion of the body and should not dramatically affects the results of this thesis, although future studies that rely more upon the results of such a region should carried out with additional care[1].

Numerical issues arising from sharp density contrasts in SPH also occur at surface boundaries. This is most apparent in the grid calculations of composition fraction, seen in Figure 3.5 and Figure 3.6. Here we see that the SPH sums are reaching

[1] A possible solution to this problem is to introduce a correction factor to the density sum based on the imbalance of the particle distribution (Reinhardt and Stadel, 2017; Ruiz-Bonilla et al., 2022).

values greater than one near the surface of the test body, which should not be possible when the input variable cannot take a value larger than 1 (they are either 1 or 0 for each particle). This corresponds with the spurious density oscillations that are known to occur in SPH sums of surface boundaries (e.g. Emsenhuber et al., 2018). This problem is also apparent near the core-mantle boundary, which similarly suffers from such oscillations. Again, this only affects a small region of our body and only appears to cause errors of ∼1%. We therefore do not consider this to strongly affect the results presented in the remainder of this thesis.

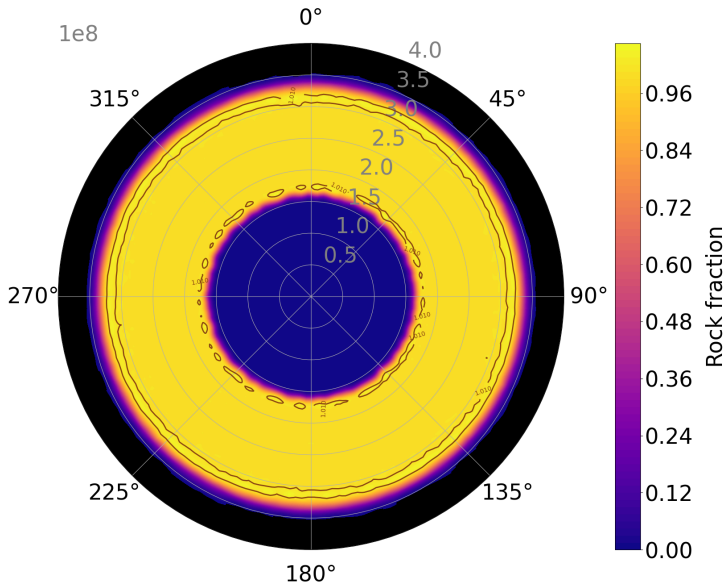

Figure 3.5: The rock fraction distribution of an SPH-simulated Mars-like body where each particle is assigned a 1 or 0 to indicate if it composed of rock or not, and then this variable has been smoothed onto a spherical grid using Eq. 2.27, with the same grid and plot parameters as Figure 3.1. The brown contour lines highlight areas with values greater than 1.01, indicating incorrect SPH sums due to a sharp density contrast (either the core mantle boundary or the surface boundary).

3.2 Crust Production Scheme

In large-scale impacts, temperatures induced within the target body can be high enough to cause melt a significant portion of the body. If the target is a planet, such as Mars, then it is usually thought to be composed of a dense iron core surrounded

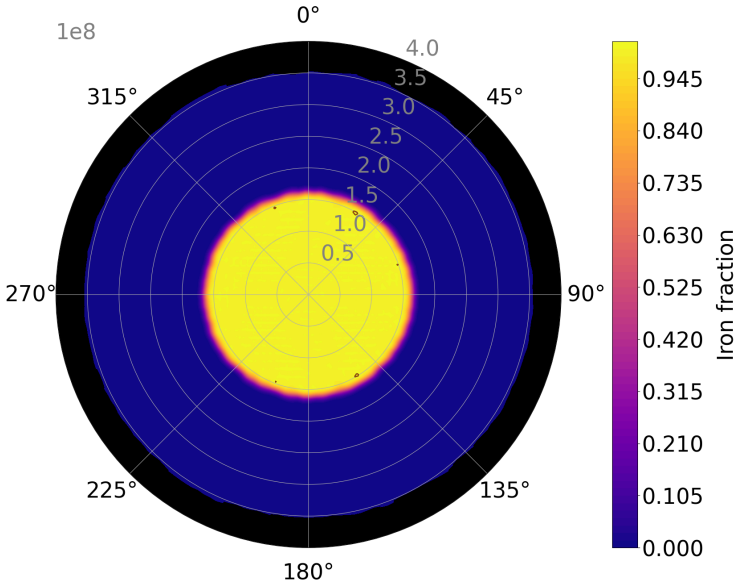

Figure 3.6: The iron fraction distribution of an SPH-simulated Mars-like body, complimentary to Figure 3.5.

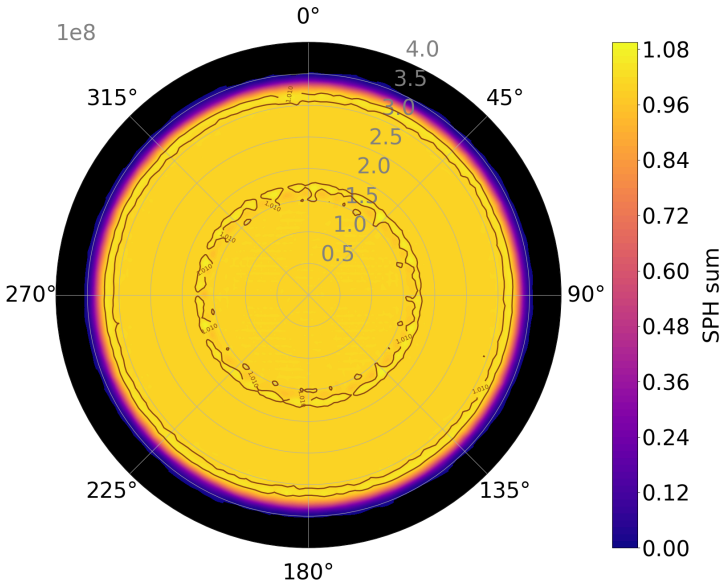

Figure 3.7: The distribution found when assigning all particles with a variable of 1 that is smoothed onto the spherical grid, as a test case. Here we see the full extent of the spurious density oscillations causing incorrect SPH sums.

by a mantle of silicate rock. When this mantle material is melted by the impact, further differentiation can occur within the silicate material as certain elements (particularly incompatible elements) rise towards the surface and form a chemically distinct crust upon crystallisation. The spherically gridded SPH results inform us on which regions of the planet are molten, which can therefore infer the approximate distribution of crust that should form as this melt crystallises.

Additionally, planets are thought to form an initial (*primordial*) crust immediately after formation. In most studies, the impact being considered is thought to have occurred after such a crust has formed. SPH simulations naturally track the motion of material, and so the initial locations of SPH particles within a body can be used to infer the distribution of this primordial crust material after an impact has occurred.

To estimate the final distribution of crust that would occur after an SPH-simulated impact, we constructed a scheme that takes both impact-induced melt and primordial crust into account to determine crustal thickness across the post-impact body. This scheme is presented in the remainder of this section, and is the same scheme applied in Ballantyne et al. (2022) (Chapter 4) to study the potential impact-origin of the Martian Dichotomy. Additionally, a slightly modified version of this scheme is used in Chapter 5 to map the distribution of impactor material after a large impact on a Pluto-like body.

3.2.1 Magma

Determining the amount of melt for a given mass of silicate material is not as simple as using a single melting curve, as these materials are made up of a mixture of chemical components with different melting points. Instead, we must use a *solidus* which defines the temperature below which the material is entirely solid for a given pressure, and a *liquidus* which defines the minimum temperature required to fully melt the material at a given pressure. At temperature intermediate to these two functions, the material is partially melted, with the mass fraction of the material that is molten being known as the *melt fraction*.

In the work of this thesis, we use the following expression to find the melt fraction ξ for each grid point on our spherical mesh (e.g. Burg and Gerya, 2005; Golabek

et al., 2011):

$$\xi = \begin{cases} 0 & T \leq T_{\text{sol}} \\ \frac{T-T_{\text{sol}}}{T_{\text{liq}}-T_{\text{sol}}}\Big|_P & T_{\text{sol}} < T < T_{\text{liq}} \\ 1 & T \geq T_{\text{liq}} \end{cases}, \tag{3.1}$$

where T is temperature and T_{sol} and T_{liq} are the solidus and liquidus temperatures corresponding to the pressure, P. The exact functions used to calculate the solidus and liquidus temperature depend on the precise composition being considered. In the case of Mars, we used the same solidus utilised in the equation of state (Eq. 2.90) from Duncan et al. (2018), along with the following liquidus from Wade and Wood (2005) modelled on peridotite:

$$T_{\text{liq}} = 1973 + 28.57P, \tag{3.2}$$

with T_{liq} in K and P in GPa.

During a phase transition from solid to liquid, additional energy is required to overcome the latent heat of fusion. As mentioned in the previous chapter, the rock parameters for the ANEOS equation of state does not include any such additional energy requirement, meaning that the temperatures for molten rock may be overestimated. To account for this, we apply an additional offset to the liquidus; in the case of the Mars study of Chapter 4, an offset of 400 K was used Turcotte and Schubert (2002).

3.2.2 Crust Crystallisation

To model the amount of crust produced by this melt, we take the input parameter, β, which is the bulk mass fraction of molten mantle material that will rise to the surface and form crust upon crystallisation. The crustal mass of each grid cell is therefore defined as

$$m_{\text{crust},ijk} = \min\left(\beta, \xi_{ijk}\right)\left(\rho V\right)_{ijk}, \tag{3.3}$$

where the $\min\left(\xi_{ijk}, \beta\right)$ term is due to the crustal material preferentially partitioning into the melt, ρ is the density and V is the volume of the grid cell given by:

$$V_{ijk} = \int_{\phi_{k-\frac{1}{2}}}^{\phi_{k+\frac{1}{2}}} \int_{\theta_{j-\frac{1}{2}}}^{\theta_{j+\frac{1}{2}}} \int_{r_{i-\frac{1}{2}}}^{r_{i+\frac{1}{2}}} r^2 \sin\theta \, \mathrm{d}r \, \mathrm{d}\theta \, \mathrm{d}\phi, \tag{3.4}$$

which when evaluated becomes:

$$V_{ijk} = \frac{\Delta\phi}{3}\left[r^3_{i+\frac{1}{2}} - r^3_{i-\frac{1}{2}}\right]\left[\cos\theta_{j-\frac{1}{2}} - \cos\theta_{j+\frac{1}{2}}\right], \tag{3.5}$$

where the indices $(i, j, k)-\frac{1}{2}$ and $(i, j, k)+\frac{1}{2}$ indicate the values at the lower and upper boundaries of the grid cell, respectively ((i, j, k) represent the grid cell centres), and $\Delta\phi = \phi_{k+\frac{1}{2}} - \phi_{k-\frac{1}{2}}$, which is constant due to our grids having equal spacing.

Through the summation of these grid cell values, a total crustal mass, $M_{\text{crust},jk}$, is calculated for each latitude and longitude (where the melt has been assumed to rise radially upward). To convert this to a crustal thickness, we assume a crustal density, ρ_{crust}, which we can divide $M_{\text{crust},jk}$ by to give us a crustal volume, $V_{\text{crust},jk}$, corresponding to a crustal thickness given by:

$$z_{\text{crust},jk} = \left[R^3 - \frac{3V_{\text{crust},jk}}{\Delta\phi\left(\cos\theta_{j-\frac{1}{2}} - \cos\theta_{j+\frac{1}{2}}\right)}\right]^{\frac{1}{3}}, \tag{3.6}$$

where R is the radius of the body. Note that this is simply a rearrangement of Equation 3.5, with $r_{i+\frac{1}{2}}$ and $r_{i-\frac{1}{2}}$ becoming $z_{\text{crust},jk}$ and R, respectively, and V_{ijk} becoming $V_{\text{crust},jk}$.

As crustal thickness can be inferred by observations, the ability to directly predict the crustal thickness distribution caused by an impact modelled with SPH is a highly useful tool.

3.2.3 Primordial Crust

Prior to the collision, a planetary body is likely to have already experienced some crust formation during initial differentiation. This crust is known as the *primordial crust* and can be of significant thickness, with estimates for Mars, for example, being ∼20–30 km (Norman, 1999). During a giant impact, the shockwave is energetic enough to excavate any primordial crust initially present at the impact site. Such crustal excavation can also occur outside of the main impact site due to re-impacting ejecta in oblique impacts, or in more head-on impacts, due to the shockwave converging at the antipode to the impact site (e.g. Marinova et al., 2008, 2011). The complex post-impact distribution of primordial crust is therefore an important aspect that must be considered if we are to accurately predict the crustal thickness across our target body after a large-scale collision.

Unfortunately, current computational limitations prohibit the inclusion of a fully-resolved crustal layer in our simulations. We therefore implement an innovative method to quantitatively estimate its influence by examining the simulation results for the initial, pre-impact target and the final, post-impact body. First, we identify the uppermost, surface SPH particles in the pre-impact target. As the primordial crustal thicknesses of interest are thinner than an SPH smoothing length, we approximate the mass fraction of crust, β_{prim}, for a given SPH particle based on its radial position relative to the mantle-crust boundary, R_{MCB}. SPH particles represent a mass that has been smeared-out radially to follow the smoothing kernel, and thus the precise 3-dimensional calculation of this crustal mass fraction is highly non-trivial. To avoid this, while still retaining good accuracy, we use the integrated 1-dimensional kernel, $W'_{\text{1D}}(r,h)$, given by

$$\int_0^r W_{\text{1D}}(r,h)\ \mathrm{d}r = W'_{\text{1D}}(r,h) = \begin{cases} \frac{2}{3}q - \frac{1}{3}q^3 + \frac{1}{8}q^4 & 0 \leq q \leq 1 \\ \frac{1}{2} - \frac{1}{24}(2-q)^4 & 1 < q < 2 \\ 0.5 & q \geq 2 \end{cases}, \tag{3.7}$$

to model the crustal mass fraction of a particle as

$$\beta_{\text{prim}} = \begin{cases} \frac{1}{2} - W'_{\text{1D}}(|r - R_{\text{MCB}}|, h) & r \leq R_{\text{MCB}} \\ \frac{1}{2} + W'_{\text{1D}}(|r - R_{\text{MCB}}|, h) & r > R_{\text{MCB}} \end{cases}, \tag{3.8}$$

where the $\frac{1}{2}$ term comes from the knowledge that a silicate particle with a central position beneath (above) the mantle-crust boundary must have at least 50% of its mass composed of mantle (crust) material, due to the the symmetric nature of W'_{1D} (and its 3D equivalent), which sums to 0.5 if integrated beyond distances of $2h$. With this in mind, we also see that the second term will either reduce β_{prim} to zero if $(r - R_{\text{MCB}}) < -2h$, correctly assigning mantles fully embedded in the mantle to have no crust mass fraction, or sum to unity if $(r - R_{\text{MCB}}) > 2h$, thus correctly deeming particles whose sphere of influence is entirely above the mantle-crust boundary as pure crust. In practice, however, the latter is only the case when the crust is thick enough to be fully resolved, which is not the case for the cases studied with this scheme.

3.2.4 Mantle Depletion

During the formation of a primordial crust, the bulk silicate layer (or primordial mantle) is depleted of the elements/minerals that compose the crust. This acts to reduce its budget of crust-bearing material, and so if this depleted mantle is melted again, it will produce a decreased mass of crust (if any at all). As a mantle that has not undergone any depletion is often called fully *fertile*, we name this mass budget of potential crust the *fertility* at a given point in the mantle. In Equation 3.3, the fertility corresponds with β.

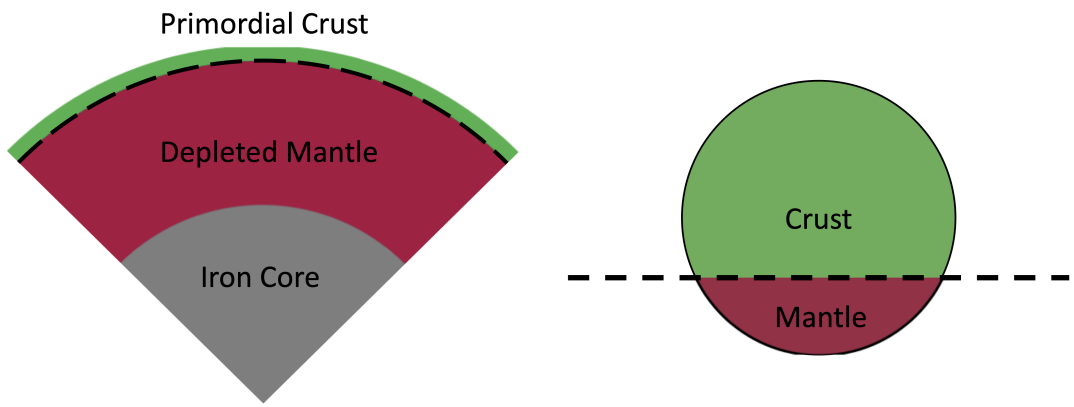

Figure 3.8: A schematic diagram of the primordial crust scheme. (Left): the interior structure of a fully differentiated planet after crystallisation of the primordial crust, with the dashed line indicating the mantle-crust boundary R_{MCB}. (Right): the physical interpretation of the crustal mass fraction scheme (Eq. 3.8), where the circle represents the smoothed mass distribution of an SPH particle with a central position beyond the mantle-crust boundary ($r > R_{\mathrm{MCB}}$). Here, we see that the mass fraction of crust is clearly greater than $\frac{1}{2}$.

To include the effect of depletion in our model, we calculate the global crustal mass $M_{\mathrm{crust,global}}$ through the summation of all previously calculated $M_{\mathrm{crust},jk}$ values, and then remove this mass from the initially fertile mantle in one of two end-member scenarios.

In the first case, we assume that the entire mantle has had time to fully mix, meaning that our β in Equation 3.3, is still constant across the mantle, but is

decreased to match the mass of fertile mantle required to produce $M_{\text{crust,global}}$, i.e. :

$$\beta_{\text{dep}} = \left(1 - \frac{M_{\text{crust,global}}}{\beta_0 M_{mantle}}\right)\beta_0, \tag{3.9}$$

where M_{mantle} is the mass of the mantle and β_0 is the initial mantle fertility prior to primordial crust formation. If we assume that all primordial crust mass will form new crust upon remelting, we therefore redefine β for each particle as:

$$\beta = \begin{cases} \beta_{\text{dep}} & r \leq R_{\text{MCB}} - 2h \\ \beta_{\text{dep}}(1 - \beta_{\text{prim}}) + \beta_{\text{prim}} & R_{\text{MCB}} - 2h < r < R_{\text{MCB}} + 2h \\ 1 & r \geq R_{\text{MCB}} + 2h \end{cases}. \tag{3.10}$$

The second case corresponds to a fully stratified mantle, whereby the mantle directly below the crust is entirely depleted ($\beta = 0$), eventually reaching untouched, fertile mantle at depth ($\beta = \beta_0$). To calculate the depth of this fertile-depleted transition, R_{FDB}, we first find the volume, V_{dep}, of mantle that would need to be melted to extract the total crust mass, $M_{\text{crust,global}}$, associated with the desired crustal thickness, using

$$V_{\text{dep}} = \frac{M_{\text{crust,global}}}{\beta_0 \overline{\rho}}, \tag{3.11}$$

where $\overline{\rho}$ is the mean density of the mantle. We then find the depth required for a spherical shell extending down from the surface to have such a volume. Geometrically, this is the same situation described by Eq. 3.6, but for all longitudes and latitudes (i.e. $\Delta\phi = 2\pi$ and $\cos\theta_{\text{start}} - \cos\theta_{\text{end}} = 2$), leading to

$$R_{\text{FDB}} = \left[R_{\text{MCB}}^3 - \frac{3V_{\text{dep}}}{4\pi}\right]^{\frac{1}{3}}. \tag{3.12}$$

We introduce this boundary using a similar method to Equation 3.8, now including both the fertile-depleted and mantle-crust boundaries as follows:

$$\beta = \begin{cases} \beta_0\left(\frac{1}{2} + W'_{1\text{D}}(|r - R_{\text{FDB}}|, h)\right) + \beta_{\text{prim}} & r < R_{\text{FDB}} \\ \beta_0\left(\frac{1}{2} - W'_{1\text{D}}(|r - R_{\text{FDB}}|, h)\right) + \beta_{\text{prim}} & R_{\text{FDB}} \leq r \leq R_{\text{FDB}} + 2h \\ \beta_{\text{prim}} & r > R_{\text{FDB}} + 2h \end{cases}. \tag{3.13}$$

A schematic diagram illustrating these two mantle depletion schemes is given in Figure 3.9. Practical examples of these depletion schemes for an SPH simulation of a Mars-like body across a range of initial fertilities and primordial crust thicknesses are shown in Figure 3.10, Figure 3.11, Figure 3.12 and Figure 3.13.

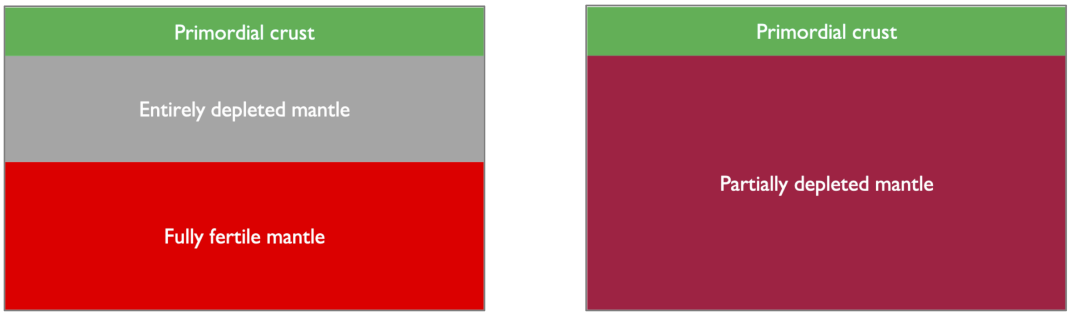

Figure 3.9: A schematic diagram illustrating the two depletion schemes. (Left): the stratified mantle case, where all crustal mass is extracted from the uppermost mantle leading to an entirely depleted region atop fully fertile region where no crust extraction has occured. (Right): the fully-mixed case, where the extracted crustal mass is assumed to come from the entire mantle equally, leading to a constant, partially-depleted fertility for all mantle material.

3.2.5 Intact Crust

Another important aspect of a pre-impact crust is the contribution to crustal thickness by primordial crustal material that has remained solid throughout the giant impact event (or has re-solidified due to a change in pressure). This material is included in our crustal calculations by simply adding the solid crust contribution to our grid cell crustal masses as follows:

$$m_{\mathrm{crust},ijk} = \left\{ \left[\min\left(\beta, \xi\right) + \beta_{\mathrm{prim}} \left(1 - \frac{\min(\beta, \xi)}{\beta} \right) \right] \rho V \right\}_{ijk}, \tag{3.14}$$

where the first term represents the molten material that will solidify into crust and the second term represents the intact primordial crust that is in the solid phase at the end of the simulation.

3.2.6 Particle Distribution

This scheme relies upon a homogeneous SPH particle distribution, as small fluctuations in position (relative to a given particle's smoothing length) can have a significant effect on a particle's primordial crust fraction, as is clear from equation 3.8. In simulations using SPHLATCH, pre-impact bodies are initially composed of particles in a Hexagonal Close-Packed (HCP) lattice. A relaxation step is then performed to

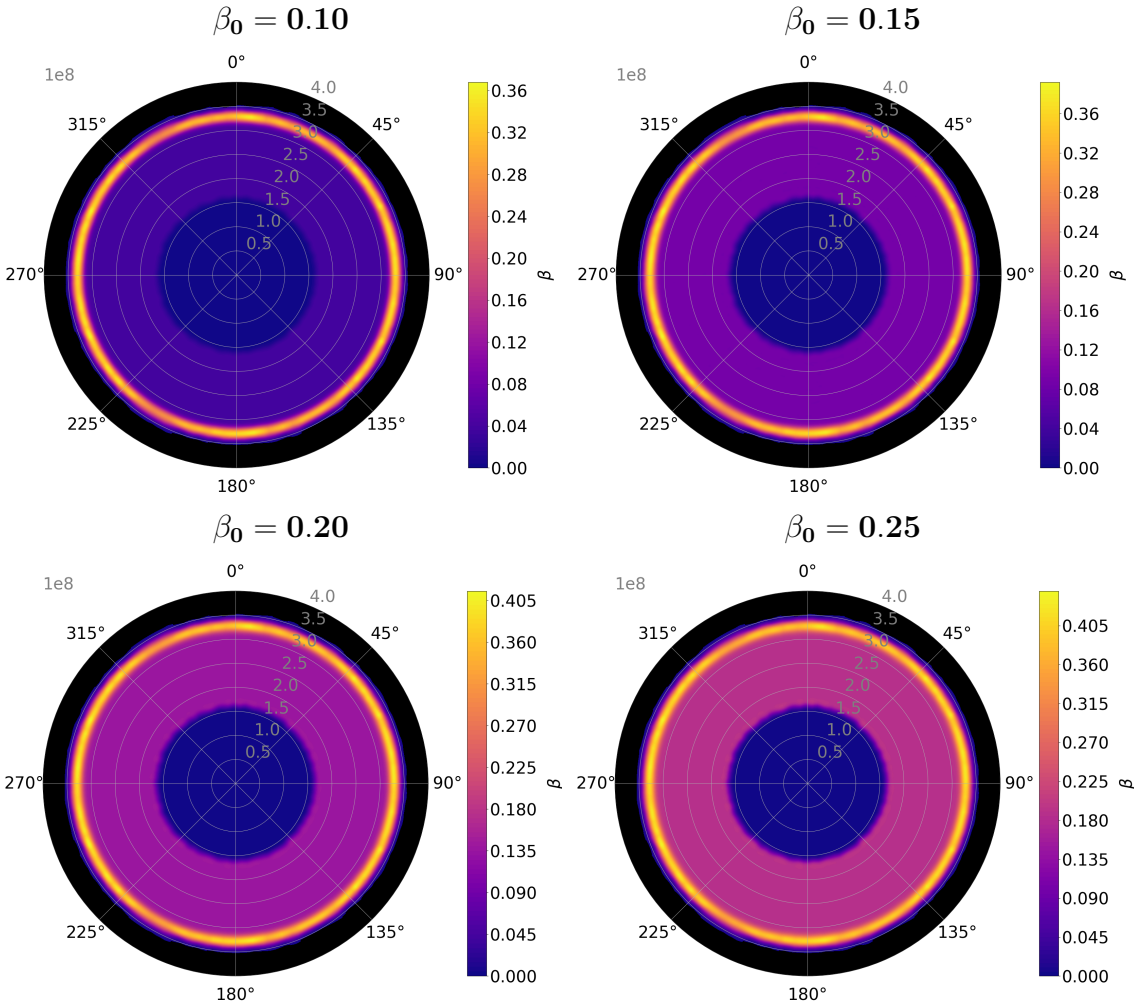

Figure 3.10: Slices through the impact-plane of a Mars-like body modelled with a 55 km thick primordial crust layer, illustrating the effect of initial fertility, β_0, on total fertility, β, for the fully-mixed mantle depletion scheme. An increased initial fertility leads to an increased fertility throughout the body after depletion, as expected. Note that the colour bar range changes between cases.

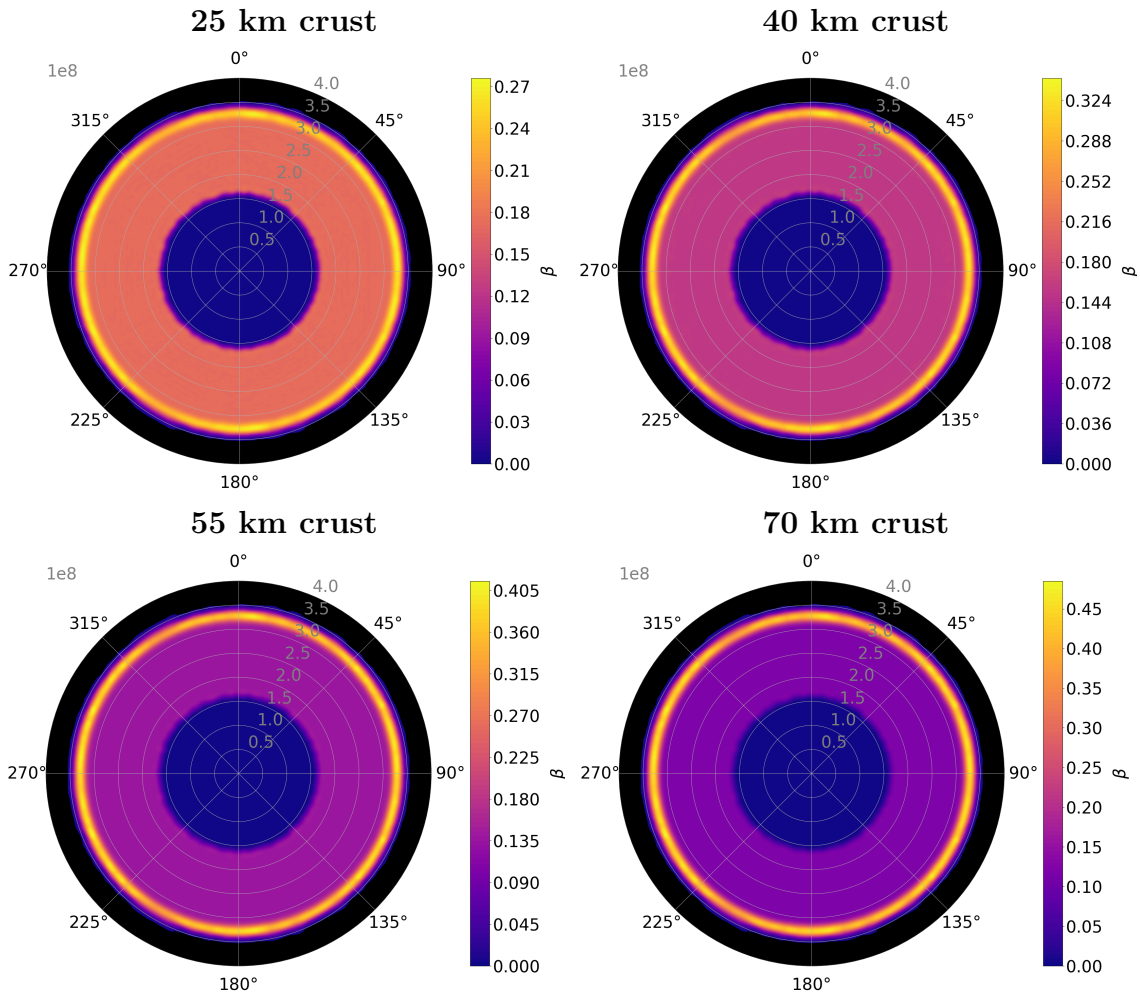

Figure 3.11: Slices through the impact-plane of a Mars-like body modelled with an initial fertility $\beta_0 = 0.2$, illustrating the effect of primordial crust thickness on total fertility, β, for the fully-mixed mantle depletion scheme. A thicker crust leads to a lower fertility in the mantle due to greater depletion, but a higher effective fertility in the uppermost layer due to an increased crust fraction, β_{prim}, in the corresponding surface particles. Note that the colour bar range changes between cases.

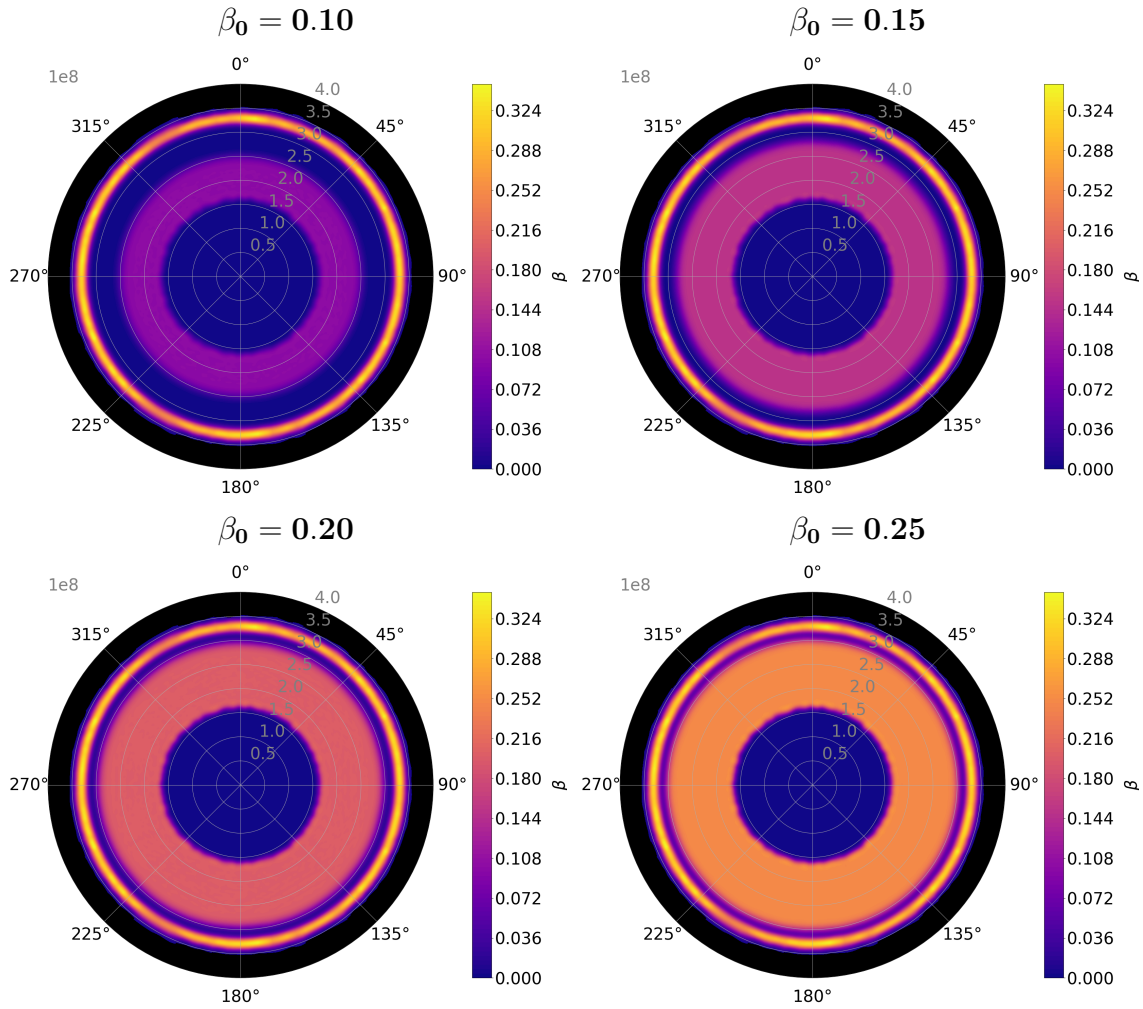

Figure 3.12: Slices through the impact-plane of a Mars-like body modelled with a 55 km thick primordial crust layer, illustrating the effect of initial fertility, β_0, on total fertility, β, for the stratified mantle depletion scheme. An increased initial fertility leads to a larger region fully-depleted ($\beta = 0$) mantle due to the primordial crust formation process requiring the depletion of a larger mass (and thus volume) of the initial, fully-fertile mantle for the same mass of crust. Beneath the fully-depleted layer is the remaining layer of fertile crust down to the core-mantle boundary. The colour bar range does not change between cases as the surface layer fertility corresponds to crust fraction only, and is thus independent of mantle fertility.

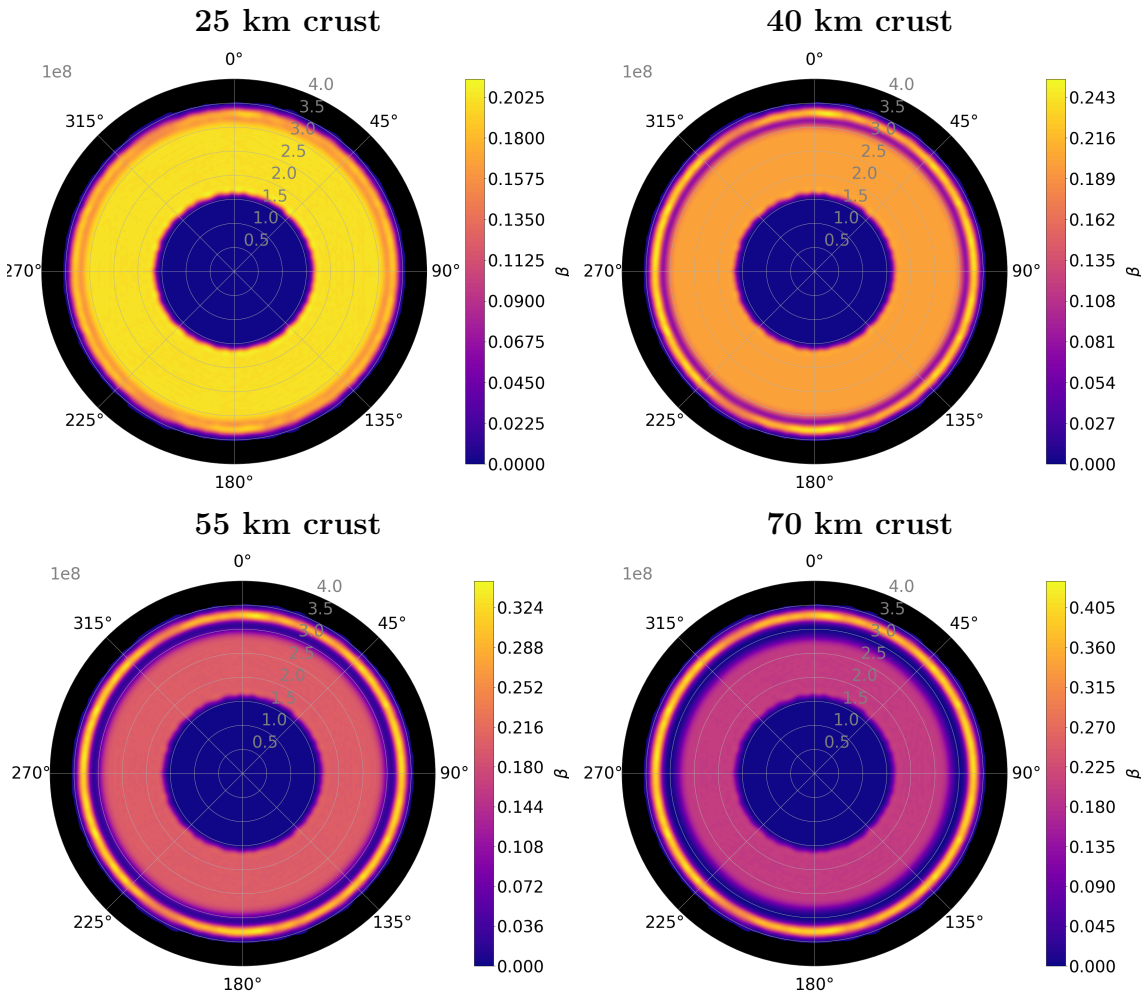

Figure 3.13: Slices through the impact-plane of a Mars-like body modelled with an initial fertility $\beta_0 = 0.20$, illustrating the effect of primordial crust thickness on total fertility, β, for the stratified mantle depletion scheme. A thicker crust leads to a larger fully-depleted layer in the mantle due to greater depletion, but a higher effective fertility in the uppermost layer due to an increased crust fraction, β_{prim}, in the corresponding surface particles. Note that the fertile mantle layer below the fully-depleted layer has the same fertility in each case, it is only differing the colour scales that cause the change in colour in the plots.

prepare these bodies for use in an impact simulation, which dampens any initial, unwanted velocities until the particles reach a stable configuration. Unfortunately, the HCP structure introduces leaves remnant heterogeneities in the particle distribution of purely numerical origin, which influences the initial primordial crust distribution.

To counteract these artefacts, we normalise the particles' radial positions used for the primordial crust calculations such that the maximum value in a given latitude-longitude range is equal to the global maximum value. This range cannot simply be that of each grid cell, as each step in longitude and latitude is equal, meaning their respective surface area (and thus volume) decreases towards the poles. This would cause a strong contrast in resolution between each sampling volume, leading in particular to significant under-sampling near the poles. To avoid this issue, a method is required that provides latitude-longitude ranges that are equal in area, and thus allow for an approximately constant number of particles sampled in each normalisation volume. For this purpose, we use the method of Malkin (2019), who developed a simple method (named *SREAG*) of dividing the surface of a sphere into equal-area isolatitudinal cells with a near-uniform latitudinal distribution.

This method first splits the surface into several latitudinal bands of constant width, ΔB. Each of these bands are then split into longitudinal divisions of width $\Delta L_i = \frac{\Delta B}{\cos b_0^i}$, where i is the band number and b_0^i central latitude of the band. If there are not an integer number of ΔL_i shifts within a circle then it is adjusted to the nearest value that would satisfy this constraint. This leads to near-square cells in the equatorial bands, and increasingly rectangular cells near the poles (in latitude-longitude space). These cells are not quite equal area, however, and each band width ΔL_i is thus refined with a final adjustment algorithm until exact equal area is achieved. The distribution of cells produced by this method, and that used in our normalisation calculations, can be seen in Figure 3.14.

The normalisation step is performed by finding the maximum radius of all particles contained in each of these latitude-longitude ranges and then normalising the radii of these particles as if this maximum radius was constant for all cells, i.e.

$$r' = \frac{r}{r_{\max}} R \tag{3.15}$$

where r and r' are the radial position of a particle before and after normalisation, respectively, $r_{\max}$ is the maximum particle radius within a given latitude-longitude

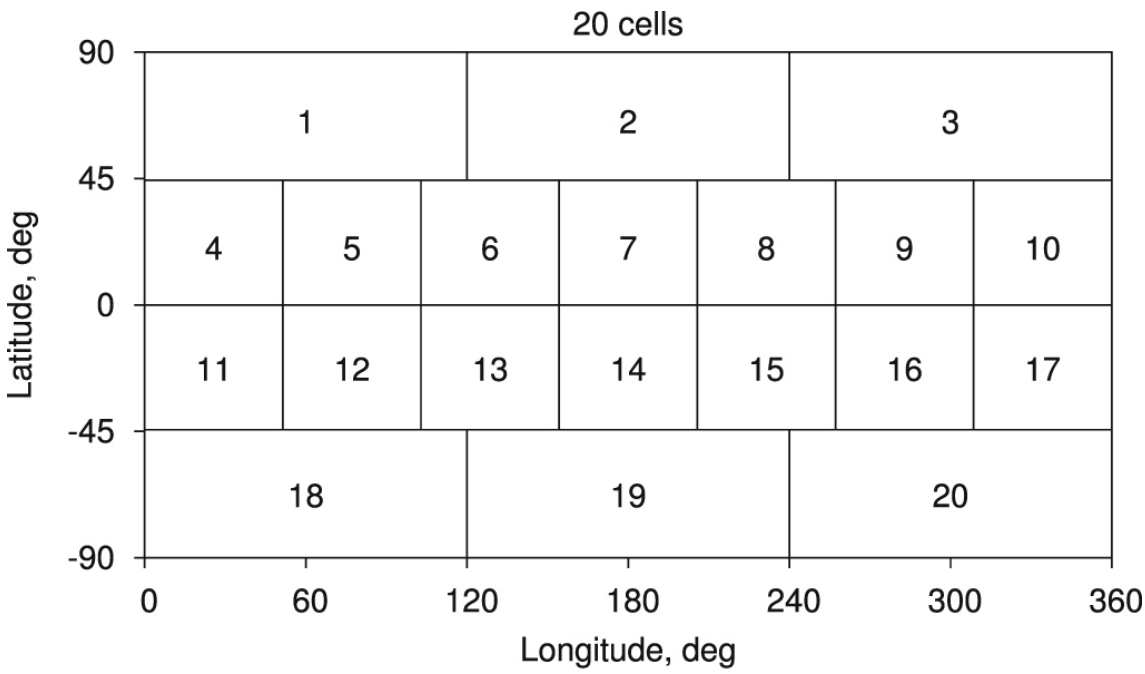

Figure 3.14: The distribution of cells in longitude and latitude used to calculate sample particles during the normalisation step for the primordial crust calculations. The figure, and method, is taken from Malkin (2019). Each cell corresponds with an equal surface area on the sphere.

cell and R is the constant maximum radius, which we use as the maximum radius across all particles in the body (i.e. maximum across all cells). Note that this procedure is only performed on the radius used in the primordial crust scheme and *not* the true radial position of the particles, as changing the latter would affect the SPH sums of all other quantities.

Example primordial crust distributions across a Mars-like body, before and after the normalisation step, are shown in Figure 3.15 and Figure 3.16, respectively.

3.3 Coupling with Long-Term Interior Evolution

Although the model described in Section 3.2 provides a valuable first-order prediction of the distribution of crust after a planetary-scale impact, it only considers crust-production caused by the immediate distribution of melt after the impact, and thus neglects any long-term evolution of the interior beyond impact-magma crystallisation. In reality, the interior of a planet can evolve significantly over time

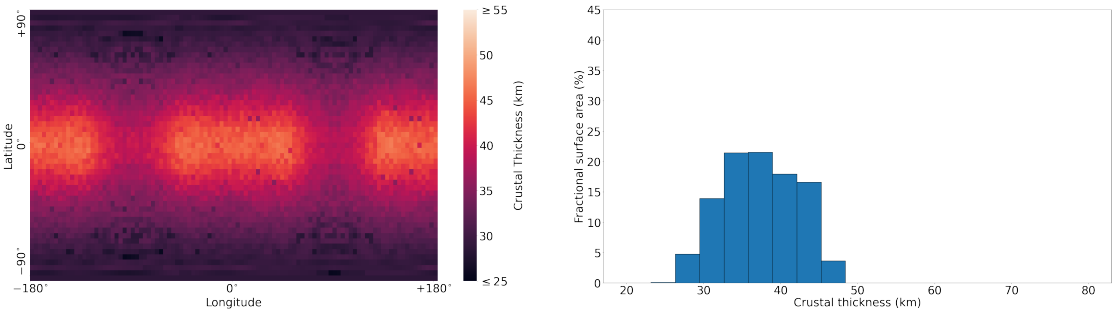

Figure 3.15: The primordial crust distribution calculated for a Mars-like body without the radius normalisation step (left) and its corresponding histogram (right).

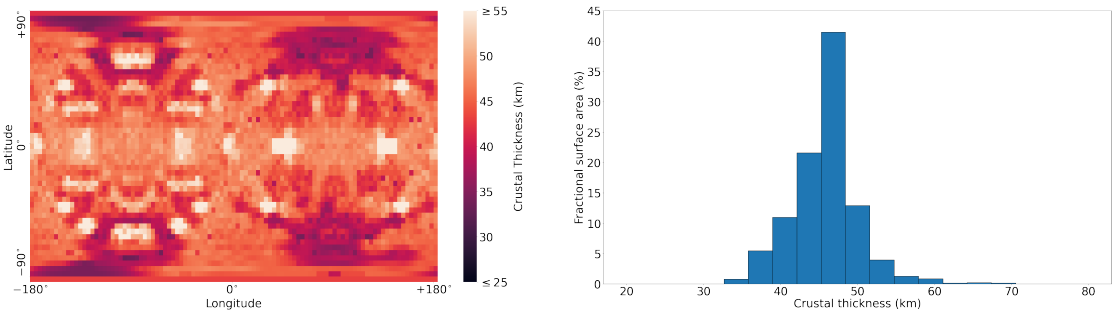

Figure 3.16: The primordial crust distribution calculated for a Mars-like body with the radius normalisation step (left) and its corresponding histogram (right).

due to convective processes, and the introduction of such a large temperature (and composition) anomaly into the mantle of the target body from a giant impact is likely to have significant influence on such evolution.

For this reason, a more thorough approach in studying the effects of a planetary-scale impact over geological timescales is to couple the results of the SPH simulations with a sophisticated thermochemical model that accurately simulates the convective evolution of the post-impact interior along with any later-stage production of crust. We implement this approach in a bid to further investigate the likelihood of a giant impact to have ultimately led to crustal dichotomy observed on Mars today. This research has been carried out in tandem with the study of Chapter 4, but is highly complimentary and thus expands upon many of the study's conclusions.

3.3.1 StagYY

For the purpose of studying the long-term interior evolution after a giant impact, we use *StagYY* (formerly known as *Stag3D*): a mantle convection code that has been a prominent and continually developing tool in the study of geodynamics for around 30 years Tackley (1993, 2008). At its core, StagYY models classical fluid dynamics, as does SPH, but in an extremely different regime than that presented in the SPH impact model. This is because, on geological timescales, the sub-solidus, rocky interior of a planet can be modelled as a viscous fluid. The viscous terms of the Navier-Stokes equation therefore cannot be neglected. Instead, the so-called *inertial* terms that make up the left-hand side of the equation are usually neglected in this regime, thus becoming

$$0 = -\vec{\nabla} p + \eta \vec{\nabla}^2 \boldsymbol{v} + \left(\zeta + \frac{1}{3}\eta\right) \vec{\nabla}\left(\vec{\nabla} \cdot \boldsymbol{v}\right) + \rho \boldsymbol{g}. \tag{3.16}$$

This approximation holds for so-called *creeping flow*, where the advective inertial forces are small compared to viscous forces. In planetary mantles, viscosities are extremely high ($\sim 10^{22}$ Pa s), which matches such a regime. Various other simplifications are also applied, such as the *inifinite-Prandtl-number approximation*; these approximations are common across geodynamic models and will therefore not be elaborated upon further in this thesis. For an in-depth review of the fluid dynamic theory behind modern geodynamic modelling, I refer the interested reader to

Turcotte and Schubert (2014) or Gerya (2019).

These equations are then numerically solved on a grid. As already mentioned, spherical coordinates are the coordinate system of choice in geophysical studies, but a simple longitude-latitude grid has gridlines that converge at the poles, leading to an uneven resolution along with other computational issues such as timestep and convergence problems. A key aspect of the StagYY code is its use of a so-called *yin-yang* grid, which avoids such pole-related issues by forming a grid through the combination of two simple longitude-latitude grids across 90° in latitude and 270° in longitude. These are spliced together with minimum overlap in a fashion similar to the two patches of a tennis ball or baseball, as shown in Figure 3.17.

In Cartesian coordinates, (x, y, z), the relation between the grid coordinates of the yin and yang grid are simply given by:

$$(x, y, z)_{\text{yang}} = (-x, z, y)_{\text{yin}} \tag{3.17}$$

which is a symmetric transformation. In spherical coordinates, this reads as

$$\begin{aligned} r_{\text{yang}} &= r_{\text{yin}} \\ \sin\theta_{\text{yang}} \cos\phi_{\text{yang}} &= -\sin\theta_{\text{yin}} \cos\phi_{\text{yin}} \\ \sin\theta_{\text{yang}} \sin\phi_{\text{yang}} &= \cos\theta_{\text{yin}} \\ \cos\theta_{\text{yang}} &= \sin\theta_{\text{yin}} \sin\phi_{\text{yin}} \end{aligned} \tag{3.18}$$

where r, θ and ϕ are the spherical coordinates of radius, polar angle (or latitude) and azimuthal angle (or longitude), respectively.

3.3.2 Coupling with SPH simulations

To prepare the output of an SPH impact simulation for use as input into the StagYY, a clear first step is to again use the method described in Section 3.1 to smooth the SPH data onto a spherical grid. To represent the yin-yang grid used in StagYY, two spherical grids are provided, one for the yin grid component and the other for the yang, with coordinate geometries corresponding with the respective case. The yin grid is first computed as a standard spherical grid with an arbitrary geometry. The yang grid is then computed by simply transforming the Cartesian coordinates of the SPH particles using Eq. 3.17 before again smoothing the data onto a spherical grid.

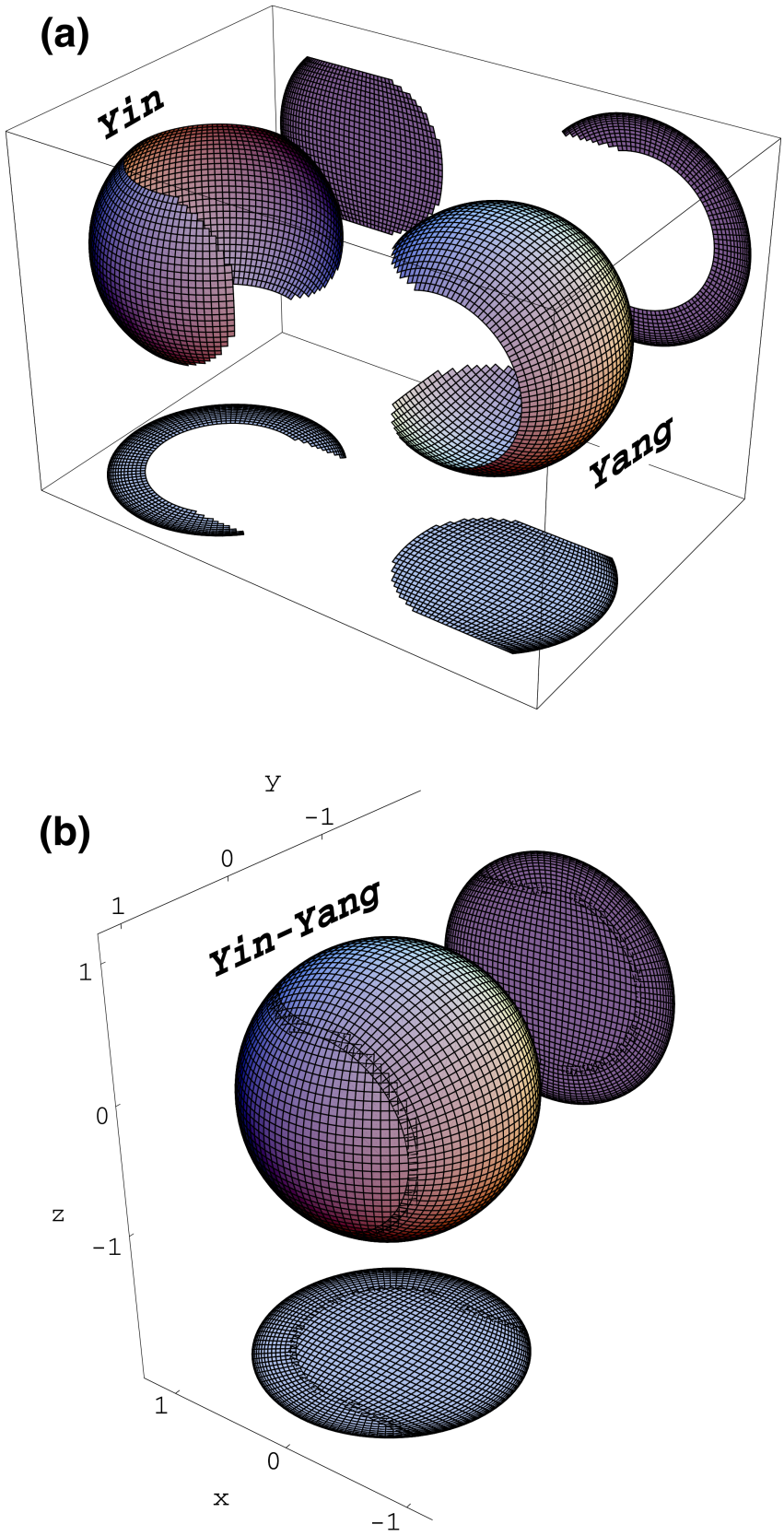

Figure 3.17: The yin-yang grid before (a) and after (b) being combined in a baseball-like fashion of minimum overlap. This figure is from Kageyama and Sato (2004).

Before the data of these grids can be used in StagYY, a few further preprocessing steps are required. The first is to approximate the SPH body as a perfect sphere, as this simplified geometry is required for the StagYY mantle convection model. This is achieved by normalising the body in two steps: first for the core and then for the mantle. This is due to the surface of these two regions being capable of exhibiting independently deformed geometries relative to one another. The core normalisation step is performed through a simply linear normalisation given by

$$r' = \frac{R_{\text{core}}}{R_{\text{max,core}}} r \tag{3.19}$$

where R_{core} is the specified core radius desired after normalisation, $R_{\text{max,core}}$ is the maximum radius of the core prior to normalisation and r and r' are the radius before and after the normalisation step, respectively. After applying this normalisation factor to all grid cell coordinates, the core is correctly normalised to a perfect sphere or radius R_{core}. The mantle is then normalised using

$$r'' = \frac{R_{\text{surf}} - R_{\text{core}}}{R'_{\text{max}} - R_{\text{core}}}(r' - R_{\text{core}}) + R_{\text{core}} \tag{3.20}$$

where r'' is the normalised mantle radius, R_{surf} is the desired surface radius for the body and R'_{max} is the maximum radius representing mantle material after the first normalisation step, i.e.

$$R'_{\text{max}} = \max(r') = \frac{R_{\text{core}}}{R_{\text{max,core}}} \max(r) \tag{3.21}$$

This secondary step using Eq. 3.20 only applies to mantle grid cells ($r' > R_{\text{core}}$), and correctly converges to $r'' = r' = R_{\text{core}}$ at the core mantle boundary. Other practical considerations made during normalisation are to exclude material with either a density below a defined limit, ρ_{min} or a radius beyond a maximum limit, R_{lim}. The density minimum is used to define the surface of the body, as the smoothed nature of SPH data means that non-zero densities occur significantly beyond the compact particle configuration that makes up the body. In our study of Mars, we use a limit of $\rho_{\text{min}} = 2.82$ g/cm^3, which is $\sim 85\%$ of the dunite reference density, and was found to be an effective surface cutoff for a dunite mantle in practice. The radius limit is included to avoid the inclusion of any nearby clumps of ejecta that could be unwillingly captured within the spherical grid. We use $R_{\text{lim}} = 3600$ km as

our limit in the study of the Martian Dichotomy, which is ∼6% beyond the Martian radius.

Normalising the grid cell radii in this manner does mean that the step-size between radial cells is no longer constant throughout the body, and that the relative grid cell positions of neighbouring latitudes and longitudes are therefore not exactly preserved. At Mars-scales, the post-impact body is large enough such that it has already relaxed into a near-spherical shape after impact before the normalisation step, meaning that the normalisation step only causes minor adjustments and is therefore a reasonable approximation. The non-uniform radial distribution of cells does mean that the data cannot be transferred directly into StagYY, however, and thus a final interpolation is performed using the simple trilinear interpolation method to map the data onto the StagYY grid.

For StagYY, it is the temperature field of the SPH results that is of most interest. More specifically, it is the temperature deviation from an adiabatic profile that induces convection, and thus interior evolution. The pre-impact SPH bodies have interior temperature profiles that are naturally adiabatic after the initial relaxation step. These profiles are approximated using a 1D solver of this relaxation step, where the specific entropy preassigned to each material and kept constant in each equal-mass Lagrangian cell that are able to move radially until a balance of gravity and hydrostatic pressure is found (with oscillations being dampened throughout). By subtracting the temperatures of this profile, T_{adiabat}, from the temperatures in the SPH results, T, at a given pressure, i.e.

$$\Delta T = T - T_{\text{adiabat}} \tag{3.22}$$

the adiabatic temperature deviation, ΔT, is provided to StagYY as required.

This method has the additional benefit of allowing the precise adiabats of the SPH and StagYY simulations to differ. This is important as the SPH adiabat is intrinsically linked to the equation of state used, which means it can only be a significant simplification of the complex interior temperature profile associated with real planets. The results of the SPH simulations are not particularly dependent on this adiabat, and so this simplification does not cause significant error in the results; mantle convection models such as StagYY, however, have a high dependence on temperature distribution and careful consideration must be taken to use the most

accurate interior profile available.

This strong temperature-dependence in StagYY makes it particularly sensitive to the errors that occur near the core-mantle boundary due to the sharp density contrast (see Figure 3.4). In particular, the sudden unexpected drop in mantle temperature in this region can have significant impact on the mantle convection model, and is therefore removed by limiting temperatures in the deep mantle to a minimum corresponding with the adiabatic temperature of the 1D Lagrangian model (i.e. $\Delta T \geq 0$ at depth).

3.3.3 Preliminary Results

The preliminary results of an SPHLATCH impact simulation coupled with the StagYY interior evolution model is shown in Figure 3.18 and Figure 3.19. This corresponds to a near head-on (15°) impact on a Mars-like body from a differentiated impactor of radius 750 km with an impact velocity at the mutual escape speed. The crustal thickness has been calculated by considering any melt above the neutral buoyancy depth to cause the production of crust at the surface of the planet in a similar manner to that of the crust-production scheme described in Section 3.2. This melt may be a direct result of the impact at very early times, or a consequence of decompression melting due to the movement of mantle material due to convection at later times. These figures display the production of crust across the Mars-like body from 36 hours after impact (the time of the SPH simulation output file) up to ∼4.5 Gyr after impact, thus providing a final distribution that is directly comparable with observations of Mars today.

The initial parameters for the impact were informed by the study of Chapter 4, matching the proposed most-likely parameter space for an impact-induced Martian Dichotomy, other than the impact velocity which is slightly lower than suggested. Although there is some late-stage crust-production visible in the northern hemisphere by the end of the simulation, the final crust distribution across the surface is a good match to the Martian Dichotomy observed today. In terms of thickness, however, the model exhibits crust at depths much greater than observed. This difference may be a result of a key simplification of these models: there is no primordial crust included prior to impact, along with no associated pre-impact mantle depletion. As

discussed extensively in Chapter 4, the primordial crust at the impact site is entirely excavated in impacts of these scales. The crust outside of the impact side (i.e. the northern hemisphere of Mars) remains intact. This therefore leads to a reduction in the crustal thickness contrast between the two hemispheres. Furthermore, the initial depletion of the mantle can significantly reduce the mass (and thus thickness) of crust produced by a given mass of melt. With this in mind, the excessive contrast in crust may in fact reach reasonable values if a primordial crust was included in the model.

In Figure 3.20 and Figure 3.21, the crust distribution over time for an alternative impact with same angle and speed but a smaller impactor of radius 500 km is show. Here, we see a similar outcome—the most prominent crust production occurs at the immediate impact site while late-stage crust is produced across the entire planet—but with a significantly smaller region of crust associated with the initial impact-induced melt. These findings support the conclusions of Chapter 4, which also find a 500 km radius impactor to be insufficient in producing a large enough magma pond to explain the Martian Dichotomy.

As a final note, it is important to remember that these are only preliminary results of an ongoing project and are therefore subject to future developments and changes before they will be published in a scientific article. Regardless of this, these results still provide a proof-of-concept for the coupling of the most sophisticated models of planetary-scale impacts with long-term (Gyr) interior evolution, and therefore serve as an exciting insight into the great possibilities of scientific study in the field.

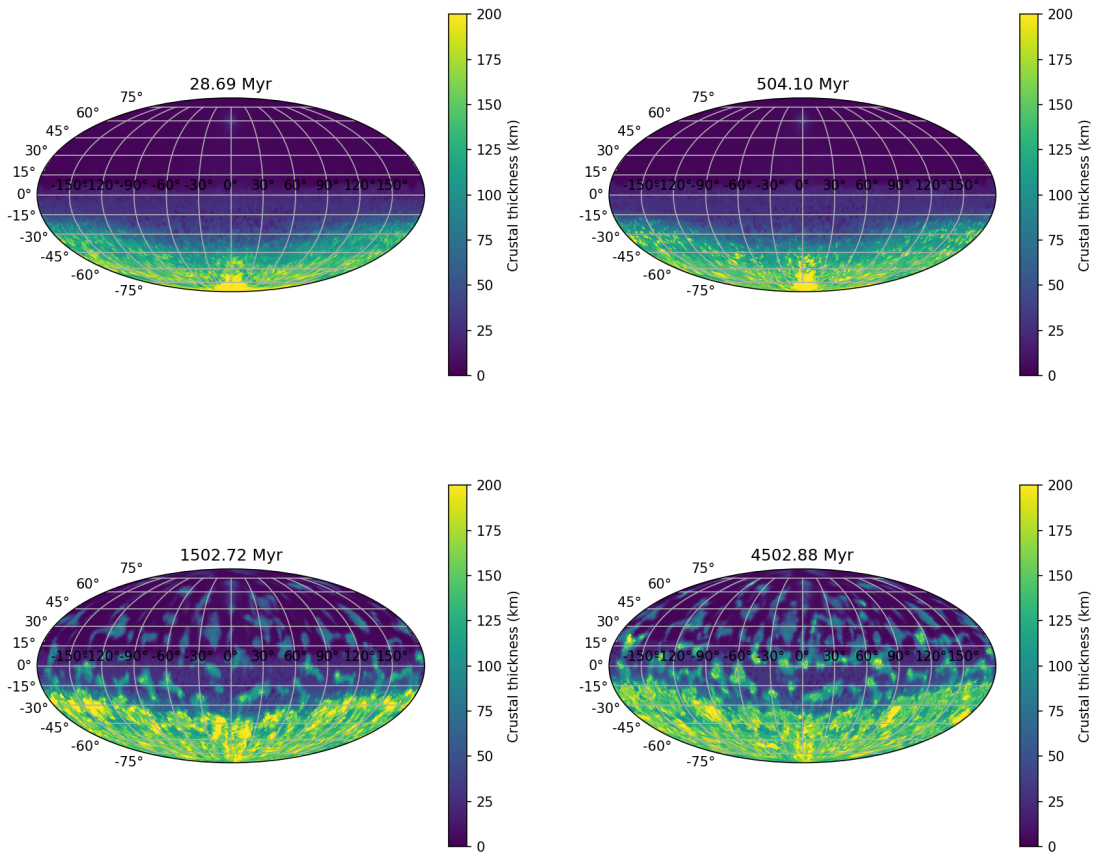

Figure 3.18: A time series showing the distribution of crust on a Mars-like body over time in the StagYY interior evolution model, up to a final time of ∼4.5 Gyr after a 15°, mutual escape speed impact from an impactor of radius 750 km, simulated with SPHLATCH. The impactor was modelled as a differentiated body with a core mass fraction of 25%. The maps use the Mollweide projection. The geometry is arranged such that the impact occurred at the south pole of the body. The colour map show crustal thickness in km. Here, we see that the crust distribution remains dominated by the initial impact site throughout the simulation. After approximately 1.5 Gyr, however, some crust production occurs in patches of the northern hemisphere.

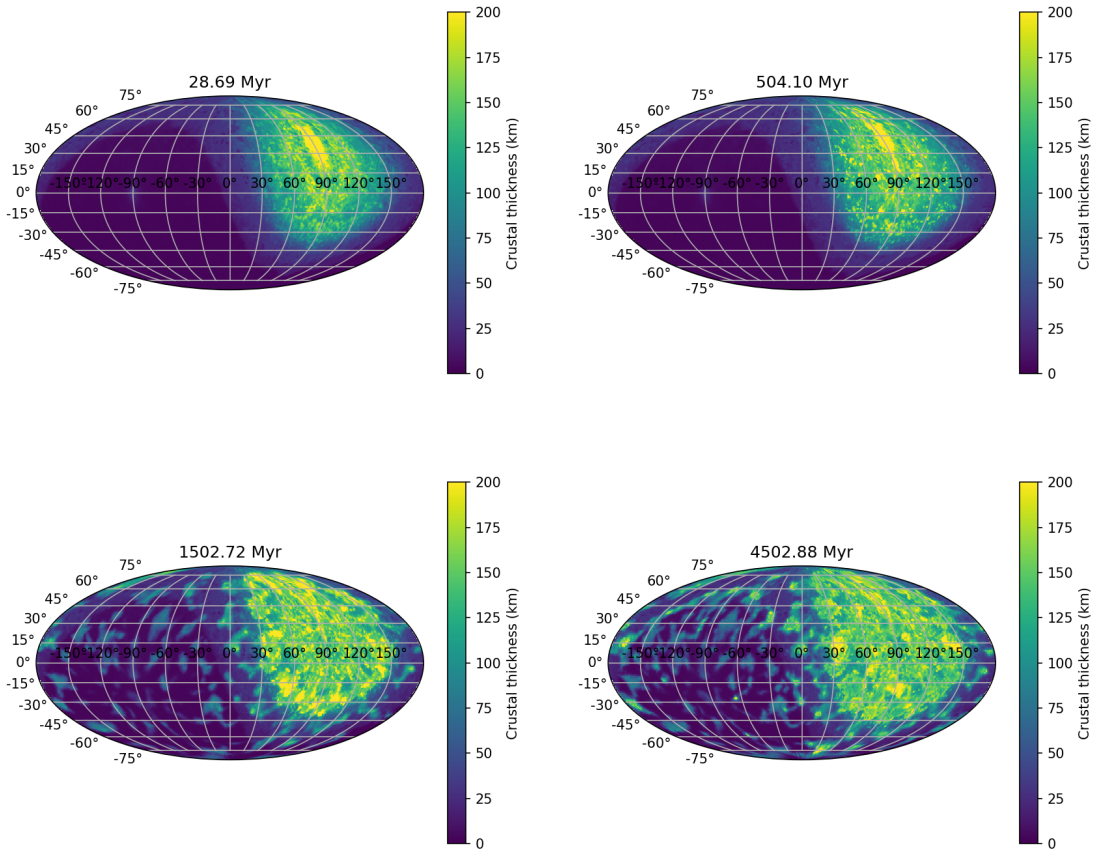

Figure 3.19: The same as Figure 3.18, but with the impact site offset from the poles. Note that the region of minimum crust production is antipodal to the main impact site.

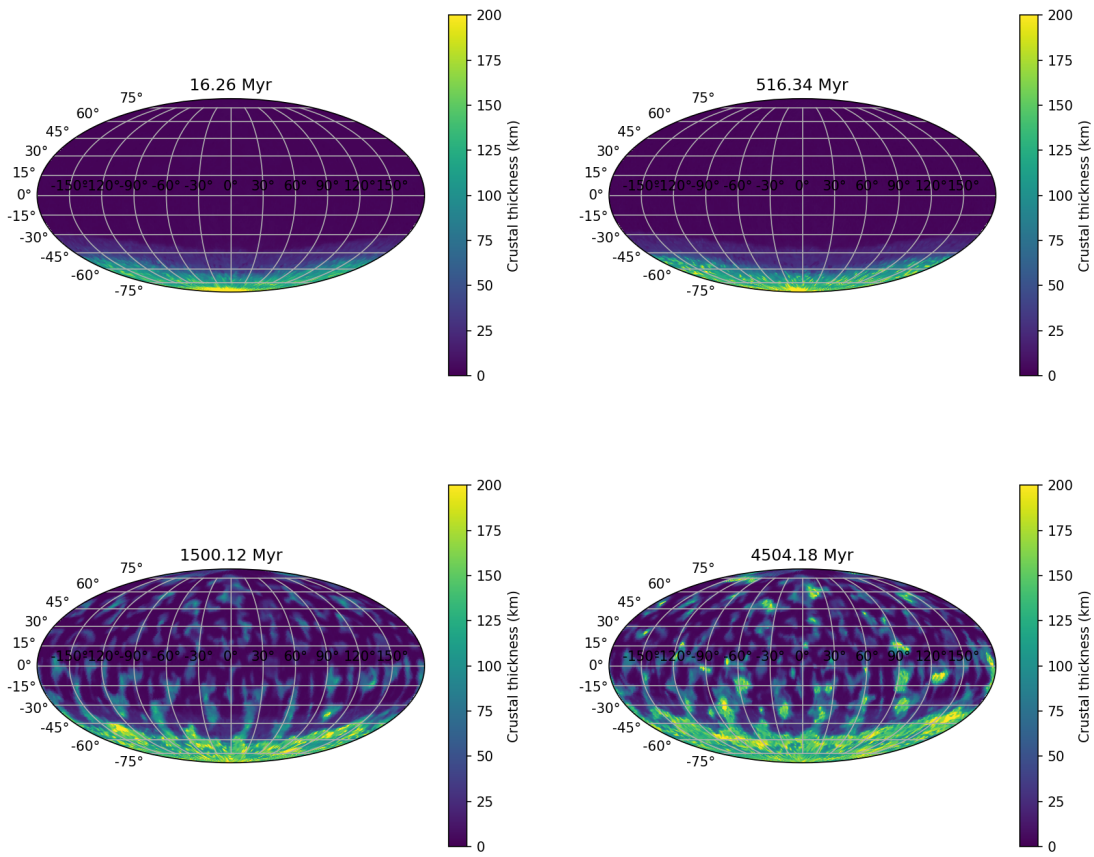

Figure 3.20: A time series showing the distribution of crust on a Mars-like body over time in the StagYY interior evolution model, up to a final time of ∼4.5 Gyr after a 15°, mutual escape speed impact from an impactor of radius 500 km, simulated with SPHLATCH. The impactor was modelled as a differentiated body with a core mass fraction of 25%. The maps use the Mollweide projection. The geometry is arranged such that the impact occurred at the south pole of the body. The colour map show crustal thickness in km. As with the 750 km radius impactor, the strongest region of crust production is at the impact site, but occurs elsewhere from around 1.5 Gyr onwards. However, the impact site is too small to produce a crustal dichtomy similar to that observed of Mars today.

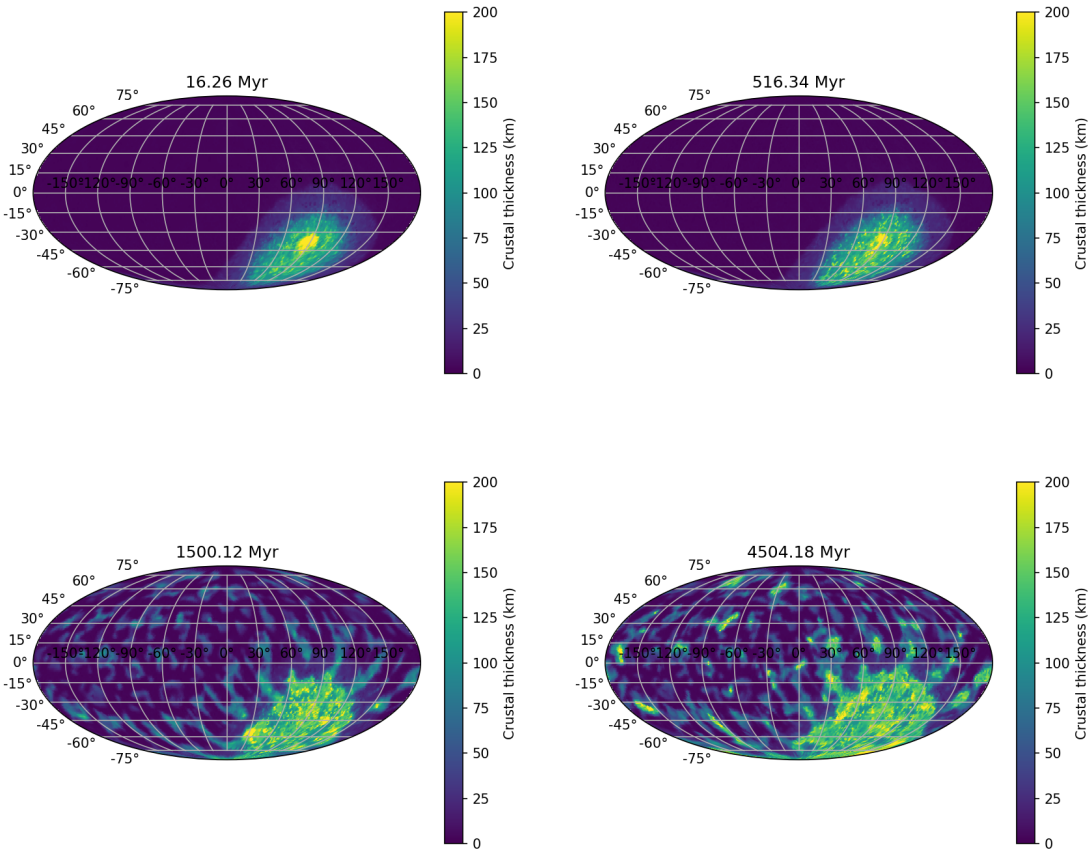

Figure 3.21: The same as Figure 3.20, but with the impact site offset from the poles. Unlike the 750 km radius impactor case of Figure 3.19, no antipodal suppression of crust production is visible.

Bibliography

H. A. Ballantyne, M. Jutzi, G. J. Golabek, L. Mishra, K. W. Cheng, A. B. Rozel, and P. Tackley. Investigating the Feasibility of an Impact-Induced Martian Dichotomy. *Icarus (in review)*, 2022.

J. P. Burg and T. V. Gerya. The role of viscous heating in Barrovian metamorphism of collisional orogens: Thermomechanical models and application to the Lepontine Dome in the Central Alps. *Journal of Metamorphic Geology*, 23(2):75–95, 2005. ISSN 02634929. doi: 10.1111/j.1525-1314.2005.00563.x.

M. S. Duncan, N. C. Schmerr, C. M. Bertka, and Y. Fei. Extending the Solidus for a Model Iron-Rich Martian Mantle Composition to 25 GPa. *Geophysical Research Letters*, pages 211–220, 2018. ISSN 19448007. doi: 10.1029/2018GL078182.

A. Emsenhuber, M. Jutzi, and W. Benz. SPH calculations of Mars-scale collisions: The role of the equation of state, material rheologies, and numerical effects. *Icarus*, 301:247–257, oct 2018. ISSN 10902643. doi: 10.1016/j.icarus.2017.09.017.

T. Gerya. *Introduction to Numerical Geodynamic Modelling*. Cambridge University Press, Cambridge, 2 edition, 2019. doi: 10.1017/9781316534243.

G. J. Golabek, T. Keller, T. V. Gerya, G. Zhu, P. J. Tackley, and J. A. Connolly. Origin of the martian dichotomy and Tharsis from a giant impact causing massive magmatism. *Icarus*, 215(1):346–357, sep 2011. ISSN 0019-1035. doi: 10.1016/J.ICARUS.2011.06.012.

A. Kageyama and T. Sato. "Yin-Yang grid": An overset grid in spherical geometry. *Geochemistry, Geophysics, Geosystems*, 5(9), 2004. ISSN 15252027. doi: 10.1029/2004GC000734.

Z. Malkin. A New Equal-area Isolatitudinal Grid on a Spherical Surface. *The Astronomical Journal*, 158:158, 2019. doi: 10.3847/1538-3881/ab3a44.

M. M. Marinova, O. Aharonson, and E. Asphaug. Mega-impact formation of the Mars hemispheric dichotomy. *Nature*, 453(7199):1216–1219, 2008. ISSN 14764687. doi: 10.1038/nature07070.

M. M. Marinova, O. Aharonson, and E. Asphaug. Geophysical consequences of planetary-scale impacts into a Mars-like planet. *Icarus*, 211(2):960–985, feb 2011. ISSN 00191035. doi: 10.1016/j.icarus.2010.10.032.

M. D. Norman. The composition and thickness of the crust of Mars estimated from rare earth elements and neodymium-isotopic compositions of Martian meteorites. *Meteoritics & Planetary Science*, 34(3):439–449, may 1999. ISSN 1945-5100. doi: 10.1111/J.1945-5100.1999.TB01352.X.

C. Reinhardt and J. Stadel. Numerical aspects of giant impact simulations. *Monthly Notices of the Royal Astronomical Society*, 467(4):4252–4263, jan 2017. ISSN 13652966. doi: 10.1093/mnras/stx322.

S. Ruiz-Bonilla, J. Borrow, V. R. Eke, J. A. Kegerreis, R. J. Massey, T. D. Sandnes, and L. F. A. Teodoro. Dealing with density discontinuities in planetary SPH simulations. *Monthly Notices of the Royal Astronomical Society*, 512(3):4660–4668, apr 2022. ISSN 0035-8711. doi: 10.1093/mnras/stac857.

P. J. Tackley. Effects of strongly temperature-dependent viscosity on time-dependent, three-dimensional models of mantle convection. *Geophysical Research Letters*, 20(20):2187–2190, 1993. ISSN 19448007. doi: 10.1029/93GL02317.

P. J. Tackley. Modelling compressible mantle convection with large viscosity contrasts in a three-dimensional spherical shell using the yin-yang grid. *Physics of the Earth and Planetary Interiors*, 171(1-4):7–18, 2008. ISSN 00319201. doi: 10.1016/j.pepi.2008.08.005.

D. Turcotte and G. Schubert. *Geodynamics*. Cambridge University Press, Cambridge, 3 edition, 2014. doi: 10.1017/CBO9780511843877.

D. L. Turcotte and G. Schubert. *Geodynamics*. Cambridge University Press, 2002.

J. Wade and B. J. Wood. Core formation and the oxidation state of the Earth. *Earth and Planetary Science Letters*, 236(1-2):78–95, jul 2005. ISSN 0012-821X. doi: 10.1016/J.EPSL.2005.05.017.

Chapter 4

Investigating an Impact-Induced Martian Dichotomy

Whether it has been its apparent retrograde motion motivating improved models of the Solar System (Copernicus, 1543; Kuhn, 1957), its illusive (or possibly elusive (Lauro et al., 2020)) bodies of water provoking astrobiological discussion (Schiaparelli, 1878), or its relatively small size posing difficult questions to conventional planet formation theory (e.g. Clement et al., 2021), the study of Mars has driven major scientific advancement throughout the history of Astronomy. With ever-improving methods and instruments, this trend has continued into the present, and shows no indication of faltering.

The most striking feature of Mars is the dramatic contrast in elevation and crustal thickness between its two hemisphere: the *Martian Dichotomy*. In this chapter, the likelihood of this feature being of giant-impact origin is investigated, using a large suite SPH(LATCH) simulations that are coupled with a newly developed scheme that predicts the post-impact distribution of crust (as described in Chapter 3). This is the first study to comprehensively evaluate both the northern excavation (*Borealis Basin*) scenario and southern crustal thickening scenario concurrently.

Investigating the Feasibility of an Impact-Induced Martian Dichotomy

Harry A. Ballantyne[a,*], Martin Jutzi[a], Gregor J. Golabek[b], Lokesh Mishra[a,c], Kar Wai Cheng[d], Antoine B. Rozel[d], Paul Tackley[d]

[a]*Space Research & Planetary Sciences (WP), University of Bern, Bern, Switzerland*
[b]*Bayerisches Geoinstitut, University of Bayreuth, Bayreuth, Germany*
[c]*Geneva Observatory, University of Geneva, Versoix, Switzerland*
[d]*Institute of Geophysics, ETH Zurich, Zurich, Switzerland*

Abstract

A giant impact is commonly thought to explain the dramatic contrast in elevation and crustal thickness between the two hemispheres of Mars known as the "Martian Dichotomy". Initially, this scenario referred to an impact in the northern hemisphere that would lead to a huge impact basin (dubbed the "Borealis Basin"), while more recent work has instead suggested a hybrid origin that produces the Dichotomy through impact-induced crust-production. The majority of these studies have relied upon impact scaling-laws inaccurate at such large-scales, however, and those that have included realistic impact models have utilised over-simplified geophysical models and neglected any material strength. Here we use a large suite of strength-including smoothed-particle hydrodynamics (SPH) impact simulations coupled with a more sophisticated geophysical scheme of crust-production and primordial crust to simultaneously investigate the feasibility of a giant impact on either hemisphere of Mars to have produced its dichotomous crust distribution, and utilise spherical harmonic analysis to identify the best-fitting cases. We find that the canonical Borealis-forming impact is not possible without both excessive crust-production and strong antipodal effects not seen on Mars' southern hemisphere today. Our results instead favour an impact and subsequent localised magma ocean in the southern hemisphere that results in a thicker crust than the north upon crystallisation. Specifically, our best-fitting cases suggest that the projectile responsible for the Dichotomy-forming event was of radius 500-750 km, and collided with Mars at an impact angle of 15-30° with a velocity of 1.2-1.4 times mutual escape speed (∼6-7 km/s).

Keywords: Mars, Impact processes, Geophysics, Accretion

*Corresponding author.
Email address: harry.ballantyne@unibe.ch (Harry A. Ballantyne)

1. Introduction

Mars is the most studied planet other than Earth, yet its most prominent feature has evaded confident explanation for nearly 50 years; the so-called "Martian Dichotomy". This moniker predominantly refers to the stark topographical disparity between the two hemispheres of the planet, with an apparent basin encompassing around 42% of the north, corresponding to an elevation difference of 4–8 km (e.g. Andrews-Hanna et al., 2008). Additional associated features include a greater density of visible impact craters and volcanoes in the south relative to the north; however, the former may be explained via the inclusion of ancient, buried depressions that could equalise the crater counts when taken into account (Frey, 2006; Buczkowski, 2007).

Gravity measurements revealed that this feature is not limited to surface properties, with the crustal thickness distribution being highly correlated with that of elevation, resulting in an average estimated crustal thickness contrast of roughly 25 km (Zuber, 2000; Neumann et al., 2004). Recent seismic measurements from NASA's InSight lander also support this claim (Knapmeyer-Endrun et al., 2021). Naturally, this has motivated many previous authors to propose geodynamic processes as the origin of such an internal structure. These studies usually support a degree-1 mantle upwelling beneath the southern hemisphere, leading to hemisphere-preferential crust production over long timescales (e.g. Zhong & Zuber, 2001).

The length of these timescales are of great importance, however, as the Dichotomy is known to be the one of the oldest observable features on Mars. Crater distributions suggest an age of at least $\sim$4.1 Gyr (Solomon et al., 2005; Nimmo & Tanaka, 2005; Frey, 2006), while recent geochemical analyses of martian meteorites push this to $\sim$4.4 Gyr (Humayun et al., 2013; Cassata et al., 2018; Bouvier et al., 2018). This leaves little time to form such a convection pattern; only being possible if Mars possessed a particular, layered viscosity profile that includes a large jump (by a factor of > 25) in the mid-mantle (Roberts & Zhong, 2006; Keller & Tackley, 2009). Moreover, such a scenario requires vigorous convection via a high Rayleigh number which would likely lead to long-term resurfacing, erasing the initial crustal dichotomy over billion year times.

Another, more outward-looking explanation for the Dichotomy's origin is that of an impact between Mars and an object on the order of 1000 km in radius: an

attractive alternative considering that such large-scale impacts were most likely during the first few 100 Myr of the Solar System (e.g. Morbidelli et al., 2018). Moreover, the debris-disc formed by such an event would naturally lead to satellites with very low eccentricities and inclinations, matching the orbital properties of the martian moons well (Murchie et al., 2015, and references therein). Traditionally, this meant excavating the crust from the northern hemisphere while leaving the southern hemisphere intact, imprinting a classical (albeit giant) impact crater dubbed the Borealis Basin (Marinova et al., 2008; Andrews-Hanna et al., 2008; Nimmo et al., 2008). A clear caveat to this approach is the significant degree of melting that accompanies these events, as this potentially induces crust production upon re-crystallisation that must be taken into account.

This leads to the most recent group of hypotheses—a giant impact occurred that invoked significant crust production on one hemisphere. Reese & Solomatov (2006); Reese et al. (2010); Reese & Solomatov (2010); Golabek et al. (2011); Leone et al. (2014) proposed this to have been in the south, whereby the heat anomaly invokes a more rapid transition to a single-plume mantle dynamic. Citron et al. (2018) suggested instead that the impact occurred in the north, stripping the hemisphere of its radiogenic-heating element enriched primordial crust and subsequently promoting a superplume in the south. In either case, the impact was modelled through highly simplified scaling laws (Senshu et al., 2002; Monteux et al., 2007). Such simplifications explicitly neglect several effects that are important on planetary-scales, such as antipodal shock-heating and re-impacting ejecta. Even when ignoring such effects, it is not clear how accurate these predictions are when extrapolated to this regime (Marinova et al., 2011).

To combat these issues, Golabek et al. (2018) successfully coupled a smoothed-particle hydrodynamics (SPH) impact model with a thermochemical model of the interior mantle dynamics for a Mars-sized object. This showed initial promise in producing a crustal dichotomy, further supporting the southern-impact hypothesis; however, only the crystallisation of the magma ocean was modelled (i.e. 0.5 Myr). Furthermore, no consideration was made for the possibility of a primordial crust, which is a highly likely pre-impact feature considering Mars' differentiated nature (Stähler et al., 2021). Finally, the study was restricted to only two impact scenarios: head-on or 45° impact angle at the mutual escape speed, with a 1000 km-radius impactor.

In this study, we explore a feasible parameter-space that could lead to such a

scenario through a large set of SPH simulations, the details of which are described in sections 2 and 3, with the aim to provide much needed refinements. To estimate the post-impact crustal thickness, we develop a crust-production model based on melt fraction and mantle fertility, also described in section 2. A significant advantage of this model over previous work is its ability to include pre-impact crusts of various thicknesses, allowing us to investigate both the case of a crust-stripped northern hemisphere and the case of a magma-thickened southern hemisphere, concurrently. In sections 4 and 5, we present and discuss the results of this study, respectively. Finally, we present our conclusions and future outlook in section 6.

2. Modelling Approach

2.1. Impact Code

To model the impacts we use SPHLATCH; an SPH code specifically designed to handle planetary-scale collisions (Reufer et al., 2012; Emsenhuber et al., 2018) that has been used to study a wide range of impact regimes (Emsenhuber & Asphaug, 2019a,b; Emsenhuber et al., 2020, 2021; Asphaug et al., 2021; Gabriel et al., 2020; Gabriel & Allen-Sutter, 2021; Cambioni et al., 2019).

2.1.1. Smoothed-Particle Hydrodynamics (SPH)

SPH is a Lagrangian method based on interpolation points (or "particles") of fixed mass that represent a continuous medium (Lucy, 1977; Gingold & Monaghan, 1977). Through the use of a Gaussian-like function known as a kernel, W, along with a measure of particle volume, V, the physical properties of the medium can be smoothed out, allowing quantities such as density and internal energy to be calculated for a given particle as a sum of the smeared-out contributions from its neighbouring particles. The degree of this smoothing is quantified by the "smoothing length", h, which is related to the density of the particle of interest, giving an approximate measure of resolution. In mathematical notation, this reads as

$$B(\mathbf{x}) = \sum_b B_b W(\mathbf{x} - \mathbf{x}_b, h), \tag{1}$$

where B is the physical quantity of interest, $\mathbf{x}$ is the associated spatial location and the subscript b indicates a specific neighbouring particle. The "standard" kernel function, also used in SPHLATCH, is the cubic B-spline given explicitly in Appendix A.1. For further details of this method, we refer the reader to an in-depth review such as those by Rosswog (2009) or Monaghan (2005).

2.1.2. Solid Strength

One advantage of SPHLATCH over other similar codes is its ability to include the effects of shear strength and plasticity. Typically, it is assumed that the force of gravity will dominate over any material strength in planetary-scale impacts, leading most previous works to neglect such effects entirely (e.g. Marinova et al., 2008). This approach conveniently allows for greatly reduced computational cost; however, Golabek et al. (2018) (and its sister study Emsenhuber et al. (2018)) showed that the inclusion of material strength in this size-regime still plays a non-negligible role, indicating important physics that cannot be ignored.

The implementation of these effects in the SPHLATCH code is described in Emsenhuber et al. (2018). To avoid unnecessary repetition, therefore, we shall only give a brief description of such aspects of the code, emphasising the key adaptations that have been made since.

At its core, adding solid mechanics to the standard, inviscid fluid SPH requires the generalisation of pressure into a stress tensor, $\sigma^{\alpha\beta}$, made up of a hydrostatic pressure component p and a shear stress component $S^{\alpha\beta}$:

$$\sigma^{\alpha\beta} = -p\delta^{\alpha\beta} + S^{\alpha\beta}, \tag{2}$$

where $\delta^{\alpha\beta}$ is the Kronecker delta. We follow Benz & Asphaug (1994, 1995), who (following Wingate & Fisher (1993); Libersky & Petschek (1991)) applied Hooke's law to expand $S^{\alpha\beta}$ as follows:

$$S^{\alpha\beta} = 2\mu(\epsilon^{\alpha\beta} - \frac{1}{3}\epsilon^{\gamma\gamma}), \tag{3}$$

where μ is the material's shear modulus, $\epsilon^{\alpha\beta}$ is the strain tensor and the superscript γ follows the Einstein summation rule. The time derivative of this equation is

$$\dot{S}^{\alpha\beta} = 2\mu(\dot{\epsilon}^{\alpha\beta} - \frac{1}{3}\dot{\epsilon}^{\gamma\gamma}) + S^{\alpha\gamma}R^{\gamma\beta} + S^{\beta\gamma}R^{\gamma\alpha}, \tag{4}$$

where $R^{\alpha\beta}$ is the rotation rate tensor. The rotation terms are necessary for reference frame independence; without them the calculations would correspond to the material reference frame, unlike all other calculations that are in the laboratory frame.

This approach has been used in a great number of subsequent papers, however there appears to be a small, but very important disparity between different works regarding the exact form of the rotation terms in Equation 4. In the original work of Benz & Asphaug (1994, 1995), the rotation terms were of the form

$$S^{\alpha\gamma}R^{\beta\gamma} + S^{\beta\gamma}R^{\alpha\gamma}, \tag{5}$$

which is the variant used for all previous work with SPHLATCH other than Emsenhuber et al. (2021) and Asphaug et al. (2021). Other studies such as Jutzi et al. (2008) replaced $S^{\alpha\gamma}$ with $S^{\alpha\beta}$. In contrast to this, Schäfer et al. (2007) (and related subsequent work such as Schäfer et al. (2016)) use the same form as Equation 4. We find that it is important to use this variation to avoid significant angular momentum conservation issues in certain impact-regimes such as those detailed in this study (see Figure E.25).[1]

Plastic deformation effects are included through a Drucker-Prager-like yield strength model, with a temperature dependence such that strength decreases as the material approaches its melting temperature (Collins et al., 2004). For this purpose, we use the Mars-specific solidus of Duncan et al. (2018).

2.1.3. Other details

SPHLATCH uses the Barnes-Hut hierarchical tree method to find the SPH nearest neighbours and calculate self-gravity through the associated multipole approximation (Barnes & Hut, 1986; Hernquist, 1987; Hernquist & Katz, 1989), with an improved neighbour-list method used to ensure force symmetry that is described in Appendix B. To calculate thermodynamic quantities such as pressure and temperature, we use the sophisticated equation of state ANEOS (Thompson & Lauson, 1972; Thompson, 1990).

2.2. Crust Production

In this study, we are investigating the immediate distribution of crust due to melt, and in the case of a pre-impact crust, displaced primordial material. Due to limitations in direct simulation output quantities and resolution, this required the development of a new post-processing scheme to convert our results into a relevant format.

2.2.1. Spherical Grid

The mesh-free nature of SPH means that the coordinates of our simulation results follow those of the SPH particles and are thus distributed in an arbitrarily uneven fashion, which can be a hindrance for in-depth analysis. We therefore use Equation 1

[1] We note that the angular momentum conservation issues related to the rotation terms only occur at large, planetary scales. Previous studies at smaller scales would experience only a negligible improvement if they were to be repeated with the correct form.

to smooth our results onto a spherical grid, uniformly-spaced in radius, latitude and longitude. Specifically, we use a resolution of $13.\dot{3}$ km in radius and $\frac{\pi}{100}$ in latitude and longitude.

Simply smoothing all of our thermodynamic quantities in this manner would be inconsistent with our equation of state, however, as it is only internal energy and density that are calculated with SPH alone. We therefore mirror the simulation method; only smoothing these two values directly onto the grid, then using these as input to the ANEOS equation of state to calculate all other thermodynamic values such as pressure and temperature. One caveat of this method is ANEOS' inability to determine the physical properties of a mixture of two (or more) materials, only using one integer material number for each calculation. As a practical solution, we assign each SPH particle the mass fraction for each material (either a 1 or 0 as each particle is made up of only 1 material) and then use Equation 1 again to calculate a continuous mass fraction at every point on our grid for each material. The material number corresponding to the largest mass fraction is then passed to ANEOS.

2.2.2. From Magma to Crust

To give a measure of melt fraction, ξ, at each grid point, we use the following expression (Burg & Gerya, 2005; Golabek et al., 2011):

$$\xi = \begin{cases} 0 & T \leq T_{\text{sol}} \\ \frac{T - T_{\text{sol}}}{T_{\text{liq}} - T_{\text{sol}}}\Big|_P & T_{\text{sol}} < T < T_{\text{liq}} \\ 1 & T \geq T_{\text{liq}} \end{cases}, \tag{6}$$

where T is temperature and T_{sol} and T_{liq} are the solidus and liquidus temperatures corresponding to the pressure, P. T_{sol} is calculated using the previously mentioned function in Duncan et al. (2018), and T_{liq} is found through the following linear relation for peridotite (Wade & Wood, 2005):

$$T_{\text{liq}} = 1973 + 28.57P, \tag{7}$$

with T_{liq} in K and P in GPa. To account for the additional energy necessary for melting due to latent heat, a temperature offset of 400 K is also added to T_{liq} (Turcotte & Schubert, 2002).

If we assume a bulk mass fraction, β, of this molten material that will rise to the surface to crystallise and form basaltic to andesitic crust, we can calculate a crustal

mass associated with each grid cell as follows:

$$m_{\text{crust},ijk} = \min\left(\beta, \xi_{ijk}\right)\left(\rho V\right)_{ijk}\,, \tag{8}$$

where the $\min\left(\xi_{ijk}, \beta\right)$ term is due to the crust-bearing material preferentially partitioning into the melt, ρ is the density and V is the volume of the grid cell given by:

$$V_{ijk} = \int_{\phi_{k-\frac{1}{2}}}^{\phi_{k+\frac{1}{2}}} \int_{\theta_{j-\frac{1}{2}}}^{\theta_{j+\frac{1}{2}}} \int_{r_{i-\frac{1}{2}}}^{r_{i+\frac{1}{2}}} r^2 \sin\theta \; \mathrm{d}r \, \mathrm{d}\theta \, \mathrm{d}\phi, \tag{9}$$

which when evaluated becomes:

$$V_{ijk} = \frac{\Delta\phi}{3}\left[r_{i+\frac{1}{2}}^3 - r_{i-\frac{1}{2}}^3\right]\left[\cos\theta_{j-\frac{1}{2}} - \cos\theta_{j+\frac{1}{2}}\right], \tag{10}$$

where the indices $(i,j,k)-\frac{1}{2}$ and $(i,j,k)+\frac{1}{2}$ indicate the values at the lower and upper boundaries of the grid cell, respectively ((i,j,k) represent the grid cell centres), and $\Delta\phi = \phi_{k+\frac{1}{2}} - \phi_{k-\frac{1}{2}}$, which is constant due to our grids having equal spacing.

As magma is more compressible than solid rock, it experiences negative buoyancy at pressures greater than around 7.4 GPa, or roughly 600 km depth (Suzuki et al., 1998; Breuer & Spohn, 2006). We therefore neglect any melt at such pressures in our crust production model. In addition, we assume that melt cannot be extracted at melt fractions below 4%. Significantly lower thresholds have been assumed in various earlier studies (e.g. Fraeman & Korenaga, 2010; Ruedas et al., 2013; Ruedas & Breuer, 2021); however, we follow the Citron et al. (2018) train of thought in that Mars should have a higher melt extraction threshold than Earth due to its lower gravity (and thus weakened buoyancy forces), where values predicted for Earth lie in the range 1-4% (Wang & Li, 2021, and references therein).

Through the summation of these grid cell values, a total crustal mass, $M_{\text{crust},jk}$, is calculated for each latitude and longitude (where the melt has been assumed to rise radially upward). To convert this to a crustal thickness, we assume a crustal density, ρ_{crust}, which we can divide $M_{\text{crust},jk}$ by to give us a crustal volume, $V_{\text{crust},jk}$, corresponding to a crustal thickness given by:

$$z_{\text{crust},jk} = \left[R_{\♂}^3 - \frac{3V_{\text{crust},jk}}{\Delta\phi\left(\cos\theta_{j-\frac{1}{2}} - \cos\theta_{j+\frac{1}{2}}\right)}\right]^{\frac{1}{3}}, \tag{11}$$

where $R_{\♂}$ is the radius of Mars. Note that this is simply a rearrangement of Equation 10, with $r_{i+\frac{1}{2}}$ and $r_{i-\frac{1}{2}}$ becoming $z_{\text{crust},jk}$ and $R_{\♂}$, respectively, and V_{ijk} becoming $V_{\text{crust},jk}$.

2.2.3. Primordial Crust

Unfortunately, current computational limitations prohibit the inclusion of a fully-resolved crustal layer in our simulations, so we must implement further post-processing approaches to quantitatively estimate its influence. Firstly, we identify the uppermost SPH particles in the original, pre-impact target body that represent the surface. As the primordial crustal thicknesses of interest are thinner than an SPH smoothing length, we approximate the mass fraction of crust, β_{prim}, for a given SPH particle based on its radial position relative to the mantle-crust boundary, R_{MCB}. SPH particles represent a mass that has been smeared-out radially to follow the smoothing kernel, and thus the precise 3-dimensional calculation of this crustal mass fraction is highly non-trivial. To avoid this, while still retaining good accuracy, we use the integrated 1-dimensional kernel, $W'_{\text{1D}}(r, h)$, given in Appendix A.2, as follows:

$$\beta_{\text{prim}} = \begin{cases} \frac{1}{2} - W'_{\text{1D}}(|r - R_{\text{MCB}}|, h) & r \leq R_{\text{MCB}} \\ \frac{1}{2} + W'_{\text{1D}}(|r - R_{\text{MCB}}|, h) & r > R_{\text{MCB}} \end{cases}, \tag{12}$$

where the $\frac{1}{2}$ term comes from the symmetric nature of W'_{1D}.

The presence of a primordial crust infers a depleted mantle that will no longer produce as much crust if melted again. To include this effect, we calculate the global crustal mass $M_{\text{crust,global}}$ through the summation of all previously calculated $M_{\text{crust},jk}$ values, and then remove this mass from the initially fertile mantle in one of two end-member scenarios.

In the first case, we assume that the entire mantle has had time to fully mix, meaning that our β in Equation 8, which from here onward we will call the "fertility", is still constant across the mantle, but is decreased to match the mass of fertile mantle required to produce $M_{\text{crust,global}}$, i.e. :

$$\beta_{\text{dep}} = \left(1 - \frac{M_{\text{crust,global}}}{\beta_0 M_{mantle}}\right) \beta_0, \tag{13}$$

where M_{mantle} is the mass of the mantle and β_0 is the initial mantle fertility prior to primordial crust formation. If we assume that all primordial crust mass will form new crust upon remelting, we therefore redefine β for each particle as:

$$\beta = \begin{cases} \beta_{\text{dep}} & r \leq R_{\text{MCB}} - 2h \\ \beta_{\text{dep}}(1 - \beta_{\text{prim}}) + \beta_{\text{prim}} & R_{\text{MCB}} - 2h < r < R_{\text{MCB}} + 2h \\ 1 & r \geq R_{\text{MCB}} + 2h \end{cases}. \tag{14}$$

The second case corresponds to a fully stratified mantle, whereby the mantle directly below the crust is entirely depleted ($\beta = 0$), eventually reaching untouched, fertile mantle at depth ($\beta = \beta_0$). The exact radial position of this fertile-depleted boundary is determined again using $M_{\text{crust,global}}$, instead converting this into a volume of depleted mantle, V_{dep}, that is used in a modified form of Equation 11 given by:

$$R_{\text{FDB}} = \left[R_{\text{MCB}}^3 - \frac{3V_{\text{dep}}}{4\pi} \right]^{\frac{1}{3}}, \tag{15}$$

with V_{dep} given by:

$$V_{\text{dep}} = \frac{M_{\text{crust,global}}}{\beta_0 \overline{\rho}}, \tag{16}$$

where $\overline{\rho}$ is the mean density of the mantle. We introduce this boundary using a similar method to Equation 12, now including both the fertile-depleted and mantle-crust boundaries as follows:

$$\beta = \begin{cases} \beta_0 \left(\frac{1}{2} + W'_{1\text{D}}(|r - R_{\text{FDB}}|, h) \right) + \beta_{\text{prim}} & r < R_{\text{FDB}} \\ \beta_0 \left(\frac{1}{2} - W'_{1\text{D}}(|r - R_{\text{FDB}}|, h) \right) + \beta_{\text{prim}} & R_{\text{FDB}} \leq r \leq R_{\text{FDB}} + 2h \\ \beta_{\text{prim}} & r > R_{\text{FDB}} + 2h \end{cases} \cdot \tag{17}$$

Another important aspect of a pre-impact crust is the contribution to crustal thickness by primordial crustal material that has remained solid throughout the giant impact event (or has re-solidified due to a change in pressure). This material is included in our crustal calculations by simply adding the solid crust contribution to our grid cell crustal masses as follows:

$$m_{\text{crust},ijk} = \left\{ \left[\min(\beta, \xi) + \beta_{\text{prim}} \left(1 - \frac{\min(\beta, \xi)}{\beta} \right) \right] \rho V \right\}_{ijk}, \tag{18}$$

where the first term represents the molten material that will solidify into crust and the second term represents the intact primordial crust that is in the solid phase at the end of the simulation.

Clearly, this primordial crust scheme relies upon a homogeneous SPH particle distribution, as small fluctuations in position (relative to a given particle's smoothing length) can have a dramatic effect on a particle's primordial crust fraction, as is clear from equation 12. Our pre-impact bodies are initially composed of a Hexagonal Close-Packed (HCP) lattice particle structure that undergoes a relaxation step before being used in the full impact simulation. Unfortunately, this leaves some remnant heterogeneities in the particle distribution of purely numerical origin, which

in turn influences the initial primordial crust distribution.[2] To counteract these artefacts, we normalise the particles' radial positions used for the primordial crust calculations such that the maximum value in a given latitude-longitude range is equal to the global maximum value. The size of these longitude-latitude ranges is given by the equal-area iso-latitudinal grid of Malkin (2019) as to keep the resolution of this normalisation step constant across the entire body.

3. Parameter Study

The chosen parameters for our impact simulations are as follows: impact angles of 0-90° in steps of 15° (with 0° being the head-on case); impact velocities of 1.0-1.4 v_{esc} (v_{esc} is the mutual escape speed of the two bodies given by $v_{\mathrm{esc}} = \sqrt{\frac{2G(m_{\mathrm{imp}}+m_{\mathrm{imp}})}{r_{\mathrm{imp}}+r_{\mathrm{imp}}}}$, where G is the gravitational constant, m is mass, r is radius and the subscripts $_{\mathrm{imp}}$ and $_{\mathrm{tar}}$ signify the impactor and target, respectively); and impactor radii of 500 km, 750 km, 1000 km, 1500 km and 2000 km. Each simulation consists of 200,000 SPH particles in total, with near head-on impacts (angles $< 45°$) simulated for 50 hours post-impact and oblique impacts (angles $\geq 45°$) simulated for 200 hours as to allow for any potential secondary impacts. Material strength is included in all cases; however, select cases were repeated without this feature for comparison.

Both impactor and target are modelled as differentiated bodies with an iron core and dunite mantle, using the input parameters of Emsenhuber et al. (2018) and Benz et al. (1989), respectively. As the impactor's internal structure is unknown, we investigate a core mass fraction of approximately 25% and 50% for each set of parameters. For our Mars-like body we use a core mass fraction of ∼25%, consistent with geodetic and seismic measurements (Rivoldini et al., 2011; Stähler et al., 2021). The internal temperature profiles of the bodies approximately match the Duncan et al. (2018) solidus at the surface, as this is the most likely scenario at early times after formation, with a ∼150 K temperature jump at the core-mantle boundary of our Mars-like body as proposed by Williams & Nimmo (2004). For the crustal density of Mars, ρ_{crust}, used in the crust-production scheme, we take a value of 2582 kg m^{-3} from Goossens et al. (2017) which matches with recent observational constraints (Knapmeyer-Endrun et al., 2021).

[2]More recently proposed initial particle distributions such as those described in Reinhardt & Stadel (2017) or Diehl et al. (2015) may lead to smaller numerical artefacts in the particle distribution.

For the primordial crust calculations, we investigate initial fertilities (β_0) of 0.1-0.25 in steps of 0.025, and crust thicknesses of 10-70 km in steps of 15 km. For the sake of simplicity, the impactor fertility was taken to be 0.2 in all cases, and any impactor crust was neglected.

4. Results

4.1. "Classical" Cases

For the sake of comparison to previous studies we will first focus upon the "classical" cases: a 1000 km-radius impactor with a 25% core fraction impacting at the mutual escape velocity at either 0°or 45°.

These cases were performed both with and without solid strength. As can be seen in Figure 1, strength clearly plays an important role in this impact regime, effectively acting to dissipate the impact-generated shockwave through increased frictional heating. This effect is most apparent in the head-on case, where the strength-less model shows a significant antipodal feature that is not present at all when strength is included.

The corresponding crustal thickness maps for the cases including material strength (calculated using the method of Section 2.2.2) can be seen in Figure 2, where no primordial crust has been included and an initial mantle fertility of 0.2 has been used. While the head-on case may have a much clearer hemispherical distribution than the oblique impact, the most overwhelming feature of both scenarios is an average crustal thickening that is significantly too large when compared to Mars' true hemispherical contrast of ~ 25 km. This effect is still apparent even when the initial mantle fertility is reduced to 0.1, where the majority of the impact-induced crust has a thickness of approximately 60 km (see Figure 3).

As described in Section 2.2.3, any primordial crust acts to deplete the Martian mantle of incompatible elements, making any remelting less efficient in producing crust. In addition, the primordial crust originally located at the impact site is excavated, with the majority being redistributed around the planet (see Appendix C.22). Both of these effects lead to a reduced final thickness of crust at the impact site. Figure 4 illustrates the result of these effects for the same impact cases as earlier through the inclusion of a 40 km pre-impact, primordial crust, for each of the mantle depletion models.

In the fully mixed case, the crust distribution largely resembles those of Figure 3

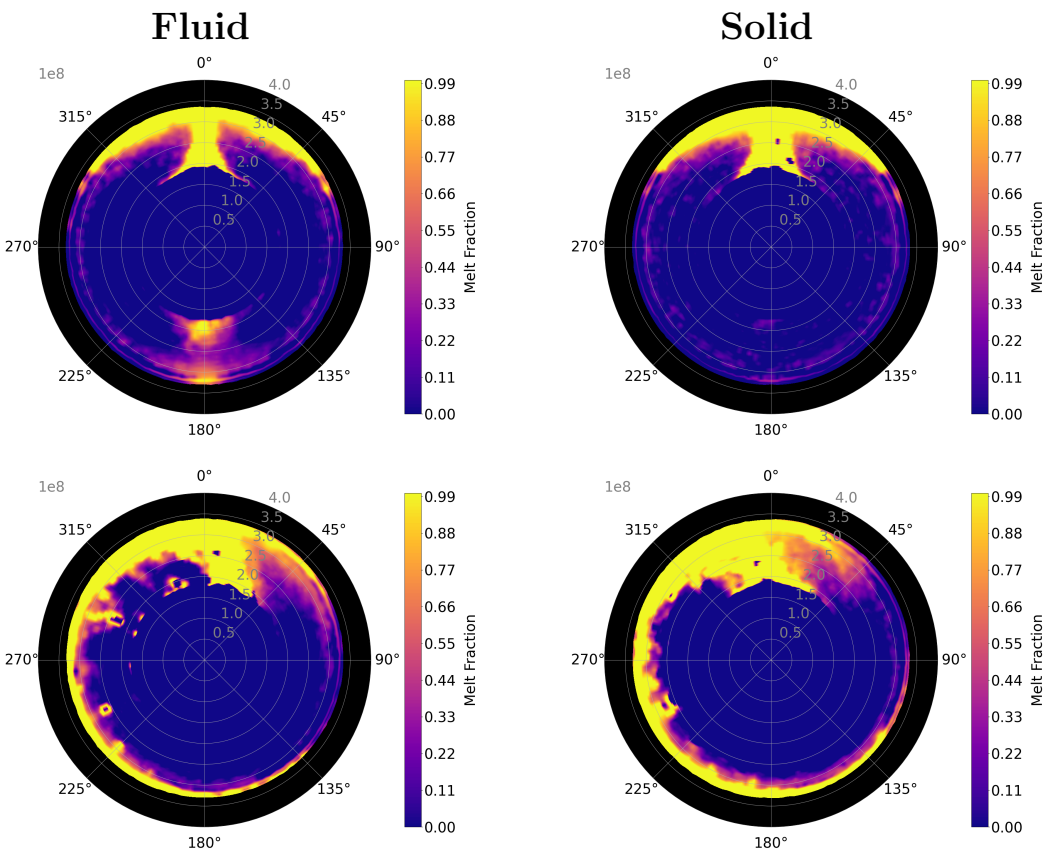

Figure 1: Melt fraction distribution for each of the classical cases, with (right) and without (left) solid strength, where a slice has been made in the impact plane to display the interior. The top row shows the head-on cases, whereas the bottom row shows the 45° cases. Note that the oblique impact induces a rotation in the anticlockwise direction.

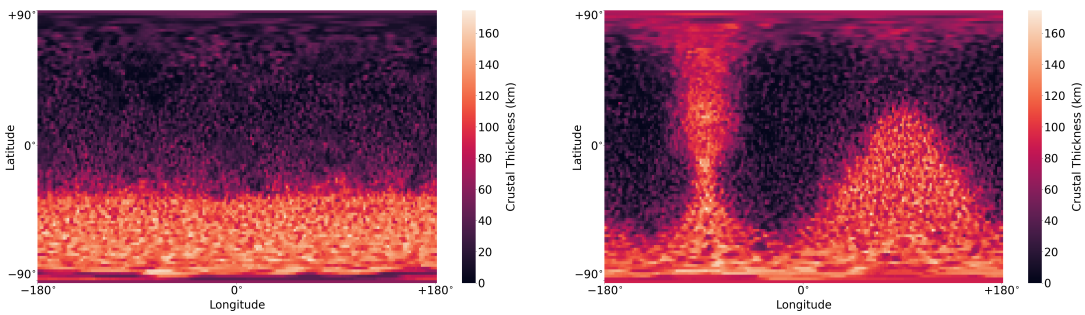

Figure 2: Crustal thickness distributions without any primordial crust calculation for the head-on (left) and 45°(right) classical cases, with an initial mantle fertility of 0.2. The simple equirectangular projection has been used for this plot, as well as all other similar plots in this paper. The 45°case displays an iso-longitudinal ring of crust-production at roughly -90°longitude due to re-impacting ejecta from the initial impact.

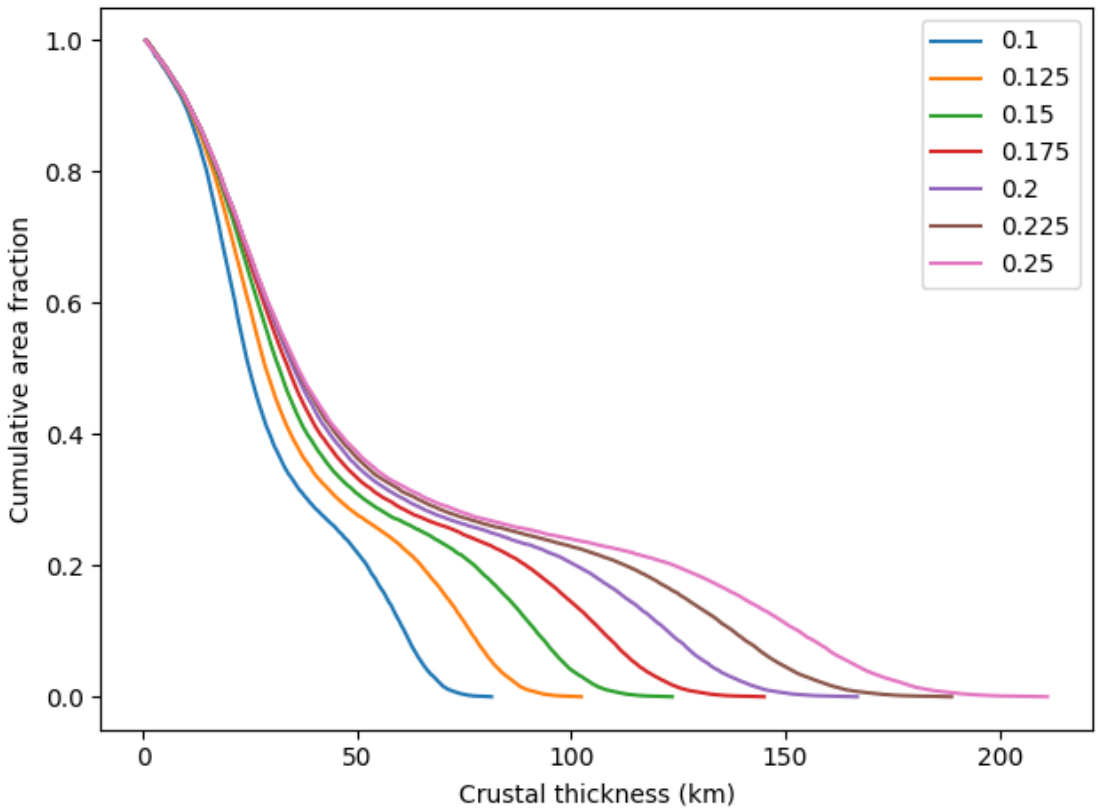

Figure 3: Cumulative fractional area as a function of crustal thickness for the classical head-on case without any primordial crust, where each colour denotes a different initial mantle fertility.

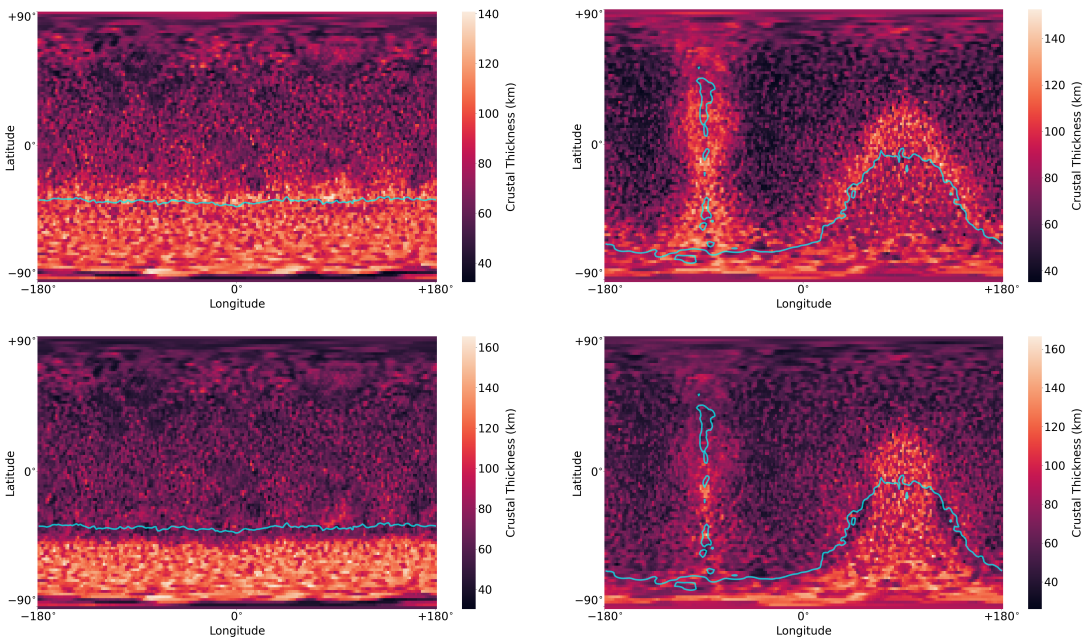

Figure 4: Crustal thickness distributions for the head-on (left) and 45°(right) classical cases, with a 40 km primordial crust and initial mantle fertility of 0.2. The upper and lower panels correspond to the mixed and stratified mantle models, respectively. The cyan contour line indicates ∼25% of primordial crust remaining, and displays the approximate transition at which primordial crust begins to contribute significantly to the post-impact crust distribution. The crust-production outside (north) of this contour is a result of a crossover region where significant melting occurs but primordial crust still remains, leading to a ridge of particularly thickened crust at the perimeter of the impact site. This effect is particularly visible in the 45°cases.

(i.e. without any primordial crust calculations), but with a reduced contrast between the thickened impact site and the mostly untouched remainder of the planet. One distinct feature that emerges, however, is a ridge of thickened crust along the perimeter of the impact site (particularly visible in the 45° case). This corresponds to a crossover region where the impact shockwave is still energetic enough to melt a significant volume of mantle, but no longer capable of excavating the primordial crust at the surface. This primordial crust material therefore acts to increase the fraction of crust-bearing material in the melt, resulting in a thin region of particularly thick crust that abruptly drops off as the impact-induced melt fraction falls to zero. In the fully stratified case, the impact features are sharper and more concentrated; the centre of the impact-site has been amplified to even larger crustal thicknesses, but this region is smaller than that of the fully-mixed scheme, with the outer regions showing little to no crustal thickening, even displaying a very thin dip in crustal thickness at the immediate edge of the impact-thickened region. The reason for this dip is two-fold: the primordial crust has been stripped from this region, and a significant fraction of the impact-induced melt corresponds to the fully-depleted mantle material, thus contributing less crustal mass as it re-crystalises. The increase in crustal thickness at the impact site is caused by the depleted material initially present in the region being both displaced and replaced by the fertile mantle material of the impactor. The crust-producing melt therefore originates almost entirely from fully fertile mantle, with a negligible contribution from depleted material (see Figure 5 for a visual representation of these effects in the head-on case).

The most significant variable in determining the precise impact-induced contrast in crustal thickness is the initial mantle fertility, β_0. This value relates to the silicate composition of Mars before crust-mantle differentiation (also known as the Bulk Silicate Mars or BSM). Higher values mean it is possible to produce more crust from a given mass of molten mantle. Lower values, on the other hand, lead to the contrary, with some parameters even producing an impact site with a lower crustal thickness than its surrounding area: an impact basin. For the same impact conditions, significantly different initial mantle fertilities can therefore imply very different crustal distributions, as illustrated in Figure 6.

4.2. Spherical Harmonic Analysis

Clearly, with so many significant variables, studying each case individually is not feasible when investigating such a large dataset, and is not particularly effective

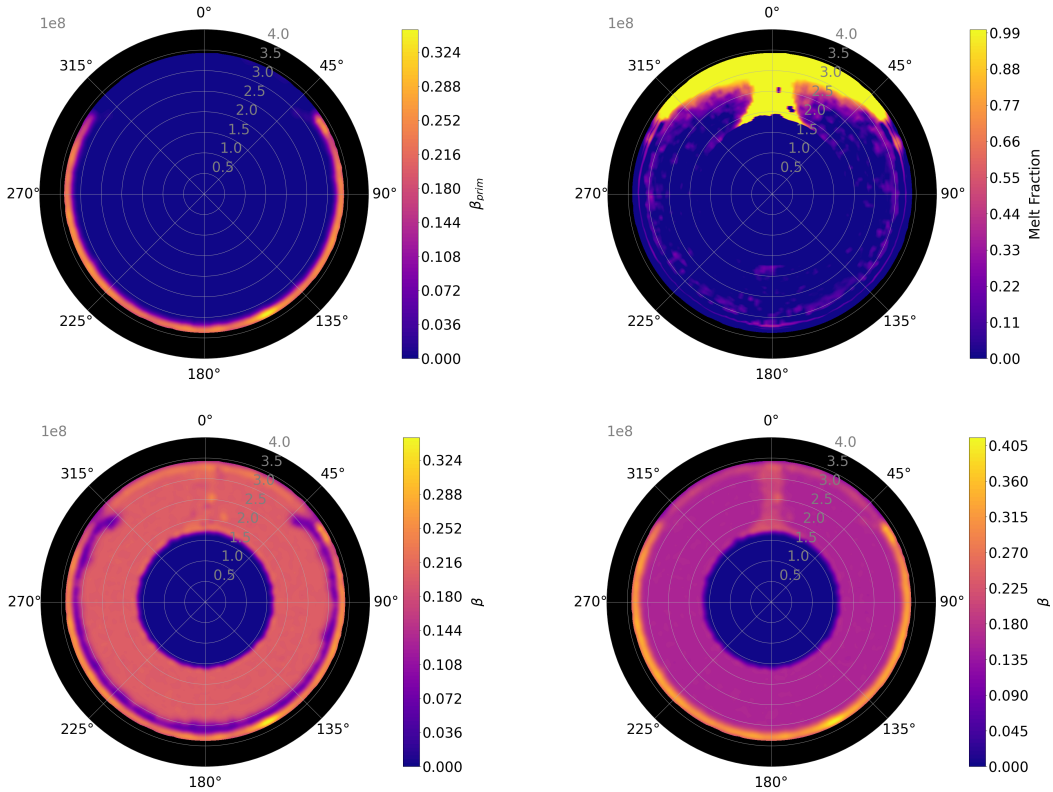

Figure 5: Various parameters related to our crust-production scheme displayed as a slice through the impact plane after the head-on classical impact with an initial fertility of $\beta_0 = 0.2$. The top row shows the crust contribution from primordial crust (left) and the melt fraction (right). The bottom row shows the fertility for the two mantle depletion schemes of fully-stratified (left) and fully-mixed (right).

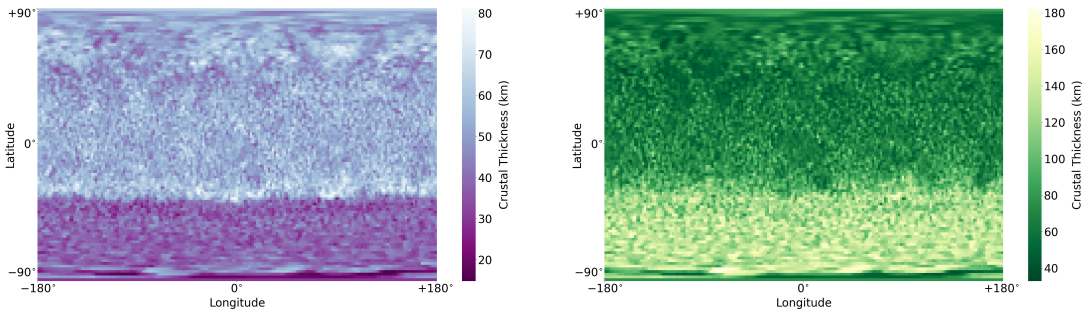

Figure 6: The crustal thickness distribution for the head-on classical case with a 40 km primordial crust and a initial mantle fertility of 0.10 (left) and 0.25 (right).

when only comparing "by eye" rather than through a quantitative, scientific method. To resolve these issues, we utilise spherical harmonic analysis as a means to compare our computed crustal thickness maps to the observationally inferred crustal thickness map of Mars.

Spherical harmonics are the natural basis functions for the surface of a sphere, allowing any quantity that varies across this surface to be expressed as a series of such functions, i.e.

$$f(\theta, \phi) = \sum_{l=0}^{\infty} \sum_{m=-1}^{l} f_{lm} Y_{lm}(\theta, \phi), \tag{19}$$

where θ is latitude, ϕ is longitude, l and m are the spherical harmonic degree and order, respectively, $f(\theta, \phi)$ is the varying quantity, f_{lm} is the spherical harmonic coefficient and Y_{lm} is the corresponding spherical harmonic function. The total power of $f(\theta, \phi)$ is usually defined as the integral of the function squared, divided by the area, Ω, of its domain[3]

$$\frac{1}{4\pi} \int_{\Omega} f^2(\theta, \phi) \, \mathrm{d}\Omega = \sum_{l=0}^{\infty} S(l), \tag{20}$$

where Parseval's theorem allows the total power to be expressed as a spectrum $S(l)$ related to the spherical harmonic coefficients by

$$S(l) = \sum_{m=-l}^{l} f_{lm}^2. \tag{21}$$

In this study, the varying quantity of interest is crustal thickness. Using the open-source SHTools Python library (Wieczorek & Meschede, 2018), we calculate the spherical harmonic coefficients for real, 4π-normalised spherical harmonic functions that can accurately represent each crustal thickness longitude-latitude map up to degree $l_{max} = 49$. Conveniently, the "power spectrum" defined in Equation 21 is independent of coordinate-system orientation, thus providing us with an ideal tool to compare each case regardless of the pole-axis location relative to the impact site (which may differ between each case due to the impact-induced rotation of the target).

For comparison with the crustal thickness inferred by observations of Mars, one must be wary of the many aeons that have passed since the crustal dichotomy's emplacement. Although Mars is considered to have a stagnant lid and to be mostly

[3]For any real, square-integrable function.

geologically inactive (particularly when compared to Earth), there have been several significant, subsequent alterations to the distribution of crust across the planet's history in certain regions (e.g. the Tharsis region or the Hellas basin). To compare our results with the crustal thickness as it would have been prior to these major geologic events, we use the data provided in Bouley et al. (2020), who developed a mass-conserving method to reconstruct the crustal thickness of Mars without the four largest impact basins (Hellas, Argyre, Isidis and Utopia) or the main volcanic provinces of Tharsis and Elysium, based on the crustal thickness model of Goossens et al. (2017). This data is converted to the same resolution as our grids via bivariate spline interpolation[4], the result of which is shown in Figure 7.

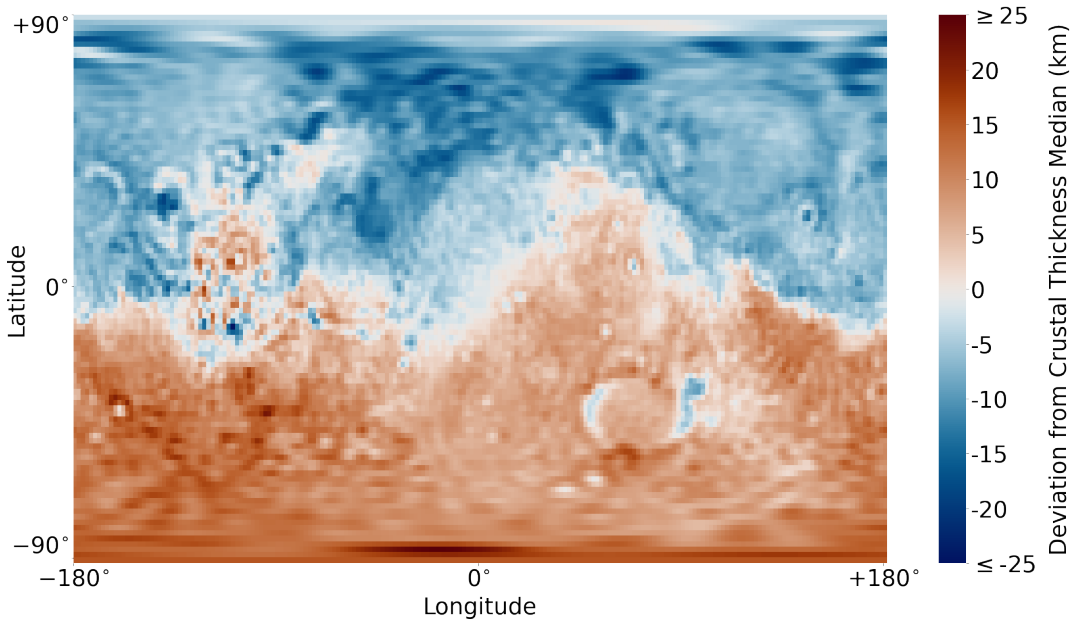

Figure 7: The crustal thickness distribution of Mars prior to any major geological events that occurred after the formation of the Martian Dichotomy, from Bouley et al. (2020). This map shows the exact distribution used to compare to our simulation results, and as such it has been converted to the spherical grid resolution used in our simulation analysis via bivariate spline interpolation, and is displayed through the equirectangular projection.

The power spectrum for this distribution is then calculated. Any differences between this spectrum and those of our impact simulations can be considered as deviations from the desired result. As such, we use the Euclidean norm of these

[4]We make use of the interpolate.RectSphereBivariateSpline function of SciPy Python library for this purpose (documentation at `https://docs.scipy.org/doc/scipy/reference/generated/scipy.interpolate.RectSphereBivariateSpline.html`)

differences as a measure of error

$$\delta_{SH} = \sqrt{\sum_{l=0}^{l_{max}} \left(S(l) - S_{\♂}(l)\right)^2}, \tag{22}$$

where $S_{\♂}(l)$ is the power spectrum related to the observed crustal thickness of Mars. It should be noted that the median crustal thickness of the Bouley et al. (2020) data is subtracted from each crustal thickness distribution before performing the spherical harmonic analysis.

Using this method, we can identify the most promising areas of the parameter-space as those with the lowest δ_{SH}. Conversely, a high δ_{SH} indicates a crust distribution that does not match well with observations, allowing us to rule out these cases as potential Dichotomy-forming events. A simple cutoff comes from the initial crust distributions on our pre-impact Mars. Using the same method as described, we can find a δ_{SH} corresponding to the distribution of crust on the pre-impact target for each primordial crust thickness investigated. The lowest of these values provides a maximum δ_{SH} cutoff for our final post-impact crust distributions, $\delta_{SH_{max}}$, as a greater value indicates that a uniform crust distribution better fits the observed data, thus implying no measurable gain from the impact.

4.2.1. Impact Angle and Impactor Radius

Applying this logic to the our entire parameter-space leads to the exclusion of many cases. In particular, a clear trend related to impactor radius is revealed, with a larger impactor indicating a lower number of feasible cases (Figure 8). This trend is still evident if we only consider those with a δ_{SH} below the first quartile of such cases, where the 1500 km and 2000 km radius impactors only represent 20 of the 169 remaining cases. If we focus on cases below the 5th percentile, however, the 750 km impactor proves to represent the most promising simulations, outnumbering the remaining 500 km and 1000 km impactor cases 22 to 12.

Understanding this trend requires further investigation through the inclusion of other physical parameters. Figure 9 again shows the distribution of cases with a δ_{SH} lower than the best pre-impact case, but now as a function of impact angle, divided into the two mantle depletion methods. Here we see that the large impactors only produced relevant cases with highly oblique impact angles, with 75° and 90° being the best impact angles for the 1500 km and 2000 km radius impactors respectively. This is to be expected if they are systematically producing too much crust (and

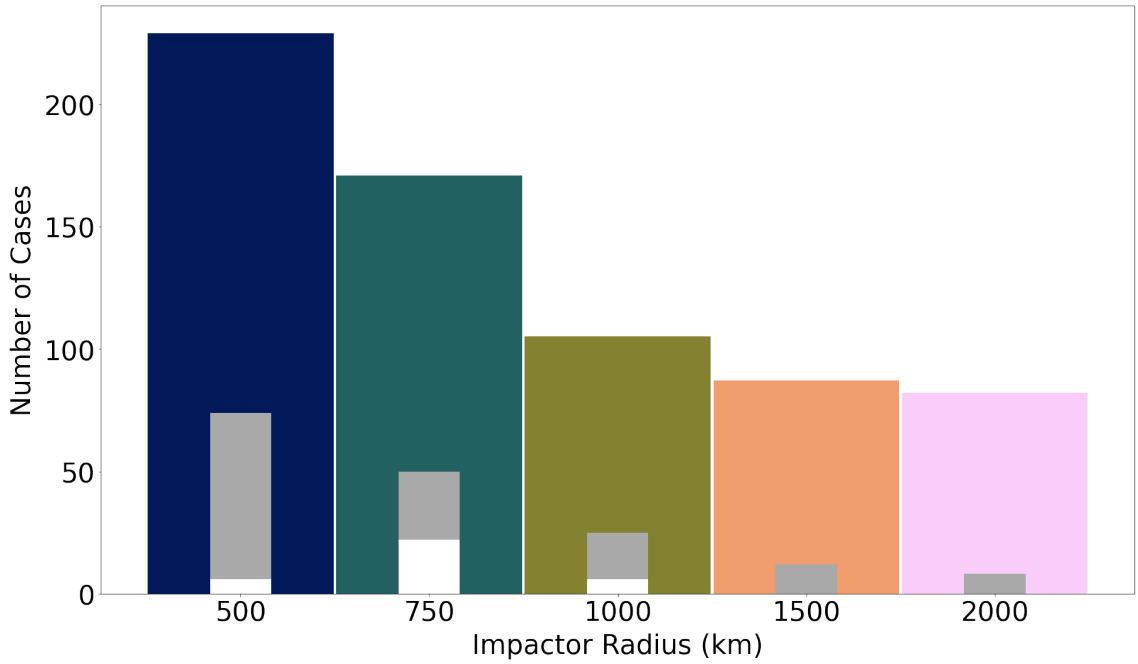

Figure 8: Histogram of cases within $\delta_{SH_{max}}$ for each impactor radius. The grey and white bars represent those within first quartile and 5th percentile of such cases, respectively.

thus melt), as higher impact angles mean more energy is carried away as ejecta or converted into target rotation rather than impact heating.

For the smaller impactors (radii of 500-1000 km) the trend is less clear and, interestingly, significantly changes as we again restrict our cases to those below certain percentile thresholds, as well as when comparing the results of the two mantle depletion schemes. When including all cases with $\delta_{SH} < \delta_{SH_{max}}$, there is a positive trend towards larger impact angles for all radii, culminating in a peak at 60° impact angle that drops off for higher angles. For cases within the first quartile, however, this peak is no longer apparent, with almost all 60° cases being excluded for the fully-mixed mantle depletion model. As we restrict further to cases within the 5th percentile, a clear trend emerges for each depletion scheme, with the fully-mixed model favouring lower impact angles, and the fully-stratified model favouring higher impact angles up to a maximum of 45° (Figure 10). The preference for near head-on impact angles in the fully-mixed model makes intuitive sense, as lower angles lead to a more distinct hemispherical contrast, reducing both the ellipticity of the impact site and the prominence iso-longitudinal ring of re-impacting ejecta. The positive trend in the fully-stratified model, on the other hand, is a consequence of the crustal thickness dip along the perimeter of the impact site (as described in Section 4.1), which causes a strong signal in the spherical harmonic analysis. At larger impact

angles this feature becomes obscured, thus leading to a smaller δ_{SH} and giving rise to the trend observed.

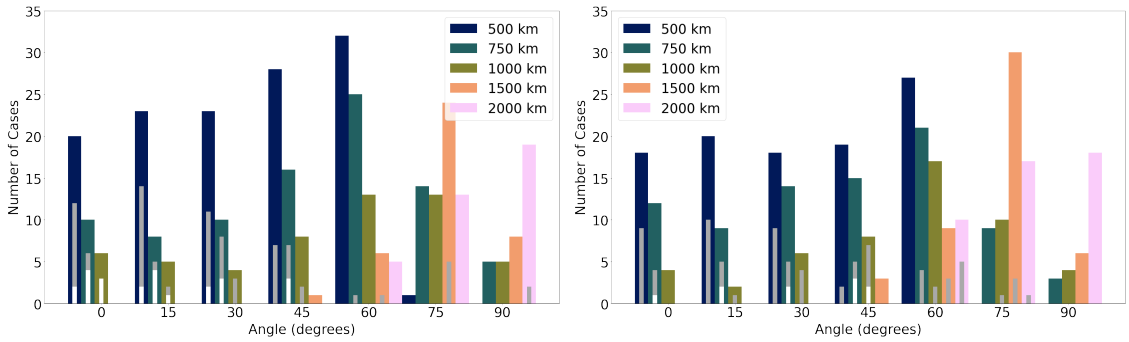

Figure 9: Histogram of cases within $\delta_{SH_{max}}$ for each impactor radius as a function of impact angle for the fully-mixed (left) and fully-stratified (right) mantle depletion schemes. The grey and white bars represent those within first quartile and 5th percentile of such cases, respectively.

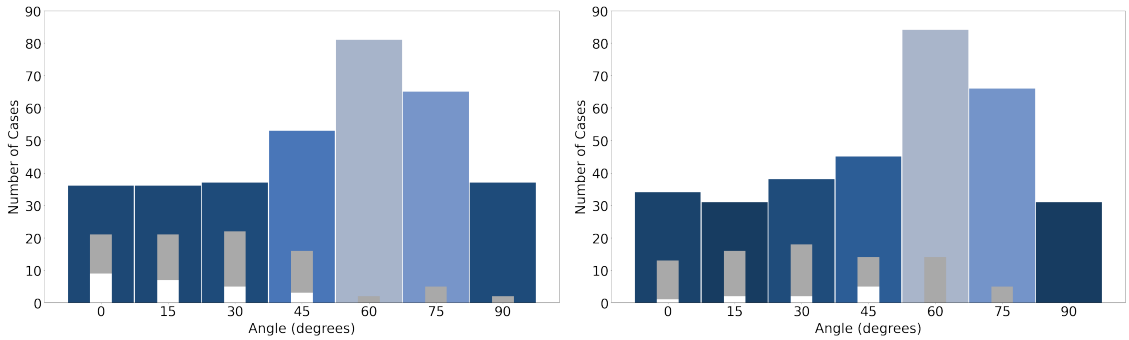

Figure 10: Histogram of cases within $\delta_{SH_{max}}$ summed across all impactor radius as a function of impact angle for the fully-mixed (left) and fully-stratified (right) mantle depletion schemes.

4.2.2. Mantle Fertility

Figure 11 shows the distribution of our cases of interest ($\delta_{SH} < \delta_{SH_{max}}$) as a function of β_0. Here, we see a strong preference for a smaller β_0, with the majority of cases within the 5th percentile corresponding to the smallest value investigated (0.1). As we look to different impactor radii, however, the dominant β_0 changes. At 1000 km radius the general trend is reflected well, with 84% (21/25) of such cases within 1st quartile corresponding to lowest fertility (0.1), and all within the 5th percentile. This value remains the most represented fertility in the 750 km case, but only by a small margin, with a fertility of 0.125 also producing a large number of promising cases. For a 500 km impactor, we find that a higher fertility of 0.15 produces the most cases of interest, particularly when we only consider cases within the 5th percentile. The largest impactors (1500 km and 2000 km) do not show any significant preference for a certain fertility.

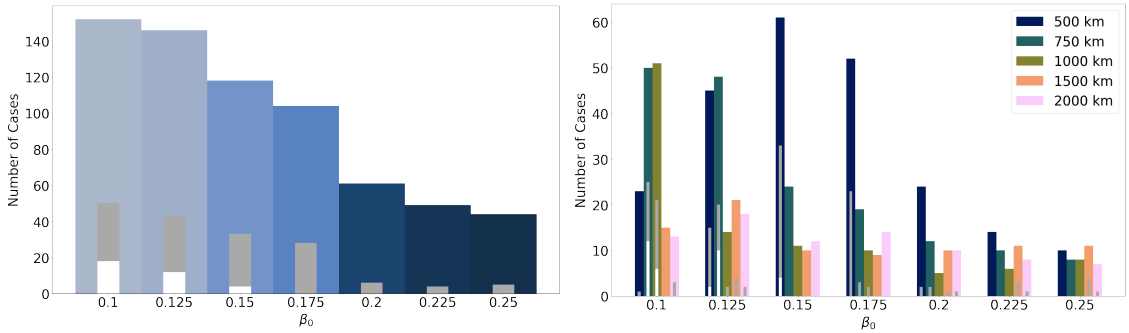

Figure 11: Histogram of cases within $\delta_{SH_{max}}$ for all impactor radius as a function of initial, pre-impact fertility β_0 either summed across all radii (left) or with each radius as a separate colour (right). The grey and white bars represent those within first quartile and 5th percentile of such cases, respectively.

4.2.3. Impact Velocity

As visible in Figure 12, the smaller impactors (radii $\leq$ 1000 km) that represent the best cases do not show any strong preference in impact velocity, other than a slight trend towards higher values for cases within the 5th percentile, which disfavour the mutual escape speed cases in particular. For the larger impactors, this preference is far more significant, with almost no mutual escape speed cases surviving our $\delta_{SH_{max}}$ threshold. Without further information from other parameters, this trend seemingly contradicts the intuition that larger impactors that systematically induce too much crust production (due to excessive impact-induced melt) should favour the less energetic, lower impact velocities in producing the best matches to the Dichotomy. As discussed in Section 4.2.1, however, the large impactor cases strongly favour high impact angles. The combination of high velocities at very oblique angles lead to grazing collisions in which the impactor retains enough kinetic energy to remain gravitationally unbound to the target-impactor system and continue on its hyperbolic path relatively unimpeded (a scenario known as "hit-and-run"). It is this regime that produces the best cases for our largest impactors.

4.2.4. Primordial Crust Thickness

Figure 13 illustrates the influence of primordial thickness in producing a Dichotomy-like crust distribution. If we include all cases below our minimum threshold of $\delta_{SH_{max}}$, a clear peak emerges in all impactor radii for a 40 km crust prior to impact. For cases below the first quartile and/or the 5th percentile thresholds, however, distinct preferences appear. The 1000 km impactor produced most of its sub-quartile cases with a 25 km primordial crust, although the majority of its cases within the 5th

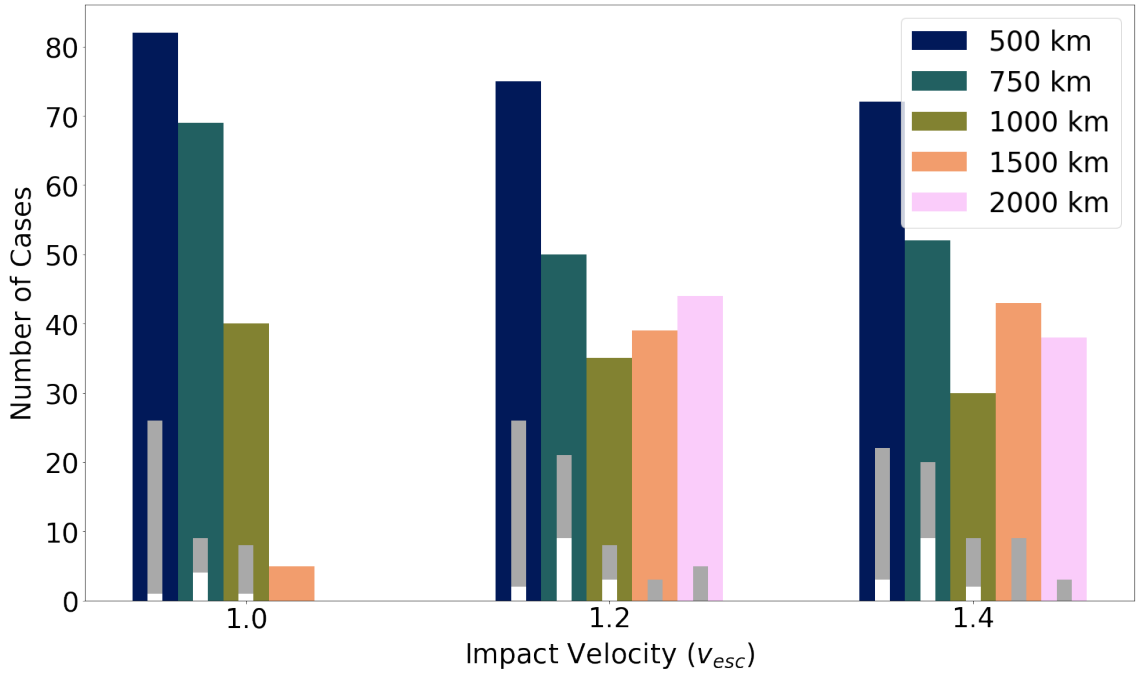

Figure 12: Histogram of cases within $\delta_{SH_{max}}$ for each impactor radius as a function of impact velocity. The grey and white bars represent those within first quartile and 5th percentile of such cases, respectively.

percentile came instead from a 10 km crust, being the sole impactor radius with any significant cases associated with such a thin pre-impact crust. The 750 km impactor shows a strong preference for a 25 km crust in its best cases, with almost all of its sub-quartile cases corresponding to this thickness. The 500 km impactor has a very strong preference for the 40 km primordial crust thickness within all δ_{SH} thresholds. The largest impactors do not show a strong preference for a single thickness within the first quartile, with a near-equal number of cases being represented by the 25 km and 40 km crustal thicknesses, and even some 55 km cases with $\delta_{SH} < \delta_{SH_{max}}$.

4.2.5. Mantle Depletion Scheme and Core Fraction

When comparing the two mantle depletion schemes for cases with δ_{SH} within $\delta_{SH_{max}}$, we see a very small preference for the fully-mixed approach over the stratified (345 compared to 329 cases, respectively). If we look at the distribution of these cases within the first quartile, however, we see that the majority of the best cases correspond to the fully-mixed cases, with this imbalance between the two schemes evening out at higher δ_{SH} (Figure 14). Although there appears to be a preference for the 50% core fraction for the very best cases (8 out the 10 best-fitting cases have this core fraction), this trend quickly disappears, even switching to a minor excess in 35% cases (91 against 78 50% core fraction cases within the first quartile).

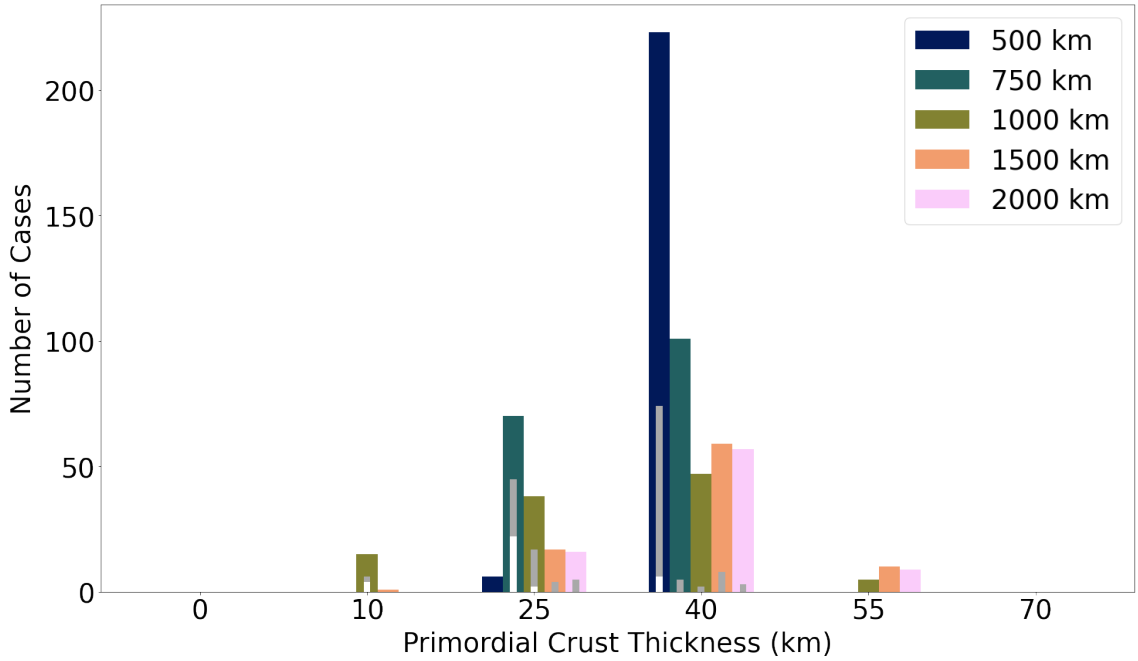

Figure 13: Histogram of cases within $\delta_{SH_{max}}$ for each impactor radius as a function of primordial crust thickness. The grey and white bars represent those within first quartile and 5th percentile of such cases, respectively.

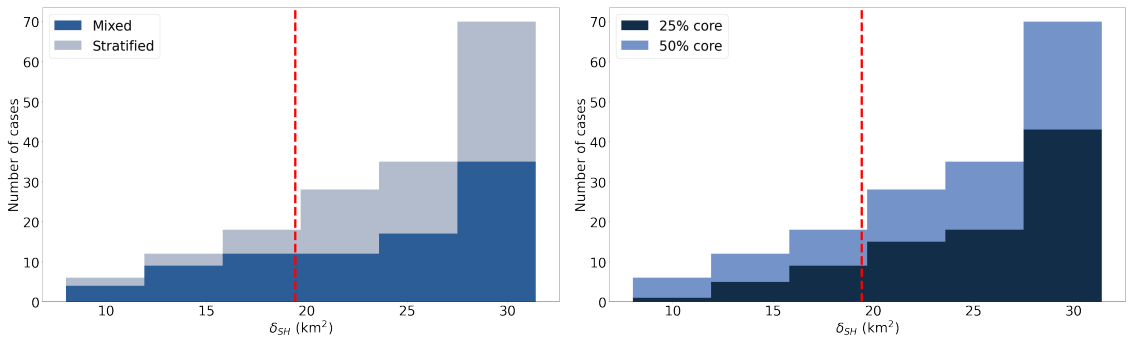

Figure 14: Cases within the 1st quartile of cases with $\delta_{SH} < \delta_{SH_{max}}$ for the two mantle depletion schemes (left) and the two impactor core fractions (right). The red line depicts the 5th percentile of cases with $\delta_{SH} < \delta_{SH_{max}}$.

4.3. Best Cases

As illustrated in Figure 15, the majority of the best cases (i.e. those within the 5th percentile) are associated with a 750 km radius impactor, including our best fit to the Martian Dichotomy data. All impactor radii are represented at least by some cases within the first quartile, however. We will therefore use this section to clarify the conditions necessary for the best fitting cases in the context of each impactor radius.

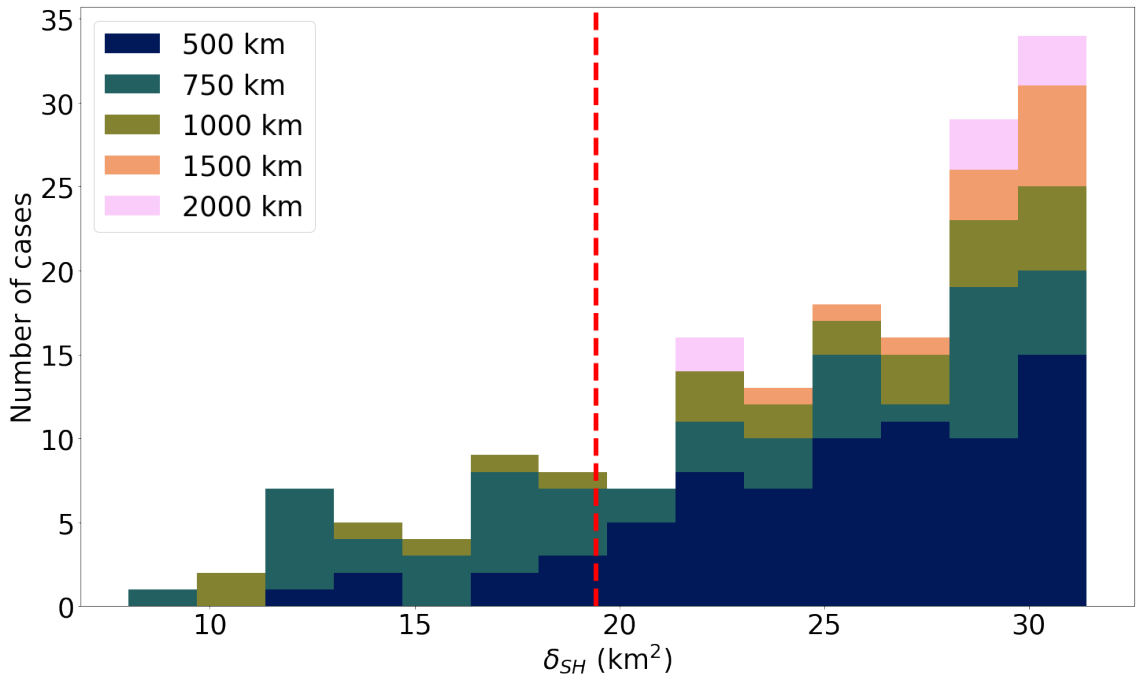

Figure 15: Cases within the 1st quartile of cases with $\delta_{SH} < \delta_{SH_{max}}$ where colour depicts impactor radius. The red line depicts the 5th percentile of cases with $\delta_{SH} < \delta_{SH_{max}}$.

4.3.1. The largest impactors (1500 km and 2000 km)

Although there are no cases within the 5th percentile for the largest impactor radii of 1500 km and 2000 km, there are 20 cases within the first quartile, the top 5 of which stand out as the best cases with significantly lower δ_{SH}, particularly for those of the 2000 km radius impactor (Figure 15). All of these cases have an impact angle of 60° and an impact velocity that is greater than mutual escape, placing them in the "hit-and-run" regime, and giving them a very similar crust distribution. This consists of an elongated ellipse at the immediate grazing impact site along with a ring of re-impacting material in the impact plane that results in an iso-longitudinal band of thickened crust antipodal to the main site (Figure 16).

All of these cases also correspond to a 25 km primordial crust, and interestingly, the stratified mantle depletion scheme. This is due to a large portion of the crust-production from the re-impacting material corresponding to melt within the depleted layer (as the melt is only present at relatively shallow depths compared to more head-on, merging collisions). The unwanted iso-longitudinal band of crust is therefore greatly reduced in the stratified scheme when compared to the mixed scheme (C.23). Additionally, the lack of deep melt also reduces the effect of the crustal thickness dip associated with the stratified scheme (introduced in Section 4.1), as this corresponds to concentrated areas of depleted mantle at the perimeter of the impact site that have been forced to lower depths (see 5). These cases also correspond to a low fertility of either $\beta_0 = 0.125$ for the 1500 km impactor or $\beta_0 = 0.1$ for the 2000 km impactor.

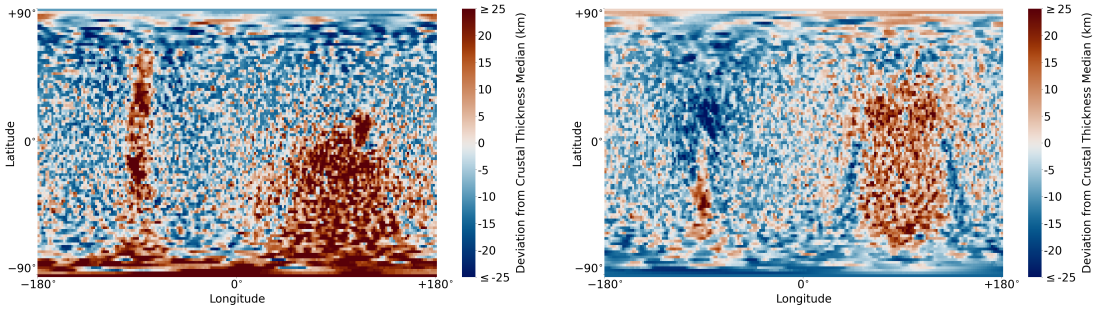

Figure 16: Equirectangular projection of post-impact crustal thickness for the best-fitting cases of the 1500 km-radius (left) and 2000 km-radius (right) impactors. The median crustal thickness of the Bouley et al. (2020) distribution has been subtracted for easy comparison to Figure 7. Both of these cases correspond to a 50% impactor core fraction, 1.2 v_{esc} impact velocity, 60° impact angle, the fully-stratified depletion scheme and a 25 km primordial crust, but differ in their initial mantle fertilities of 0.125 (left) and 0.1 (right).

4.3.2. 1000 km Impactor

While there are fewer 1000 km impactor cases within the 5th percentile than that of the 500 km or 750 km impactors, they represent some of the best-fitting cases of our entire parameter space. Two cases stand out in particular, with our spherical harmonic analysis placing them as the second and third best fits overall (Figure 17). Both of these cases require the lowest fertility of $\beta_0 = 0.1$; however, their other parameters differ greatly. The most important difference is the impact angle, with the lowest δ_{SH} case having a 45° angle, while the other is head-on (0°). Although the two cases differ in their deviation from the Martian Dichotomy (the

45° case is too non-uniform while the head-on case produces too much antipodal crust), a clear issue in both cases is a crustal thickness contrast between the two hemispheres that is too large. This is a trend across all 1000 km cases, and explains their low representation within the 5th percentile as they only give a reasonable match to the Dichotomy with highly specific parameters.

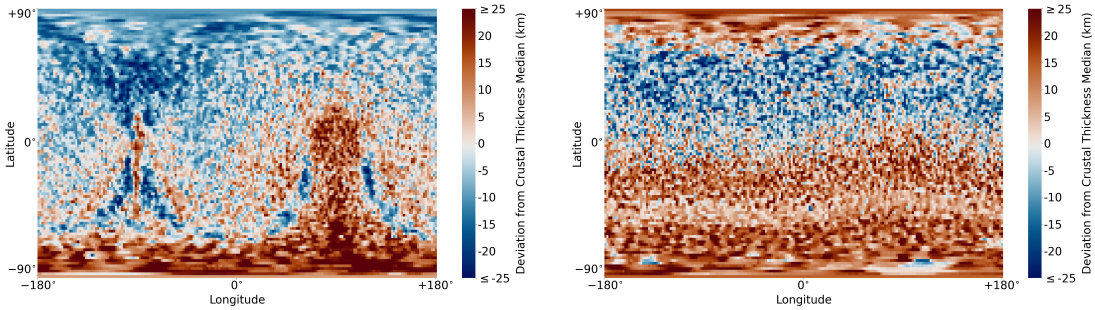

Figure 17: Equirectangular projection of post-impact crustal thickness for the first (left) and second (right) best-fitting cases of the 1000 km radius impactor. The median crustal thickness of the Bouley et al. (2020) distribution has been subtracted for easy comparison to Figure 7. The corresponding parameters for these cases are: (left) 1000 km radius, 50% impactor core fraction, 1.0 v_{esc} impact velocity, 45° impact angle, fully-stratified depletion scheme, 25 km primordial crust and 0.1 initial mantle fertility; and (right) 1000 km radius, 50% impactor core fraction, 1.4 v_{esc} impact velocity, 0° impact angle, fully-mixed depletion scheme, 10 km primordial crust and 0.1 initial mantle fertility.

4.3.3. 500 km Impactor

As noted in Section 4.2.1, the 500 km-radius impactor represents the most cases within the first quartile (44%), yet only 18% of those within the 5th percentile. If we look at the best case for this radius (and 7th best-fitting across all radii), we see that the average crustal thickness in each hemisphere is a much closer fit than the cases previously discussed (Figure 18, left). In comparison to the lower δ_{SH} 1000 km impactor cases of Figure 17, however, the region of impact-induced crust falls significantly short of the equator. Additionally, the effects associated with crustal stripping at the impact site are greatly amplified, with the fully-mixed scheme leading to a sharp band of thickened crust where significant melt is present beneath un-excavated crust, while the stratified scheme leads to a band of crust with a thickness below pre-impact values where crust has been stripped and the impact-induced melt lies predominantly in the depleted mantle layer. The underlying cause of these effects being more significant in the 500 km cases compared to the large impactors also accounts for the smaller contrast between the two hemispheres: the

impact-induced melt only reaches to relatively low depths, meaning crust-production is reduced overall but any remaining primordial crust represents a larger fraction of the crust-producing melt.

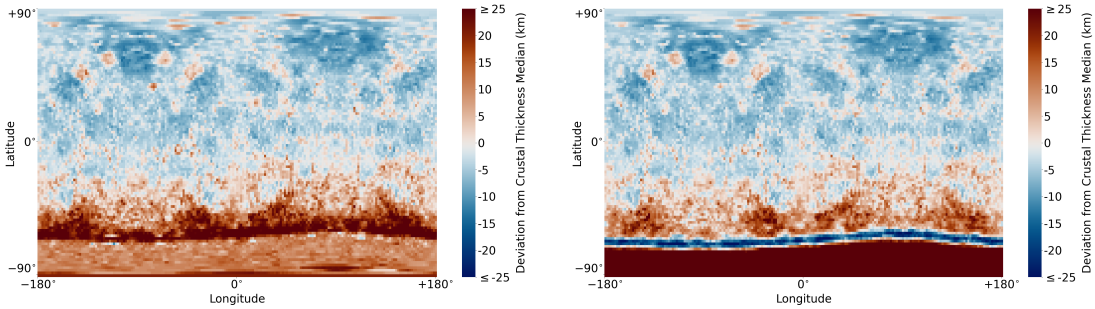

Figure 18: Equirectangular projection of post-impact crustal thickness for the best-fitting case of the 500 km radius impactor (left) and the equivalent case but with the fully-stratified scheme instead (right). The median crustal thickness of the Bouley et al. (2020) distribution has been subtracted for easy comparison to Figure 7. The corresponding parameters for these cases are: 500 km radius, 25% impactor core fraction, 1.4 v_{esc} impact velocity, 0° impact angle, 40 km primordial crust and 0.125 initial mantle fertility. The case using the stratified mantle depletion scheme is the 35th best-fitting case overall (the 5th percentile corresponds to 34th best case).

4.3.4. 750 km Impactor

The overwhelming majority of the best-fitting cases come from the 750 km impactor (65% of those within the 5th percentile, see 15), including the best case overall (Figure 19). After reviewing the drawbacks of both the 500 km and 1000 km impactors this comes as no surprise; the impactor is large enough to produce crust close to (or sometimes beyond) the equator at low impact angles, while being small enough to avoid excessive crust-production and/or strong antipodal effects. Impact melting is still increased relative to 500 km cases, however, pushing the best cases to the lowest fertilities and a primordial crust thickness of 25 km.

Although there are cases with impact angles ranging from 0° to 45° within the 5th percentile, the head-on impacts fall short of the very best-fitting cases (the best head-on fit is only the 17th best-fitting case overall). Similar to the 500 km cases, the head-on cases suffer from an inability to produce melt all the way to the Martian equator. In addition, the oblique cases produce a closer match to the equator-crossing regions of the southern highlands north of the Hellas basin such as Terra Sabaea. The signal of this feature in the spherical harmonic analysis is strong, causing some cases to yield low δ_{SH} values with a visibly incorrect fit for large fractions of the Martian surface. The 45° cases suffer from this effect in

particular, displaying significant iso-longitudinal bands of thickened crust from re-impacting ejecta yet corresponding with some of the lowest δ_{SH} values of the entire parameter space due to their reasonable match with the region described. Such a distinct feature would probably be visible today, making the 45° cases difficult to justify as potential Dichotomy-forming impacts.

The best case has an impact velocity of 1.4 times the mutual escape speed, and the top cases are shared between between cases with impact velocities of 1.2 v_{esc} and 1.4 v_{esc}. 1.2 v_{esc} cases are still represented within the 5th percentile; however, it is clear that they do not have enough kinetic energy to produce the required area of melt.

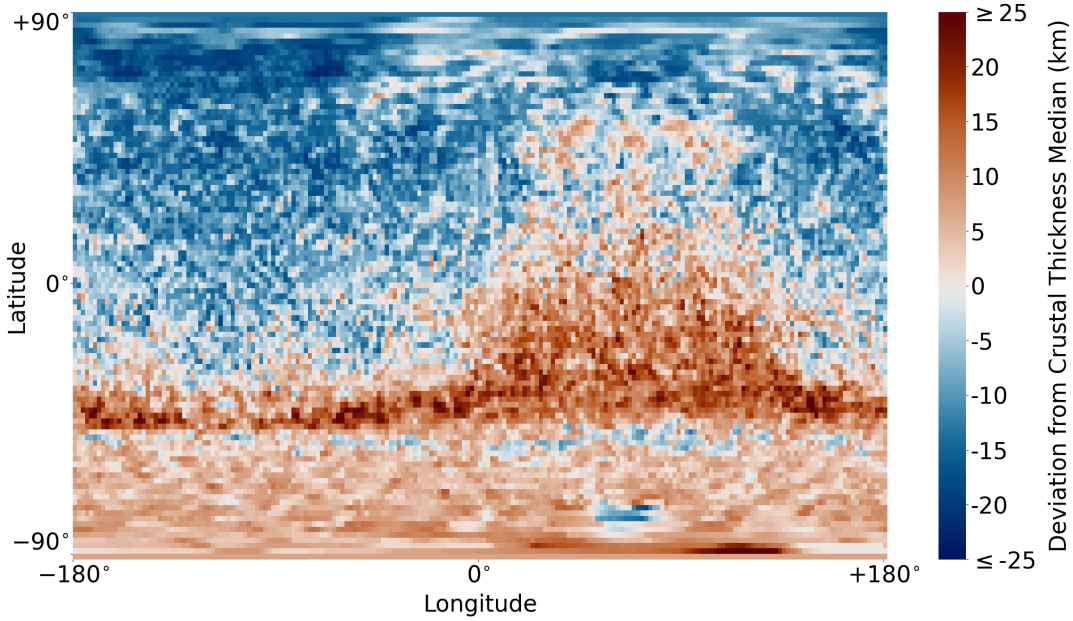

Figure 19: Equirectangular projection of post-impact crustal thickness for the best-fitting case of the 750 km radius impactor and the best-fitting case overall. The median crustal thickness of the Bouley et al. (2020) distribution has been subtracted for easy comparison to Figure 7. The specific parameters of this case are: 750 km radius, 25% impactor core fraction, 1.4 v_{esc} impact velocity, 15° impact angle, 25 km primordial crust and 0.1 initial mantle fertility.

4.4. Northern Excavation

The spherical harmonic analysis did not identify any Dichotomy-like cases that resulted in a thinner crust within the impact site than outside of it. The only cases with $\delta_{SH} < \delta_{SH_{max}}$ corresponding to such a distribution are a handful of highly oblique, high velocity hit-and-run impacts with the largest impactors; however, these produce basins that are far too small in comparison to the northern depression of

Mars. This issue of an undersized impact basin is widespread across our parameter space. Even at our largest impactor radii, the region of excavated crust falls short of the Dichotomy boundary. In addition, such energetic collisions cause strong antipodal effects not seen in Mars' southern hemisphere today (Figure 20). These effects result from the impact-induced shockwave travelling through the planet until converging at the antipodal free-surface boundary, leading to significant disruption of this antipodal material. If the antipodal stresses are greater than the tensile strength of the material then fracturing will occur (Schultz & Gault, 1975), and for planetary-scale impacts the shock is energetic enough to excavate the antipodal material. In our simulations, these effects result in a crustal thickness of this antipodal region that is lower than that of the impact site, as the crust is entirely excavated but with far less melt. As expected, these cases require the lowest fertility ($\beta_0 = 0.1$) to avoid too much crust production at the impact site; however, further depletion through primordial crust formation is necessary to reduce impact-induced thickness to the desired range. This additional mantle depletion causes a trend in crustal thickness distribution, whereby larger primordial thicknesses lead to deeper impact basins, due to both reduced crust-production at the impact site and a thicker pre-impact crust. This therefore pushes the northern excavation scenario to larger primordial crust thicknesses which, with the addition of any global interior melting caused by the impact shockwave, result in a crust outside the impact site that is significantly too thick.

5. Discussion

5.1. Borealis Basin or Southern Magma Ocean?

A clear result of this work is a lack of support for the Martian Dichotomy to have formed through the canonical northern impact basin hypothesis (the so-called "Borealis Basin"), contrary to previous works (Marinova et al., 2008; Andrews-Hanna et al., 2008; Nimmo et al., 2008; Marinova et al., 2011). We attribute our alternative findings to our method of crust-production calculation, which uses separate solidus and liquidus models relevant for Martian mantle to quantify melt along with a modern estimate of crustal density (see Section 2.2), rather than a simplified approach based on internal energy and/or pressure limits. We also use the more sophisticated ANEOS equation of state than the Tillotson (1962) semi-empirical formula used in previous studies, and include material strength in our models which we show to be

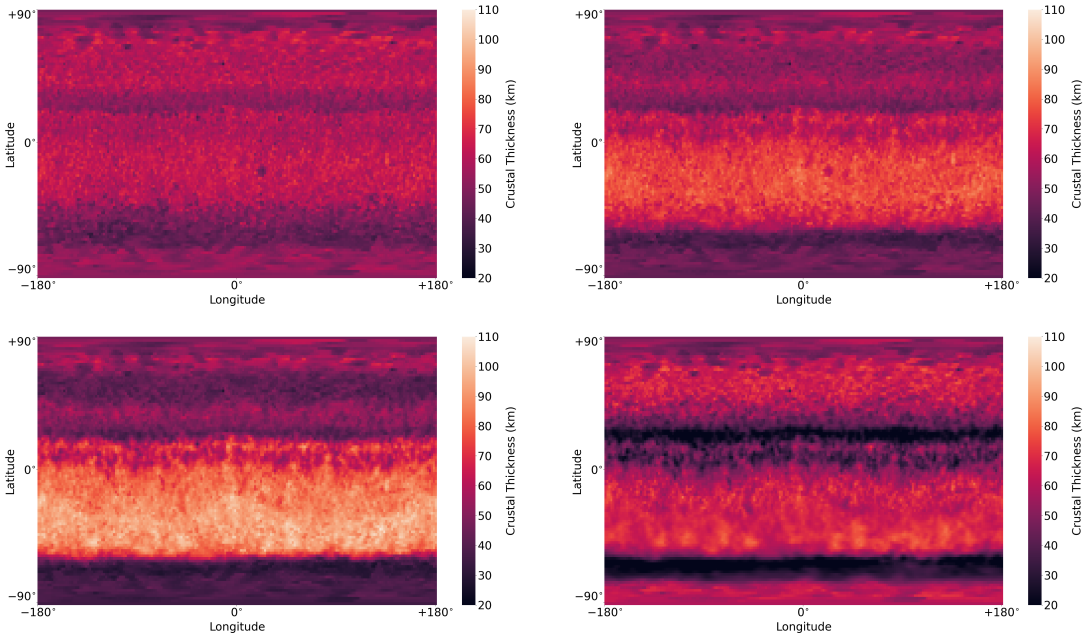

Figure 20: Equirectangular projection of post-impact crustal thickness for an example northern excavation case. The top row shows this case with a 10 km (left) and a 25 km (right) primordial crust thickness using the fully-mixed mantle depletion scheme. The bottom row shows this case with a 40 km primordial crust thickness for the fully-mixed (left) and fully-stratified (right) mantle depletion schemes. The other parameters are: 1500 km radius, 25% impactor core fraction, 1.0 v_{esc} impact velocity, 0° impact angle and 0.1 initial mantle fertility. The orientation of the projection has been inverted compared to the other crustal thickness maps of this study such that the impact occurred in the northern hemisphere, as to represent the "Borealis Basin" hypothesis for the Martian Dichotomy.

important on these scales. Furthermore, we employed a more sophisticated model of primordial crust than that of previous work. These differences lead to our results yielding much more significant crustal thickening from the impact, largely due to more widespread melt. One possibility that could reduce the prominence of this effect is that Mars was far colder than considered in this study prior to the impact, with interior temperatures significantly below the solidus temperature. Additional cooling time may be permitted if the Martian magma ocean crystallised extremely rapidly within 20 Myr after Solar System formation, as suggested by the radiometric dating of martian meteorite zircons (Bouvier et al., 2018). For efficient cooling to occur, however, Mars would need an alternative tectonic regime to its current insulating stagnant lid, such as plate tectonics (Breuer & Spohn, 2003). However, there is no strong evidence for a plate tectonics episode on early Mars (Pruis & Tanaka, 1995; Zuber, 2001; Halliday et al., 2001). Moreover, the precise time of Martian magma ocean crystallisation remains a topic of debate, with several studies proposing significantly longer timescales (e.g. Borg et al., 2016; Debaille et al., 2007; Kruijer et al., 2017, 2020). Alternatively, Mars may have started cool from birth if it formed predominantly via "pebble accretion" rather than more traditional planetesimal accretion-based methods (Johansen et al., 2021); however, this may prohibit any silicate melting, making planetary differentiation and primordial crust formation difficult.

The excavation of crust antipodal to the impact site associated with our basin-forming impacts is an aspect that is particularly difficult to reconcile with present day observations. If the northern hemisphere truly is the result of such an impact, an extremely deep canyon should be present near the Martian south pole, which is clearly not the case. Although the presence of solid strength in our model does act to reduce antipodal effects, the crustal stripping remains prominent. With all these considerations in mind, we consider the Borealis Basin case very unlikely.

5.2. An HPE-induced Crustal Dichotomy

Citron et al. (2018) suggested that the Martian Dichotomy may have been caused by a giant impact in the north that led to degree-1 mantle convection with an upwelling beneath the southern hemisphere, antipodal to the impact site. This results from heat-producing elements (HPE) expected to be concentrated in a primordial crust (Elkins-Tanton et al., 2003, 2005) being stripped from the impact site, leading to a southern hemisphere crust that is both enriched in HPE and thicker than

its northern counterpart. The insulating effect of these properties would cause a temperature increase in the mantle below the southern highlands, causing the aforementioned upwelling and subsequent crust-production in the southern hemisphere. Such a scenario relies upon the same assumptions as a Borealis-forming impact: crustal excavation of the entire northern lowlands region with very little melt and thus crust-production at the impact site. For the same reasons detailed in Section 5.1, therefore, our results do not support this hypothesis.

5.3. Explaining low fertility

At all impactor radii in our model, the best cases have Martian bulk silicate fertilities of 0.1-0.125. These values are significantly lower than that of the bulk silicate Earth which, if we use the pyroxene fraction as a proxy for potential crust fraction due to its prominence as the main component of a basaltic to andesitic crust, is predicted to be ~ 0.2 (Mckenzie & Bickle, 1988). Predictions for the bulk silicate composition of Mars are consistently different to those of Earth (Taylor, 2013; Yoshizaki & McDonough, 2020, and references therein), but whether these differences could account for such a lower crust-production budget is unclear. Some effects during magma ocean crystallisation not included in our simplified model may reduce crust-production efficiency, such as permeability barriers (Schools & Montési, 2018); however, these effects are generally only significant at lower melt fractions than those associated with this study.

One effect that may be of significance is the tendency for iron-enriched cumulates to solidify last during magma ocean solidification (Elkins-Tanton et al., 2003, 2005). As the mantle liquidus is steeper than its adiabat, the magma ocean should freeze "bottom-up" with lower depths solidifying first (e.g. Abe, 1997). This therefore leads to a compositional gradient of increasing iron-enrichment and hence density towards the surface; a gravitationally unstable configuration susceptible to Rayleigh-Taylor overturns that may drive much of this material down into the deep mantle (Samuel et al., 2021; Boukaré et al., 2018; Ballmer et al., 2017), thus removing a significant portion of crustal material. Whether or not a magma ocean would truly solidify in this way is a matter of debate, however, with various studies suggesting that magma oceans may in fact freeze "middle-out" whereby intermediate depths solidify first, creating an expanding solid region between two simultaneously-crystallising magma oceans (Caracas et al., 2019; Labrosse et al., 2007; Nomura et al., 2011), although such studies generally consider depths (and thus pressures) much greater than those

of Mars. Moreover, the hot material that would rise from depth during such an overturn may experience melting due to adiabatic decompression (Elkins-Tanton et al., 2003), making it difficult to estimate the final influence of this phenomenon on our results.

5.4. Primordial crust thickness

The most promising primordial crust thickness in this study was found to be 25 km; however, reasonable fits were still found with 10 km and 40 km thicknesses, depending on the impactor radius. Thicknesses of 55 km and above, however, did not yield any cases of interest. These findings agree with geochemical analyses of martian meteorites, which place an upper limit of $\sim$ 45 km (Norman, 1999), and suggest a most probable value of 20-30 km which matches with geophysical models (Morschhauser et al., 2011). A primary crust as thin as 10 km may be difficult to justify; however, all cases of interest with such a crust correspond to the 1000 km-radius impactor, which still result in far too much crust at the impact site (and often its antipode) and can likely be ruled out (as discussed in Section 4.3.2).

5.5. Additional features of the simulations

Strong antipodal effects are not the only features present in some of our best-fitting cases that may be difficult to reconcile with observational knowledge of Mars. In all of our 45° cases, for instance, we find a strong band of thickened crust that forms an iso-longitudinal ring of thickened crust in the impact plane around the target body; something not seen on Mars today. However, as our crust-production model is based on the immediate position of post-impact melt and is unable to simulate smaller-scale spreading at the surface that would occur over longer timescales, such a sharp feature may relax into a much shallower region that covers a large area in reality. The extent of this spreading is strongly dependent on post-impact topography, however, and our simulations display significant excavation in these regions due to the re-impacting material (Appendix C). Thus, the majority of this melt should be contained within this excavated valley until crystallisation ultimately freezes the feature's morphology to the present day. Considering Mars' low level of resurfacing due to its lack of tectonic activity, we therefore consider such cases to be highly unlikely candidates for the Dichotomy-forming impact.

Another feature that is present in almost all of our cases, and particularly those using the fully-mixed mantle depletion scheme, is a thickened band of crust at the

perimeter of the impact site. As described in Section 4.1, this is caused by a crossover region whereby the impact shockwave is no longer energetic enough to strip the region of crust, but is still capable of non-negligible melting, thus resulting in a region that receives crust contributions from both the undisturbed primordial crust and any melting of the mantle below. Unlike the iso-longitudinal rings, the spreading of this melt as it cools would likely be very important in determining the final distribution of crust. With little excavation, there is no reason to think that this melt would remain contained to its immediate longitude-latitude coordinates and would likely spread out considerably across the surface, leading to a much weaker feature in the final crust distribution. This impact-perimeter thickening is most prevalent in the 500 km-radius impactor cases, and such melt-spreading may in fact improve their likelihood in explaining the Dichotomy, as they all suffer from an impact site that is too small, but may increase in size considerably if such spreading was accounted for. On the other hand, cases that under-produced melt, such as many of the 500 km cases with the lowest fertility, would experience even thinner crusts than predicted here, making them unlikely candidates.

5.6. Depletion schemes

The nature of Mars' mantle differentiation is still under scientific debate. Unlike Earth or the Moon, ancient chemical heterogeneities are preserved within Mars' mantle which provide evidence for both the presence of an early magma ocean phase and a lack of vigorous whole mantle convection and/or active plate tectonics, although some degree of mixing through convection immediately after the magma ocean stage is likely (Mezger et al., 2013, and references therein). The depth of the magma ocean during this phase is unclear, with estimates ranging from 700 km to the entire mantle down to the core-mantle boundary (e.g. Righter et al., 1998; Righter & Chabot, 2011; Debaille et al., 2008; Elkins-Tanton et al., 2003, 2005); however, a fully molten mantle is not consistent with with observed depletions of moderately siderophile elements (Mezger et al., 2013; Righter & Chabot, 2011). A relatively shallow magma ocean and lack of whole mantle convection implies that stratification within the Martian mantle is possible. Indeed, even the interior of Earth has been proposed to contain an undepleted layer of primordial mantle below $\sim$1000 km depth (Xiang et al., 2021). A primordial-depleted boundary is not the only form of compositional stratification that can occur, however: the mantle overturn described in Section 5.3 may cause a build-up of heat-producing elements

at Mars' core-mantle boundary that can have a dramatic influence on the planet's thermo-chemical evolution (Samuel et al., 2021). On the other hand, if the magma ocean phase lasts sufficiently long ($\gtrsim$ 1 Myr, which may be the case due to the build-up of a thick, insulating atmosphere generated by volatile degassing (Lebrun et al., 2013; Zahnle et al., 2007; Nikolaou et al., 2019)), then solid-state convection may occur in the mantle during magma ocean crystallisation, which would avoid any global overturn and lead to a much more homegeneous, well-mixed mantle (Maurice et al., 2017). Clearly, the Martian interior is very unlikely to be described by a "one-size fits all" style of approach, and the reality of its compositional layering prior to impact was most likely at some intermediate between our two end-member cases.

While our results favour the fully-mixed mantle depletion scheme over the fully-stratified model, this is predominantly due to the latter model producing a crustal pattern at the immediate impact site that generally consists of too much crust at the centre encircled by a region of very thin crust. All of these features are contained within the excavated region of the impact site, meaning that such a sharp contrast would likely disappear if we were to take turbulent mixing of the entirely molten magma ocean into account. The overall excess in post-impact crustal thickness relative to the fully-mixed model is a robust result, however, as we see that the impact causes large-scale displacement of the depleted material away from the impact site (5). Our analysis should therefore still identify the most likely parameters for a Dichotomy-forming impact, regardless of mantle depletion scheme; however, any potential mantle stratification that involves less depleted material at depth will act to increase crust-production at the impact site, thus suggesting that our pre-impact fertility values may in fact need to be lower than those suggested in our fully-mixed cases.

5.7. Impact Statistics

The probability distribution of impacts on Mars in the early Solar System is not well understood. Various N-body models have been used to investigate the formation and accretionary evolution of the Solar System, but these generally cannot resolve individual impactors smaller than $\sim$1000 km radius, instead using tracers representative of swarms of smaller bodies (e.g. Jacobson et al., 2014; Rubie et al., 2015; O'Brien et al., 2006). In addition, classical models systematically produce planets at Mars' semi-major axis that are 5-10 times too massive (Wetherill, 1991;

Chambers, 2001; Raymond et al., 2009), leading to various proposed scenario's such as particularly eccentric (Raymond et al., 2009; Morishima et al., 2010) or migrating (Walsh et al., 2011; Raymond & Morbidelli, 2014) gas giants, making concrete predictions even more difficult. Nonetheless, it is certain that smaller bodies are more common, as this is both predicted by models (Raymond et al., 2014, and references therein) and verified by observations of near-Earth objects (Michel & Morbidelli, 2007), the main asteroid belt (Bottke et al., 2005; Ryan et al., 2015) and the Kuiper belt (Bernstein et al., 2004; Fraser et al., 2014; Adams et al., 2014; Morbidelli et al., 2021). For impact velocities, values of $\sim$1.4 v_{esc} are expected according to classical arguments considering self-stirring of similar-sized bodies (Safronov, 1969), and N-body simulations confirm this, with Emsenhuber et al. (2020, 2021) finding a median impact velocity of 1.6 v_{esc} but with an increased probability for lower values (the first and third quartiles are at 1.22 v_{esc} and 2.12 v_{esc}, respectively). Impact angles are also stochastic in nature, and are usually considered to follow the Shoemaker (1962) probability distribution $dp(\theta_{coll}) = \sin 2\theta_{coll}\ d\theta_{coll}$ which predicts 50% of impacts to occur within angles of 30-60°, centred on the most probable angle of 45°.

Using this statistical knowledge, we can further speculate on which of our cases represent the most-likely impact scenario to form the Dichotomy. The largest impactors (radii $\geq$ 1500 km) can almost certainly be ruled out, as their sizes make them highly unlikely impactors and they do not represent any significant cases. Their ability to produce large, shallow magma ponds that leave very little compositional traces from the target are certainly an interesting regime that should be further examined in future studies, however. As already stated, the 1000 km impactor is difficult to justify, and its size only weakens its case further. Apart from their differing radii, the remaining impactor sizes (radii of 500 km and 750 km) are remarkably similar in their impact angle and velocity preferences. Most notably they both favour velocities of 1.2-1.4 v_{esc} and angles of 15-30°, in contrast to previous studies (Golabek et al., 2018; Marinova et al., 2011, 2008). As the 750 km impactor proved to be the best-fitting radius in our analysis, we still consider it to be the most likely size to form the Dichotomy in spite of the probability trend towards smaller impactors; however, we predict that many cases would be favourable at radii in the intermediate of our two smallest impactors.

6. Conclusions and future outlook

6.1. Conclusions

Through a large suite of SPH impact simulations coupled to a simplified crust-production model, we have identified the most favourable parameters for an impact-induced Martian Dichotomy. The most important conclusions can be summarised as follows:

1. The northern lowlands of Mars cannot have formed through a classical impact basin forming impact event, as it is not possible to produce such a large crater without excessive crust production due to a deep magma ocean at the impact site and/or strong antipodal effects. If the Martian Dichotomy formed through an impact it must therefore have occurred in the southern hemisphere of Mars, where the impact-induced melt crystallised to form a thicker crust at the impact site than its relatively undisturbed antipode.
2. We find the most likely candidate for the projectile in such an impact to be a 500-750 km radius body impacting at an impact angle of 15-30° and impact velocity of 1.2-1.4 times mutual escape speed (∼6-7 km/s).
3. To avoid an over-thickened post-impact southern highlands, the bulk silicate fertility of Mars (i.e. maximum mass fraction of crust that can be extracted from a given mass of primordial mantle before silicate differentiation) must be less than or equal to 12.5%. The reason for such a low crust-production efficiency is unclear.
4. Solid strength plays a significant role in the distribution of melt after a giant impact on a body as large as Mars, and must therefore be included in any future impact studies on these scales.

6.2. Outlook

This work serves as an in-depth insight into the immediate consequences of a giant impact on Mars and its feasibility in forming the Martian Dichotomy; however, it is not without limitations and thus motivates future studies on the topic. One clear improvement that could be made is an increase in resolution (i.e. more particles if using the SPH method). This would lead to more accurate results overall, with the calculations of primordial crust being improved in particular due to their under-resolved nature. All of these results represent Mars directly after the crystallisation of the impact-induced magma ocean and neglect any long-term interior evolution.

A natural follow-up to this work would therefore involve a sophisticated geodynamic model to investigate any further crust production due to decompression melting associated with convection processes in the mantle, and would potentially allow for direct comparison to present-day observations of Mars (such a study utilising the StagYY mantle convection code (Tackley, 2008) is currently underway (Cheng et al. in prep.)). A more sophisticated geophysical model could also include the effects of heat-producing elements that are expected to be concentrated in the primordial crust. Finally, the parameter space explored could be further refined with a particular focus on impactors with radii within our preferred range of 500-750 km impacting at intermediate 15-30° angles, and with a larger range of impact velocities.

Acknowledgements

We thank David Baratoux for providing us with the Bouley et al. (2020) crustal thickness data. Supported by SNSF grant 200021_175630.

Appendix A. Cubic Spline Function

Appendix A.1. Standard Form

$$W(r,h) = \alpha \begin{cases} 1 - \frac{3}{2}q^2 + \frac{3}{4}q^3 & 0 \leq q \leq 1 \\ \frac{1}{4}(2-q)^3 & 1 < q < 2 \\ 0 & q \geq 2 \end{cases}, \tag{A.1}$$

where $q = r/h$ and α is $\frac{2}{3h}$, $\frac{10}{7\pi h^2}$ or $\frac{1}{\pi h^3}$ in the 1, 2 and 3 dimensional cases, respectively.

Appendix A.2. Integrated 1D Form

$$\int_0^r W_{1\mathrm{D}}(r,h)\ \mathrm{d}r = W'_{1\mathrm{D}}(r,h) = \begin{cases} \frac{2}{3}q - \frac{1}{3}q^3 + \frac{1}{8}q^4 & 0 \leq q \leq 1 \\ \frac{1}{2} - \frac{1}{24}(2-q)^4 & 1 < q < 2 \\ 0.5 & q \geq 2 \end{cases}, \tag{A.2}$$

where $W_{1\mathrm{D}}(r,h)$ is the 1-dimensional form of $W(r,h)$.

Appendix B. Improved SPH Neighbour Symmetry

The smoothing kernel is almost always chosen to have compact support, with the function (usually) decaying to zero at distances greater than $2h$, as is the case for our function in Appendix A.1. Because of this convenient property, when calculating the SPH sums for a given particle, a, the previous versions of SPHLATCH neglected any neighbours at distances greater than twice the smoothing length, h_a, of said particle. This allowed for very efficient neighbour searching via the Barnes-Hut octree method. However, in order to maintain symmetric forces between particles with different smoothing lengths, the "true" smoothing length, h_{ab}, used for the force calculations is in fact the arithmetic mean of the central particle smoothing length and the contributing neighbour smoothing length, h_b, i.e. $h_{ab} = \frac{h_a+h_b}{2}$. Of course, for this symmetry to hold, particle b must be included in particle a's SPH sum *and* vice versa. Unfortunately, this is not always the case when our search radius is only h_a rather than h_{ab}. If the distance between the two particles is x_{ab}, the asymmetry occurs when $x_{ab} > 2h_b$ but $x_{ab} < 2h_a$ and $x_{ab} < 2h_{ab}$. Here, particle b will contribute to particle b's SPH sum, but not the other way round, as is illustrated in Figure B.21.

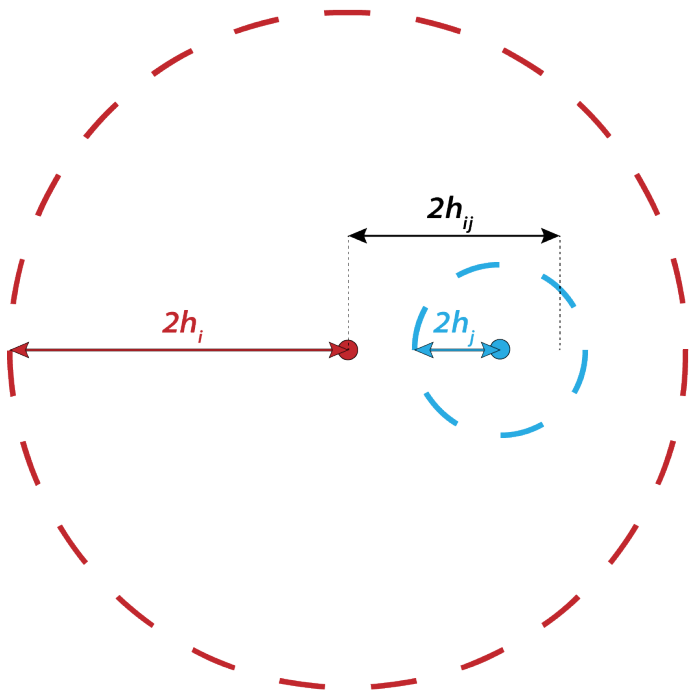

Figure B.21: A schematic diagram illustrating the asymmetry in the SPH sum calculations. Here, the distance between the two particles is less than $2h_{ab}$, meaning they will contribute to each other's SPH sums; however, particle a will not be found in particle b's neighbour search within $2h_b$.

To resolve this in the updated SPHLATCH code, we create a list of neighbours for each particle when performing the tree walk, and add the central particle to the neighbour's neighbour-list if the above conditions for asymmetry are met. These lists are then used for any future SPH sums, which has the additional benefit of a reduced number of tree-walks and thus a reduced computational cost.

Appendix C. Primordial Crust Excavation at the Impact Site

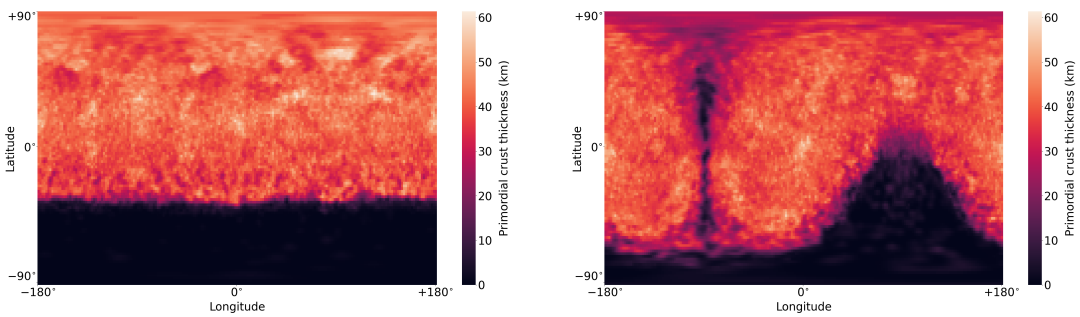

Figure C.22: Crustal thickness contribution from primordial crust alone for the classical cases of a 1000 km radius body impacting at the mutual escape speed with an impact angle of 0° (left) and 45° (right).

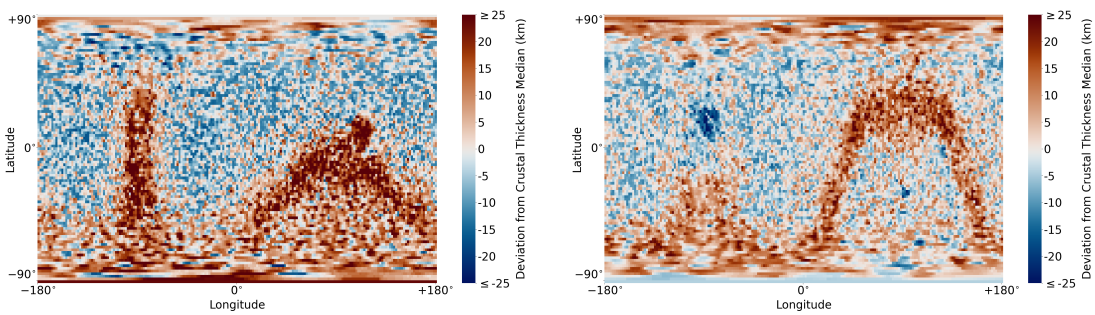

Figure C.23: The best-fitting cases for impactor radii of 1500 km (left) and 2000 km (right) but with the fully-mixed mantle depletion scheme. The same cases with the fully-stratified scheme can be seen in Figure 16.

Appendix D. Core Fraction

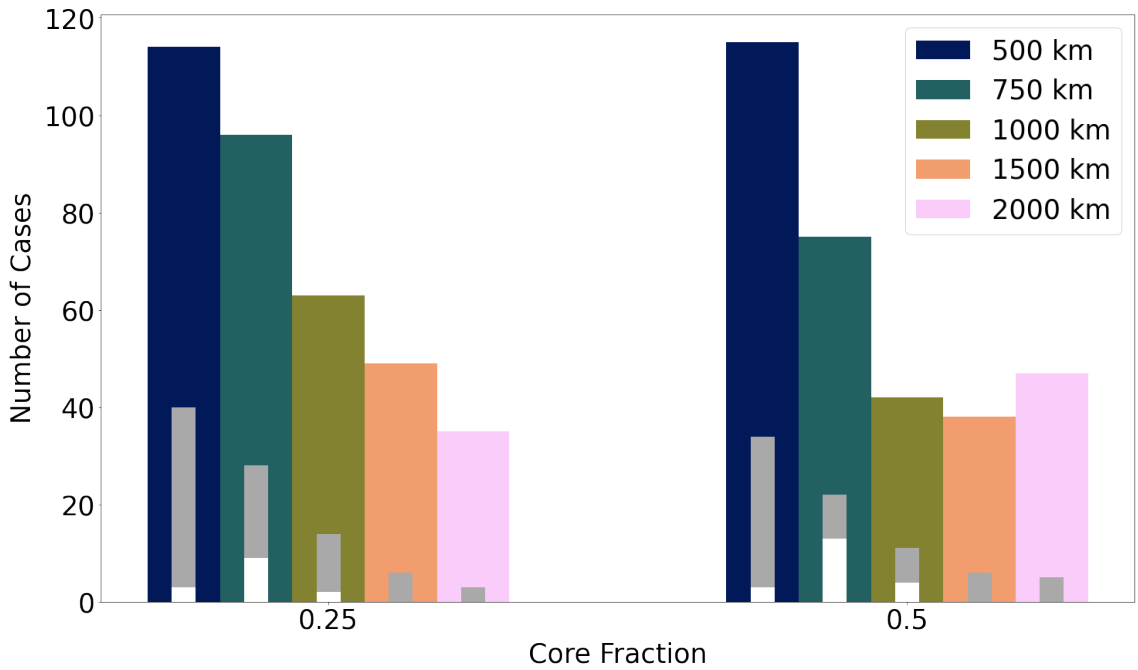

Figure D.24: Histogram of cases within $\delta_{SH_{max}}$ for each impactor radius as a function of impactor core fraction.

Appendix E. Angular Momentum Conservation

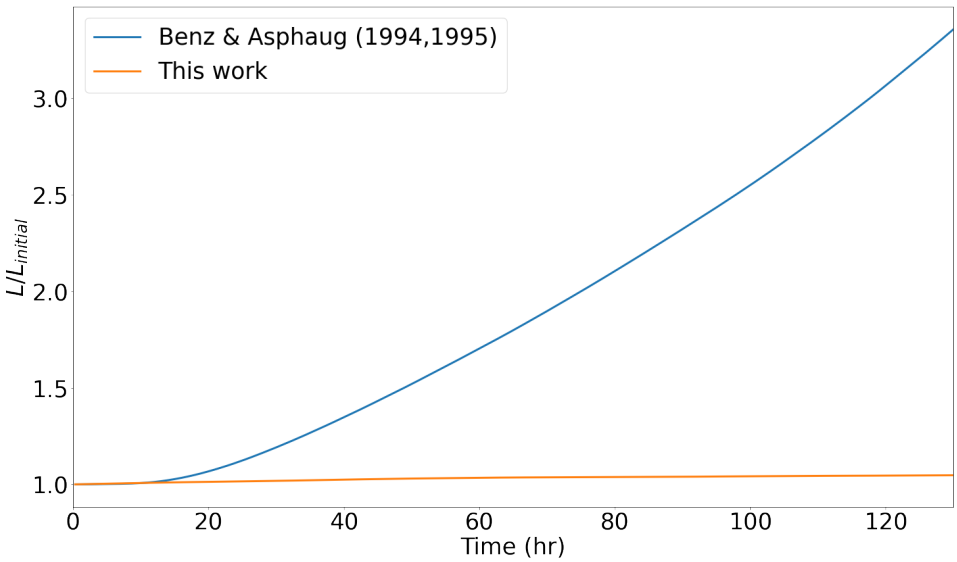

Figure E.25: Angular momentum as a function of time with and without the rotation rate tensor corrections described in Section 2.1.2. These values correspond to a Mars-like body rotating with a 10 hr period. Angular momentum is given relative to its value at the beginning of the simulation.

Appendix F. Pre-Impact Crust Distributions

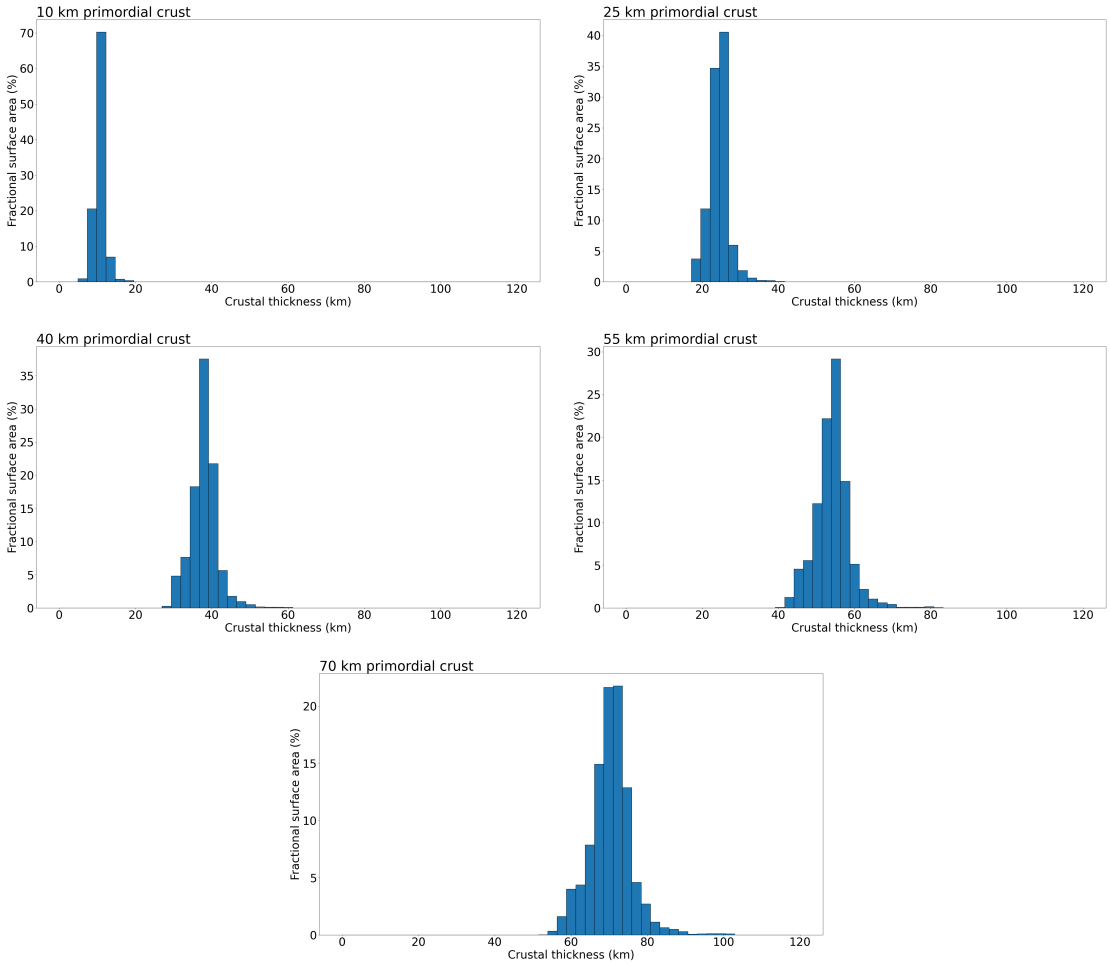

Figure F.26: Histograms depicting the pre-impact distribution of crust on our Mars-like body, for each primordial thickness investigated in this study. Each bin displays the percentage of the Martian surface corresponding to the given crustal thickness range.

References

Abe, Y. (1997). Thermal and chemical evolution of the terrestrial magma ocean. *Physics of the Earth and Planetary Interiors*, *100*, 27–39. doi:10.1016/S0031-9201(96)03229-3.

Adams, E. R., Gulbis, A. A., Benecchi, S. D., Buie, M. W., Trilling, D. E., & Wasserman, L. H. (2014). De-biased populations of Kuiper belt objects from the deep ecliptic survey. *Astronomical Journal*, *148*, 55. doi:10.1088/0004-6256/148/3/55.

Andrews-Hanna, J. C., Zuber, M. T., & Banerdt, W. B. (2008). The Borealis basin and the origin of the martian crustal dichotomy. *Nature*, *453*, 1212–1215. doi:10.1038/nature07011.

Asphaug, E., Emsenhuber, A., Cambioni, S., Gabriel, T. S. J., & Schwartz, S. R. (2021). Collision Chains among the Terrestrial Planets. III. Formation of the Moon. *The Planetary Science Journal*, *2*, 200. doi:10.3847/PSJ/AC19B2.

Ballmer, M. D., Lourenço, D. L., Hirose, K., Caracas, R., & Nomura, R. (2017). Reconciling magma-ocean crystallization models with the present-day structure of the Earth's mantle. *Geochemistry, Geophysics, Geosystems*, *18*, 2785–2806. doi:10.1002/2017GC006917.

Barnes, J., & Hut, P. (1986). A hierarchical O(N log N) force-calculation algorithm. *Nature 1986 324:6096*, *324*, 446–449. doi:10.1038/324446a0.

Benz, W., & Asphaug, E. (1994). Impact Simulations with Fracture. I. Method and Tests. *Icarus*, *107*, 98–116. doi:10.1006/icar.1994.1009.

Benz, W., & Asphaug, E. (1995). *Simulations of brittle solids using smooth particle hydrodynamics*. Technical Report.

Benz, W., Cameron, A. G., & Melosh, H. J. (1989). The origin of the Moon and the single-impact hypothesis III. *Icarus*, *81*, 113–131. doi:10.1016/0019-1035(89)90129-2.

Bernstein, G. M., Trilling, D. E., Allen, R. L., Brown, M. E., Holman, M., & Malhotra, R. (2004). *The Size Distribution of Trans-Neptunian Bodies*. Technical Report 3. doi:10.1086/422919. arXiv:0308467.

Borg, L. E., Brennecka, G. A., & Symes, S. J. (2016). Accretion timescale and impact history of Mars deduced from the isotopic systematics of martian meteorites. *Geochimica et Cosmochimica Acta*, *175*, 150–167. doi:10.1016/J.GCA.2015.12.002.

Bottke, W. F., Durda, D. D., Nesvorný, D., Jedicke, R., Morbidelli, A., Vokrouhlický, D., Levison, H., Bottke, W. F., Durda, D. D., Nesvorný, D., Jedicke, R., Morbidelli, A., Vokrouhlický, D., & Levison, H. (2005). The fossilized size distribution of the main asteroid belt. *Icarus*, *175*, 111–140. doi:10.1016/J.ICARUS.2004.10.026.

Boukaré, C. E., Parmentier, E. M., & Parman, S. W. (2018). Timing of mantle overturn during magma ocean solidification. *Earth and Planetary Science Letters*, *491*, 216–225. doi:10.1016/J.EPSL.2018.03.037.

Bouley, S., Keane, J. T., Baratoux, D., Langlais, B., Matsuyama, I., Costard, F., Hewins, R., Payré, V., Sautter, V., Séjourné, A., Vanderhaeghe, O., & Zanda, B. (2020). A thick crustal block revealed by reconstructions of early Mars highlands. *Nature Geoscience*, . doi:10.1038/s41561-019-0512-6.

Bouvier, L. C., Costa, M. M., Connelly, J. N., Jensen, N. K., Wielandt, D., Storey, M., Nemchin, A. A., Whitehouse, M. J., Snape, J. F., Bellucci, J. J., Moynier, F., Agranier, A., Gueguen, B., Schönbächler, M., & Bizzarro, M. (2018). Evidence for extremely rapid magma ocean crystallization and crust formation on Mars. *Nature*, *558*, 586–589. doi:10.1038/s41586-018-0222-z.

Breuer, D., & Spohn, T. (2003). Early plate tectonics versus single-plate tectonics on Mars: Evidence from magnetic field history and crust evolution. *Journal of Geophysical Research: Planets*, *108*, 5072. doi:10.1029/2002JE001999.

Breuer, D., & Spohn, T. (2006). Viscosity of the Martian mantle and its initial temperature: Constraints from crust formation history and the evolution of the magnetic field. *Planetary and Space Science*, *54*, 153–169. doi:10.1016/j.pss.2005.08.008.

Buczkowski, D. L. (2007). Stealth quasi-circular depressions (sQCDs) in the northern lowlands of Mars. *Journal of Geophysical Research E: Planets*, *112*, E09002. doi:10.1029/2006JE002836.

Burg, J. P., & Gerya, T. V. (2005). The role of viscous heating in Barrovian metamorphism of collisional orogens: Thermomechanical models and application to the Lepontine Dome in the Central Alps. *Journal of Metamorphic Geology*, *23*, 75–95. doi:10.1111/j.1525-1314.2005.00563.x.

Cambioni, S., Asphaug, E., Emsenhuber, A., Gabriel, T. S. J., Furfaro, R., & Schwartz, S. R. (2019). Realistic On-the-fly Outcomes of Planetary Collisions: Machine Learning Applied to Simulations of Giant Impacts. *The Astrophysical Journal*, *875*, 40. doi:10.3847/1538-4357/ab0e8a. arXiv:1903.04507.

Caracas, R., Hirose, K., Nomura, R., & Ballmer, M. D. (2019). Melt–crystal density crossover in a deep magma ocean. *Earth and Planetary Science Letters*, *516*, 202–211. doi:10.1016/j.epsl.2019.03.031.

Cassata, W. S., Cohen, B. E., Mark, D. F., Trappitsch, R., Crow, C. A., Wimpenny, J., Lee, M. R., & Smith, C. L. (2018). Chronology of martian breccia NWA 7034 and the formation of the martian crustal dichotomy. *Science Advances*, *4*, eaap8306. doi:10.1126/sciadv.aap8306.

Chambers, J. E. (2001). Making More Terrestrial Planets. *Icarus*, *152*, 205–224. doi:10.1006/ICAR.2001.6639.

Citron, R. I., Manga, M., & Tan, E. (2018). A hybrid origin of the Martian crustal dichotomy: Degree-1 convection antipodal to a giant impact. *Earth and Planetary Science Letters*, *491*, 58–66. doi:10.1016/J.EPSL.2018.03.031.

Collins, G. S., Melosh, H. J., & Ivanov, B. A. (2004). Modeling damage and deformation in impact simulations. *Meteoritics and Planetary Science*, *39*, 217–231. doi:10.1111/j.1945-5100.2004.tb00337.x.

Debaille, V., Brandon, A. D., Yin, Q. Z., & Jacobsen, B. (2007). Coupled 142Nd–143Nd evidence for a protracted magma ocean in Mars. *Nature 2007 450:7169*, *450*, 525–528. doi:10.1038/nature06317.

Debaille, V., Yin, Q. Z., Brandon, A. D., & Jacobsen, B. (2008). Martian mantle mineralogy investigated by the 176Lu–176Hf and 147Sm–143Nd systematics of shergottites. *Earth and Planetary Science Letters*, *269*, 186–199. doi:10.1016/J.EPSL.2008.02.008.

Diehl, S., Rockefeller, G., Fryer, C. L., Riethmiller, D., & Statler, T. S. (2015). Generating Optimal Initial Conditions for Smoothed Particle Hydrodynamics Simulations. *Publications of the Astronomical Society of Australia*, *32*. doi:10.1017/PASA.2015.50.

Duncan, M. S., Schmerr, N. C., Bertka, C. M., & Fei, Y. (2018). Extending the Solidus for a Model Iron-Rich Martian Mantle Composition to 25 GPa. *Geophysical Research Letters*, (pp. 211–220). doi:10.1029/2018GL078182.

Elkins-Tanton, L. T., Hess, P. C., & Parmentier, E. M. (2005). Possible formation of ancient crust on Mars through magma ocean processes. *Journal of Geophysical Research: Planets*, *110*, 1–11. doi:10.1029/2005JE002480.

Elkins-Tanton, L. T., Parmentier, E. M., & Hess, P. C. (2003). Magma ocean fractional crystallization and cumulate overturn in terrestrial planets: Implications for Mars. *Meteoritics & Planetary Science*, *38*, 1753–1771. doi:10.1111/J.1945-5100.2003.TB00013.X.

Emsenhuber, A., & Asphaug, E. (2019a). Fate of the Runner in Hit-and-run Collisions. *The Astrophysical Journal*, *875*, 95. doi:10.3847/1538-4357/ab0c1d. arXiv:1903.04508.

Emsenhuber, A., & Asphaug, E. (2019b). Graze-and-merge Collisions under External Perturbers. *The Astrophysical Journal*, *881*, 102. doi:10.3847/1538-4357/ab2f8e. arXiv:1908.07557.

Emsenhuber, A., Asphaug, E., Cambioni, S., Gabriel, T. S. J., & Schwartz, S. R. (2021). Collision Chains among the Terrestrial Planets. II. An Asymmetry between Earth and Venus. *The Planetary Science Journal*, *2*, 199. doi:10.3847/PSJ/AC19B1.

Emsenhuber, A., Cambioni, S., Asphaug, E., Gabriel, T. S. J., Schwartz, S. R., & Furfaro, R. (2020). Realistic On-the-fly Outcomes of Planetary Collisions. II. Bringing Machine Learning to N-body Simulations. *The Astrophysical Journal*, *891*, 6. doi:10.3847/1538-4357/AB6DE5. arXiv:2001.00951.

Emsenhuber, A., Jutzi, M., & Benz, W. (2018). SPH calculations of Mars-scale collisions: The role of the equation of state, material rheologies, and numerical effects. *Icarus*, *301*, 247–257. doi:10.1016/j.icarus.2017.09.017. arXiv:1710.03245.

Fraeman, A. A., & Korenaga, J. (2010). The influence of mantle melting on the evolution of Mars. *Icarus*, *210*, 43–57. doi:10.1016/J.ICARUS.2010.06.030.

Fraser, W. C., Brown, M. E., Morbidelli, A., Parker, A., & Batygin, K. (2014). The absolute magnitude distribution of kuiper belt objects. *Astrophysical Journal*, *782*, 100. doi:10.1088/0004-637X/782/2/100. arXiv:1401.2157.

Frey, H. V. (2006). Impact constraints on, and a chronology for, major events in early Mars history. *Journal of Geophysical Research*, *111*, E08S91. doi:10.1029/2005JE002449.

Gabriel, T. S. J., & Allen-Sutter, H. (2021). Dependencies of Mantle Shock Heating in Pairwise Accretion. *The Astrophysical Journal Letters*, *915*, L32. doi:10.3847/2041-8213/abffd1.

Gabriel, T. S. J., Jackson, A. P., Asphaug, E., Reufer, A., Jutzi, M., & Benz, W. (2020). Gravity-dominated Collisions: A Model for the Largest Remnant Masses with Treatment for "Hit and Run" and Density Stratification. *The Astrophysical Journal*, *892*, 40. doi:10.3847/1538-4357/ab528d.

Gingold, R. A., & Monaghan, J. J. (1977). Smoothed particle hydrodynamics: theory and application to non-spherical stars. *Monthly Notices of the Royal Astronomical Society*, *181*, 375–389. doi:10.1093/MNRAS/181.3.375.

Golabek, G. J., Emsenhuber, A., Jutzi, M., Asphaug, E. I., & Gerya, T. V. (2018). Coupling SPH and thermochemical models of planets: Methodology and example of a Mars-sized body. *Icarus*, *301*, 235–246. doi:10.1016/j.icarus.2017.10.003. arXiv:1710.03250.

Golabek, G. J., Keller, T., Gerya, T. V., Zhu, G., Tackley, P. J., & Connolly, J. A. (2011). Origin of the martian dichotomy and Tharsis from a giant impact causing massive magmatism. *Icarus*, *215*, 346–357. doi:10.1016/J.ICARUS.2011.06.012.

Goossens, S., Sabaka, T. J., Genova, A., Mazarico, E., Nicholas, J. B., & Neumann, G. A. (2017). Evidence for a low bulk crustal density for Mars from gravity and topography. *Geophysical Research Letters*, *44*, 7686–7694. doi:10.1002/2017GL074172.

Halliday, A. N., Wänke, H., Birck, J. L., & Clayton, R. N. (2001). The Accretion, Composition and Early Differentiation of Mars. *Space Science Reviews*, *96*, 197–230. doi:10.1023/A:1011997206080.

Hernquist, L. (1987). Performance Characteristics of Tree Codes. *ApJS*, *64*, 715. doi:10.1086/191215.

Hernquist, L., & Katz, N. (1989). TREESPH: A UNIFICATION OF SPH WITH THE HIERARCHICAL TREE METHOD. *The Astrophysical Journal Supplement Series*, *70*, 419–446. doi:10.1017/CBO9781107415324.004. arXiv:arXiv:1011.1669v3.

Humayun, M., Nemchin, A., Zanda, B., Hewins, R. H., Grange, M., Kennedy, A., Lorand, J. P., Göpel, C., Fieni, C., Pont, S., & Deldicque, D. (2013). Origin and age of the earliest Martian crust from meteorite NWA 7533. *Nature*, *503*, 513–516. doi:10.1038/nature12764.

Jacobson, S. A., Morbidelli, A., Raymond, S. N., O'brien, D. P., Walsh, K. J., & Rubie, D. C. (2014). Highly siderophile elements in Earth's mantle as a clock for the Moon-forming impact, . doi:10.1038/nature13172.

Johansen, A., Ronnet, T., Bizzarro, M., Schiller, M., Lambrechts, M., Nordlund, A., & Lammer, H. (2021). A pebble accretion model for the formation of the terrestrial planets in the solar system. *Science Advances*, *7*, 1–14. doi:10.1126/sciadv.abc0444. arXiv:2102.08611.

Jutzi, M., Benz, W., & Michel, P. (2008). Numerical simulations of impacts involving porous bodies. I. Implementing sub-resolution porosity in a 3D SPH hydrocode. *Icarus*, *198*, 242–255. doi:10.1016/j.icarus.2008.06.013. arXiv:0807.1264.

Keller, T., & Tackley, P. J. (2009). Towards self-consistent modeling of the martian dichotomy: The influence of one-ridge convection on crustal thickness distribution. *Icarus*, *202*, 429–443. doi:10.1016/j.icarus.2009.03.029.

Knapmeyer-Endrun, B., Panning, M. P., Bissig, F., Joshi, R., Khan, A., Kim, D., Lekić, V., Tauzin, B., Tharimena, S., Plasman, M., Compaire, N., Garcia, R. F., Margerin, L., Schimmel, M., Stutzmann, É., Schmerr, N., Bozdag, E., Plesa, A. C., Wieczorek, M. A., Broquet, A., Antonangeli, D., McLennan, S. M., Samuel, H., Michaut, C., Pan, L., Smrekar, S. E., Johnson, C. L., Brinkman, N.,

Mittelholz, A., Rivoldini, A., Davis, P. M., Lognonné, P., Pinot, B., Scholz, J. R., Stähler, S., Knapmeyer, M., van Driel, M., Giardini, D., & Banerdt, W. B. (2021). Thickness and structure of the martian crust from InSight seismic data. *Science*, *373*, 438–443. doi:10.1126/SCIENCE.ABF8966.

Kruijer, T. S., Borg, L. E., Wimpenny, J., & Sio, C. K. (2020). Onset of magma ocean solidification on Mars inferred from Mn-Cr chronometry. *Earth and Planetary Science Letters*, *542*, 116315. doi:10.1016/j.epsl.2020.116315.

Kruijer, T. S., Kleine, T., Borg, L. E., Brennecka, G. A., Irving, A. J., Bischoff, A., & Agee, C. B. (2017). The early differentiation of Mars inferred from Hf–W chronometry. *Earth and Planetary Science Letters*, *474*, 345–354. doi:10.1016/j.epsl.2017.06.047.

Labrosse, S., Hernlund, J. W., & Coltice, N. (2007). A crystallizing dense magma ocean at the base of the Earth's mantle. *Nature*, *450*, 866–869. doi:10.1038/nature06355.

Lebrun, T., Massol, H., Chassefière, E., Davaille, A., Marcq, E., Sarda, P., Leblanc, F., & Brandeis, G. (2013). Thermal evolution of an early magma ocean in interaction with the atmosphere. *Journal of Geophysical Research: Planets*, *118*, 1155–1176. doi:10.1002/jgre.20068.

Leone, G., Tackley, P. J., Gerya, T. V., May, D. A., & Zhu, G. (2014). Three-dimensional simulations of the southern polar giant impact hypothesis for the origin of the Martian dichotomy. *Geophysical Research Letters*, *41*, 8736–8743. doi:10.1002/2014GL062261.

Libersky, L. D., & Petschek, A. G. (1991). Smooth particle hydrodynamics with strength of materials. *Advances in the Free-Lagrange Method Including Contributions on Adaptive Gridding and the Smooth Particle Hydrodynamics Method*, (pp. 248–257). doi:10.1007/3-540-54960-9_58.

Lucy, L. B. (1977). A numerical approach to the testing of the fission hypothesis. *The Astronomical Journal*, *82*, 1013–1024. doi:10.1086/112164.

Malkin, Z. (2019). A New Equal-area Isolatitudinal Grid on a Spherical Surface. *The Astronomical Journal*, *158*, 158. doi:10.3847/1538-3881/ab3a44.

Marinova, M. M., Aharonson, O., & Asphaug, E. (2008). Mega-impact formation of the Mars hemispheric dichotomy. *Nature*, *453*, 1216–1219. doi:10.1038/nature07070.

Marinova, M. M., Aharonson, O., & Asphaug, E. (2011). Geophysical consequences of planetary-scale impacts into a Mars-like planet. *Icarus*, *211*, 960–985. doi:10.1016/j.icarus.2010.10.032.

Maurice, M., Tosi, N., Samuel, H., Plesa, A. C., Hüttig, C., & Breuer, D. (2017). Onset of solid-state mantle convection and mixing during magma ocean solidification. *Journal of Geophysical Research: Planets*, *122*, 577–598. doi:10.1002/2016JE005250.

Mckenzie, D., & Bickle, M. J. (1988). The volume and composition of melt generated by extension of the lithosphere. *Journal of Petrology*, *29*, 625–679. doi:10.1093/petrology/29.3.625.

Mezger, K., Debaille, V., & Kleine, T. (2013). Core formation and mantle differentiation on Mars. *Space Science Reviews*, *174*, 27–48. doi:10.1007/s11214-012-9935-8.

Michel, P., & Morbidelli, A. (2007). Population of Impactors and the Impact Cratering Rate in the Inner Solar System. *Impact Cratering: Processes and Products*, *42*, 1861–1869. doi:10.1002/9781118447307.ch2.

Monaghan, J. J. (2005). Smoothed particle hydrodynamics. *Reports on Progress in Physics*, *68*, 1703–1759. doi:10.1088/0034-4885/68/8/R01. arXiv:0507472.

Monteux, J., Coltice, N., Dubuffet, F., & Ricard, Y. (2007). Thermo-mechanical adjustment after impacts during planetary growth. *Geophysical Research Letters*, *34*, L24201. doi:10.1029/2007GL031635.

Morbidelli, A., Nesvorny, D., Bottke, W. F., & Marchi, S. (2021). A re-assessment of the Kuiper belt size distribution for sub-kilometer objects, revealing collisional equilibrium at small sizes. *Icarus*, *356*, 114256. doi:10.1016/J.ICARUS.2020.114256. arXiv:2012.03823.

Morbidelli, A., Nesvorny, D., Laurenz, V., Marchi, S., Rubie, D. C., Elkins-Tanton, L., Wieczorek, M., & Jacobson, S. (2018). The timeline of the lunar bombard-

ment: Revisited. *Icarus*, *305*, 262–276. doi:10.1016/j.icarus.2017.12.046. arXiv:1801.03756.

Morishima, R., Stadel, J., & Moore, B. (2010). From planetesimals to terrestrial planets: N-body simulations including the effects of nebular gas and giant planets. *Icarus*, *207*, 517–535. doi:10.1016/J.ICARUS.2009.11.038. arXiv:1007.0579.

Morschhauser, A., Grott, M., & Breuer, D. (2011). Crustal recycling, mantle dehydration, and the thermal evolution of Mars. *Icarus*, *212*, 541–558. doi:10.1016/j.icarus.2010.12.028.

Murchie, S. L., Thomas, P. C., Rivkin, A. S., & Chabot, N. L. (2015). Phobos and Deimos. *Asteroids IV*, (pp. 451–467). doi:10.1038/scientificamerican0277-30.

Neumann, G. A., Zuber, M. T., Wieczorek, M. A., McGovern, P. J., Lemoine, F. G., & Smith, D. E. (2004). Crustal structure of Mars from gravity and topography. *Journal of Geophysical Research E: Planets*, *109*, E08002. doi:10.1029/2004JE002262.

Nikolaou, A., Katyal, N., Tosi, N., Godolt, M., Grenfell, J. L., & Rauer, H. (2019). What Factors Affect the Duration and Outgassing of the Terrestrial Magma Ocean? *The Astrophysical Journal*, *875*, 11. doi:10.3847/1538-4357/AB08ED. arXiv:1903.07436.

Nimmo, F., Hart, S. D., Korycansky, D. G., & Agnor, C. B. (2008). Implications of an impact origin for the martian hemispheric dichotomy. *Nature*, *453*, 1220–1223. doi:10.1038/nature07025.

Nimmo, F., & Tanaka, K. (2005). Early crustal evolution of Mars. *Annual Review of Earth and Planetary Sciences*, *33*, 133–161. doi:10.1146/annurev.earth.33.092203.122637.

Nomura, R., Ozawa, H., Tateno, S., Hirose, K., Hernlund, J., Muto, S., Ishii, H., & Hiraoka, N. (2011). Spin crossover and iron-rich silicate melt in the Earth's deep mantle. *Nature*, *473*, 199–202. doi:10.1038/nature09940.

Norman, M. D. (1999). The composition and thickness of the crust of Mars estimated from rare earth elements and neodymium-isotopic compositions of Martian mete-

orites. *Meteoritics & Planetary Science*, *34*, 439–449. doi:10.1111/J.1945-5100.1999.TB01352.X.

O'Brien, D. P., Morbidelli, A., & Levison, H. F. (2006). Terrestrial planet formation with strong dynamical friction. *Icarus*, *184*, 39–58. doi:10.1016/J.ICARUS.2006.04.005.

Pruis, M. J., & Tanaka, K. L. (1995). The Martian northern plains did not result from plate tectonics. *Abstracts of the Lunar and Planetary Science Conference*, *26*, 1147.

Raymond, S. N., Kokubo, E., Morbidelli, A., Morishima, R., & Walsh, K. J. (2014). Terrestrial Planet Formation at Home and Abroad. *Protostars and Planets VI*, . doi:10.2458/azu_uapress_9780816531240-ch026. arXiv:1312.1689.

Raymond, S. N., & Morbidelli, A. (2014). The Grand Tack model: A critical review. *Proceedings of the International Astronomical Union*, *9*, 194–203. doi:10.1017/S1743921314008254. arXiv:1409.6340.

Raymond, S. N., O'Brien, D. P., Morbidelli, A., & Kaib, N. A. (2009). Building the terrestrial planets: Constrained accretion in the inner Solar System. *Icarus*, *203*, 644–662. doi:10.1016/J.ICARUS.2009.05.016. arXiv:0905.3750.

Reese, C. C., Orth, C. P., & Solomatov, V. S. (2010). Impact origin for the Martian crustal dichotomy: Half emptied or half filled? *J. Geophys. Res*, *115*. doi:10.1016/j.icarus.2011.03.028.

Reese, C. C., & Solomatov, V. S. (2006). Fluid dynamics of local martian magma oceans. *Icarus*, *184*, 102–120. doi:10.1016/j.icarus.2006.04.008.

Reese, C. C., & Solomatov, V. S. (2010). Early martian dynamo generation due to giant impacts. *Icarus*, *207*, 82–97. doi:10.1016/j.icarus.2009.10.016.

Reinhardt, C., & Stadel, J. (2017). Numerical aspects of giant impact simulations. *Monthly Notices of the Royal Astronomical Society*, *467*, 4252–4263. doi:10.1093/mnras/stx322. arXiv:1701.08296.

Reufer, A., Meier, M. M. M., Benz, W., & Wieler, R. (2012). A hit-and-run Giant Impact scenario. *Icarus*, *221*, 296–299. doi:10.1016/j.icarus.2012.07.021. arXiv:1207.5224.

Righter, K., & Chabot, N. L. (2011). Moderately and slightly siderophile element constraints on the depth and extent of melting in early Mars. *Meteoritics and Planetary Science*, *46*, 157–176. doi:10.1111/j.1945-5100.2010.01140.x.

Righter, K., Hervig, R. L., & Kring, D. A. (1998). Accretion and core formation on Mars: molybdenum contents of melt inclusion glasses in three SNC meteorites. *Geochimica et Cosmochimica Acta*, *62*, 2167–2177. doi:10.1016/S0016-7037(98)00132-X.

Rivoldini, A., Van Hoolst, T., Verhoeven, O., Mocquet, A., & Dehant, V. (2011). Geodesy constraints on the interior structure and composition of Mars. *Icarus*, *213*, 451–472. doi:10.1016/j.icarus.2011.03.024.

Roberts, J. H., & Zhong, S. (2006). Degree-1 convection in the Martian mantle and the origin of the hemispheric dichotomy. *Journal of Geophysical Research E: Planets*, *111*. doi:10.1029/2005JE002668.

Rosswog, S. (2009). Astrophysical smooth particle hydrodynamics. *New Astronomy Reviews*, *53*, 78–104. doi:10.1016/J.NEWAR.2009.08.007.

Rubie, D. C., Jacobson, S. A., Morbidelli, A., O'Brien, D. P., Young, E. D., de Vries, J., Nimmo, F., Palme, H., & Frost, D. J. (2015). Accretion and differentiation of the terrestrial planets with implications for the compositions of early-formed Solar System bodies and accretion of water. *Icarus*, *248*, 89–108. doi:10.1016/J.ICARUS.2014.10.015.

Ruedas, T., & Breuer, D. (2021). Electrical and seismological structure of the martian mantle and the detectability of impact-generated anomalies. *Icarus*, *358*. doi:10.1016/j.icarus.2020.114176. arXiv:2003.06799.

Ruedas, T., Tackley, P. J., & Solomon, S. C. (2013). Thermal and compositional evolution of the martian mantle: Effects of phase transitions and melting. *Physics of the Earth and Planetary Interiors*, *216*, 32–58. doi:10.1016/j.pepi.2012.12.002.

Ryan, E. L., Mizuno, D. R., Shenoy, S. S., Woodward, C. E., Carey, S. J., Noriega-Crespo, A., Kraemer, K. E., & Price, S. D. (2015). The kilometer-sized Main Belt asteroid population revealed by Spitzer. *Astronomy and Astrophysics*, *578*, A42. doi:10.1051/0004-6361/201321375. arXiv:1204.1116.

Safronov, V. (1969). Evolution of the protoplanetary cloud and formation of the earth and the planets copy translated from russian, .

Samuel, H., Ballmer, M. D., Padovan, S., Tosi, N., Rivoldini, A., & Plesa, A. C. (2021). The Thermo-Chemical Evolution of Mars With a Strongly Stratified Mantle. *Journal of Geophysical Research: Planets*, *126*, e2020JE006613. doi:10.1029/2020JE006613.

Schäfer, C., Riecker, S., Maindl, T. I., Speith, R., Scherrer, S., & Kley, W. (2016). A smooth particle hydrodynamics code to model collisions between solid, self-gravitating objects. *Astronomy & Astrophysics*, *590*, A19. doi:10.1051/0004-6361/201528060.

Schäfer, C., Speith, R., & Kley, W. (2007). Collisions between equal-sized ice grain agglomerates. *Astronomy and Astrophysics*, *470*, 733–739. doi:10.1051/0004-6361:20077354.

Schools, J. W., & Montési, L. G. (2018). The Generation of Barriers to Melt Ascent in the Martian Lithosphere. *Journal of Geophysical Research: Planets*, *123*, 47–66. doi:10.1002/2017JE005396.

Schultz, P. H., & Gault, D. E. (1975). Seismic effects from major basin formations on the moon and mercury. *The Moon*, *12*, 159–177.

Senshu, H., Kuramoto, K., & Matsui, T. (2002). Thermal evolution of a growing Mars. *Journal of Geophysical Research E: Planets*, *107*, 1–13. doi:10.1029/2001je001819.

Shoemaker, E. M. (1962). *Interpretation of lunar craters*. Academic Press.

Solomon, S. C., Aharonson, O., Aurnou, J. M., Banerdt, W. B., Carr, M. H., Dombard, A. J., Frey, H. V., Golombek, M. P., Hauck, S. A., Head, J. W., Jakosky, B. H., Johnson, C. L., McGovern, P. J., Neumann, G. A., Phillips, R. J., Smith, D. E., & Zuber, M. T. (2005). New perspectives on ancient Mars. doi:10.1126/science.1101812.

Stähler, A. S. C., Khan, A., Banerdt, W. B., Lognonné, P., Ceylan, S., Drilleau, M., Duran, A. C., Garcia, R., Quancheng, H., Kim, D., Lekic, V., Samuel, H., Schimmel, M., Schmerr, N., Sollberger, D., Stutzmann, É., Xu, Z., Antonangeli,

D., Constantinos, C., Davis, P., Irving, J. C., Kawamura, T., Knapmeyer, M., Maguire, R., Marusiak, A. G., Panning, M. P., Perrin, C., Plesa, A.-C., Rivoldini, A., Schmelzbach, C., Zenhäusern, G., Beucler, É., Clinton, J., Dahmen, N., van Driel, M., Gudkova, T., Horleston, A., Pike, T., Plasman, M., & Smrekar, S. (2021). Seismic detection of the Martian core. *Science*, *448*, 443–448. doi:10.1126/science.abi7730.

Suzuki, A., Ohtani, E., & Kato, T. (1998). Density and thermal expansion of a peridotite melt at high pressure. *Physics of the Earth and Planetary Interiors*, *107*, 53–61. doi:10.1016/S0031-9201(97)00123-4.

Tackley, P. J. (2008). Modelling compressible mantle convection with large viscosity contrasts in a three-dimensional spherical shell using the yin-yang grid. *Physics of the Earth and Planetary Interiors*, *171*, 7–18. doi:10.1016/j.pepi.2008.08.005.

Taylor, G. J. (2013). The bulk composition of Mars. *Chemie der Erde*, *73*, 401–420. doi:10.1016/j.chemer.2013.09.006.

Thompson, S. (1990). ANEOS Analytic Equations of State for shock physics codes input manual. *SANDIA Report*, *3*.

Thompson, S., & Lauson, H. (1972). *Improvements in the CHART-D Radiation-hydrodynamic Code III: Revised Analytic Equations of State*. Technical Report Sandia National Laboratories.

Tillotson, J. H. (1962). *Metallic equations of state for hypervelocity impact*. Technical Report General Dynamics San Diego CA General Atomic DIV.

Turcotte, D. L., & Schubert, G. (2002). *Geodynamics*. Cambridge University Press.

Wade, J., & Wood, B. J. (2005). Core formation and the oxidation state of the Earth. *Earth and Planetary Science Letters*, *236*, 78–95. doi:10.1016/J.EPSL.2005.05.017.

Walsh, K. J., Morbidelli, A., Raymond, S. N., O'brien, D. P., & Mandell, A. M. (2011). A low mass for Mars from Jupiter's early gas-driven migration, . doi:10.1038/nature10201.

Wang, Y., & Li, M. (2021). The interaction between mantle plumes and lithosphere and its surface expressions: 3-D numerical modelling. *Geophysical Journal International*, *225*, 906–925. doi:10.1093/gji/ggab014.

Wetherill, G. (1991). Why isn't Mars as big as Earth? In *Lunar and Planetary Science Conference* (p. 1495). volume 22.

Wieczorek, M. A., & Meschede, M. (2018). SHTools: Tools for Working with Spherical Harmonics. *Geochemistry, Geophysics, Geosystems*, *19*, 2574–2592. doi:10.1029/2018GC007529.

Williams, J. P., & Nimmo, F. (2004). Thermal evolution of the Martian core: Implications for an early dynamo. *Geology*, *32*, 97–100. doi:10.1130/G19975.1.

Wingate, C., & Fisher, H. (1993). Strength modeling in SPHC. *Los Alamos Laboratory Report LA-UR-93-3942*, .

Xiang, G., Wang, Z., & Kusky, T. M. (2021). Density and viscosity changes between depleted and primordial mantle at ∼1000 km depth influence plume upwelling behavior. *Earth and Planetary Science Letters*, *576*, 117213. doi:10.1016/J.EPSL.2021.117213.

Yoshizaki, T., & McDonough, W. F. (2020). The composition of Mars. *Geochimica et Cosmochimica Acta*, *273*, 137–162. doi:10.1016/j.gca.2020.01.011. arXiv:1909.07560.

Zahnle, K., Arndt, N., Cockell, C., Halliday, A., Nisbet, E., Selsis, F., Sleep, N. H., Zahnle, K., Arndt, N., Halliday, A., Nisbet, E., Selsis, F., & Sleep, N. H. (2007). Emergence of a Habitable Planet. *Space Sci Rev*, *129*, 35–78. doi:10.1007/s11214-007-9225-z.

Zhong, S., & Zuber, M. T. (2001). Degree-1 mantle convection and the crustal dichotomy on Mars. *Earth and Planetary Science Letters*, *189*, 75–84. doi:10.1016/S0012-821X(01)00345-4.

Zuber, M. T. (2000). Internal structure and early thermal evolution of Mars from Mars global surveyor topography and gravity. *Science*, *287*, 1788–1793. doi:10.1126/science.287.5459.1788.

Zuber, M. T. (2001). The crust and mantle of Mars. *Nature*, *412*, 220–227. doi:10.1038/35084163.

Bibliography

M. S. Clement, N. A. Kaib, S. N. Raymond, and J. E. Chambers. The early instability scenario: Mars' mass explained by Jupiter's orbit. *Icarus*, 367, jun 2021. doi: 10.1016/j.icarus.2021.114585.

N. Copernicus. De revolutionibus orbium coelestium. *Norimbergae, Apud J. Petreium*, 1543.

T. S. Kuhn. *The Copernican revolution: Planetary astronomy in the development of western thought*. Harvard University Press, 1957.

S. E. Lauro, E. Pettinelli, G. Caprarelli, L. Guallini, A. P. Rossi, E. Mattei, B. Cosciotti, A. Cicchetti, F. Soldovieri, M. Cartacci, F. Di Paolo, R. Noschese, and R. Orosei. Multiple subglacial water bodies below the south pole of Mars unveiled by new MARSIS data. *Nature Astronomy 2020 5:1*, 5(1):63–70, sep 2020. ISSN 2397-3366. doi: 10.1038/s41550-020-1200-6.

G. V. Schiaparelli. *Osservazioni astronomiche e fisiche sull'asse di rotazione e sulla topografia del planeta Marte: fatte nella Reale Specola di Brera in Milano coll'equatoriale di Merz...; memoria. Durante l'opposizione del 1877*, volume 1. 1878.

Chapter 5

Sputnik Planitia as an Impactor Remnant

While Pluto may have lost full planetary status back in 2006, the dwarf planet has invigorated the scientific community in recent years due to the astonishing images returned by the New Horizons space probe that made its closest approach to Pluto in 2015. The most striking feature discovered was a huge, nitrogen-filled basin now known as *Sputnik Planitia* (Stern et al., 2015; Schenk et al., 2018), whose precise origin and geophysical implications have been debated ever since (Nimmo et al., 2016; Johnson et al., 2016; Denton et al., 2021).

In this chapter, a novel impact mechanism relevant to the cold conditions of icy dwarfs such as Pluto is described, and its potential explanation of the Sputnik Planitia basin is investigated. The key result of this study is that large impacts into icy dwarfs from differentiated (ice mantle and rock core) impactors can produce regions dominated by impactor material, and that the rocky core of the impactor can be buried beneath the the impactor ice as a hidden mass excess at the core-mantle boundary. Such hidden heterogeneities in a body's interior can drive geophysical processes such as true polar wander and isostatic relaxation that may be responsible for the properties of Sputnik Planitia observed today.

Sputnik Planitia as an impactor remnant indicates an ancient rocky mascon in an oceanless Pluto

Harry A. Ballantyne[1], Erik Asphaug[2], C. Adeene Denton[3], Alexandre Emsenhuber[4] and Martin Jutzi[1]

[1]Physics Institute, University of Bern, Gesellschaftsstrasse 6, 3012 Bern, Switzerland.
[2]Lunar and Planetary Laboratory, University of Arizona, 1629 E. University Boulevard, Tuscon, 85721, Arizona, USA.
[3]Department, Organization, Street, City, 610101, State, Country.
[4]University Observatory, Ludwing-Maximilians Universität München, Scheinerstr. 1, 81679 München, Germany.

Contributing authors: harry.ballantyne@unibe.ch; asphaug@lpl.arizona.edu; denton15@purdue.edu; emsenhuber@usm.lmu.de; martin.jutzi@unibe.ch;

Abstract

In 2015, the New Horizons space probe revealed Pluto's surface to be geologically complex[1]; dominated by a huge, nitrogen-ice filled basin named Sputnik Planitia[1,2]. While the feature's shape hints at an impact origin[3], previous studies have been incapable of explaining its peculiar, elongated geometry[4,5]. Moreover, its current position on Pluto's equator suggests a hidden concentration of mass (or "mascon") present beneath the basin[6], currently attributed[7,8] to the sustained uplift of liquid water directly below the impact site. Such a scenario, however, requires the simultaneous retention of a cold, stiff ice shell capable of preserving extensive post-impact topographic variation atop a warm subsurface ocean: two seemingly contradictive propositions. Here we propose a novel impact mechanism that introduces a long-lived rocky mascon beneath Sputnik Planitia, and that reproduces the topographical shape of the feature in three dimensions, without requiring a present-day subsurface ocean. Using a suite of smoothed-particle hydrodynamics

(SPH) simulations, we show that an approximately 800-km-diameter, differentiated body impacting an oceanless (sub-solidus) Pluto at an angle of around 30° creates a distinct region of impactor material with a morphology remarkably similar to that observed. The result relies on the effects of material strength, usually ignored at these scales[9,10,11,12], represented by friction. The rocky impactor core thereby remains intact as it descends to the ice-rock boundary of Pluto, to which it accretes as a deep mascon. Beyond providing a new, more plausible explanation for Sputnik Planitia's origin and migration to Pluto's equator, our results highlight a previously undiscovered impact regime—collisions between rigid, low temperature bodies leading to distinctive impactor-material dominated regions—that may be of great importance in shaping the complex interiors of icy dwarf planets[13].

1 Main

Large-scale impacts are thought to be responsible for some of the most distinctive features of the Solar System's planetary residents, such as Mars' stark hemispherical dichotomy[14,15], or Earth's oversized moon[16]. When investigating these events using computational methods, the material properties (or "strength") of the solid matter that makes up the colliding bodies are usually ignored under the assumption that hydrostatic and impact-induced pressure forces dominate over their effects in this size regime. Recent work has disputed this claim[17], illustrating the importance of shear strength even at Mars-scale. We find that strength plays a substantial role in shaping both the surface and deep interior of small, cold icy-dwarfs such as Pluto during large-scale impacts, and that the unusual morphology of Sputnik Planitia is a natural consequence of such events.

We simulate a range of potential large-scale collisions into a Pluto-like body using the planetary-scale specialised SPH code SPHLATCH[18,17] that has recently been used to study a wide range of impact regimes[19,20,21,22,23,24,25,26]. Shear strength and plasticity are included through a Drucker-Prager-like yield criterion, which is a function of both pressure and temperature. At lower temperatures, yield strength is more important, making Pluto's icy conditions particularly stress-resistant. For smaller bodies, such as asteroids, some impact models also include further geophysical parameters such as cohesion, tensile fracture and porosity[27], however these effects are negligible at the size-scales considered here. We therefore model our bodies to be composed of granular material without cohesion. The specific strength parameters follow those of previous impact studies[28,29,30,31].

Pluto is modelled as a differentiated body with a rocky core making up two thirds of the total mass, as inferred by observations[32]. The phase-state of the surrounding H_2O-mantle is unknown, however various recent works have sought to justify a subsurface water ocean beneath a thick ice-shell[7,8]. Such a

scenario may require special conditions that prevent the freezing of this ocean over geological time, such as an unusually high concentration of ammonia that reduces the water's melting temperature[7] and/or a continually-replenished layer of gas hydrates that provides insulation between the ice-shell and the relatively warm liquid ocean[8]. For the majority of our simulations, we model Pluto's mantle to be composed entirely of water-ice. The temperature of this ice-shell is varied between 70 K and 250 K in steps of 60 K.

The parameters of the impacting body (or "impactor") are far less constrained. Kuiper Belt Objects (KBOs) are known to have a wide range of radii[33,34,35,36]. While more than 2000 KBOs have been observed[37], only a handful have meaningful mass estimates[38], making their densities (and thus internal compositions) hard to define. Even those with estimates for both radius and mass yield a large range of possible rock-to-ice ratios within 1σ[38]. We therefore allow for a broad spectrum of impactors, with radii of 200-550 km and internal compositions ranging from undifferentiated (composed entirely of rock or ice) to differentiated with rocky core mass fractions of 5-66%.

The angles and velocities of our simulated impacts are 0-45° and 1.0-1.4 v_{esc}, respectively, where v_{esc} is the mutual escape speed of the two bodies (~ 1.2 km/s) given by $v_{\mathrm{esc}} = \sqrt{\frac{2G(m_{\mathrm{imp}}+m_{\mathrm{imp}})}{r_{\mathrm{imp}}+r_{\mathrm{imp}}}}$, where m is mass, r is radius, G is the gravitational constant and the subscripts $_{\mathrm{tar}}$ and $_{\mathrm{imp}}$ denote the target and impactor, respectively. These were chosen to lie within the "merging" impact regime whereby the majority of the impactor is rapidly accreted onto the target[21,26].

Upon examining the outcomes of our parameter space, we find that distinct trends emerge, with some examples of these being illustrated in Figure 1. For head-on (0°) impacts involving a body composed entirely of ice, the impactor undergoes dramatic deformation upon impact with Pluto's ice mantle, spreading out across the surface in a "splat"-like distribution similar to previous work investigating the formation of the Moon's dichotomous landscape[39]. A rock impactor, on the other hand, pierces through Pluto's ice-shell in a head-on impact while staying largely intact, only experiencing major deformation upon contact with the stiff, rocky core. The impactor then spreads across the surface of the core, again resulting in a thin, circular, "splat" distribution. While both scenarios cause a transient crater in Pluto's mantle, the greatly deformed ice impactor remains at the surface throughout the subsequent crater-collapse, essentially "surfing" atop the Pluto mantle that evolves below, whereas the rock impactor is undisturbed by the crater-collapse above, being buried by the infalling Pluto ice and leading to a hidden rocky reservoir at the core-mantle boundary. Additionally, the transient crater is significantly larger for the ice impactor when comparing impactors of the same mass and impact velocity, owing predominantly to the larger radius due to ice's much lower density than rock.

At higher impact angles, the distribution of impactor material becomes progressively more asymmetric, extending downrange in the impact plane. For the ice impactor, the majority of its material again remains above the ice

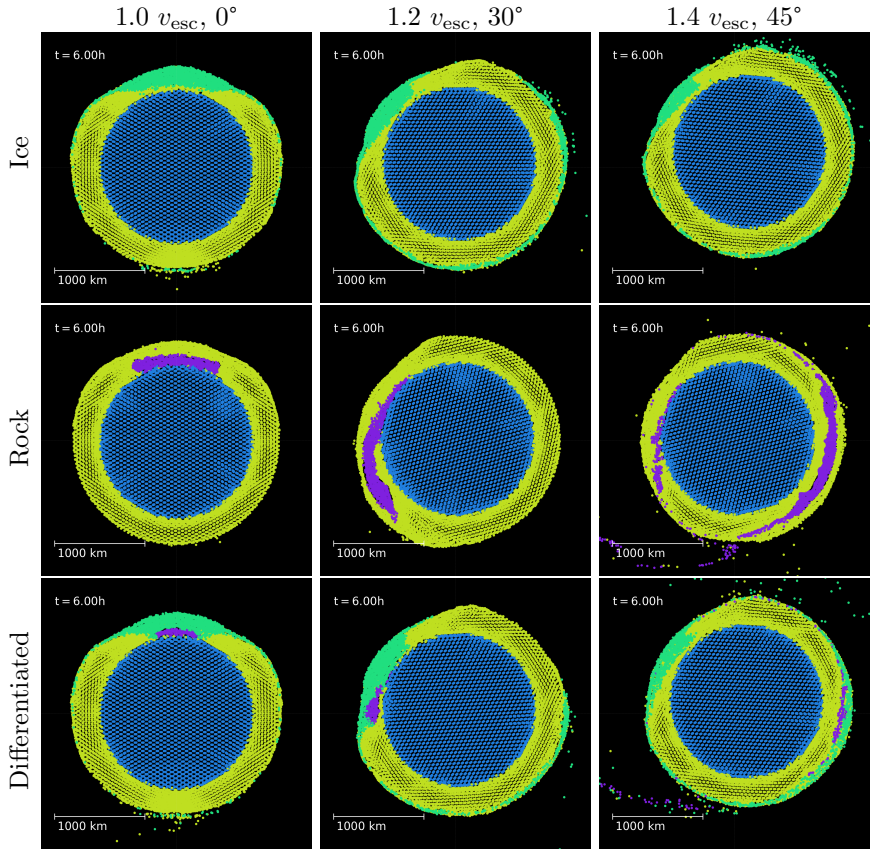

Fig. 1: SPH simulation results illustrating various regimes in the parameter space. Each plot is a slice of thickness 300 km in the impact plane, and displays the target 6 hours after first contact with the impactor. Colour signifies material composition and original parent body; blue denotes target rock, yellow target ice, purple impactor rock and green impactor ice. The impactor's mass in each case is equal, and corresponds to our best-fitting case (approximately the mass of Vesta). The interior temperature profiles of the two bodies prior to impact correspond to the nominal case.

mantle of Pluto, however the break-up of the body upon impact leads to some of its material to be thrust into orbit, resulting in a prominent ring of impactor ice that forms along the impact plane as the majority of this material re-impacts. The extent of this ring depends on both impact angle and speed, with higher values leading to more ejected material and thus a more extensive ring.

For the rock impactor, its higher density, melting temperature and material strength make it much more resistant to deformation and break-up. For lower impact angles (usually $\lesssim$30°, depending on impactor radius and velocity) the impactor is able to remain largely intact, albeit with increasing spread along

the impact plane with higher speeds and angles. As in the head-on case, the rock impactor is buried beneath Pluto's ice mantle following crater collapse; however, after reaching the core mantle boundary, the impactor is unable to overcome the strength of the rigid core and is thus partially deflected onto a more radially-outward path. While some of the rocky impactor material remains stationary at the core mantle boundary, the portion of material with a radially-outward velocity component spreads through the mantle towards the surface.

The impactor's rise towards the surface is additionally supported by the strength of the cold, stiff ice below, which extends through mantle material outside of the initial impact site that has not experienced significant heating, and thus retains most of its pre-impact strength. At lower impact velocities and/or angles, the impactor eventually comes to a halt before reaching Pluto's surface, and either slides back down the cold ice towards the core mantle boundary, or if massive enough to overcome the strength of the mantle ice, sinks directly through the mantle towards the core. At higher impact velocities and/or angles (usually $\gtrsim$45°; lower angles possible for high impactor masses and velocities) the impactor reaches the surface and breaks-up to form an iso-longitudal ring of impactor material similar to the oblique cases for the ice impactor.

A differentiated impactor leads to scenarios that are essentially a superposition of the two end-member, one-material cases, with head-on impacts leading to the impactor's rocky core being deposited at Pluto's core-mantle boundary, buried below the impactor ice that fills the transient crater above. A key difference from the undifferentiated cases that arises, however, is that significant impactor ice is dragged down to core-mantle boundary with the impactor core, causing the impact site to consist almost entirely of impactor material down to Pluto's core.

It is these intermediate parameters that lead to the most promising cases to produce Sputnik Planitia: core mass fractions 5-30%, impact angles 15-30°, and an impactor radius of approximately 400 km (corresponding to a mass similar to that of Vesta). An example simulation in this range (and also our best-fitting case to observations) is shown in Figure 2. Here, the impactor initially excavates the material of the immediate impact site (Figure 2a), creating an elliptical transient crater. As the ice shell is first to make contact with Pluto, it acts to initially shield the core from significant deformation and heating upon impact. This effect, along with rock's aforementioned extra resistance to deformation compared to ice, allows the impactor core to remain almost entirely intact as it slides along the Pluto's ice shell towards the surface, eventually coming to a stop while still embedded in within mantle (Figure 2b). The transient crater is then filled with the infalling impactor ice, and the impactor core slides back towards Pluto's core along the same path it had carved out towards the surface, ultimately settling as a mascon near the core-mantle boundary (Figure 2c). Figure 3 shows the final distribution of the impactor material, with a remarkable resemblance to Sputnik Planitia. The near-spherical shape

in the northern hemisphere corresponds to the initial point of impact where a more classical crater forms and collapses, whereas the pointed, triangular shape in the south corresponds to the sliding region of the impactor core.

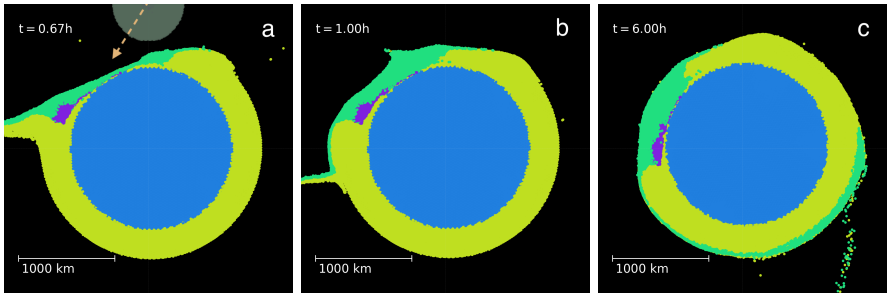

Fig. 2: Time series of the best case ($\sim$ 400 km radius impactor with 15% core mass fraction, 30° impact angle and 1.2 v_{imp} impact velocity). Slice depth is 300 km in the impact plane. Colours represent composition and parent body, as in Figure 1. (a) Shortly after impact; the transient crater is still present and the impactor core has risen towards the surface after deflection from Pluto's core, but has almost slowed to a halt. The faded object indicates the impactor's initial position and size upon impact, and the arrow displays it's velocity vector. (b) Immediately after transient crater collapse, which has been filled by infalling ice of the impactor mantle. The impactor core has begun sliding back towards the core-mantle boundary. (c) Pluto's post-impact state, 6 hours after the collision.

We propose that the overall shape of this feature could remain intact if the impactor mantle's precise composition had a slightly higher density than that of the primordial Pluto, as its greater load on the silicate core would lead to a local depression via isostasy. Furthermore, the dense buried mascon provided by the impactor's rocky core would produce a significantly deeper region of the basin. N_2 ice would quickly accumulate in the basin[40], culminating in the positive mass anomaly that drove Sputnik Planitia into its current position through true polar wander. The region of the basin with the strongest positive anomaly—the southernmost, narrow section directly above the mascon—would be forced closest to the equator, matching present day observations. In addition, as true polar wander best explains the distribution of extensional features on Pluto[6], a more dominant positive anomaly provided by such a rocky mascon may be a better match to observational constraints.

Such a density contrast between the mantle of the impactor and that of (primordial) Pluto may be related to their dramatic contrast in size. Smaller objects are less likely to have undergone chemical differentiation, if they did experience differentiation it is likely to only be partial[41]. Such partial differentiation has even been suggested for bodies as large as Charon[42,43,44,45]. The

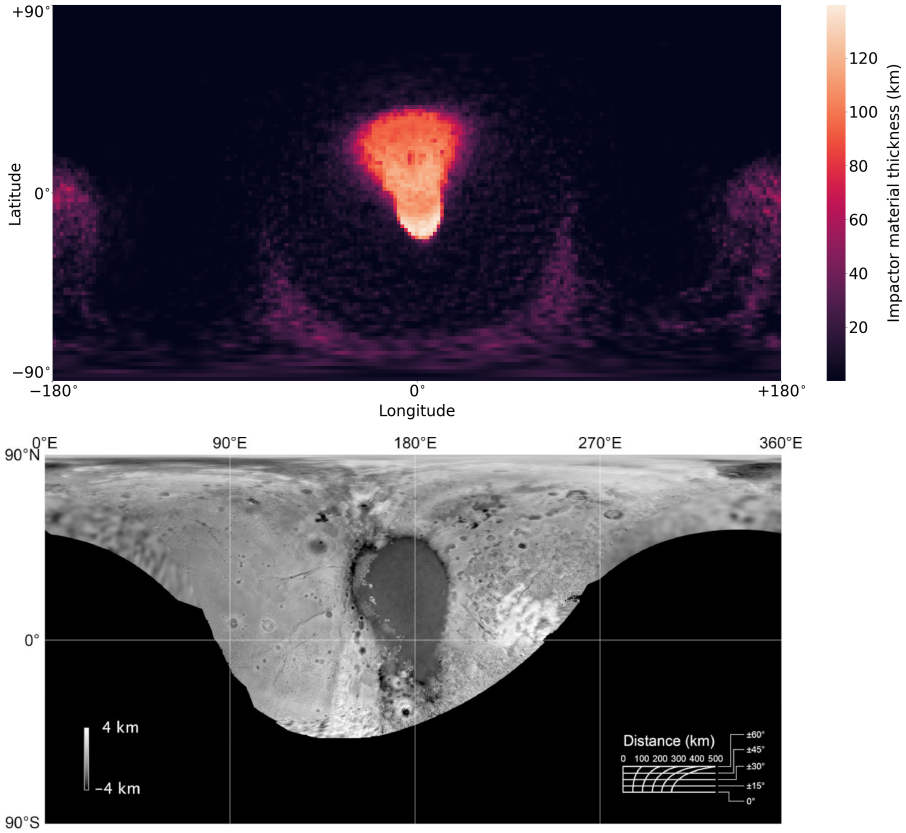

Fig. 3: (Top) Equirectangular projection of the distribution of impactor material post-impact, for the same case as Figure 2. The thickness is measure to a depth of $\sim$ 150 km. The near-elliptical region north of the equator corresponds to the initial impact site and initial transient crater. The tail of the distribution that extends south of the equator is due to the impactor core sliding through Pluto's mantle. (Bottom) The observed elevation distribution of Pluto, with Sputnik Planitia in the centre. Taken from ref.[2].

impactor responsible for Sputnik Planitia may therefore have possessed a partially differentiated mantle of "dirty ice" containing both rock and ice, thus explaining our proposed higher density. In addition, less efficient differentiated could also lead to more contaminants in the impactor core, which would help this material to remain stationary at the core-mantle boundary to the present day as its lower density relative to that of the Pluto core would provide buoyancy and thus prevent viscous relaxation.

The proposed impact scenario occurs for a significant range of parameters, as described, with different impactor parameters controlling various aspects of the impactor material distribution's final outcome. As one would expect,

impactor radius controls the overall size of the distribution. Impactor core mass fraction determines the width of the "tail" of our teardrop-like distribution, due to its proportionality to core radius. Although impact velocity does affect the size of the transient crater and thus the size of the elliptical, ice-dominated region of the impact site, its dominant effect is its influence on the length of the distribution's tail, as higher velocities lead to the core travelling further through the mantle before coming to a halt and descending back towards the core-mantle boundary. Taking all of these parameters into consideration, we find the most promising case to produce Sputnik Planitia is a ∼400 km radius impactor with a core fraction of 15% colliding into Pluto with a velocity of 1.2 times mutual escape (∼6 km/s) and at an angle of 30° (Figure 2).

All of the cases described so far correspond to our nominal Pluto model, which has a mantle temperature of ∼130 K and a core temperature of ∼195 K. This mantle temperature agrees with average ice shell temperatures used in previous impact studies for Pluto[4,5], as well as those predicted by studies of Pluto's thermal evolution, at least for early times ($\lesssim$ 250-500 Myr after formation)[46,47] consistent with the greatly increased likelihood of giant impacts during this period[48]. These temperatures, however, are not well constrained, making it necessary to investigate other mantle temperatures and observe the effect on our results. At a lower ice temperature of ∼70 K, we find that our distribution looks very similar to that of the nominal case (Figure 9 (top)). At ∼190 K, the distribution also looks similar; however, the impactor core sinks slightly into the ice mantle towards Pluto's core, causing more primordial Pluto ice to penetrate the region between the impactor mantle and core material (Figure 9 (middle)). At our highest mantle temperature of ∼250 K, the impact causes significant melting and thus induces far more mixing between the Pluto's primordial ice/water the impactor ice. This causes the impactor distribution to be less well-defined, and more ellipitical in shape (Figure 9 (bottom)).

Our nominal core temperature was chosen to avoid an excessive temperature contrast at the core-mantle boundary, as to decrease numerical error due to limitations of the SPH method, however it is consistent with the average initial core temperature used in some previous models[49,47]. After ∼500 Myr, it has been suggested that the core will heat to an average of ∼500-700 K due to radiogenic heating[49,50,47]. We therefore repeated our best-fitting impact simulation using a core temperature of ∼500, and find only negligible differences from our nominal case.

As already noted, several previous studies have suggested a subsurface ocean to be present in Pluto. To examine the effect of such an ocean on our results we again repeated our best-fitting impact but with the inclusion of a liquid water layer below our ice shell. We investigated three ocean thicknesses of 50 km, 100 km, and 150 km, following previous studies[5]. We find that the distribution of impactor material still matches reasonably well with a subsurface ocean of 50 km thickness, albeit with a more compact morphology, with the elliptical region formed by the impactor's first contact with Pluto being most

notably reduced in area (Figure 12). This trend continues for the 100 km and 150 km ocean thicknesses, which display final impactor distributions with an even smaller contrast in area between the elliptical region of immediate impact and the tail carved out by the impactor core. These cases no longer bear great resemblance to the morphology of Sputnik Planitia we observe today, and are therefore unlikely candidates for the scenario presented in this study.

These results provide an explanation for Sputnik Planitia's unusual morphology and proposed positive gravity contribution without the need for a subsurface ocean suggested by previous studies. Indeed, we find that thinner oceans ($\lesssim$ 50 km thickness) are favoured for our proposed scenario. This is consistent with previous estimates of subsurface ocean thickness in Pluto inferred by thermal evolution models for a typical ice reference viscosity (10^{14} Pa s) and a comparable ammonia content to other KBOs ($\lesssim$ 1%)[51,52,46,49,53,54]. Moreover, if the effect of ammonia is negligible then Pluto may not have any subsurface ocean at all[51,49]. Finally, we note that the mechanism presented here need not be restricted to the study of Sputnik Planitia's formation; our results show that merging impacts between icy bodies up to the mass of Pluto readily produce heterogeneous interior structures that may remain to the present day, and may therefore play an important role in determining the properties (both interior and exterior) of the icy worlds that inhabit the frigid outer edges of planetary systems.

2 Methods

2.1 Smoothed Particle Hydrodynamics (SPH)

In this study, we performed three-dimensional impact simulations using the SPHLATCH code, which utilises the SPH method. SPH is a lagrangian-based method whereby a continuum medium is represented by a collection of so-called "particles" that each correspond to a fixed mass that is smoothed out over a sphere of radius h (the smoothing length). Physical quantities such as density and internal energy for a given particle are calculated through a kernel-based interpolation method across all neighbouring particles within $2h$. To maintain an approximately constant number of neighbours within each particle's smoothing sphere, the smoothing length is variable, and thus controlled by density (lower density regions correspond to higher smoothing lengths). Each simulation used a total of 200,000 particles, but the best case was repeated with 1,000,000 particles to check that our results had converged. Although the high-resolution run was used for the best case plots (Figure 2 and Figure 3), only negligible differences were seen between the two resolutions, and we therefore consider all of our simulations to be sufficiently resolved.

2.2 Material Properties

Pressure and temperature are determined via the ANEOS equation of state[55,56], using input parameters for dunite[28] and ice[57,58,59,60]. Material

strength is modelled using a Drucker-Prager yield criterion that is a function of pressure and temperature[61,27]. A full description of the strength model used in SPHLATCH is given in ref.[17] (note that we include the corrections detailed in ref.[62]).

The input parameters for our strength model are given in Table 1. For dunite we follow ref.[28]. For ice, we use slightly modified values of ref.[31]; these parameters are based on ref.[30], who derived values by fitting to experimental data on the quasi-static shear strength, friction and dynamic tensile strength. Ref.[31] adapted these parameters to represent the cold temperatures of large icy satellites such as Ganymede and Europa, which better fit the conditions of this study. We note that other, more recent studies have used different strength parameters for ice that would result in significantly higher yield strength[63,64,5]. These studies do not give in-depth justification of these parameters, and state some values that appear to be erroneous (e.g. a damaged coefficient of friction, μ_d, of 0.8, which should be 0.2 according to their reference[65]). We therefore opt for the more rigorously justified parameters of ref.[31], with our only modification being the calculation of yield strength for damaged (fractured) ice, where we use the following equation given in ref.[65]:

$$Y_d = \min(Y_{d,l}, Y_{d,h}) \tag{1}$$

with

$$Y_{d,l} = \mu_{d,l} P \tag{2}$$

and

$$Y_{d,h} = \mu_{d,h} P + Y_{0,h} \tag{3}$$

where P is pressure, $\mu_{d,l}$ and $\mu_{d,h}$ are the coefficients of friction for damaged ice at low and high pressures, respectively, and $Y_{0,h}$ is the y-intercept of empirical fit to the high pressure experiment data. Due to the large, planetary-scale of the impacts considered in this study, we consider all material to be fully-damaged.

2.3 Impactor Distribution Maps

To calculate the distribution of the impactor material we utilise a spherical grid similar to ref.[62]. First, we assign an impactor mass fraction, $\beta_{\rm imp}$, to each particle, which is simply $\beta_{\rm imp}$=1 for impactor particles and $\beta_{\rm imp}$=0 for the remaining particles making up the target. Using an SPH sum, we can calculate this value for any point in space, i.e.:

$$\beta_{\rm imp}(\mathbf{x}) = \sum_b \beta_{\rm imp} W(\mathbf{x} - \mathbf{x}_b, h_b) \tag{4}$$

where $\mathbf{x}$ is the spatial point of interest and b indicates a specific particle neighbour. Using this method, we calculate $\beta_{\rm imp}$ for each point on a spherical grid with a resolution of 7 km in radius and $\frac{\pi}{100}$ in latitude and longitude. The total thickness of impactor material, $z_{\rm imp}$, for each latitude and longitude is then calculated as the sum of all $\beta_{\rm imp}$ down to a specified depth, multiplied by the grid resolution in radius, Δr:

$$z_{\mathrm{imp},jk} = \Delta r \sum_{i=i_{\min}} \beta_{\mathrm{imp},ijk} \tag{5}$$

where the subscripts i, j and k correspond to the grid cell index for each radius, latitude and longitude, respectively, and $i_{\min}$ is the index corresponding to the specified depth. We use a depth of ∼150 km.

3 Supplementary Information

3.1 Parameters for the Strength Model

Table 1: Parameters used in the material strength model. The parameters for ice come from ref.[31] and ref.[65]. The parameters for rock (dunite) are from ref.[28].

Parameter	Description	Value for ice	Value for rock
Y_m	Shear strength at $P = \infty$	115 MPa	3.5 GPa
Y_0	Cohesion	0	0
$Y_{0,h}$	Y-intercept of high pressure model	8.3 MPa	0
μ_i	Coefficient of friction for intact material	2	2
$\mu_{d,l}$	Coefficient of friction for damaged material at low pressure	0.55	0.8
$\mu_{d,h}$	Coefficient of friction for damaged material at high pressure	0.2	0.8
T_m	Melting temperature	273.2 K	1500 K
ξ	Thermal softening parameter	1.84	1.2
G	Shear modulus	3.52 GPa	72 GPa

3.2 Interior profiles

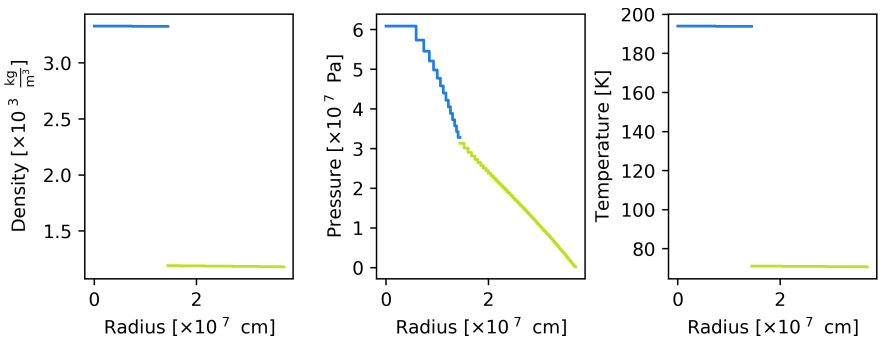

Fig. 4: Interior profiles for the nominal impactor (core mass fraction of 15%). Colour indicates composition, with blue corresponding with rock material and green with ice.

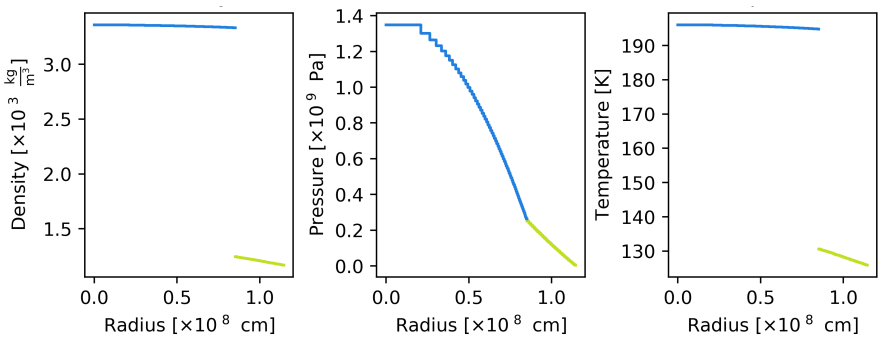

Fig. 5: Interior profiles for the nominal target body. Colour denotes composition, as in Figure 4.

3.3 Example impact simulation without strength.

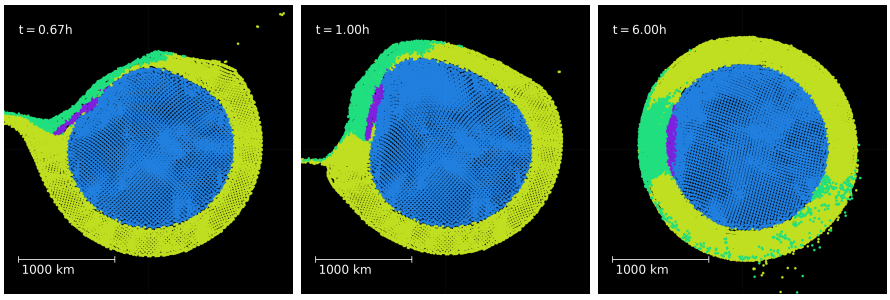

Fig. 6: Time series of the nominal impact case (same as Figure 2) without any strength. Here we see that Pluto's core is greatly deformed during the impact process, in great contrast to our simulations including strength. Colour denotes composition and parent body, as in Figure 2.

3.4 Effect of Mantle Temperature

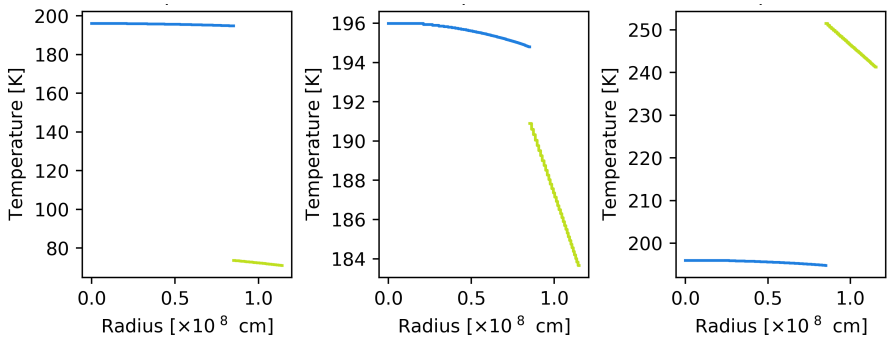

Fig. 7: Temperature profiles explored for the Pluto mantle other than the nominal case of Figure 2. Colour denotes composition, as in Figure 4.

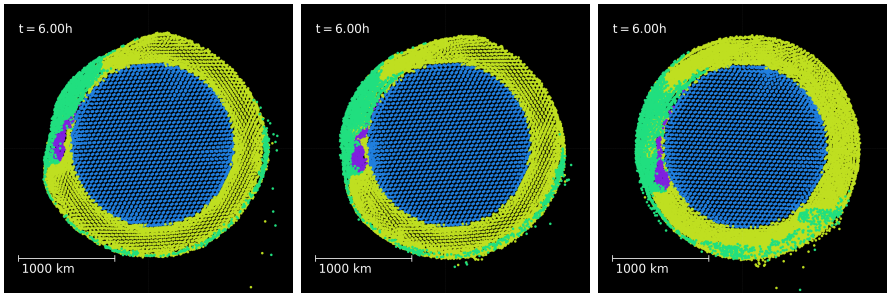

Fig. 8: 300 km slices in the impact plane showing the distribution of material after the nominal impact for each pre-impact ice mantle temperature profile shown in Figure 7 (in the same order from left to right). Colour denotes composition and parent body, as in Figure 2.

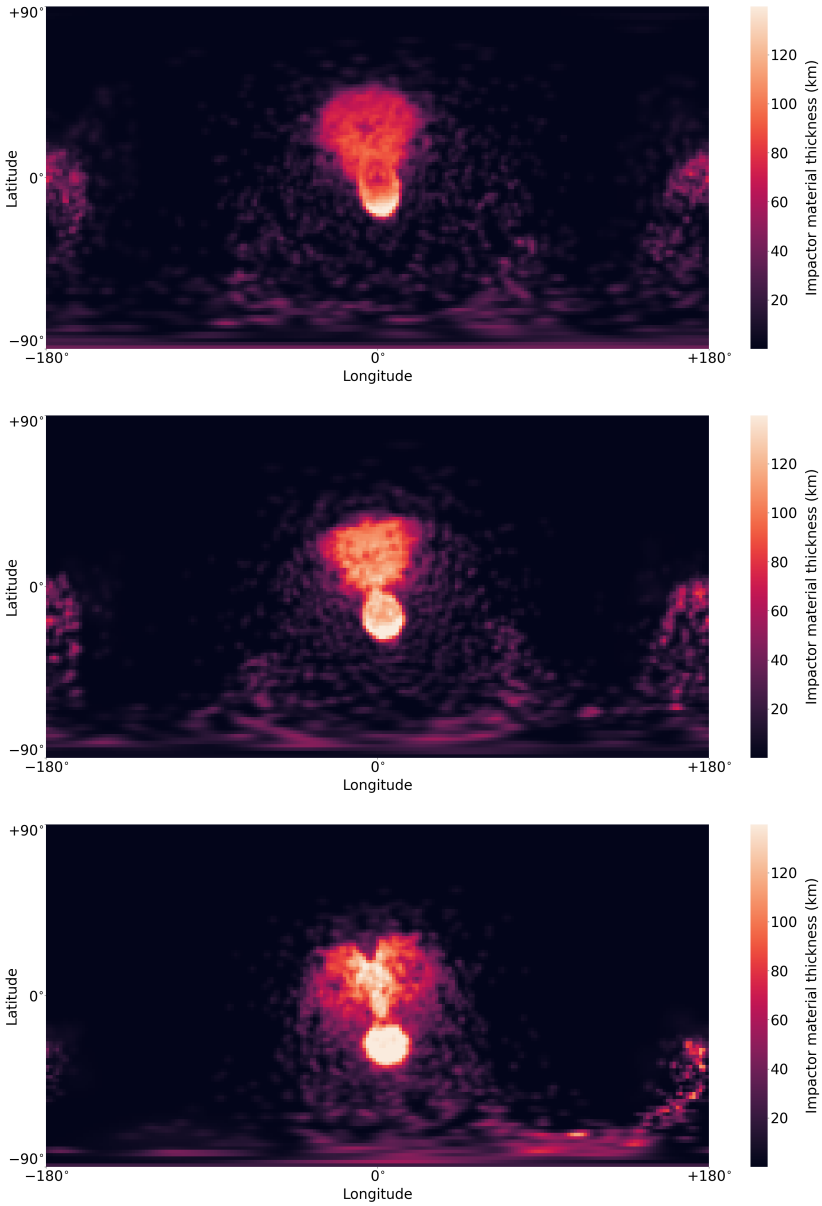

Fig. 9: Equirectangular projection of the post-impact impactor material distribution for each temperature profile of Figure 7, with increasing temperature from top to bottom (i.e. the uppermost case corresponds with the leftmost case of Figure 7).

3.5 Subsurface Ocean

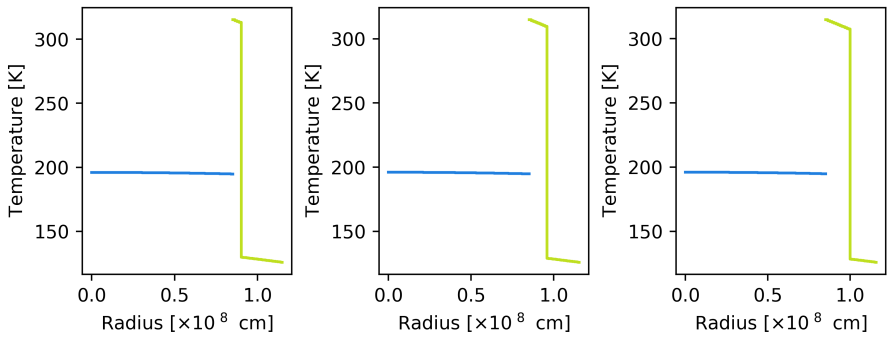

Fig. 10: Temperature profiles for each subsurface ocean thickness investigated for Pluto (50 km, 100 km and 150 km from left to right). Colour denotes composition, as in Figure 4.

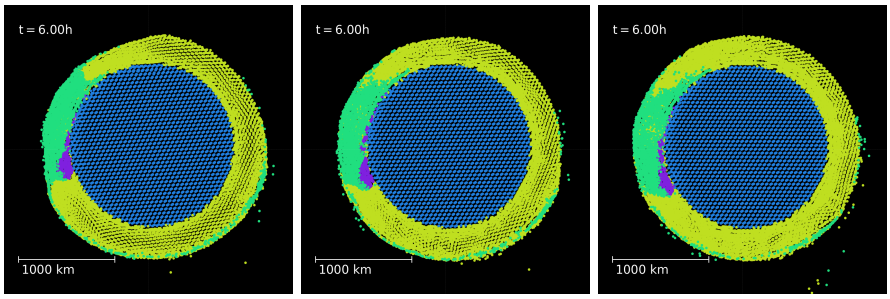

Fig. 11: 300 km slices in the impact plane showing the distribution of material after the nominal impact for each pre-impact subsurface ocean thickness (50 km, 100 km, 150 km from left to right). Colour denotes composition and parent body, as in Figure 2.

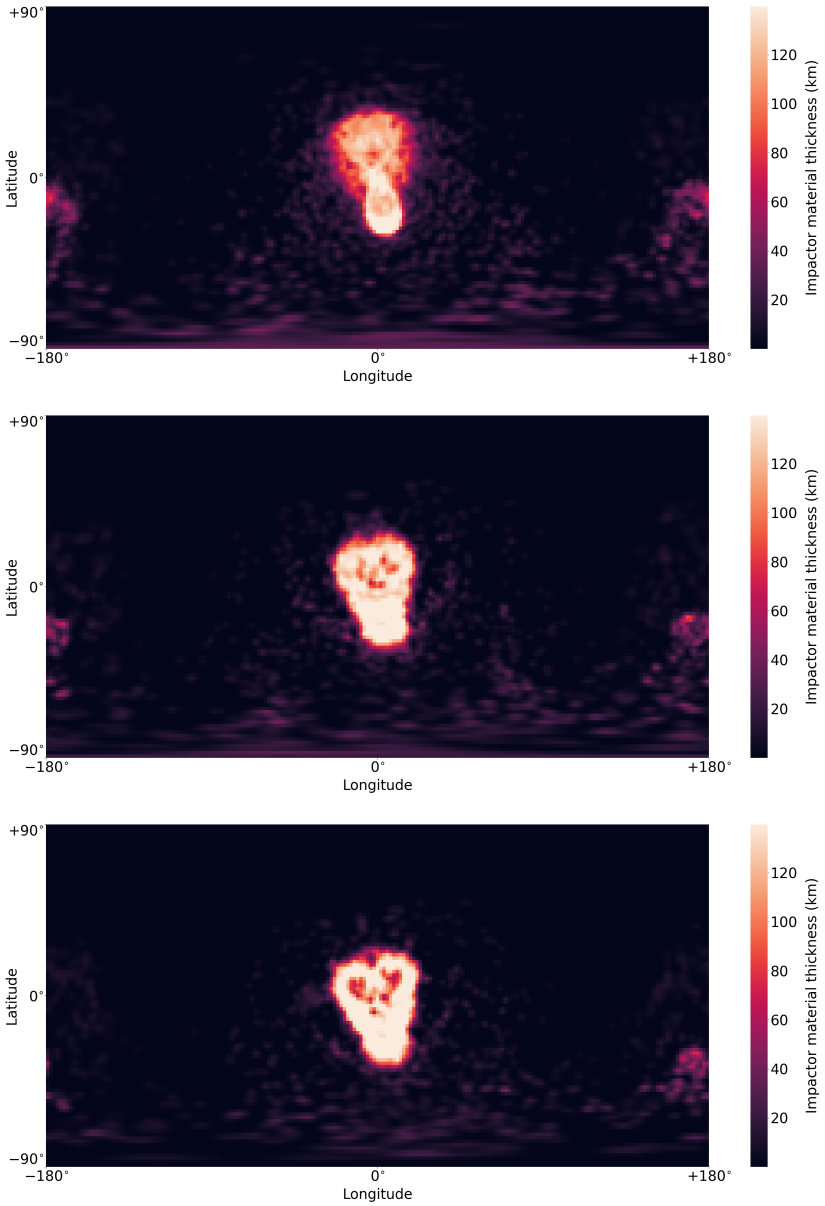

Fig. 12: Equirectangular projection of the post-impact impactor material distribution for each subsurface ocean thickness (50 km, 100 km and 150 km from top to bottom).

References

[1] Stern, S. A. *et al.* The pluto system: Initial results from its exploration by New Horizons. *Science* **350** (6258) (2015). https://doi.org/10.1126/science.aad1815 .

[2] Schenk, P. M. *et al.* Basins, fractures and volcanoes: Global cartography and topography of Pluto from New Horizons. *Icarus* **314**, 400–433 (2018). https://doi.org/10.1016/J.ICARUS.2018.06.008 .

[3] Moore, J. M. *et al.* The geology of Pluto and Charon through the eyes of New Horizons. *Science* **351** (6279), 1284–1293 (2016). https://doi.org/10.1126/SCIENCE.AAD7055/SUPPL_FILE/MOORE.SM.PDF .

[4] Johnson, B. C., Bowling, T. J., Trowbridge, A. J. & Freed, A. M. Formation of the Sputnik Planum basin and the thickness of Pluto's subsurface ocean. *Geophysical Research Letters* **43** (19), 10,068–10,077 (2016). https://doi.org/10.1002/2016GL070694 .

[5] Denton, C. A. *et al.* Pluto's Antipodal Terrains Imply a Thick Subsurface Ocean and Hydrated Core. *Geophysical Research Letters* **48** (2), e2020GL091596 (2021). https://doi.org/10.1029/2020GL091596 .

[6] Keane, J. T., Matsuyama, I., Kamata, S. & Steckloff, J. K. Reorientation and faulting of Pluto due to volatile loading within Sputnik Planitia. *Nature 2016 540:7631* **540** (7631), 90–93 (2016). https://doi.org/10.1038/nature20120 .

[7] Nimmo, F. *et al.* Reorientation of Sputnik Planitia implies a subsurface ocean on Pluto. *Nature 2016 540:7631* **540** (7631), 94–96 (2016). https://doi.org/10.1038/nature20148 .

[8] Kamata, S. *et al.* Pluto's ocean is capped and insulated by gas hydrates. *Nature Geoscience* **12** (June), 407–410 (2019) .

[9] Canup, R. M. A giant impact origin of Pluto-Charon. *Science* **307** (5709), 546–550 (2005). https://doi.org/10.1126/science.1106818 .

[10] Canup, R. M. On a giant impact origin of charon, Nix, and Hydra. *Astronomical Journal* **141** (2), 35 (2011). https://doi.org/10.1088/0004-6256/141/2/35 .

[11] Sekine, Y., Genda, H., Kamata, S. & Funatsu, T. The Charon-forming giant impact as a source of Pluto's dark equatorial regions. *Nature Astronomy* **1** (2017). https://doi.org/10.1038/s41550-016-0031 .

[12] Arakawa, S., Hyodo, R. & Genda, H. Early formation of moons around large trans-Neptunian objects via giant impacts (2019).

[13] Tancredi, G. & Favre, S. Which are the dwarfs in the Solar System? *Icarus* **195** (2), 851–862 (2008). https://doi.org/10.1016/j.icarus.2007.12.020 .

[14] Marinova, M. M., Aharonson, O. & Asphaug, E. Mega-impact formation of the Mars hemispheric dichotomy. *Nature* **453** (7199), 1216–1219 (2008). https://doi.org/10.1038/nature07070 .

[15] Golabek, G. J., Emsenhuber, A., Jutzi, M., Asphaug, E. I. & Gerya, T. V. Coupling SPH and thermochemical models of planets: Methodology and example of a Mars-sized body. *Icarus* **301**, 235–246 (2018). https://doi.org/10.1016/j.icarus.2017.10.003, arXiv:1710.03250 .

[16] Canup, R. M., Ward, W. R. & Cameron, A. G. W. A Scaling Relationship for Satellite-Forming Impacts. *Icarus* **150** (2), 288–296 (2001). https://doi.org/10.1006/icar.2000.6581 .

[17] Emsenhuber, A., Jutzi, M. & Benz, W. SPH calculations of Mars-scale collisions: The role of the equation of state, material rheologies, and numerical effects. *Icarus* **301**, 247–257 (2018). https://doi.org/10.1016/j.icarus.2017.09.017, arXiv:1710.03245 .

[18] Reufer, A., Meier, M. M. M., Benz, W. & Wieler, R. A hit-and-run Giant Impact scenario. *Icarus* **221** (1), 296–299 (2012). https://doi.org/10.1016/j.icarus.2012.07.021, arXiv:1207.5224 .

[19] Emsenhuber, A. & Asphaug, E. Fate of the Runner in Hit-and-run Collisions. *The Astrophysical Journal* **875** (2), 95 (2019). https://doi.org/10.3847/1538-4357/ab0c1d, arXiv:1903.04508 .

[20] Emsenhuber, A. & Asphaug, E. Graze-and-merge Collisions under External Perturbers. *The Astrophysical Journal* **881** (2), 102 (2019). https://doi.org/10.3847/1538-4357/ab2f8e, arXiv:1908.07557 .

[21] Emsenhuber, A. *et al.* Realistic On-the-fly Outcomes of Planetary Collisions. II. Bringing Machine Learning to N-body Simulations. *The Astrophysical Journal* **891** (1), 6 (2020). https://doi.org/10.3847/1538-4357/AB6DE5, arXiv:2001.00951 .

[22] Emsenhuber, A., Asphaug, E., Cambioni, S., Gabriel, T. S. J. & Schwartz, S. R. Collision Chains among the Terrestrial Planets. II. An Asymmetry between Earth and Venus. *The Planetary Science Journal* **2** (5), 199 (2021). https://doi.org/10.3847/PSJ/AC19B1 .

[23] Asphaug, E., Emsenhuber, A., Cambioni, S., Gabriel, T. S. J. & Schwartz, S. R. Collision Chains among the Terrestrial Planets. III. Formation of the Moon. *The Planetary Science Journal* **2** (5), 200 (2021). https://doi.org/10.3847/PSJ/AC19B2 .

[24] Gabriel, T. S. J. *et al.* Gravity-dominated Collisions: A Model for the Largest Remnant Masses with Treatment for "Hit and Run" and Density Stratification. *The Astrophysical Journal* **892** (1), 40 (2020). https://doi.org/10.3847/1538-4357/ab528d .

[25] Gabriel, T. S. J. & Allen-Sutter, H. Dependencies of Mantle Shock Heating in Pairwise Accretion. *The Astrophysical Journal Letters* **915** (2), L32 (2021). https://doi.org/10.3847/2041-8213/abffd1 .

[26] Cambioni, S. *et al.* Realistic On-the-fly Outcomes of Planetary Collisions: Machine Learning Applied to Simulations of Giant Impacts. *The Astrophysical Journal* **875** (1), 40 (2019). https://doi.org/10.3847/1538-4357/ab0e8a, arXiv:1903.04507 .

[27] Jutzi, M., Holsapple, K., Wünneman, K. & Michel, P. Modeling asteroid collisions and impact processes. *Asteroids IV* 679–699 (2015). https://doi.org/10.48550/arXiv.1502.01844, arXiv:1502.01844 .

[28] Benz, W., Cameron, A. G. & Melosh, H. J. The origin of the Moon and the single-impact hypothesis III. *Icarus* **81** (1), 113–131 (1989). https://doi.org/10.1016/0019-1035(89)90129-2 .

[29] Meier, T., Reinhardt, C. & Stadel, J. G. The EOS/resolution conspiracy: Convergence in proto-planetary collision simulations. *Monthly Notices of the Royal Astronomical Society* **505** (2), 1806–1816 (2021). https://doi.org/10.1093/mnras/stab1441, arXiv:2104.03559 .

[30] Senft, L. E. & Stewart, S. T. Impact crater formation in icy layered terrains on Mars. *Meteoritics & Planetary Science* **43** (12), 1993–2013 (2008). https://doi.org/10.1111/J.1945-5100.2008.TB00657.X .

[31] Senft, L. E. & Stewart, S. T. Modeling the morphological diversity of impact craters on icy satellites. *Icarus* **214** (1), 67–81 (2011). https://doi.org/10.1016/J.ICARUS.2011.04.015 .

[32] McKinnon, W. B. *et al.* Origin of the Pluto–Charon system: Constraints from the New Horizons flyby. *Icarus* **287**, 2–11 (2017). https://doi.org/10.1016/J.ICARUS.2016.11.019 .

[33] Bernstein, G. M. *et al.* The Size Distribution of Trans-Neptunian Bodies. Tech. Rep. 3 (2004). 0308467.

[34] Fraser, W. C., Brown, M. E., Morbidelli, A., Parker, A. & Batygin, K. The absolute magnitude distribution of kuiper belt objects. *Astrophysical Journal* **782** (2), 100 (2014). https://doi.org/10.1088/0004-637X/782/2/100, arXiv:1401.2157 .

[35] Adams, E. R. *et al.* De-biased populations of Kuiper belt objects from the deep ecliptic survey. *Astronomical Journal* **148** (3), 55 (2014). https://doi.org/10.1088/0004-6256/148/3/55 .

[36] Morbidelli, A., Nesvorny, D., Bottke, W. F. & Marchi, S. A re-assessment of the Kuiper belt size distribution for sub-kilometer objects, revealing collisional equilibrium at small sizes. *Icarus* **356**, 114256 (2021). https://doi.org/10.1016/J.ICARUS.2020.114256, arXiv:2012.03823 .

[37] Malhotra, R. Resonant Kuiper belt objects: a review. *Geoscience Letters* **6** (1), 12 (2019). https://doi.org/10.1186/s40562-019-0142-2 .

[38] Bierson, C. J. & Nimmo, F. Using the density of Kuiper Belt Objects to constrain their composition and formation history. *Icarus* **326**, 10–17 (2019). https://doi.org/10.1016/j.icarus.2019.01.027 .

[39] Jutzi, M. & Asphaug, E. Forming the lunar farside highlands by accretion of a companion moon. *Nature* **476** (7358), 69–72 (2011). https://doi.org/10.1038/nature10289, arXiv:arXiv:1603.04536 .

[40] Bertrand, T. & Forget, F. Observed glacier and volatile distribution on Pluto from atmosphere-topography processes. *Nature* **540** (7631), 86–89 (2016). https://doi.org/10.1038/nature19337 .

[41] McKinnon, W. B., Prialnik, D., Stern, S. A. & Coradini, A. Structure and Evolution of Kuiper Belt Objects and Dwarf Planets. *The Solar System Beyond Neptune* (January 2008), 213 (2008) .

[42] Desch, S. J., Cook, J. C., Doggett, T. C. & Porter, S. B. Thermal evolution of Kuiper belt objects, with implications for cryovolcanism. *Icarus* **202** (2), 694–714 (2009). https://doi.org/10.1016/j.icarus.2009.03.009 .

[43] Desch, S. J. Density of Charon formed from a disk generated by the impact of partially differentiated bodies. *Icarus* **246** (C), 37–47 (2015). https://doi.org/10.1016/j.icarus.2014.07.034 .

[44] Rubin, M. E., Desch, S. J. & Neveu, M. The effect of Rayleigh-Taylor instabilities on the thickness of undifferentiated crust on Kuiper Belt Objects. *Icarus* **236**, 122–135 (2014). https://doi.org/10.1016/j.icarus.2014.03.047 .

[45] Neumann, W., Jaumann, R., Castillo-Rogez, J., Raymond, C. A. & Russell, C. T. Ceres' partial differentiation: undifferentiated crust mixing with a water-rich mantle. *Astronomy and Astrophysics* **633**, 1–27 (2020). https://doi.org/10.1051/0004-6361/201936607 .

[46] Bierson, C. J., Nimmo, F. & McKinnon, W. B. Implications of the observed Pluto–Charon density contrast. *Icarus* **309**, 207–219 (2018). https://doi.

org/10.1016/j.icarus.2018.03.007 .

[47] Bagheri, A. *et al.* The tidal–thermal evolution of the Pluto–Charon system. *Icarus* **376**, 114871 (2022). https://doi.org/10.1016/j.icarus.2021.114871, arXiv:2109.13206 .

[48] Canup, R. M. *On the Origin of the Pluto System* (University of Arizona Press, 2021).

[49] Kimura, J. & Kamata, S. Stability of the subsurface ocean of pluto. *Planetary and Space Science* **181**, 104828 (2020). https://doi.org/10.1016/J.PSS.2019.104828 .

[50] Bierson, C. J., Nimmo, F. & Stern, S. A. Evidence for a hot start and early ocean formation on Pluto. *Nature Geoscience 2020 13:7* **13** (7), 468–472 (2020). https://doi.org/10.1038/s41561-020-0595-0 .

[51] Robuchon, G. & Nimmo, F. Thermal evolution of Pluto and implications for surface tectonics and a subsurface ocean. *Icarus* **216** (2), 426–439 (2011). https://doi.org/10.1016/J.ICARUS.2011.08.015 .

[52] Hammond, N. P., Barr, A. C. & Parmentier, E. M. Recent tectonic activity on Pluto driven by phase changes in the ice shell. *Geophysical Research Letters* **43** (13), 6775–6782 (2016). https://doi.org/10.1002/2016GL069220, arXiv:1606.04840 .

[53] Bagheri, A., Khan, A., Efroimsky, M., Kruglyakov, M. & Giardini, D. Dynamical evidence for Phobos and Deimos as remnants of a disrupted common progenitor. *Nature Astronomy* 2–6 (2021). https://doi.org/10.1038/s41550-021-01306-2 .

[54] Le Roy, L. *et al.* Inventory of the volatiles on comet 67P/Churyumov-Gerasimenko from Rosetta/ROSINA. *Astronomy and Astrophysics* **583** (2015). https://doi.org/10.1051/0004-6361/201526450 .

[55] Thompson, S. & Lauson, H. Improvements in the CHART-D Radiation-hydrodynamic Code III: Revised Analytic Equations of State. Tech. Rep., Sandia National Laboratories (1972).

[56] Thompson, S. ANEOS Analytic Equations of State for shock physics codes input manual. *SANDIA Report* **3** (1990) .

[57] Reufer, A. *et al.* Models of high velocity impacts into dust-covered ice: Application to Martian northern lowlands. *Planetary and Space Science* **58** (10), 1160–1168 (2010). https://doi.org/10.1016/j.pss.2010.04.008 .

[58] Reufer, A. *Collisions in Planetary Systems.* Ph.D. thesis, Universität Bern (2011).

[59] Reufer, A., Meier, M. M., Benz, W. & Wieler, R. A hit-and-run giant impact scenario. *Icarus* **221** (1), 296–299 (2012). https://doi.org/10.1016/j.icarus.2012.07.021 .

[60] Asphaug, E. & Reufer, A. Late origin of the Saturn system. *Icarus* **223** (1), 544–565 (2013). https://doi.org/10.1016/j.icarus.2012.12.009 .

[61] Collins, G. S., Melosh, H. J. & Ivanov, B. A. Modeling damage and deformation in impact simulations. *Meteoritics and Planetary Science* **39** (2), 217–231 (2004). https://doi.org/10.1111/j.1945-5100.2004.tb00337.x .

[62] Ballantyne, H. A. *et al.* Investigating the Feasibility of an Impact-Induced Martian Dichotomy. *Icarus (in review)* (2022) .

[63] Bray, V. J., Collins, G. S., Morgan, J. V., Melosh, H. J. & Schenk, P. M. Hydrocode simulation of Ganymede and Europa cratering trends – How thick is Europa's crust? *Icarus* **231**, 394–406 (2014). https://doi.org/10.1016/J.ICARUS.2013.12.009 .

[64] Silber, E. A., Osinski, G. R., Johnson, B. C. & Grieve, R. A. Effect of impact velocity and acoustic fluidization on the simple-to-complex transition of lunar craters. *Journal of Geophysical Research: Planets* **122** (5), 800–821 (2017). https://doi.org/10.1002/2016JE005236 .

[65] Beeman, M., Durham, W. B. & Kirby, S. H. Friction of ice. *Journal of Geophysical Research* **93** (B7), 7625–7633 (1988). https://doi.org/10.1029/JB093iB07p07625 .

Bibliography

C. A. Denton, B. C. Johnson, S. Wakita, A. M. Freed, H. J. Melosh, and S. A. Stern. Pluto's Antipodal Terrains Imply a Thick Subsurface Ocean and Hydrated Core. *Geophysical Research Letters*, 48(2):e2020GL091596, jan 2021. ISSN 1944-8007. doi: 10.1029/2020GL091596.

B. C. Johnson, T. J. Bowling, A. J. Trowbridge, and A. M. Freed. Formation of the Sputnik Planum basin and the thickness of Pluto's subsurface ocean. *Geophysical Research Letters*, 43(19):10,068–10,077, oct 2016. doi: 10.1002/2016GL070694.

F. Nimmo, D. P. Hamilton, W. B. McKinnon, P. M. Schenk, R. P. Binzel, C. J. Bierson, R. A. Beyer, J. M. Moore, S. A. Stern, H. A. Weaver, C. B. Olkin, L. A. Young, and K. E. Smith. Reorientation of Sputnik Planitia implies a subsurface ocean on Pluto. *Nature 2016 540:7631*, 540(7631):94–96, nov 2016. ISSN 1476-4687. doi: 10.1038/nature20148.

P. M. Schenk, R. A. Beyer, W. B. McKinnon, J. M. Moore, J. R. Spencer, O. L. White, K. Singer, F. Nimmo, C. Thomason, T. R. Lauer, S. Robbins, O. M. Umurhan, W. M. Grundy, S. A. Stern, H. A. Weaver, L. A. Young, K. E. Smith, and C. Olkin. Basins, fractures and volcanoes: Global cartography and topography of Pluto from New Horizons. *Icarus*, 314:400–433, nov 2018. ISSN 0019-1035. doi: 10.1016/J.ICARUS.2018.06.008.

S. A. Stern, F. Bagenal, K. Ennico, G. R. Gladstone, W. M. Grundy, W. B. McKinnon, J. M. Moore, C. B. Olkin, J. R. Spencer, H. A. Weaver, L. A. Young, T. Andert, J. Andrews, M. Banks, B. Bauer, J. Bauman, O. S. Barnouin, P. Bedini, K. Beisser, R. A. Beyer, S. Bhaskaran, R. P. Binzel, E. Birath, M. Bird, D. J. Bogan, A. Bowman, V. J. Bray, M. Brozovic, C. Bryan, M. R. Buckley, M. W. Buie,

B. J. Buratti, S. S. Bushman, A. Calloway, B. Carcich, A. F. Cheng, S. Conard, C. A. Conrad, J. C. Cook, D. P. Cruikshank, O. S. Custodio, C. M. Dalle Ore, C. Deboy, Z. J. Dischner, P. Dumont, A. M. Earle, H. A. Elliott, J. Ercol, C. M. Ernst, T. Finley, S. H. Flanigan, G. Fountain, M. J. Freeze, T. Greathouse, J. L. Green, Y. Guo, M. Hahn, D. P. Hamilton, S. A. Hamilton, J. Hanley, A. Harch, H. M. Hart, C. B. Hersman, A. Hill, M. E. Hill, D. P. Hinson, M. E. Holdridge, M. Horanyi, A. D. Howard, C. J. Howett, C. Jackman, R. A. Jacobson, D. E. Jennings, J. A. Kammer, H. K. Kang, D. E. Kaufmann, P. Kollmann, S. M. Krimigis, D. Kusnierkiewicz, T. R. Lauer, J. E. Lee, K. L. Lindstrom, I. R. Linscott, C. M. Lisse, A. W. Lunsford, V. A. Mallder, N. Martin, D. J. McComas, R. L. McNutt, D. Mehoke, T. Mehoke, E. D. Melin, M. Mutchler, D. Nelson, F. Nimmo, J. I. Nunez, A. Ocampo, W. M. Owen, M. Paetzold, B. Page, A. H. Parker, J. W. Parker, F. Pelletier, J. Peterson, N. Pinkine, M. Piquette, S. B. Porter, S. Protopapa, J. Redfern, H. J. Reitsema, D. C. Reuter, J. H. Roberts, S. J. Robbins, G. Rogers, D. Rose, K. Runyon, K. D. Retherford, M. G. Ryschkewitsch, P. Schenk, E. Schindhelm, B. Sepan, M. R. Showalter, K. N. Singer, M. Soluri, D. Stanbridge, A. J. Steffl, D. F. Strobel, T. Stryk, M. E. Summers, J. R. Szalay, M. Tapley, A. Taylor, H. Taylor, H. B. Throop, C. C. Tsang, G. L. Tyler, O. M. Umurhan, A. J. Verbiscer, M. H. Versteeg, M. Vincent, R. Webbert, S. Weidner, G. E. Weigle, O. L. White, K. Whittenburg, B. G. Williams, K. Williams, S. Williams, W. W. Woods, A. M. Zangari, and E. Zirnstein. The pluto system: Initial results from its exploration by New Horizons. *Science*, 350(6258), 2015. ISSN 10959203. doi: 10.1126/science.aad1815.

Chapter 6

Acknowledgements

Firstly, and above all, I would like to thank Martin Jutzi for guiding me through my PhD experience. As one would expect, your knowledge and passion for science has inspired me throughout; however, your unwavering support and consistent belief in me even when I did not necessarily believe in myself has been invaluable. I may have taken an unconventional approach at times, but you always gave me freedom to complete tasks "Harry style", riding the rather tumultuous journey along with me right until it reaches the light on the other side.

Next, I would like to thank my colleagues associated with the geodynamics group at ETH, for their constant support and scientific discussion. These include: Gregor Golabek, who I could always count on for ideas over a cold evening beverage, be it on the topic of the Martian Dichotomy or an associated name for a musical collaboration; Paul Tackley, whose voice would always be heard, both in countless Zoom meetings and in unforgettable Karaoke nights; Antoine Rozel, who would never be shy to help debug code over screen share, or discuss the quality of Swiss "croissants"; and finally, Karwai Cheng, who I have shared the PhD journey with from day one, even if I never turned up to our shared office space.

I would also like thank my other collaborators, be it located nearby or over the pond, for the exciting new discoveries that our discussions have led (and continue to lead) to. These include Erik Asphaug, Adeene Denton, Alexandre Emsenhuber and Steve Mojzsis.

At the more informal end, I would like to thank all of the friends that I have made at the University of Bern. Your presence may have occasionally made this

wild PhD ride even wilder, but what's life without some excitement. In particular, I would like to thank my office-mates: Tobias Meier for always sleeping on the sofa "bed" when sharing a room at conferences; Beatrice Kulterer for allowing me to keep her poster tube indefinitely (and for her continued support for my pet snake, Noah); Marko Sestovic, for always bringing the debate whether its on the optimum colour of bananas or the solution to unsolvable conundrums; and Erik Meier for his consistent delivery of the most potent Mexican snacks (and beverages). Beyond the office, I would like to thank Lokesh Mishra for his willingness to accompany me on spontaneous music events, be it performed by others or by the one and only Chai Tee; Esther Linder, for extensive chats on the precise logistics of world travel; and Thibaut Roger for the countless road trips, along with a particular helping hand in the construction of my wedding cake. To any others at Gesellschaftsstrasse 6 that I have missed, don't think that I have forgotten you, I just need to cut this off eventually...

I would also like to thank my fellow members of the premier metal band in the world: Omissis. It is always an honour to share the stage with some of my best friends, and the constant support from the Omi-family will always be appreciated.

I would like to thank my family for always being behind me, even when we've been on the phone for more than 3 hours and have completely forgotten what we were supposed to be discussing. In particular, I would like to thank my mum, who will always proudly wear her t-shirt declaring my Swiss PhD status no matter the strange looks (maybe you will need an upgrade when I become a doctor).

Finally, I thank my wonderful wife, Kennedy. You have been my rock throughout this journey to Switzerland that we embarked on together, and I couldn't possibly have made it this far without you.

Declaration of consent

on the basis of Article 18 of the PromR Phil.-nat. 19

Name/First Name: Ballantyne/Harry

Registration Number: 18-124-958

Study program: PhD in Physics with special qualification in Astronomy

Bachelor ☐ Master ☐ Dissertation ☑

Title of the thesis: Planetary-Scale Impacts and their Geophysical Consequences

Supervisor: PD Dr. Martin Jutzi

I declare herewith that this thesis is my own work and that I have not used any sources other than those stated. I have indicated the adoption of quotations as well as thoughts taken from other authors as such in the thesis. I am aware that the Senate pursuant to Article 36 paragraph 1 litera r of the University Act of September 5th, 1996 and Article 69 of the University Statute of June 7th, 2011 is authorized to revoke the doctoral degree awarded on the basis of this thesis.
For the purposes of evaluation and verification of compliance with the declaration of originality and the regulations governing plagiarism, I hereby grant the University of Bern the right to process my personal data and to perform the acts of use this requires, in particular, to reproduce the written thesis and to store it permanently in a database, and to use said database, or to make said database available, to enable comparison with theses submitted by others.

3012 Bern, 15.08.2022

Place/Date

Signature